Studies on the gamma-ray burst phenomenon and on its use to probe the high redshift universe

S.D. Vergani

PhD Thesis

Dublin City University

School of Physical Sciences

Supervisors:

Prof. E. J. A. Meurs

Dr. E. Cunningham

October 2008

Vol. 1/1

I hereby certify that this material, which I now submit for assessment on the programme of study leading to the award of PhD is entirely my own work, that I have exercised reasonable care to ensure that the work is original, and does not to the best of my knowledge breach any law of copyright, and has not been taken from the work of others save and to the extent that such work has been cited and acknowledged within the text of my work.

Signed:

(Candidate) ID No.: 55149588
Date: 29 October 2008

Too soon from the cave, too far from the stars.

We must ignore the whispers from the cave which say ‘stay’.

We must listen to the stars that say ‘come’.

- Ray Bradbury -

To Daniele

To my Mum, to Tommaso

Contents

List of Figures

List of Tables

S.D. Vergani

Studies on the gamma-ray burst phenomenon
and on its use to probe the high redshift universe

Abstract

Gamma-ray bursts (GRBs) are an enigmatic phenomenon whose physics and origins are still to be fully understood. Furthermore, thanks to their exceptional brightness they can be used as a tool to retrieve information on the high redshift universe. In my thesis work, I explore some of the research areas that can be investigated using GRBs.

Using the REM observations of GRB 060418 and GRB 060607, the initial Lorentz factor of the GRB explosion could be measured. The value found for both bursts is $\Gamma_0 \sim 400$ and the inferred radius at which the forward shock with the external medium took place is of $R \approx 10^{17}$ cm, in agreement with theoretical predictions. The analysis of the X-ray-to-optical spectral energy distribution of 22 GRBs shows that synchrotron emission works well for most afterglows as a simple spectral model, on the other hand the dynamical model of the expansion is difficult to reconcile with the observations. A low dust-to-gas ratio is confirmed. The X-ray radiation during X-ray flares and the initial steep light curve decay phases, is not (or not only) due to the afterglow emission.

Another way to investigate the ISM medium associated with the GRB is through high resolution spectroscopy of GRB afterglows. I report results on the analysis of the spectrum of GRB 050922C showing a highly complex circumburst environment. Distances from less than 200 pc to more than 700 pc have been associated with the different components, allowing a better representation of the medium surrounding the GRB. Using the entire UVES GRB spectra sample, I carried out a statistical study on the MgII absorbers present along the GRB lines of sight. The results of the survey confirm the unexplained excess of strong (equivalent width $W_r > 1$ Å) MgII absorption systems (and more generally of sub-DLAs) compared to QSO lines of sight, and support the idea that current sample of GRB lines of sight could be biased by a subtle gravitational lensing effect.

Considering the class of short duration GRBs, I worked on the data of the afterglow GRB 070707. Its light curve shows a very steep decay challenging the external shock models. Deep VLT observations reveal a very faint host galaxy at $m_R = 27.3$, suggesting caution when associating short GRBs with bright, offset galaxies.

Acknowledgements

This thesis work has been possible thanks to collaboration with many people working in different European Countries, mainly Italy and France, where I also spent part of the last three years.

IRELAND

Work I would like to thank my supervisor, Evert J. A. Meurs, for giving me the opportunity to do this PhD and for the many experiences I could take advantage of thanks to the freedom he afforded me. I would also like to thank all the DCU staff, in particular my supervisor at DCU, Eamonn Cunnigham, for his kindness and endless help especially with all the bureaucracy, Laura Norci for the irreplaceable 'Italian-side' support, John Costello, Vincent Ruddy, Eilish McLoughlin, Tony Cafolla, Enda McGlynn and Ray Murphy.

My gratitude goes also to Brian McBreen and Felix Aharonian for the interest expressed for my research and my career and of course to the Science Foundation of Ireland for paying me.

Friends What would have been my life in Dublin without my friends??? First of all my two 'little Irish boys' Colin and Paul. Thanks guys for all the special moments we shared, for all the pacience you had with me and for trying to make me feel home! A big thanks also to the DCU handball team, fundamental for my start up life in Dublin and in particular to Melanie with whom I shared house hunting, a fantastic apartment and lots of laughs! GRAZIE to my 'Italian friends in a foreign Land' Elisa, Linda e lo Sgabici: a real blessing for my last months in DIAS and in Ireland! Linda, your are simply marvellous. Stefano, who would have bet that Dublin would have brought us such a friendship?!

FRANCE

Work My special thanks go to Robert Mochovitch, who suggested me to apply for the EARA-EST Marie Curie grant and come to IAP and therefore being the cause of my meeting with (what I thought to be) the most irritating man I have ever met in my life, a 'certain' Patrick Petitjean :) ...Cher Patrick, things have changed a lot since our first meeting! Now I bless the day we met: to work with you is really challenging! There are not many people I appreciate as much as you... Merçi!!!

I would also like to thank the IAP staff, in particular Emmanuel Rollinde de Beaumont for his warm welcoming smile, and Elisabeth Vangioni, Patrick Boissé and Frédéric Daigne for the kind attention they always demonstrated in my regards.

My sincere gratitude goes also to Paolo Goldoni for ending my search for a post-doc position :)

Friends A huge thanks to the marvelous *los Pimpollos* family!!! Pasquier, without your help I would have really been lost in spectra!

Merci beaucoup also to all the other people with which I enjoyed my (long) Parisian parenthesis, in particular to Mauro e Lisi.

ITALIA

Work A large part of this thesis work has been achieved thanks to my participation in the Italian Swift-XRT Team in Merate and in the REM and MISTICI collaboration. I would like to thank all the people who made this possible, in particular Guido Chincarini, Niel Gehrels, Emilio Molinari, Fabrizio Fiore, Pat Romano, Cristiano Guidorzi, Paolo D'Avanzo, Giampiero Tagliaferri and Filippo Zerbi. A special thank to my XRT-trainer and lunch-mate Alberto Moretti, and to Stefano Covino for all his patience and his essential help!

I'd like also to thank Gabriele Ghisellini for the interest expressed for my research and my career e Giancarlo Ghirlanda, a wonderful person and conference mate.

Friends This Grazie is for you all, my Italian friends spread in the world! In particular I want to thank Valentina, Silvia and Francy for their valuable support in the difficult moments.

REST of the WORLD

Muchas Graçias to my external examiner Dr Alberto J. Castro-Tirado, an extremely kind person, with whom it has been very interesting to discuss my thesis and thanks to, I will always have a nice souvenir of my VIVA.

Tak to Jens Jorth for the very interesting period I spent as a visitor at the amazing DARK Cosmology Centre in Copenhagen.

Dank to Paul Vreeswijk for his help and his friendship. Paul, it's very fun for me to think about the way I looked at you as an unreachable person when I saw your name on papers or when I saw you speaking at conferences and then, a few years later, being velibbing with you in Paris!

And, to end, I want to thank the people this thesis is dedicated to: my Mum, who always supported my choice to go to Dublin and to go on with my research work; Tommaso who always stands me and loves me and who gave me a fundamental IT help; and Daniele, a really amazing friend, without whom, simply, this thesis would not be here.

Chapter 1

Introduction

Gamma-ray bursts (GRBs) were discovered in the late Sixties (Klebesadel et al. 1973) by military satellites devoted to detecting nuclear explosions in space. They are brief, intense flashes of gamma radiation, coming from random directions in space (see Fig. 1.1).

Over the years, several spaceborn missions have studied these enigmatic objects, among which *GINGA*, *BeppoSAX*, *HETE-II* and *INTEGRAL*. The most comprehensive sample was collected by the BATSE instrument onboard the *Compton Gamma-Ray Observatory*, including more than 3000 events.

Currently, most of the space observations are carried out by the *Swift* observatory (Fig. 1.2), a spacecraft specifically devoted to GRB science. In addition to the gamma-ray detector (BAT), *Swift* carries two telescopes to observe at optical (UVOT) and X-ray

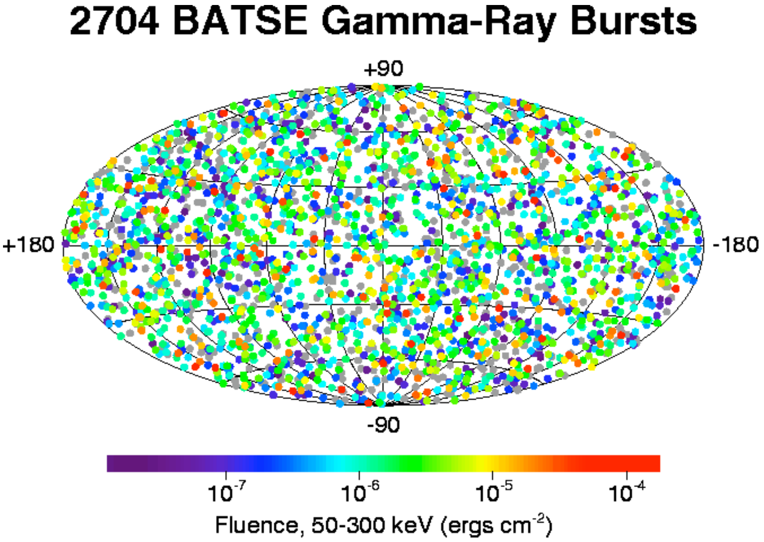

Figure 1.1 Angular distribution in Galactic coordinates of BATSE GRBs (see http://f64.nsstc.nasa.gov/batse/grb/skymap/).

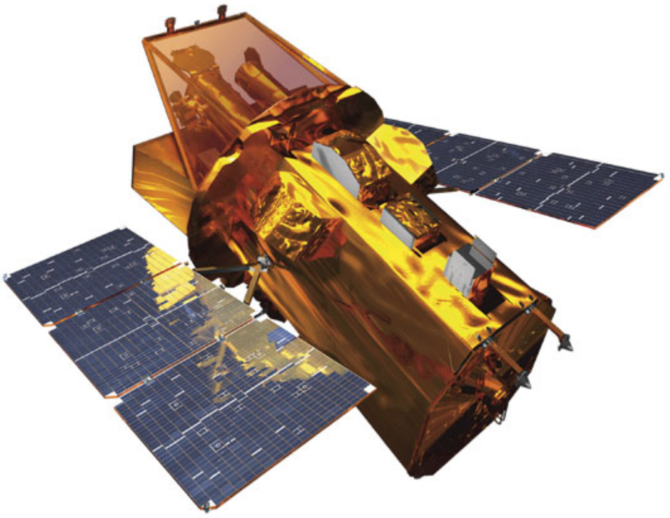

Figure 1.2 3D rendered image of the *Swift* satellite (Credit NASA).

(XRT) frequencies (see Sect. 2.2). Very recently, 11 June 2008, the Fermi Gamma-ray Space Telescope has been launched. This satellite will be able to detect the GRB emission over a very wide energy range, extending from about 10 keV to 300 GeV.

There are two main phases of the gamma-ray burst phenomenon: the so-called *prompt emission* and *afterglow*. The prompt emission occurs primarily at gamma-ray energies, and lasts at most few minutes. The afterglow is a multiwavelength emission covering a very broad spectral range (from radio to X-rays) that follows the main GRB. It can be studied on very different timescales, from few seconds after the burst up to a year or more.

GRBs are interesting from different points of view. First of all, its physics is not yet fully determined. Even if the overall properties of the prompt and afterglow emission have found a theoretical explanation accepted by almost all the community, there are still many observational results left without a solid explanation, in particular concerning the engine producing the GRBs. Furthermore, since GRB progenitors are thought to be particular types of stars at the final stages of their lives, the study of GRB is also connected to the study of stellar evolution. Finally, being bright extragalactic objects detectable also in the far universe, GRBs are also of cosmological interest, allowing the study of the properties and the evolution of galaxies and of the intergalactic medium.

1.1 Observational properties

1.1.1 The prompt emission

The prompt emission is the proper “gamma-ray burst”. It is usually observed in the gamma-rays and lasts between tenths and tens of seconds. GRBs show very different temporal structures: some have smooth, broad profiles, while others have large variability on timescales much shorter than the overall duration (Fig. 1.3). Some have a weak precursor followed by a quiescent period.

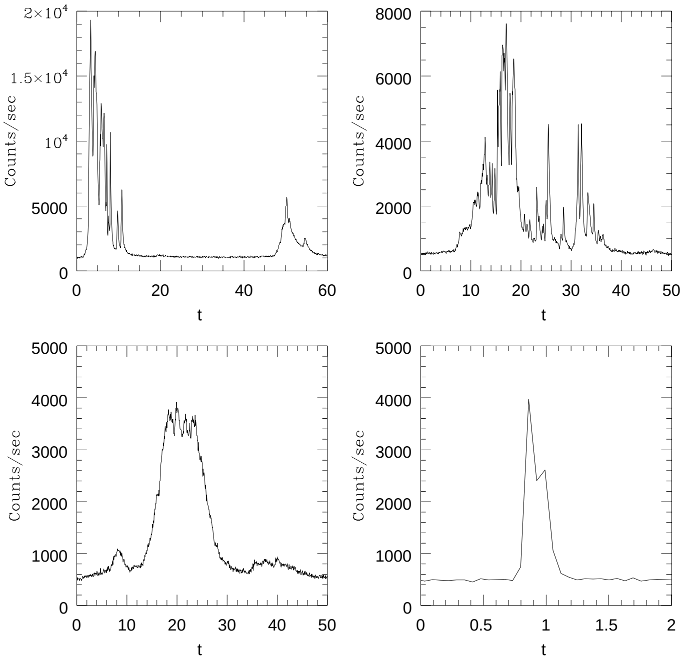

Figure 1.3 Examples of gamma-ray light curves as observed by BATSE. Note the different morphologies: some profiles are smooth, others are spiky. Variability can be present on timescales much shorter than the burst duration. Some quiescent intervals are also apparent (see http://f64.nsstc.nasa.gov/batse/grb/lightcurve/).

In contrast to their complex temporal behaviour, GRB spectra are relatively simple. In the vast majority of cases, they are well described by a broken power law (Band et al. 1993). Thus, they are characterised by three fundamental parameters: the peak energy (at which most of the energy is radiated), and the power-law slopes, at low and high energy. Typically, the peak energy is located in the soft gamma-ray/hard X-ray interval, $100 - 1000$ keV. High-energy emission (in the MeV-GeV range) has been reported for a few cases (e.g. Hurley et al. 1994).

Burst spectra show significant temporal evolution. Both the peak energy and the spectral slopes change during the burst (Ghirlanda et al. 2002). The general trend is from hard to soft, but in case of multi-peaked events the patterns are more complicated (Ford et al. 1995).

An important classification can be made for GRBs, mostly based on their temporal properties. The distribution of burst durations, as measured by the BATSE instrument, is clearly bimodal, with a gap at about 2 s (Kouveliotou et al. 1993). This led to the definition of two classes of GRBs called short and long (also indicated as SGRB and LGRB, respectively). As observed by BATSE, the short events comprise $\sim 1/4$ of the total. *Swift* appears to be less sensitive to short GRBs, due to its different spectral response, and only less than $\sim 1/10$ of events it detects are short. In the BATSE sample, the time bimodality is confirmed by spectral properties: shorter bursts are on average harder (Fig. 1.4) and they have a negligible spectral lag between different energy bands of the prompt emission. However, *Swift* observations showed that this short/hard vs. long/soft dichotomy not always holds, leading to new classification schemes (Zhang 2006; Gehrels et al. 2006) that take into account also progenitors and host galaxy properties (see Sect. 1.3 and Chapter 5).

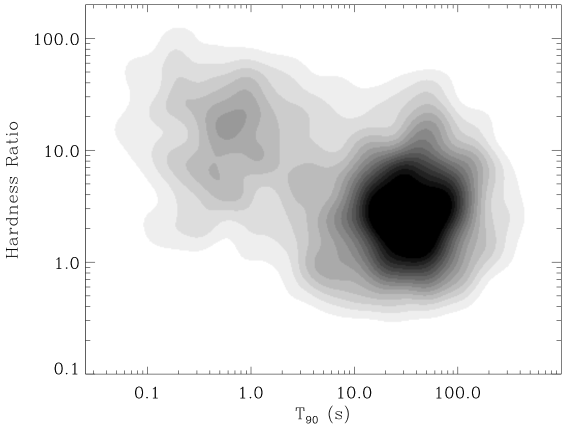

Figure 1.4 Distribution of BATSE bursts in the duration versus hardness ratio plane. T_{90} is the time encompassing the 5'th to the 95'th percentiles of the total counts in the instrument gamma energy range($20 - 2000$keV for BATSE). Short and long bursts are distinguished both spectrally and temporally. From Lazzati et al. (2001).

Thanks in particular to the *BeppoSAX* and *HETE-II*-II satellites, a class of softer events peaking at lower energy ($2 - 50$ keV) has been discovered, consisting in the so-called X-ray rich GRBs and X-ray flashes (XRR or XRFs; Heise 2003; Lamb et al. 2004;

Sakamoto et al. 2004). The present evidence indicates that XRFs are likely low-energy extensions of classical GRBs (Sakamoto et al. 2005). Apart from the lower peak energy, both classes have similar spectra and the same duration range. On the other hand, XRF afterglow light curves tend to have a longer shallow decay compared to those of GRBs, and the overall luminosity of XRF X-ray afterglows is systematically smaller by a factor of two or more compared to that of GRBs (Sakamoto et al. 2008). Nevertheless, the three classes seem to form a continuum and therefore to belong to the same phenomenon.

1.1.2 Afterglows

The main problem in the study of GRBs has for long been the lack of a precise localization due to the poor spatial resolution of gamma-ray detectors. Only in the last decade have instruments become sensitive enough to provide accurate positions to GRBs, allowing meaningful searches at longer wavelengths.

The breakthrough in GRB research happened about a decade ago, with the discovery of long-lasting X-ray, optical and radio counterparts (afterglows) to long-duration GRBs (Costa et al. 1997; van Paradijs et al. 1997; Frail et al. 1997). This first counterpart of a long-duration GRB was discovered thanks to the *BeppoSAX* satellite (see Fig. 1.5). In the following years, several afterglows could be discovered and studied (now more than 300 are known).

Afterglows for short GRBs (Fig. 1.6) were discovered only in 2005 (e.g. Gehrels et al. 2005; Covino et al. 2006c; Hjorth et al. 2005b) so that our understanding of these events is comparably smaller.

1.1.2.1 Light curves

The afterglow flux shows a steady decay with a powerlaw time dependence. One or more breaks are usually observed in the well studied cases, where the decay rate changes. In addition, there are examples of irregular light curves, where there is short-term variability superimposed on the general decay, and in some cases bumps and rebrightenings emerge. This has been demonstrated both in the X-ray, where powerful flares are often present in the early-time decay, (e.g. Burrows et al. 2005, see Figs. 3.1 and 3.2 for examples) and optical ranges, where variability is usually less pronounced (e.g. Galama et al. 1998; Bersier et al. 2003; Stanek et al. 2007).

The X-ray Telescope (XRT) onboard *Swift* has provided a large sample of X-ray light curves, showing the emergence of a “canonical” behaviour (Nousek et al. 2006). In the first

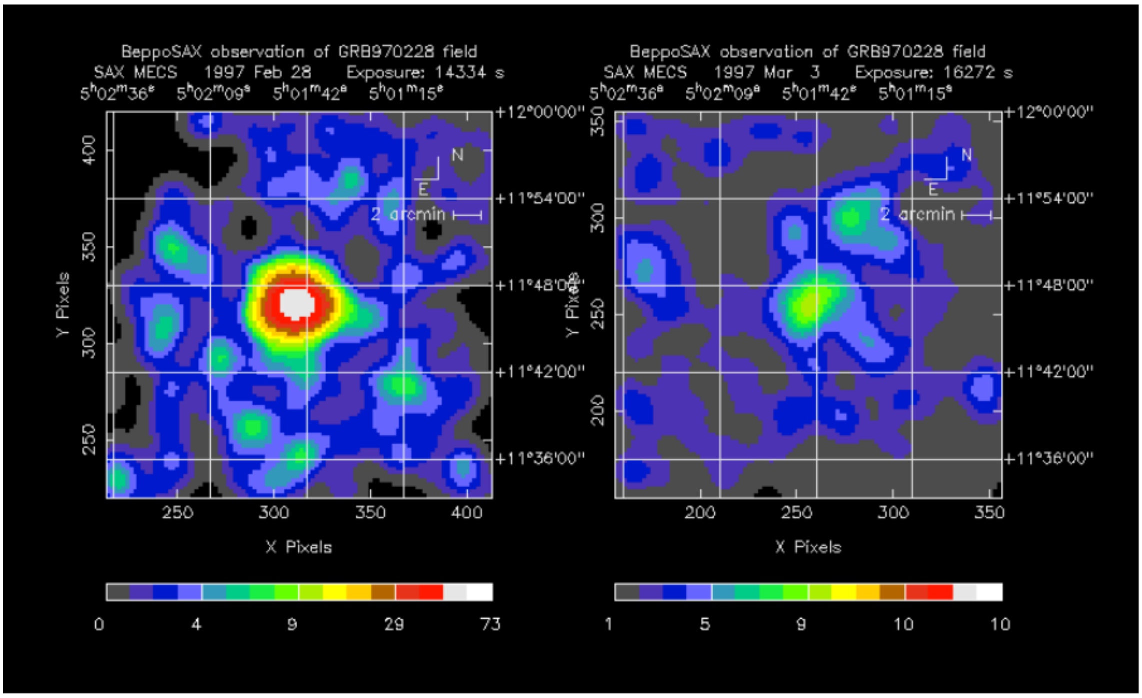

Figure 1.5 GRB970228 X-ray afterglow observed a few hours after the prompt event (left) and 3 days after (right). From Costa et al. (1997).

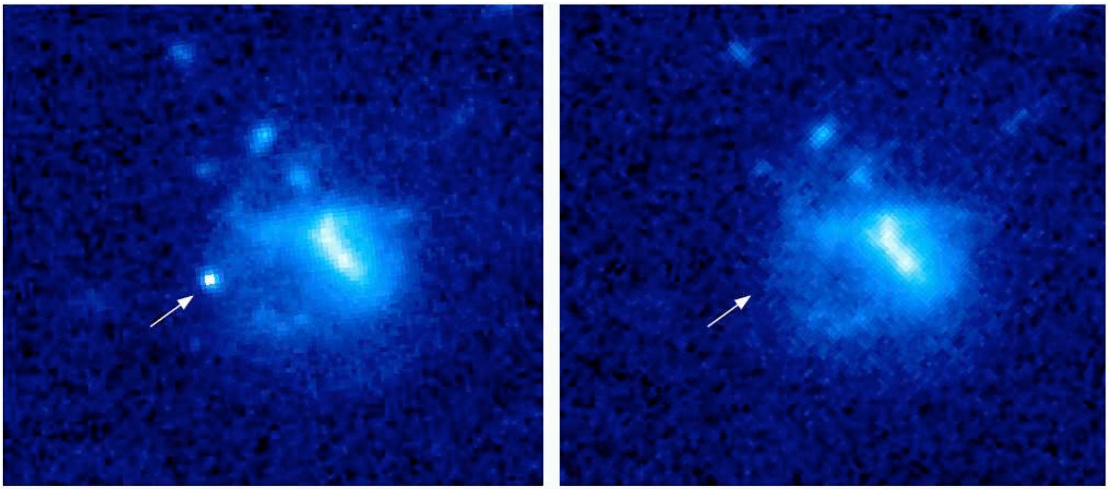

Figure 1.6 Hubble Space Telescope images from Berger (2006) of the field of GRB 050709. In the left panel the afterglow (indicated by the arrow) is clearly evident, while it is faded away in the right images taken at later times.

$\sim 100 - 500$ s, there is a phase of steep decay (Tagliaferri et al. 2005b), which subsequently becomes very shallow (sometimes almost constant) to steepen again around $\sim 1\ 000 - 10\ 000$ s. Flares are often superimposed on this general decay (see Fig. 1.7).

At optical wavelengths, the light curves are more diversified (see Fig. 1.8). In some

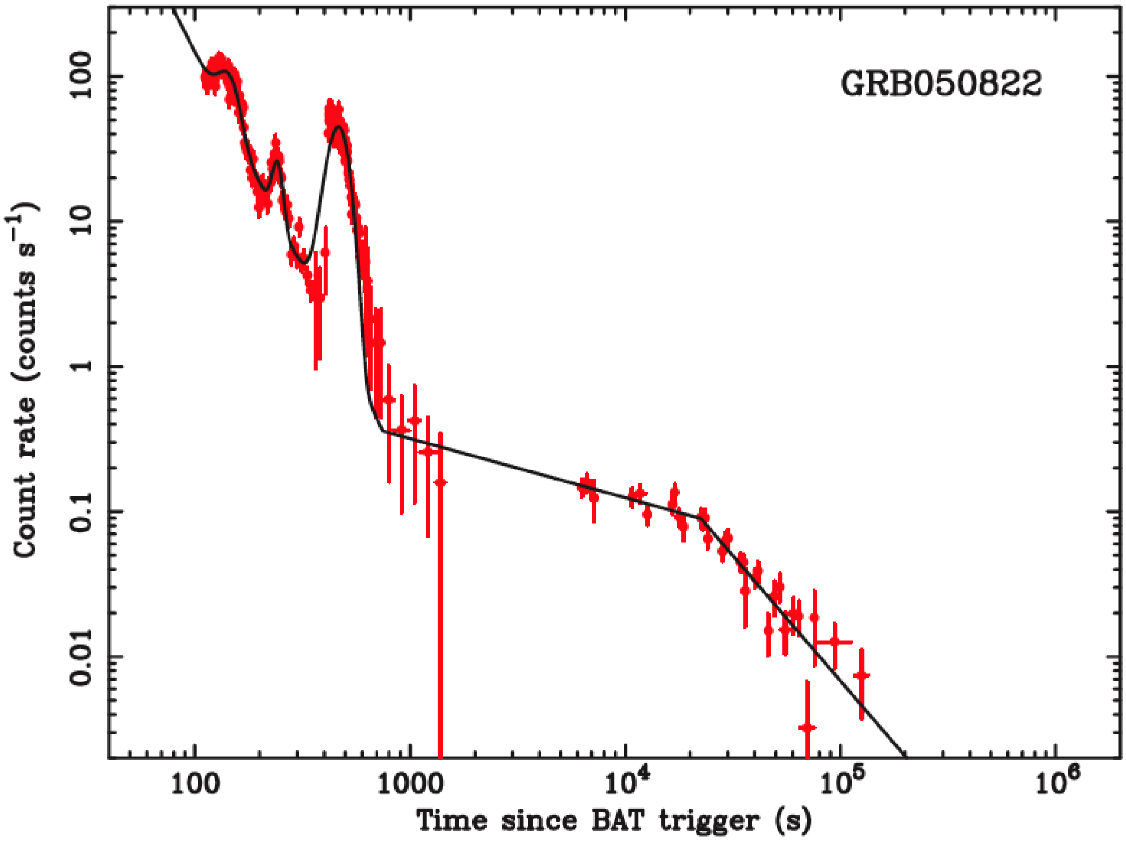

Figure 1.7 X-ray afterglow light curve of GRB 050822 and its fit. Following the early maximum the light curve shows a first steep phase with two big flares superimposed, followed by a milder decay and a steepening in the last phase. From Chincarini et al. (2007).

cases, the early decay simply continues unbroken up to a day or longer. Sometimes, on the contrary, it is initally flat (e.g. Fox et al. 2003) and subsequently steepens. In a few cases, the emission at early time is dominated by the so-called optical flash (Akerlof et al. 1999), a fast-decaying component which rapidly fades. Lastly, as illustrated in Chap. 3, for some very early time observations it has been possible to detect the afterglow onset (e.g. Molinari et al. 2007) or to see an optical emission somehow correlated with the prompt one (Blake et al. 2005; Vestrand et al. 2006; Bloom et al. 2008). For a collection of optical afterglow light curves see Kann et al. (2007b) and Melandri et al. (2008), as well as Panaitescu & Vestrand (2008) in particular for the early time light curves.

Radio light curves are initially rising (the radio spectrum is heavily self-absorbed) and peak a few days after the GRB. Radio emission is the most powerful at late times, and can be observed for a very long time (e.g. Frail et al. 2000, Fig. 1.9).

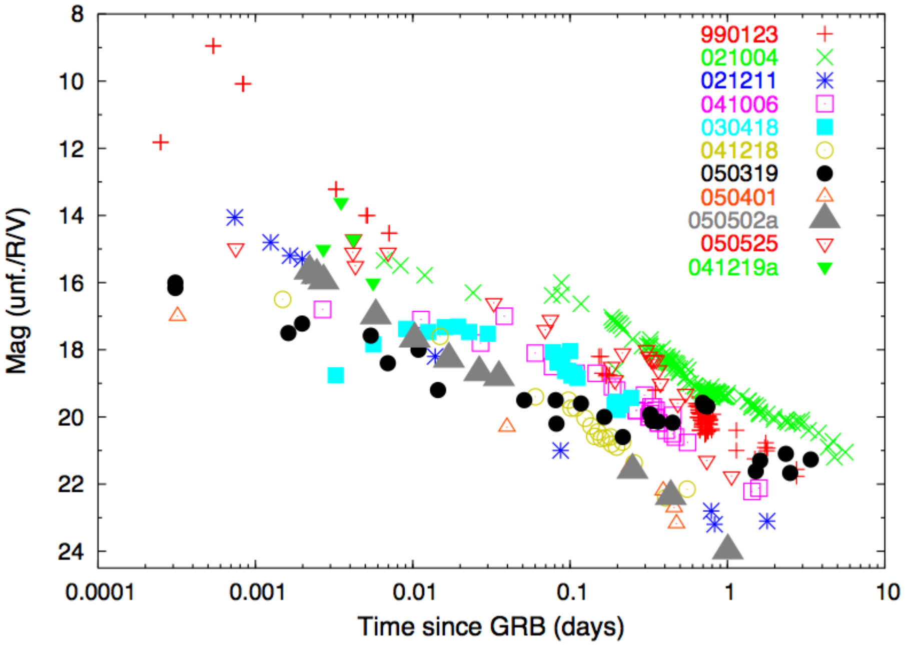

Figure 1.8 Early light curves (unfiltered, R- and V-bands) for a set of GRBs. From Guidorzi et al. (2005).

1.1.2.2 Other properties

Broadband afterglow spectra are usually composed of a set of power-law segments, separated by several break frequencies (as illustrated in Fig. 1.10) shifting in time. The commonly used theoretical model to explain this behavior will be introduced in the next section.

To a GRB detection does not always correspond an afterglow detection. After the launch of *Swift*, the 98% of the *Swift* BAT GRB triggers were detected also at X-ray energies (O'Brien et al. 2006). Searches in the optical before the *Swift* launch have been more tricky, leading to a varying percentage of GRBs (as large as $\sim$ 50%; e.g. Fynbo et al. 2001; Lazzati et al. 2002; Berger et al. 2002) without an associated optical afterglow. These GRBs are commonly called *dark* GRBs. While instrumental and observational effects are clearly involved in the determination of this fraction (see Vergani et al. 2004), the confirmation of the same percentage of dark GRBs observed in the *Swift* era (`http://www.mpe.mpg.de/~jcg/grbgen.html`) has been a surprise (Roming et al. 2005). It is still not clear which is the role played by dust extinction and intrinsic faintness in causing the lack of optical detection.

The optical afterglow light is (slightly) polarized (Covino et al. 1999; Wijers et al. 1999; Greiner et al. 2003; Gorosabel et al. 2004). Linear polarization at the level of a few percent has been detected in several cases, showing variability in both its intensity and position

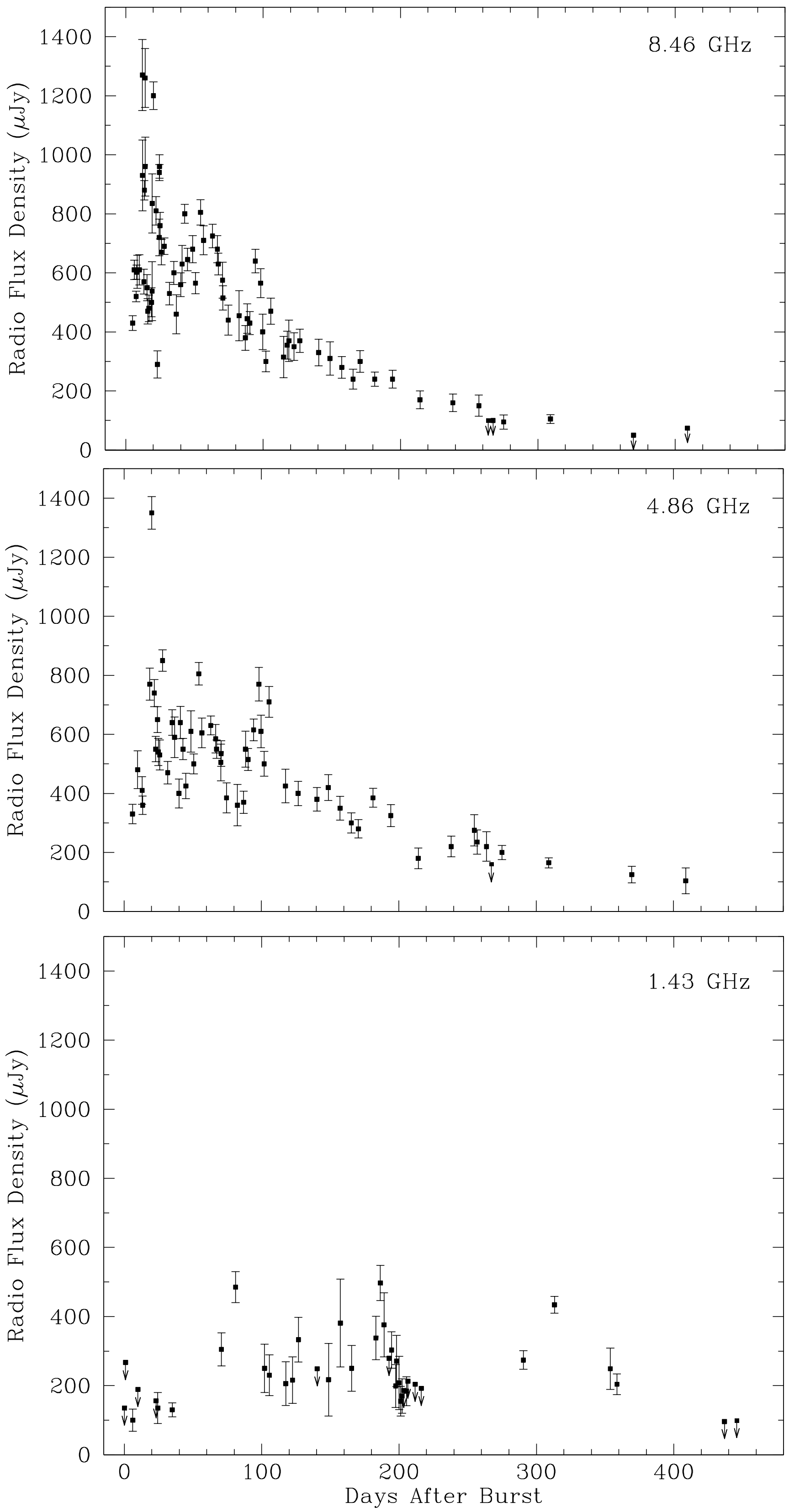

Figure 1.9 The radio light curves of GRB 970508 at 8.46, 4.86 and 1.43 GHz. From Frail et al. (2000).

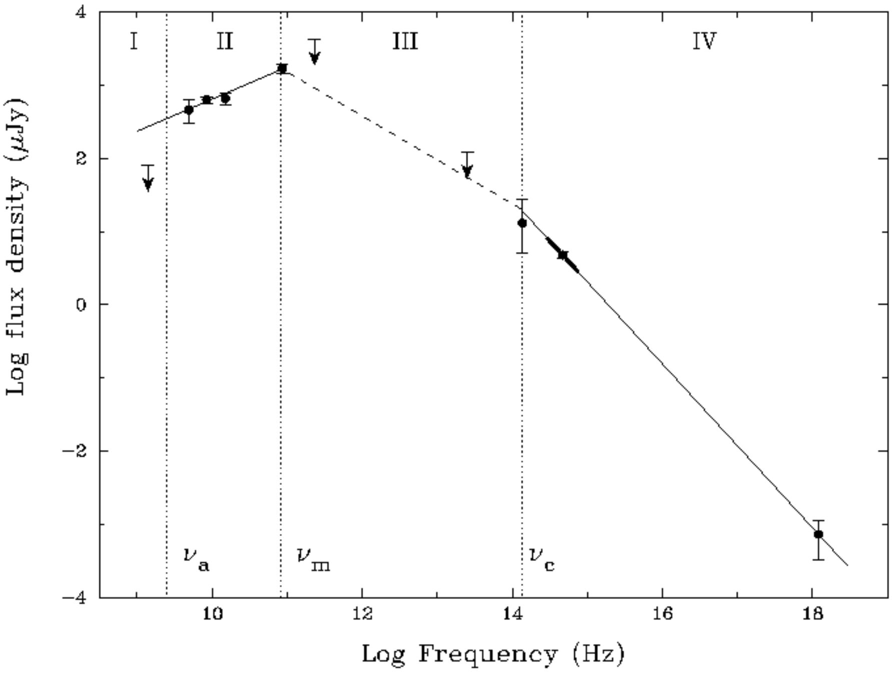

Figure 1.10 The X-ray to radio spectrum of GRB 970508 about 12 days after the event. From Piran (2000).

angle (see e.g. Barth et al. 2003). This indicates that some asymmetry must be present in the emitting region. Polarization measurements can be very important to discriminate between different emission models (see Sect. 1.2).

1.1.3 GRBs and cosmology

The discovery of optical counterparts, besides bringing new elements into the GRB picture, has also allowed two major advances. First, the accurate position which can be achieved at these frequencies has led to establishing that GRBs are hosted inside galaxies (e.g. Sahu et al. 1997). Second, and perhaps even more important, optical spectra have allowed the measurement of redshifts for these objects (Metzger et al. 1997) showing that GRB are truly cosmological events, with an average redshift of $\langle z \rangle = 2.2$ (Fig. 1.11). The *Swift* sample has a larger median value ($\langle z \rangle = 2.2$). The current record-holder is GRB 080913 $z = 6.695$ (Fynbo et al. 2008a; Greiner et al. 2008b; Perez-Ramirez et al. 2008), and there are several examples in the range $z = 4 - 5$. There is also a low-redshift tail ($z \leq 0.1$), comprising very few but peculiar objects. These bursts are quite faint, and they would easily escape detection at larger distances. It must be noticed that the redshift distribution is strongly biased because the spectral lines useful for the redshift determination lie outside the optical range for redshift between ~ 1.5 and ~ 2.

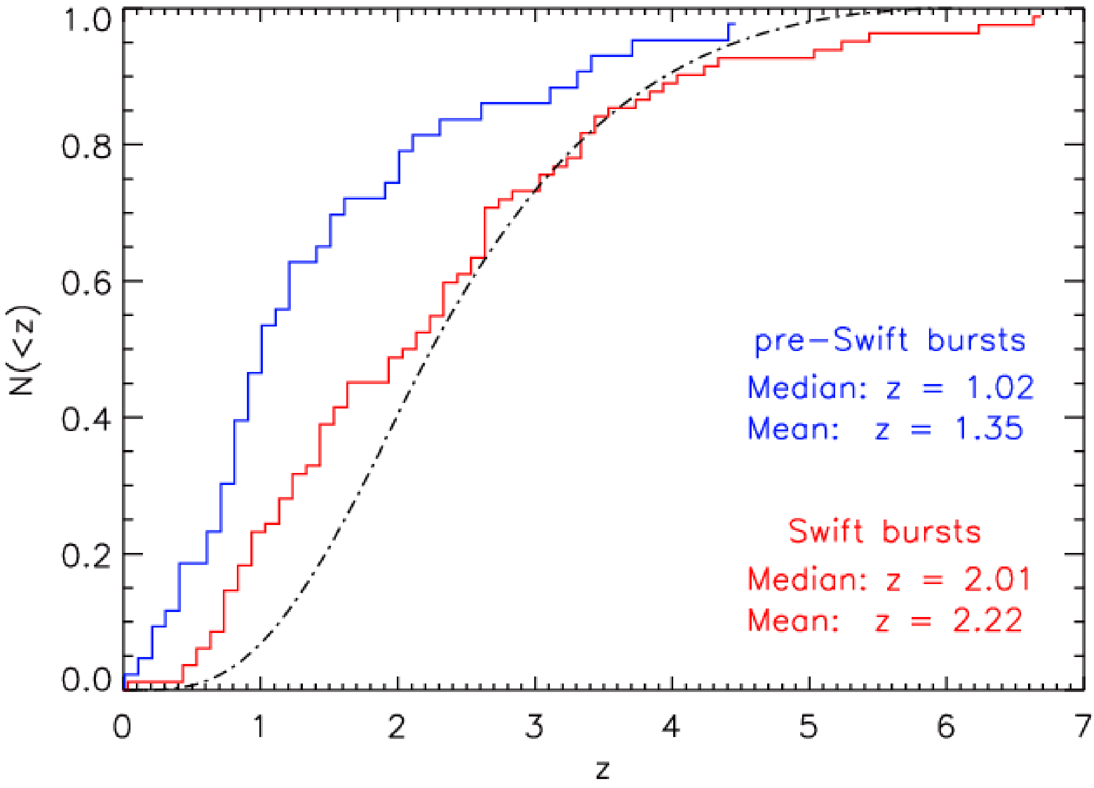

Figure 1.11 The figure displays the cumulative fraction of GRBs as a function of redshift for pre-*Swift* bursts (blue stepwise curve) and *Swift* bursts (red stepwise curve). Overplotted is a simple model for the expectation of the redshift distribution of GRBs (see Jakobsson et al. 2006b for details). The average and median redshift values of both samples are indicated. From P. Jakobsson web page : http://raunvis.hi.is/∼pja/GRBsample.html.

The determination of GRB distances leads to an energy scale of these events. The observed gamma-ray energy $E_{\gamma iso} = 4\pi d_L^2 F_\gamma (1+z)^{-1}$ (where d_L is the luminosity distance, F_γ is the gamma-ray fluence and z is the GRB redshift) ranges from 10^{48} to more than 10^{54} erg. However, this emission is not isotropic, and the beaming corrected estimates $E_\gamma = (1-\theta_j)E_{\gamma iso}$ (where θ_j is the beaming angle) are lower, of the order of 10^{50}-10^{51} erg (Frail et al. 2001). It should be noticed that the beaming fraction is not easily determined and a break in the light curve (see section 1.2.2, page 17) not necessarily indicates beaming. In any case, such large values constrain GRB models and render GRBs very powerful probes of the far Universe. Their high power can easily outshine other astronomical objects, including AGN (Watson et al. 2006c). Current estimates of the GRB rates amount to ~ 1 event Gpc^{-3} yr^{-1} (e.g. Schmidt 1999), but they depend critically on the degree of collimation presented by GRBs (see section 1.2.2 page, 17).

If long GRBs are associated to the death of massive stars, as seems to be the case (see Sect. 1.3.1), they represent a powerful tracer of the cosmic star formation history up to the far Universe. GRBs can be also a unique tool to investigate the IGM (intergalactic medium; Chapter 6), even at primordial star formation and reionization epochs (see Lamb & Reichart 2000). Differently from quasars and galaxies, whose flux reduces quickly as the redshift increases, GRB afterglows have fairly constant infrared flux for a fixed time in the observer reference frame. This is due to the particular values of the spectral and temporal indices β and α of the GRB afterglow luminosity $L_\nu = \nu^\beta t^\alpha$. The spectral energy flux F_ν of GRB afterglows in a given frequency band and at a fixed time of observation after the GRB can be written as

$$F_\nu(\nu, t) = \frac{L_\nu(\nu, t)}{4\pi D(z)^2 (1+z)^{1-\beta+\alpha}} \tag{1.1}$$

where F is the afterglow flux and $D(z)$ is the burst comoving distance. The typical α values (e.g. $\sim -4/3$), the relation between α and β (see Sect. 1.2.2 and Chapter 4; e.g. $\alpha = 3\beta/2$) and the fact that $D(z)$ increases very slowly as a function of z for large enough z, imply that the afterglow spectral flux decreases slowly for $z \geq 3$.

Afterglow spectra (Fig. 1.12) carry important information on the gas and dust composition at high redshift, enabling the study of the physical, chemical and dynamical status of the circumburst environment and of the interstellar matter (ISM) of the GRB host galaxies, and also to retrieve important information on the systems present along the GRB lines of sight (see Chapter 6).

Lastly, several methods have been proposed to use GRBs to measure the geometry of the Universe (see Ghirlanda et al. 2006 for a review) even if their validity is still to be assessed.

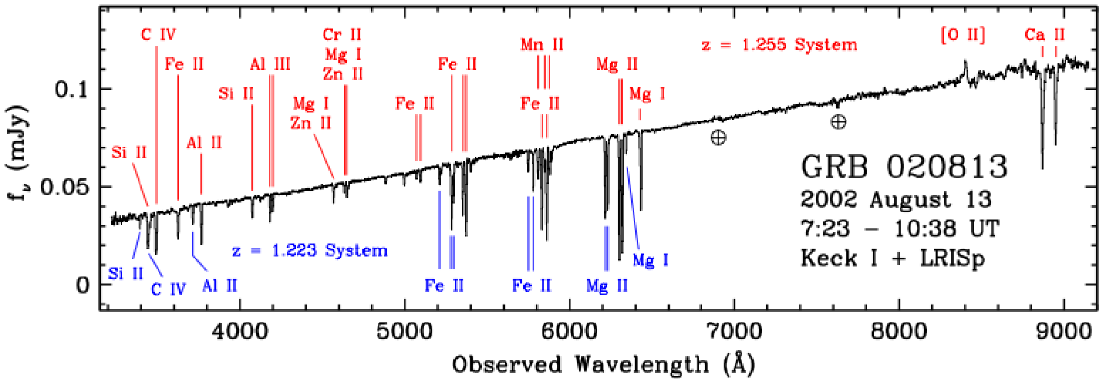

Figure 1.12 Optical spectrum of GRB 020813, taken with the Keck telescope (Barth et al. 2003). Several absorption features are present, grouped at two different redshifts. The larger is the burst redshift, as confirmed by the O II emission line from the host galaxy. The brightness of the afterglows allows the acquisition of spectra with high signal-to-noise ratio.

1.2 Theoretical models

1.2.1 Prompt emission

Over the years, the efforts to understand the GRB phenomenon have led to a sort of "standard" model, which provides a framework capable to explain most of the observed features. In particular, it accounts for both the prompt and the afterglow emission (the latter being actually a prediction; Meszaros & Rees 1997). For excellent reviews, see Piran (1999a); Zhang & Mészáros (2004); Mészáros (2006). It should be said, however, that several issues are far from settled.

The observed energies, coupled with the short variability timescales and nonthermal spectra, provide the main ingredients. Causal arguments imply that the GRB emission region needs to be small ($R \leq c\,\delta t$). The large resulting photon densities would imply an optical depth to pair production exceedingly large ($\tau \sim 10^{13}$; Piran & Shemi 1993). In this context, the energy would be released as a thermal spectrum, with an unreasonably low efficiency.

The solution to this riddle is to invoke relativistic motion. If the explosion region is expanding relativistically (with Lorentz factor $\Gamma \gg 1$) the optical depth in the comoving frame is significantly reduced (by a factor $\sim \Gamma^4$; Lithwick & Sari 2001). Assuming $\Gamma \geq 100$, a low optical depth can be achieved. Such relativistic motion is basic to any model of gamma-ray bursts. Afterglow observations have confirmed relativistic motion (Taylor et al. 2004; Molinari et al. 2007; see also Chapter 3) .

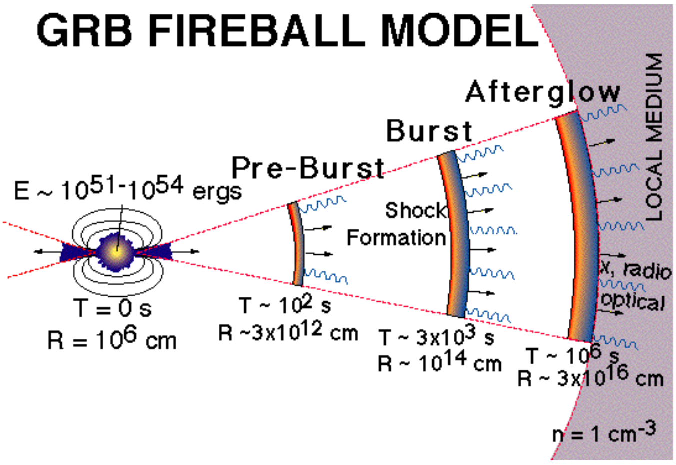

Figure 1.13 Diagram representing the different phases of the GRB standard model, from the fireball generation to the external shock dissipation (Piran 1999b; Ghisellini 2001).

The standard solution to escape the compactness problem leads to the so-called fireball model (see Fig. 1.13). A large amount of energy (in the form of a photon/pair relativistic plasma) is "polluted" with a small quantity of baryons. The plasma expands relativistically, but, due to the high optical depth, it is radiatively very inefficient. As the expansion goes on, the internal energy is gradually transferred to protons, in the form of bulk kinetic energy. The energy can be thus transported out to large radii, where the opacity is low enough so that nonthermal spectra can be radiated. However, there is the need to re-convert the bulk kinetic energy into internal energy. This can be achieved through the generation of shocks. Two kinds of shocks can be envisaged:

- external shocks (Meszaros & Rees 1993): the whole fireball may interact with some surrounding material, and decelerate against it;
- internal shocks (Rees & Meszaros 1994): different portions of the fluid with slightly different velocity can collide between themselves.

External shocks are expected to provide smooth temporal profiles, contrary to what is observed in several examples (Fig. 1.3). External shocks may still be a viable solution if the central engine expels several shells of matter (multiple fireballs). However, each shell is expected to interact with the external medium at a progressively later time. A widening of the gamma-ray pulses over the course of the burst is thus expected. This behaviour has not been observed (Fenimore et al. 1999). On the other hand, the bursts exhibiting single gamma-ray pulses with no short time scale variability at late times could also be entirely interpreted as external shocks (see Chapter 3 for an example).

Internal shocks are currently the preferred solution, since interaction between several shells may occur always at the same small scale. If the initial separation between shells is Δ, the interaction radius is of the order of $\sim \Gamma^2\Delta$. The interaction radius should be large enough ($\sim 10^{13}\,\mathrm{cm}$) for the optical depth to be low so that radiation can escape. This leads to a constraint $\Gamma \geq 100$, in accordance with the value derived from the compactness argument. In the internal shock scenario, the burst duration corresponds to the time that the central engine is active.

It is not clear by means of which mechanism the internal energy is radiated. One promising candidate is synchrotron emission, which however suffers some problems (namely, the fast electron cooling, which is required to yield high radiative efficiency, would imply spectra softer than observed; Ghisellini et al. 2000). Other possibilities have been outlined (e.g Liang 1997; Medvedev 2000; Pe'er et al. 2006; Ryde et al. 2006), but there is no general consensus on this issue.

Alternative mechanisms have also been proposed to power the gamma-ray emission. Much attention has been attracted by magnetically-dominated models (see Lyutikov 2006 for a review). Such models envisage a dynamical role for the magnetic field, which is supposed to carry a significant fraction of the energy. Energy may be dissipated through a reconnection process. These models avoid the need to transform the internal energy into bulk energy and then going back. A large degree of magnetization seems also necessary to explain the prompt event pulse characteristics (Quilligan et al. 2002) and might further justify the lack of an optical flash, which is expected to be ubiquitous in the fireball model (Zhang & Kobayashi 2005). However, it is not clear if such large magnetic fields exist and, above all, if they can be transported out to large radii. The ultimate test for the two models may be to observe (or not observe) polarization in the early stages of the afterglows, since in magnetic models a large, ordered magnetic field is expected, which should give rise to highly polarized synchrotron radiation (Lazzati 2004). The recent tight limit put by the early afterglow polarization measurements of GRB 060418 made by Mundell et al. (2007) challenges the presence of such an ordered magnetic field.

Other more exotic models to explain both the prompt and afterglow origin are the "cannonball" (Dado et al. 2007), the "fireshell" (Bianco & Ruffini 2005) and the "quark nova" (Staff et al. 2007) models.

1.2.2 Afterglow emission

After the prompt emission, the fireball still carries a significant fraction of its initial energy. At a critical radius (which depends on both the fireball and circumburst medium properties), it starts decelerating due to the interaction with the surrounding material. Further kinetic energy is dissipated into internal energy, and, possibly, radiation. This emission (actually coming from an external shock) is believed to power the afterglow (Meszaros & Rees 1997). Impacting against the external medium, a shock is also expected to heat the fireball, leading to a fast-decaying component (reverse shock) which can power an early optical flash.

During the afterglow phase, synchrotron radiation is widely believed to be the main emission mechanism. Significant inverse Compton emission can be also radiated (Sari & Esin 2001), but it should lie above the usually observed spectral windows. A relatively simple theory predicts light curves and spectra with properties consistent with the observed ones (Sari 1998; Panaitescu & Kumar 2000), even if *Swift* observations are challenging the theory, especially concerning the X-ray early afterglow behaviour (see also Chapter 4). It is generally assumed that the emitting electrons have a power law energy distribution $N(E) \propto E^{-p}$. A snapshot of the afterglow spectrum at any given time should consist in a four segment power law with three breaks (see Fig. 1.14) associated to three critical frequencies:

- ν_m : the peak synchrotron frequency,
- ν_c : the cooling frequency, defined as the the synchrotron frequency of an electron that cools during the local hydrodynamic time scale. The afterglows are in the so-called slow cooling regime, where $\nu_m < \nu_c$,
- ν_a : the self absorption frequency, for which the system becomes optically thick to synchrotron self absorption (usually at very low frequency as the radio ones; $\nu_a \ll \nu_m$),

giving $F_\nu \propto \nu^\beta$ with:

$$\beta = \begin{cases} 2 & \nu < \nu_a \,\text{self absorption;} \\ 1/3 & \nu_a < \nu < \min(\nu_m, \nu_c); \\ -(p-1)/2 & \nu_m < \nu < \nu_c; \\ -p/2 & \text{for } \max(\nu_m, \nu_c) < \nu. \end{cases} \tag{1.2}$$

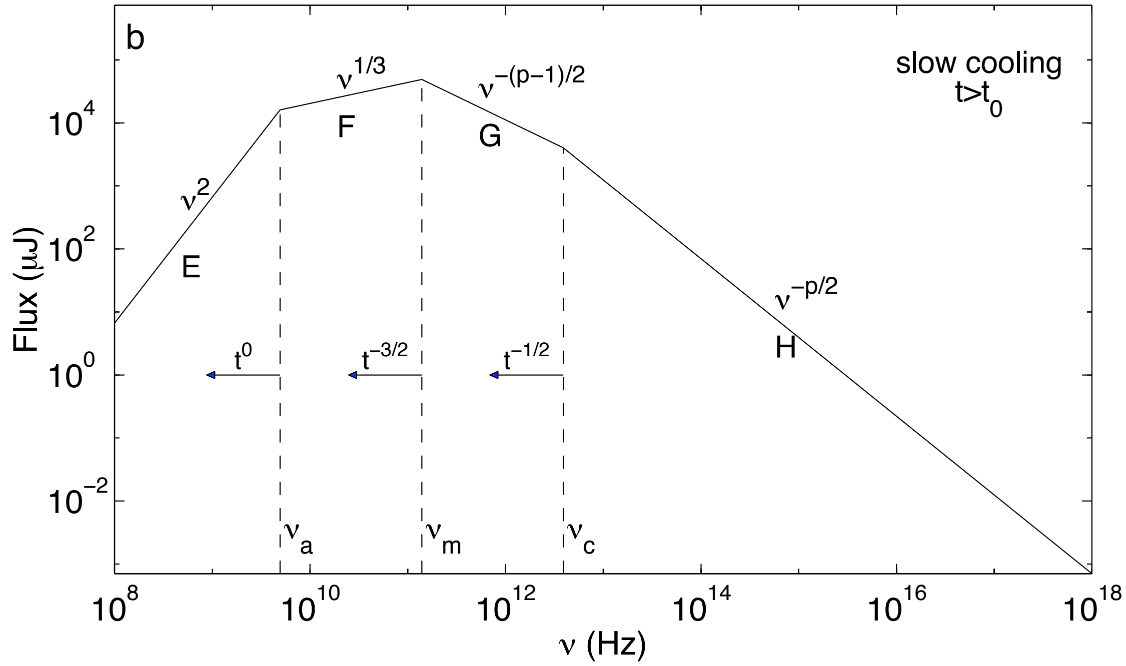

Figure 1.14 Synchrotron spectrum of a relativistic shock with a power-law distribution of electrons: the slow cooling case. From Sari et al. (1998).

As the remnant expands, the photon spectrum moves to lower frequencies, and the flux in a given band decays as a power law in time, whose index can change as the characteristic frequencies move through it. Assuming adiabatic evolution and propagation into a constant density surrounding medium, the classical fireball model predicts very simple relations between the temporal and spectral index, the so-called *closure relations*: $\alpha = 3\beta/2$ and $\alpha = (3\beta - 1)/2$ for $\nu < \nu_c$ and $\nu > \nu_c$, respectively. The afterglow spectral behaviour as well as the closure relations will be investigated in Chapter 4.

The steep light curves displayed by several afterglows at late times (mostly in the optical and radio bands) have been explained as due to a jetted outflow (Rhoads 1999; Sari et al. 1999). At early times, due to the relativistic aberration, only a small fraction of the shell surface (of the order of $\frac{1}{\Gamma^2}$) is visible to the observer. This means that there is no difference between a jetted or spherical configuration, as long as Γ is large enough. When Γ drops below the critical value $\sim \frac{1}{\theta}$ (where θ is the jet opening angle), the aspherical geometry can be seen, and this results in a steeper decay (Castro-Tirado et al. 1999; Kulkarni et al. 1999). The break time allows an estimate of θ, usually of the order of a few degrees. A jetted emission also helps alleviate the large energy requirements inferred by assuming spherical geometry. After beaming correction, the observed energies are lower, of the order of $\sim 10^{51}$ erg, comparable to the kinetic energy of a supernova explosion.

Remarkably, the beaming-corrected energies show a lower scatter than the isotropic values. Moreover, a very tight correlation has been found between the gamma-ray energies (after beaming correction) and the peak frequency of the GRB prompt spectrum (Ghirlanda et al. 2004). This strengthens both the afterglow model (used to infer the opening angle) and the jet hypothesis. It should be said, however, that very few *Swift* bursts have shown a convincing jet signature (Panaitescu et al. 2006), whereas other breaks probably not linked to the beaming of the fireball have been observed, so that the whole issue requires further investigation.

1.3 Progenitors

The fireball model outlined above provides a very general scenario for explaining the GRB phenomenon. This is possible since the outcome is largely independent of the initial conditions. Simply releasing a large amount of energy in a small volume leads to fireball formation, the evolution of which does not keep track of the details of the initial explosion. While this implies that the model can be applied under wide ranges of conditions (for example, it works for both short and long GRBs), the physical engine which triggers the explosion remains undetermined, and difficult to constrain. There are several conditions that such an engine must satistfy:

Compactness The small scales implied by the rapid variability of many (but not all) GRB light curves require small emission radii. Radii smaller than $\sim 10\,000$km are necessary.

Energetics GRBs can release large amounts of energy. Taking into account the non-spherical geometry, current estimates indicate up to 10^{51} erg or even more in electromagnetic form.

Relativistic motion With such large luminosities, relativistic motion is unavoidable to cope with the compactness problem. Any GRB progenitor model must be capable of launching matter close to the speed of light.

Rate The rate of GRB explosions is very small (about 10^{-6}-$10^{-5}\,\mathrm{y}^{-1}$), just a small fraction of that of supernovæ (about $10^{-2}\,\mathrm{y}^{-1}$). Thus, very special conditions are needed to give rise to a GRB.

Such constraints lead to the need for a central engine tied to a compact object, most likely a stellar-mass black hole or a neutron star. Typical examples are collapsing cores of massive stars (Woosley 1993; Paczynski 1998), collapsing neutron stars (Usov 1992; Vietri & Stella 1998), or binary compact object systems undergoing merger (Eichler et al. 1989; Belczynski et al. 2002).

Over the years, evidence has been accumulating that most long-duration GRBs are connected to the death of massive stars (see further below). The origin of short burst events is more uncertain, albeit there is growing, indirect evidence indicating that they may originate in merging systems of binary compact objects (see Lee & Ramirez-Ruiz 2007 and Nakar 2007 for exhaustive reviews on this subject). A more detailed discussion on short GRB progenitors is presented in Chapter 5.

1.3.1 Long duration GRBs

The first line of evidence pointing towards a connection between long-duration GRBs and star formation comes from the study of their host galaxies and environments (see Fig. 1.15). GRB hosts show distinct signs of active star formation. Their colours are bluer than average (Le Floc'h et al. 2003), indicating the presence of hot, massive stars. They show prominent nebular emission lines (Djorgovski et al. 1998; Prochaska et al. 2004) and show, on average, very large Lyman-α equivalent widths (Fynbo et al. 2003). Spectral modeling indicates large specific star formation rates (Christensen et al. 2004; Gorosabel et al. 2005; Savaglio et al. 2008). However, it is still debated whether GRB host galaxies belong to a special population or if their properties are those expected for normal star-forming galaxies (see Tanvir et al. 2004; Le Floc'h et al. 2006; Savaglio et al. 2008 and references therein). It has to be noticed that up to now most information comes from optically-bright GRBs (i.e. GRBs which had an optical afterglow), while little is known about optically-dark events (which may be preferentially hosted by dusty and more metallic systems).

Further clues for an association between GRBs and star formation come from the spatial offset distribution of bursts with respect to their host galaxy centres. This distribution is similar to that of the ultraviolet light, again indicative of an association with young stars (Bloom et al. 2002; Fruchter et al. 2006, Fig. 1.15).

All the evidence presented above strongly argues for an association between long-duration GRBs and star formation. This allows selection of promising progenitor candidates. Core-collapse supernovae (SNe), magnetars, and collapsing neutron stars are in principle suitable candidates. Also binary compact object systems undergoing merging in relatively short times could be suitable candidates. Observations favour a direct association between core-collapse SNe and GRBs. Some afterglow light curves show a flattening,

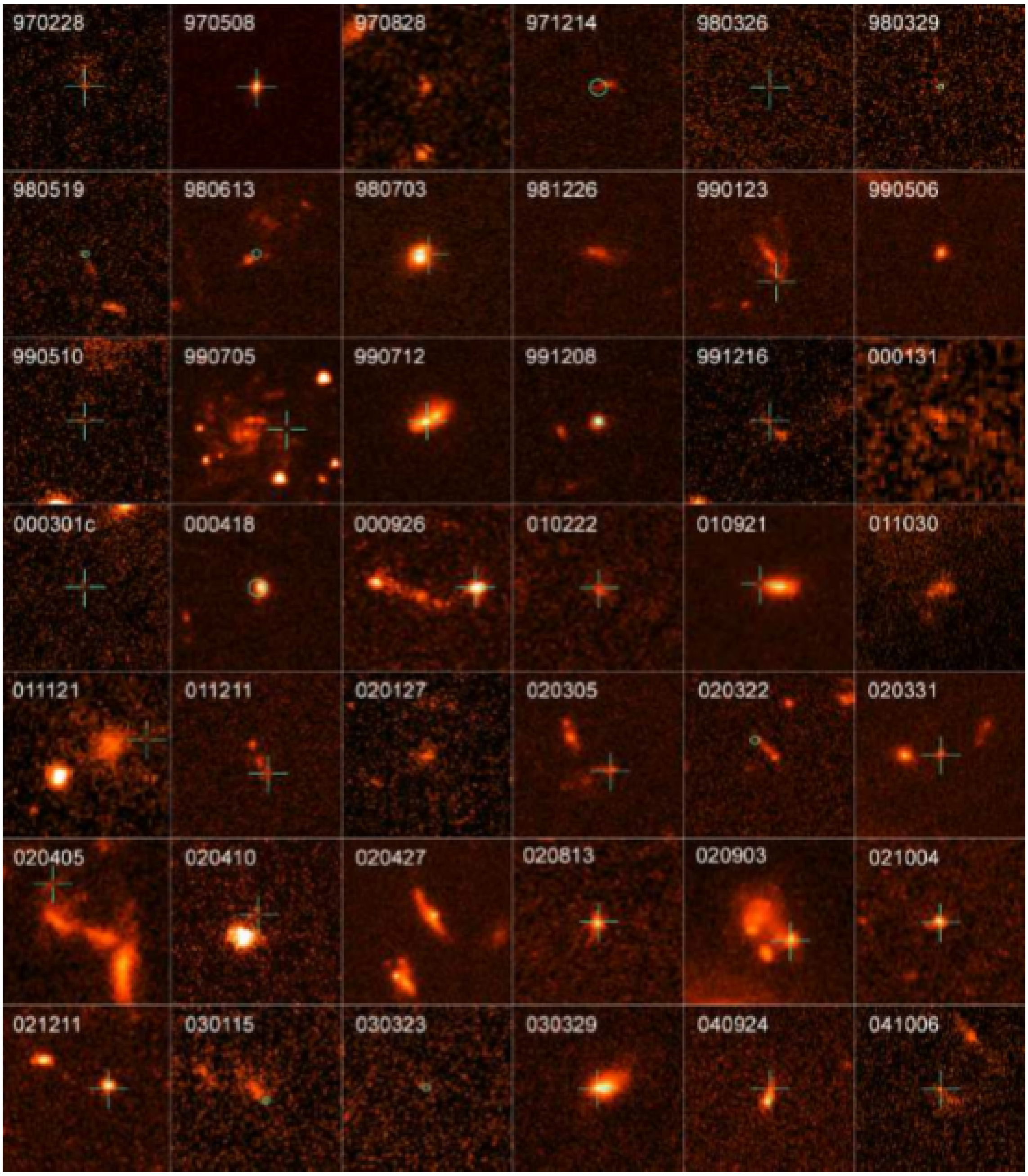

Figure 1.15 Mosaic of HST images of 42 GRB host galaxies. Crosses indicate the afterglow position. From Fruchter et al. (2006).

or even a rebrightening, at about 15-30 days after the GRB. Such bumps could be due, in principle, to the emergence of a SN (Castro-Tirado & Gorosabel 1999; Bloom et al. 1999). Since SN light curves peak at about that epoch, they might outshine the afterglow which has declined significantly by that time. The spectroscopic analysis performed for some of these bumps confirm the association (Della Valle et al. 2006b). Examples are GRB 031203/SN 2003lw, GRB 060218/SN 2006aj (Malesani et al. 2004; Pian et al. 2006).

Using Hubble Space Telescope data, Fruchter et al. (2006) showed that long GRBs are far more concentrated on the very brightest regions of their host galaxies than are the core-collapse supernovae. Furthermore, the host galaxies of the long GRBs are significantly fainter and more irregular than the hosts of the core-collapse supernovae. Together these results suggest that long-duration GRBs are associated with the most massive stars and may be restricted to galaxies of limited chemical evolution. On the other hand, Kelly et al. (2007) found that, at least at low redshift, the population of type Ic SNe (the sub-class of core-collapse SNe usually associated to GRBs) occurs in a environment similar to the GRB one.

Woosley (1993), proposed that, under certain circumstances, a collapsing star might launch relativistic jets capable of powering a gamma-ray burst, accompanied by a SN. The current version of the so-called *collapsar model* (MacFadyen & Woosley 1999) predicts that a massive star ($\sim 20-40 M_{\odot}$) (where $M_{\odot}$ indicate the mass of the Sun) endowed with fast enough rotation could form an accretion disk encircling the new-born black hole. Such an accretion disk would power the jet emission (as confirmed also by the analysis of the gamma-ray light-curves, see McBreen et al. 2002), in a way similar to AGNs and Galactic X-ray binaries.

1.3.1.1 Wolf -Rayet stars as progenitors

The necessary conditions for the production of a GRB are three. First, the star needs to form a black hole after collapse, so that a large star mass is required. Second, the star needs to have lost its external hydrogen envelope, otherwise the jets would not be able to erupt out of the star surface. Lastly, the stellar core needs to be fast rotating, otherwise the matter would not form an accretion disk, but directly fall onto the black hole.

Wolf - Rayet (WR) stars are the most massive stars in the final stages of evolution and have lost (or are in the process of losing the last remnants of) their hydrogen envelopes. Observationally they are very luminous, with broad emission lines indicating a fast and dense wind. For a recent review on WR properties see Crowther (2007). WR stars are the preferred progenitors of type Ibc SNe due to the lack of a hydrogen envelope. Considering WR properties and the fact that observations of the SNe associated with GRBs indicate that they belong indeed to the SN-Ic class, WR stars have become the leading candidates to be the progenitors of long GRBs.

The first question to answer is which kind of WR stars can produce a GRB instead of dying as a normal SNe Ibc as most of WR stars do.

To satisfy both requirements of being a fast rotator and to have lost the external hydrogen envelope is not an easy matter. Hirschi et al. (2005) and Petrovic et al. (2005) have shown that stellar models without magnetic fields can have enough specific angular momentum in their core to produce a GRB within the collapsar model. On the other hand magnetic fields seem to play an important role in the stellar evolution process and stellar evolution models which include angular momentum transport from the core to the hydrogen envelope by magnetic torques indicate that most single stars end up with too slowly rotating cores (Spruit 2002). Moreover the mass loss needed to remove the external envelope can be able to efficiently spin-down the star even without magnetic effects. The mass loss rate is linked to the metallicity Z (the metallicity is the abundance of an element heavier than He compared to hydrogen, see Chapter 6) of the star. Lower metallicity implies a small mass loss rate but this may have the consequence that the star will never reach a WR stage.

Possible solutions to these issues have been investigated for both single and binary star models, as illustrated below.

Chemically homogeneous evolution

In the first case (single star models) Yoon & Langer (2005),Woosley & Heger (2006) and Yoon & Langer (2006) invoke the so-called chemically homogeneus evolution scenario (Maeder & Meynet 2000; Heger et al. 2000), where a very efficient chemical mixing persists in massive rapid rotator stars so that the the star remains chemically homogeneous, never developing the core-envelope structure and avoiding the giant phase. This scenario coupled with low metallicity can lead to the formation of rapidly rotating helium massive stars which satisfy all the requirements of the collapsar even with the inclusion of magnetic field. This is possible since mixing the hydrogen envelope into the core rather than losing it into a wind avoids the angular momentum loss due to mass loss, and the lack of a core envelope structure prevents the spin down due to the magnetic core-envelope coupling. Nevertheless it has to be stressed that this possible evolution picture has yet to pass observational test to be confirmed as a real evolutionary path. Vink (2007) report observational evidence that the percentage of rapidly rotating WR stars is low not only in the Milky Way but also in the Large Magellanic Cloud (LMC). This can also mean that GRBs should explode in galaxies with a metallicity (Z) still lower than the LMC (that is $Z < 0.5Z_{\odot}$), in order to get enough rotation. This is in agreement with what is currently observed from emission spectroscopy of GRB host galaxies (Savaglio et al. 2008).

In the chemically homogeneous evolution context, GRB progenitors are expected to be fast rotator Wolf-Rayet stars of WN, WC or WO type with an initial mass $M_{init} =$

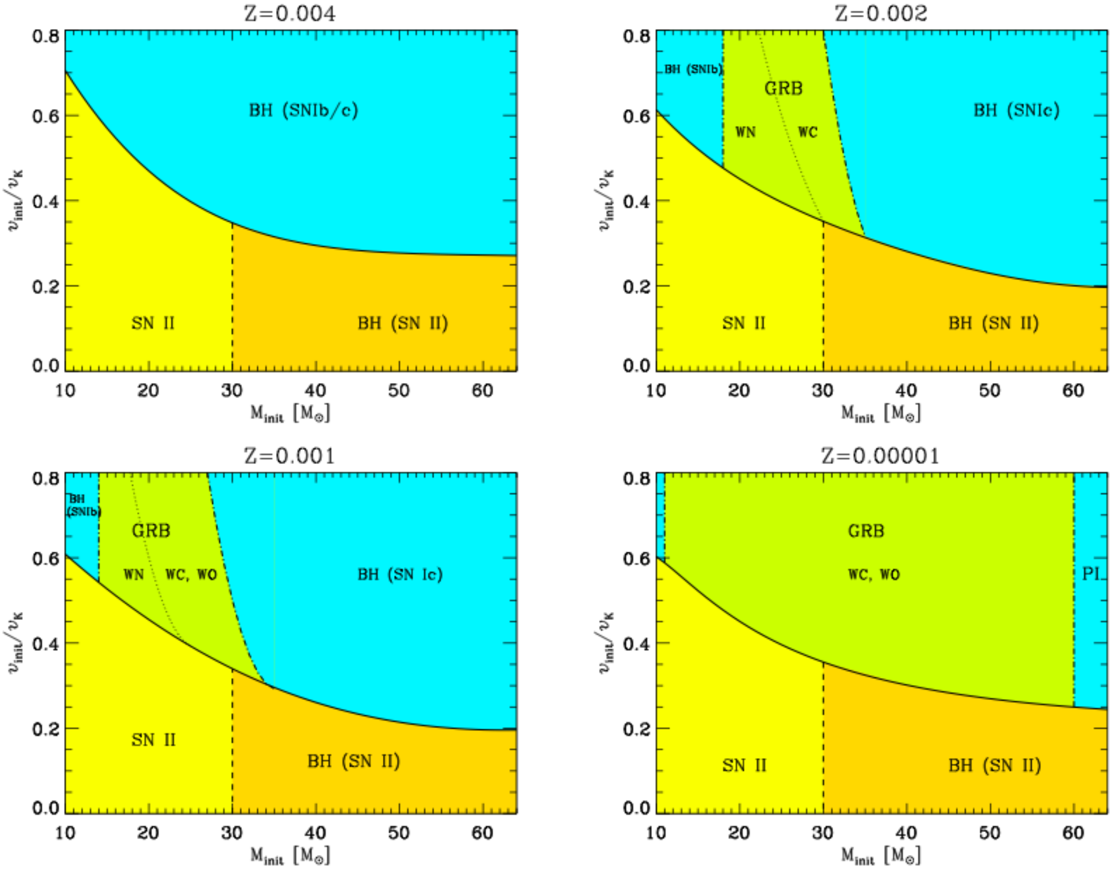

Figure 1.16 Plane of the final fate of a rotating star for different metallicities, from Yoon & Langer (2006). Above the solid line the star evolves quasi-chemically homogeneously, while under the solid line the classic core-envelope evolution is represented.

$25 - 30 M_\odot$ and a metallicity lower than $Z \sim 0.004$ ($Z < 0.2 Z\odot$) (see Fig. 1.16). Recent results by Campana et al. (2008) on the study of the absorption in the X-ray spectrum of GRB 060218 are in agreement with the model predictions.

This model can also account for the number ratio of GRBs versus core-collapse SNe and predicts that the observed number of GRBs is expected to increase with redshift with more the 50% of GRBs exploding at $z > 4$.

The chemically homogeneous scenario can also apply to the case of a binary star model (Yoon et al. 2008). In this context the GRB will be produced a few to several hundred parsecs away form the original binary site by the secondary star of a system that became unbound due to the supernova kick resulting from the explosion of the primary star.

Binary star models

An alternative way to keep the progenitor sufficiently rotating could be achieved using a binary star model. The more realistic case is the one of a WR-compact object system.

Detmers et al. (2008) demonstrate that the spin-up via tidal interaction with a binary companion is possible but would lead to two possible situations depending on a mass loss rate threshold having an extremely low probability of producing a collapsar:

- **mass loss rate higher than the threshold**

  After being initially spun-up, the WR star will spin down and the orbit will widen;

- **mass loss late lower than the threshold**

  The WR is spun-up, the orbit will shrink and the system will merge in the end.

On the other hand, it is possible that such mergers (Helium star-compact object mergers) can produce GRBs (see also Fryer et al. 1999; Fryer & Heger 2005). In the merger picture there is no need of a strong stellar wind to lose the hydrogen envelope because it can be removed in the common envelope phase, therefore there is no angular momentum loss due to wind mass loss.

1.3.2 Observational signatures

Wolf-Rayet stars are known to have strong winds with mass outflow rates beyond $10^{-5}\mathrm{M}_{\odot}\mathrm{y}^{-1}$ and wind velocities above $1000\mathrm{km\,s}^{-1}$. Stellar winds sweep out the environment surrounding the star and, depending upon the density of the ambient medium, these wind-blown bubbles can extend beyond 10 pc (see Fryer et al. 2006 and references therein).

Before becoming a WR, a star goes through different stages, therefore the medium profile surrounding a WR can be quite complicated. A simplified picture of the density profile is given in Fig. 1.17. Close to the star, the density profile is that of a free-streaming wind. This is simply determined by mass conservation, and has a r^{-2} radial dependence when a constant wind velocity is assumed. A possible slow expanding stalled wind region can be present at larger radii ending in the shell of shocked ISM, before reaching the unperturbed constant density ISM.

The temporal index of the afterglow light curve depends also on the medium the afterglow expands into (see Chapter 4), therefore the first expected signature of a WR progenitor would be the evidence of a wind profile medium, as well as a possible signature of the wind termination shock when the afterglow reaches the constant density environment of the stalled-wind region, or the ISM. Fig. 1.18 shows the result of simulations by Eldridge et al. (2006) of the light curves of an afterglow expanding in a WR surrounding medium, for different stalled wind radii. The light curves are characterised by an initial slope

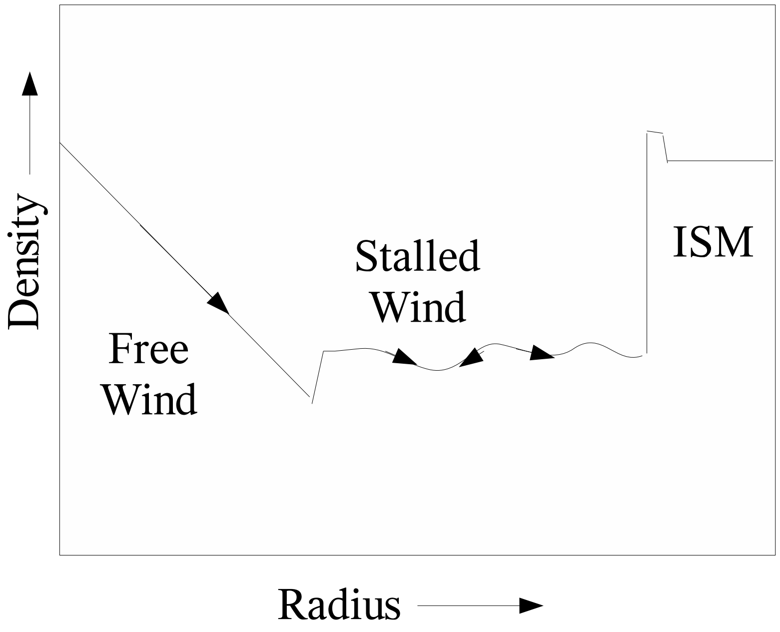

Figure 1.17 A schematic simplified picture of the different density profile regions surrounding a WR star. From Eldridge et al. (2006).

corresponding to a wind environment, a jump when the shock reaches the stalled wind radius followed by a shallower slope in the constant density medium.

The classical afterglow model applied on afterglow observations shows that more than half of the afterglows for which the cooling frequency was above the X-ray frequencies (when it is below X-ray frequencies, the afterglow evolution does not depend on the density profile) evolve as in a constant ISM (Panaitescu 2007; see also Woosley & Bloom 2006). Moreover no secure features of the transition between the two density regimes have ever been found. A possible but not fully satisfying way to solve the issue is a downstream of the termination shock in the stellar wind (Wijers 2001).

Recently a promising solution has been proposed by Eldridge (2007) thanks to the discovery of asymmetric WR winds (see for example Villar-Sbaffi et al. 2006). Even if this phenomenon has to be further investigated, the wind asymmetry can decrease both the wind density and the wind termination shock along the rotation axis, making the afterglow evolution in a constant density environment more likely (see Fig. 1.19). The presence of a strong wind asymmetry in space, density and velocity is indeed expected for rapidly rotating massive stars (Bjorkman & Cassinelli 1993). Very recently, van Marle et al. (2008) made 1D and 2D simulations including wind asymmetry and the chemically homogeneous evolution scenario. They found that the GRB is not expanding in a free

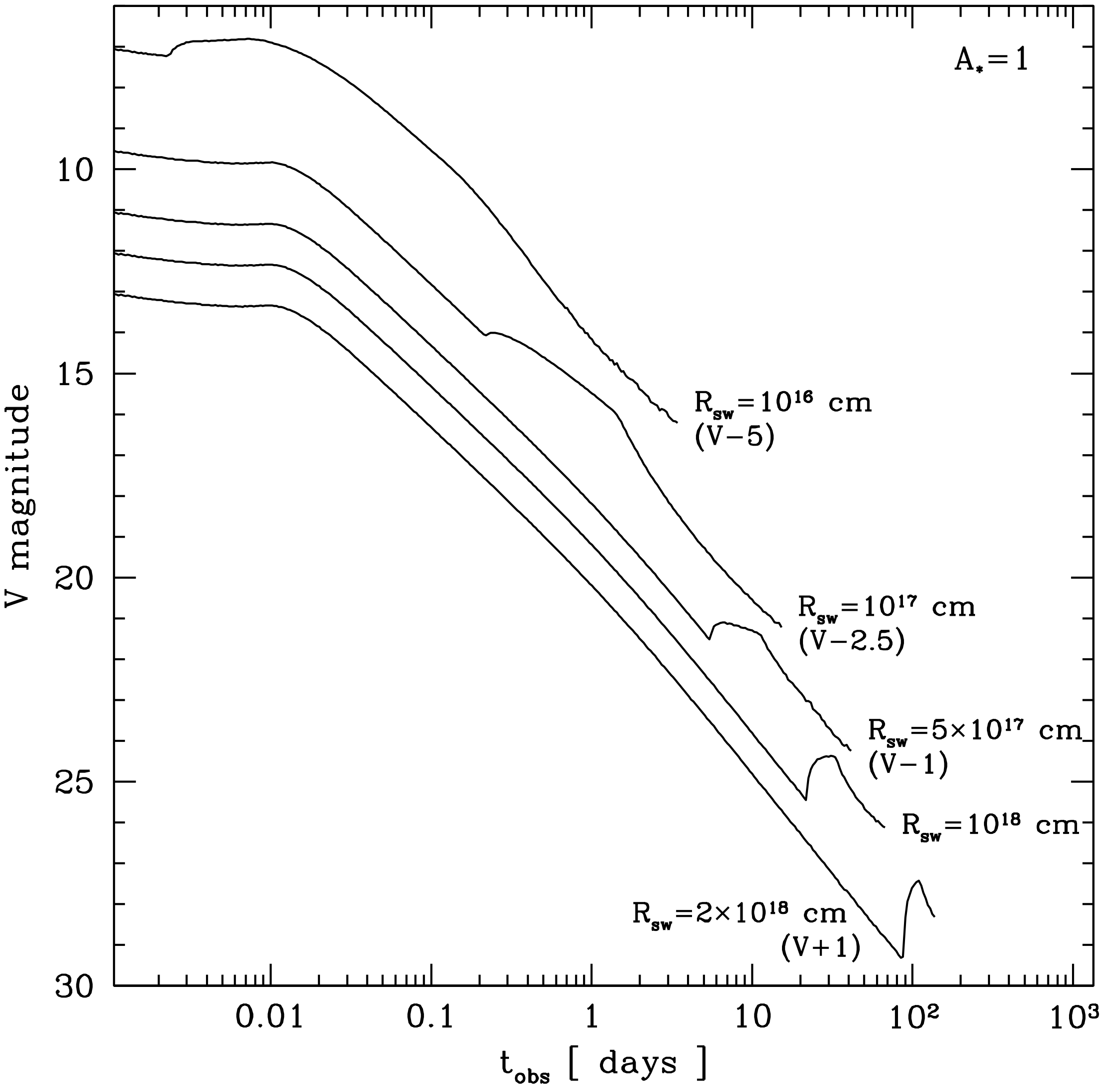

Figure 1.18 Simulations of the light curves of an afterglow expanding in a WR surrounding medium, for different stalled wind radii (R_{SW}. From Eldridge et al. (2006).

streaming wind, but in a medium that has a far more complex structure. In particular, the density slope in the innermost few parsecs, even if inside the wind termination shock, may differ significantly from the classical r^{-2} wind profile, and may also show significant changes as function of radius. In any case, it requires the consideration of a large grid of stellar evolution models to find out what the typical final density profiles would be.

Additional information on the progenitor medium can come from the afterglow spectroscopy. Very recently, Prochaska et al. (2008) reported on survey of NV absorption line in the afterglow spectra. Considering the properties of these features, they conclude that the progenitor's stellar wind is confined to $r < 10\,\mathrm{pc}$ suggesting also that the GRB progenitors occur within dense ($n > 10^3\,\mathrm{cm}^{-3}$) environments, typical of molecular clouds, as

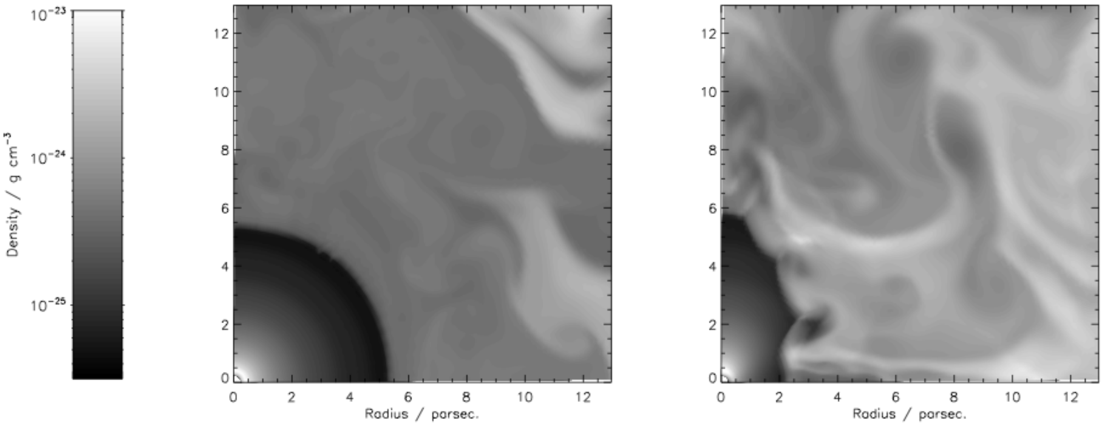

Figure 1.19 Greyscale plots of the stellar-wind bubble structure a few years before core-collapse of a simulated WR star from Eldridge (2007). The left panel shows the case for a spherically symmetric wind while the right panel shows a possible asymmetric case.

expected in the case of massive stars.

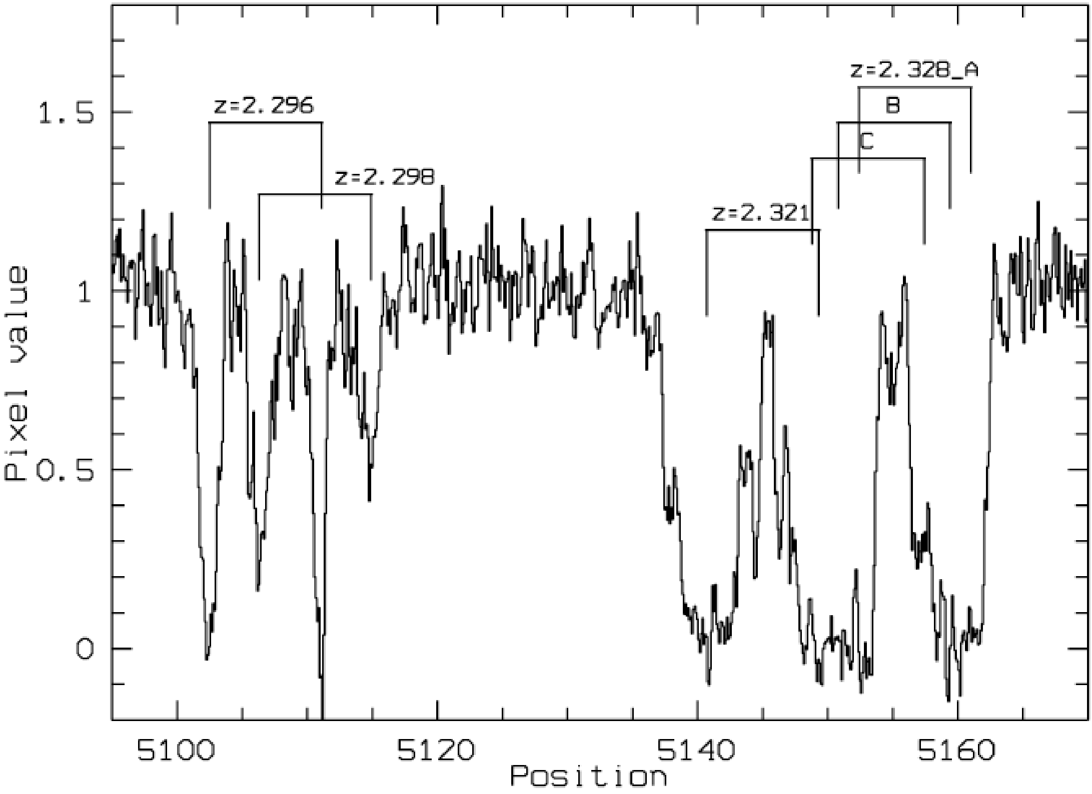

Figure 1.20 CIV absorption lines present in the high resolution spectrum of the afterglow of GRB 021004. The velocity shift between the 2 groups of absorption systems is of ~ 3000 km s^{-1}. From Fiore et al. (2005)

Some WR signatures would also be expected in afterglow spectra. WR evolution models by van Marle et al. (2008) predict that the medium in front of the jet does not have a constant velocity. Assuming that not all of this material is fully ionized by the GRB, it may be observable in the form of multiple blue-shifted absorption lines at high velocity. Schaefer et al. (2003), Mirabal et al. (2003) and Fiore et al. (2005) indeed detected high velocity CIV absorption lines in the spectra of GRB 021004 (see Fig. 1.20) that could be interpreted as of circumstellar origin. This has been up to date the only claim of such signatures and it has been recently contradicted by Chen et al. (2007).

Suggestive progenitor signatures could come from the study of the GRB hosts as has been claimed by Hammer et al. (2006). Using HST imaging and VLT spectroscopy of the GRB host galaxies of three low redshift GRBs with SN association, these authors suggest that it could be that the GRB progenitors were WR runaway stars exploding in a low metallicity region located few hundreds of parsecs away from a very high density stellar region including a large number of WR stars. These results may imply that the ejection from the star cluster can lead to a spin-up of the star producing the loss of the hydrogen envelope. This scenario, if confirmed, provides a natural explanation of the very small fraction of massive stars producing a GRB at the end of their life.

It should also be noticed that the lack of wind medium profile signatures and the lack of SN detection associated with GRB 060614 (Della Valle et al. 2006a; Gal-Yam et al. 2006; Fynbo et al. 2006b) leave open the possibility of a different kind of progenitors, at least for some GRBs, such as the merger of neutron stars and white dwarfs proposed by King et al. (2007).

1.4 Plan of this thesis

As illustrated in the previous sections, GRBs are a very powerful source of information for many different fields. They are still an enigmatic phenomenon whose physics and origins are still to be fully understood, moreover thanks to their exceptional brightness they can be use has a tool to retrieve information on the high redshift universe. In my thesis work I explore some of the research area that can be investigated using GRBs.

Chapter 2 : **The REM telescope and the *Swift* satellite.**

One major aspect of successful GRB research is the speed at which observations can be performed. The *Swift* satellite and the REM telescope have been built with the aim of satisfying this need. A significant part of my thesis work has been performed using *Swift* and REM data. In this Chapter I will describe these two utilities and I will explain my involvement in both the *Swift* and REM teams.

Chapter 3 : **The onset of the afterglow and the prompt optical-NIR emission by REM observations.**

This Chapter is dedicated to the afterglow studies performed mainly thanks to the REM early time observations. I will present in great detail the observations of the early afterglow light curve of GRB 060418 and GRB 060607 allowing the determination of the initial lorentz factor of the GRB fireball, as well as a multiwavelength study of both the prompt and the afterglow emission of GRB 070311 leading to the test of different emission mechanisms. Finally, the REM observations of GRB 060908, GRB 071010A and GRB 080319B, for which I was only marginally involved, are briefly reported.

Chapter 4 : **The early afterglow spectral energy distribution.**

Coupling the X-ray data from the Swift-XRT and the optical ones from the *Swift*-UVOT and the ground based telescopes, it is possible to build the spectral energy distribution (SED) of the GRB afterglows at different times. The SEDs allow the test of the GRB emission models and the study of the medium into witch the GRBs explode. In this Chapter I will present preliminary results of the analysis of the SEDs of 22 GRBs.

Chapter 5 : **Short GRB afterglows and host galaxies: the cae of GRB 050724 and GRB 070707.**

This Chapter is dedicated to the class of short GRB. I will present the study of two of the best sampled short GRBs (GRB 050724 and GRB 070707), bringing relevant information to the short GRB picture, in particular concerning their host galaxies and the central engine activity. I was deeply involved in the data acquisition, analysis and interpretation of GRB 070707, while my participation to the work on GRB 050724 was more marginal, therefore for this last GRB I report only the main results and not a detailed analysis.

Chapter 6 : **High resolution spectroscopy of GRB afterglow.**

A powerful way to investigate the ISM associated to the GRB environments, as well as the IGM, is through high resolution spectroscopy of GRB afterglows. With a Rapid-Response Mode (RRM) now available on ESO-VLT (Very Large Telescope), it is now possible to begin observations with UVES (Ultra-violet Visibe Echelle Spectrograph) within minutes after the initial trigger. In this Chapter I will report the results of the GRB environment investigation performed using the UVES spectrum of GRB 050922C, as well as the results of a statistical study I carried out on the MgII absorbers present along the GRB lines of sight.

Chapter 2

The REM telescope and the *Swift* satellite

2.1 The REM telescope

Many fascinating questions remain open about GRB origin and structure. Some of these questions should be answered by collecting data in the early phases of the afterglow. For this reason the international astronomical community developed space borne observatories dedicated mainly (HETE II, *Swift*) or partly (AGILE, INTEGRAL, GLAST) to detect GRBs and send promptly a trigger with the GRB positions to ground-based follow-up telescopes. The aim of these latter facilities is to monitor the early afterglow, to record in a timely manner relevant information and act as an inter-mediate step to activate Target of Opportunity (ToO) procedures at telescopes with larger area. A fast response automatic facility is then highly desirable and the international community built in the last years a large number of robotic telescopes. Particularly important are robotic telescopes that can observe at both optical and near-infrared (NIR) wavelengths, because they may allow the follow-up of high redshift or highly optically extinguished afterglows. REM (Rapid Eye Mount; `http://www.rem.inaf.it`) is one of these (Zerbi et al. 2001; Chincarini et al. 2003; Covino et al. 2004).

2.1.1 Technical characteristics

REM is a fully robotic fast-slewing telescope, installed at la Silla Observatory Chile (see Fig. 2.1), primarily designed to follow the early phases of the afterglow of GRBs detected by space-borne gamma-ray alert systems such as *Swift*. REM is the result of a collaboration between a group of Italian research institutes, coordinated by the Astronomical Ob-

Figure 2.1 The REM telescope at ESO-La Silla, Chile.

servatory of Brera-Merate (INAF), the Astrophysics Service of the CEA-Saclay (France), Dunsink Observatory and UCD University (Ireland).

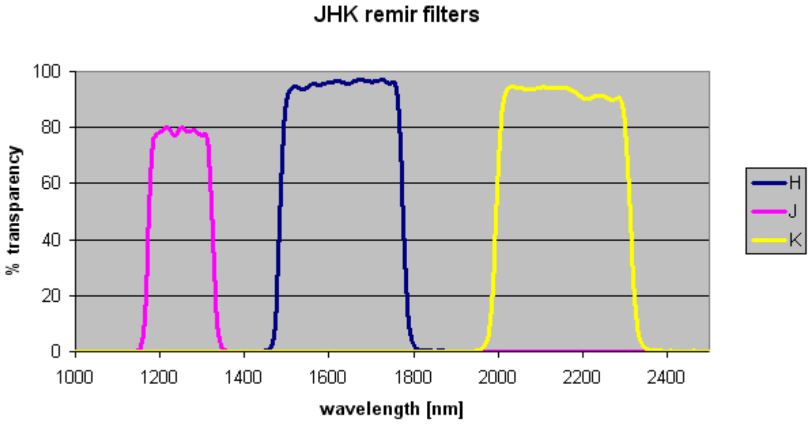

Figure 2.2 Response curves of the REMIR J, H and K' filters.

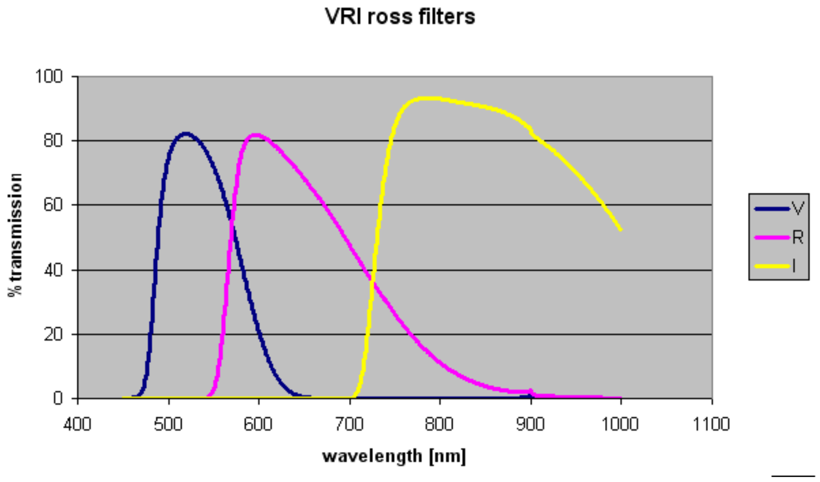

Figure 2.3 Response curve of the ROSS V, R and I filters.

REM hosts a NIR camera (REMIR) covering the $0.95 - 2.3\,\mu$m range with 4 filters (z',J,H,K') and an optical slitless spectrograph (ROSS) covering the range $0.45 - 0.95\,\mu$m with also photometry in the V, R and I filters (see Figs.: 2.2, 2.3, 2.4, 2.5). They have a field of view (FOV) of $9.9 \times 9.9\,\mathrm{arcmin}^2$ on a 512×512 chip, selected to match the typical error-boxes of gamma-ray alert systems. A dichroic present at the telescope focal station splits the convergent light beam to feed the two cameras that therefore can work simultaneously. For a 10 s exposure time, magnitude limits of 14.5 and 15.5 with a signal to noise $S/N = 10$ are obtained in the H and R filters, respectively (see Figs. 2.4 and 2.5).

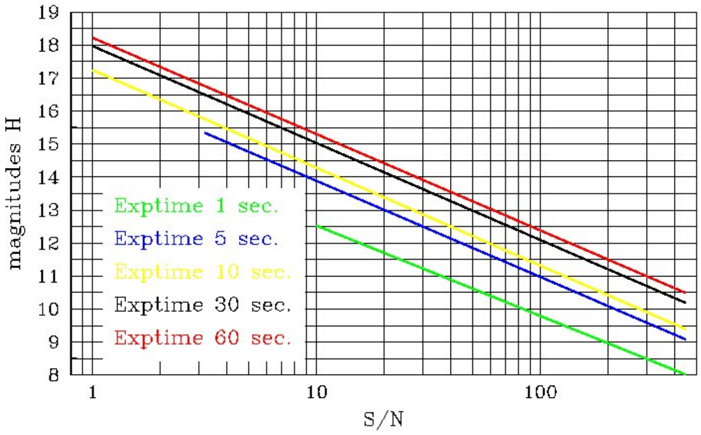

Figure 2.4 Typical performances of the H filter of the REMIR camera.

The REMIR camera needs dithering of the images for noise reduction and sky subtraction. However such a dithering can not be provided moving the telescope since ROSS needs a stable image for longer integrations. The dithering will then be provided by a plate

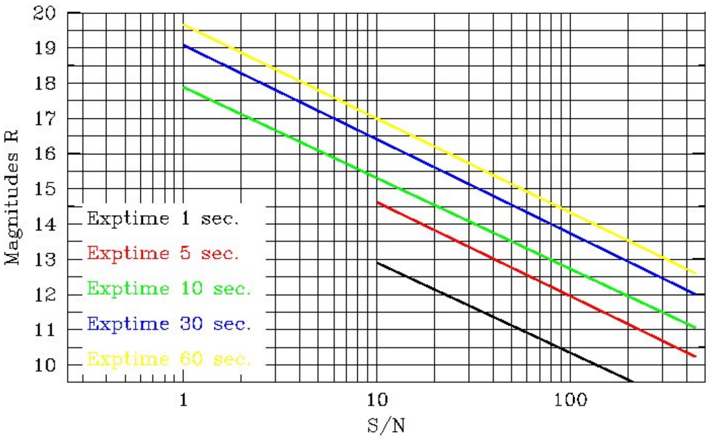

Figure 2.5 Typical performances of the R filter of the ROSS camera.

with plane parallel surfaces inserted with a given tilt (18°) after the dichroic (see Fig. 2.6). The effect of the plate is to translate the image by 20 pixels from the nominal position (no plate inserted) along a given direction. By rotating the plate in the beam the direction and hence the displacement of the image can be changed, providing the dithering.

TORTORA, an automatic Wide Field Optical Camera developed and tested at the Special Astrophysical Observatory (SAO) in agreement with Bologna University-Astronomy Department, has been recently added to REM as a parallel instrument. This optical sky monitoring system (12 cm diameter, 20x25 deg FOV, TV-CCD, unfiltered) is able to recognize flashes in real time. In particular the camera can detect possible optical precursors, the prompt optical emission and the hypothetical orphan afterglows (afterglow with no gamma-ray prompt counterparts). The data flow from the camera is processed on several time scales simultaneously. The shortest time scale is that of frame acquisition (0.13 s), the transient may be detected and classified if seen for 0.4 s - i.e., on three successive frames (this with the aim to filter out noise and moving objects such as satellites and meteors). The limiting magnitude on this timescale is roughly 10.5 in a spectral band close to V. On the second time scale, sums of 100 successive frames are examined; this leads to a magnitude limit of 12 with 13 s temporal resolution and allows the detection of slowly rising transients. Some amazing TORTORA data are reported in Chapter 3.

Besides GRBs, other topics of interest for TORTORA could be optical outbursts related to Soft Gamma Repeaters, possible fast optical supernova precursors, optical flashes from X-ray binaries, and other X-ray transients, such as cataclysmic variables and related stars.

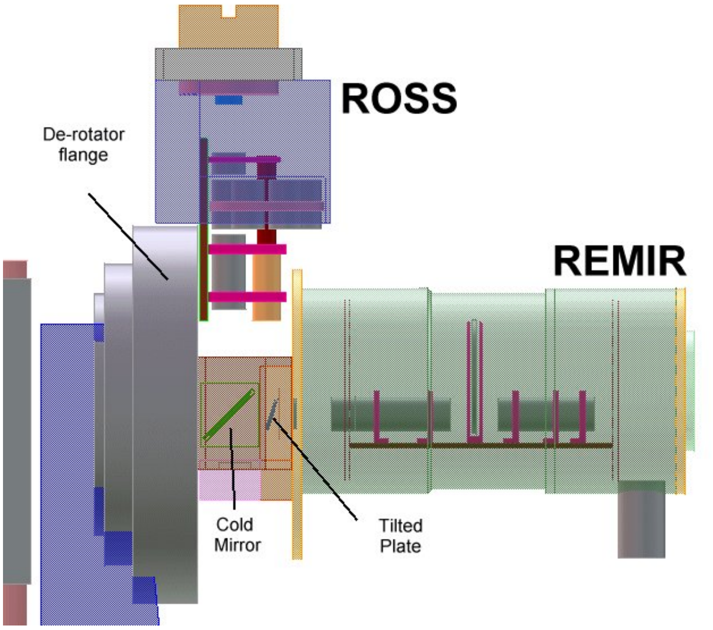

Figure 2.6 The general design of the Nasmyth focus of the REM telescope. The position of the two cameras is shown as well as the dichroic ("Cold Mirror") and the dither plate which allows the infrared images to be shifted thus producing dithered images for sky subctraction.

2.1.2 Telescope control and scientific rationale

The aim of the REM system is to be able to take decisions in a few seconds without any human intervention. However, an adequate interface to allow a remote human control of operations in case of necessity has been also developed.

In its first phase REM, was completely managed by its Project Office, consisting of a technical director, in charge of the operations, and two Science Branch responsible persons, one for GRB science and one for additional science. The whole REM Team was participating to this phase and all the data flow was controlled and exploited by the Science Team. During this period REM science duties were carried out by a group of Duty Scientists (DS), with shifts of one week every 2 months, to which I belonged. The DS charge involved the remote check of the correct working of the entire system, the quick data reduction looking for the GRB counterpart in the case of a GRB observation, and the preparation of the schedule of the targets to be observed for the additional science programs.

Starting 2007, INAF took the control of the complete financial support for REM and the telescope became the second Italian National Facility (after the Telescopio Nazionale

Galileo[1] (TNG) located at the Canary Islands). A REM Team, with one Director and nine Work Package responsible persons entered as Observatory manager.

The REM telescope, as all other robotic facilities dedicated to GRB science, reacts to a trigger from a space-borne satellite. This means that for a considerable amount of time REM is idle in the sense that it is not pointing at any GRB transient. During the idle phase REM serves the community as a fast pointing NIR and optical imager, particularly suitable for multi-frequency monitoring of highly variable and transient sources such as AGN and variable stars (Fuhrmann et al. 2006; Dolcini et al. 2007; Pian et al. 2007). There are semestral call for proposals and the GRB follow-up is a guaranteed time program, automatically renewed every semester and authored in turn by the members of the REM GRB Team. Furthermore, a 10% of the useful time is allocated for the Chilean Institution.

Considering the GRB follow-up, the most general working scenario starts with the reception of an alert message from the GCN[2], a system that has the capability to distribute timely information on GRBs to the GRB research community. Such messages announce the detection of a GRB and also the results of follow-up observations. The REM Observing Software (REMOS) checks if the possible target satisfies some minimum visibility constraints (hour angle, altitude, Sun and Moon distance, etc.). If these conditions are verified, information from REM Environmental Control Software is retrieved and if observations are possible (humidity, wind, sun altitude, etc., within safety and operational limits) REMOS checks if the system is already busy with observations of a different target. If this is the case, and the source is another GRB, a decisional algorithm is applied. Depending on the specific case a decision is taken. In the positive case (new GRB to be observed) or in case the telescope was observing some lower priority target, REMOS sends a message via socket connection to the REM Telescope Control System stopping operations and moving the telescope to the new target. As soon as the telescope is on target (after $\sim 20-40\,\mathrm{s}$) REMOS sends messages to begin observations with some predefined templates and immediately after the first frames are obtained. The dithered NIR frames are automatically recomposed into one single image with the respective photometry. The whole set of images is immediately sent to a dedicated archive as soon as they are processed.

The quick data reduction for the GRB follow-up is performed with the SRP (Swift Reduction Package), a package of UNIX-like commands for quick basic reduction and photometry of optical/NIR imaging data, especially developed for quick GRB follow-up. The software can detect the sources present in the image and carry out instrumental

---

[1] http://www.tng.iac.es/instruments/

[2] http://gcn.gsfc.nasa.gov/gcn/

photometry for each of them. A cross check is made between the sources detected in the REM images and those in the optical or 2MASS[3] catalogues, looking for a transient source. Once a candidate afterglow is found, a set of stars in the image is selected and their catalogued magnitudes are compared with the instrumental ones to estimate the intrinsic shift. The procedure is repeated for successive images and the magnitude variation of the possible counterpart confirms the afterglow detection. A GCN is then written reporting the afterglow detection and its magnitude (or magnitude limit in case of no detection). For the subsequent refined analysis the ESO-MIDAS tool[4] is used.

REM can detect afterglows during the first hours even with an exposure time of a few seconds, giving the possibility to study the light curve and eventual flickering in great detail, to detect possible (even if short) variations from the smooth power-law behaviour and to define any possible break. REM is capable to be on target and to start the observations simultaneously with REMIR and ROSS after only 15 s from the alert, allowing an intensive monitor of the shape of the early optical-NIR afterglow. These data can help to constrain the models for the prompt afterglow emission providing also useful informations about GRB progenitors and GRB environments (see Chapters 3 and 4).

Up to date REM observed 20 GRB afterglows. For 4 of them, REM data led to the publication of a paper (Molinari et al. 2007; Guidorzi et al. 2007c; Covino et al. 2008), whereas data of other 8 will soon be published (GRB GRB060908, GRB 070420, GRB 071025, XRF 080109, GRB 080310, GRB 080319B, GRB 080330, GRB 080413B).

2.2 The *Swift* satellite

Swift (`http://heasarc.gsfc.nasa.gov/docs/swift/swiftsc.html`) is a space observatory dedicated to the study of GRB science (Gehrels et al. 2004). It is equipped with three telescopes working together to observe GRBs and afterglows in the gamma-ray, X-ray, ultraviolet, and optical wavelengths (Fig. 2.7). *Swift* is part of NASA's medium explorer (MIDEX) program and was launched into a low-Earth orbit on a Delta 7320 rocket on November 20, 2004.

Swift's Burst Alert Telescope detects GRBs and relays to the ground a position estimate with 1-4 arcminute accuracy within 15 seconds. After the initial burst detection, the spacecraft autonomously repoints itself in approximately 20 to 75 seconds to bring the burst location within the field of view of the sensitive narrow-field X-ray and UV/optical

---

[3] http://www.ipac.caltech.edu/2mass/

[4] http://www.eso.org/projects/esomidas/

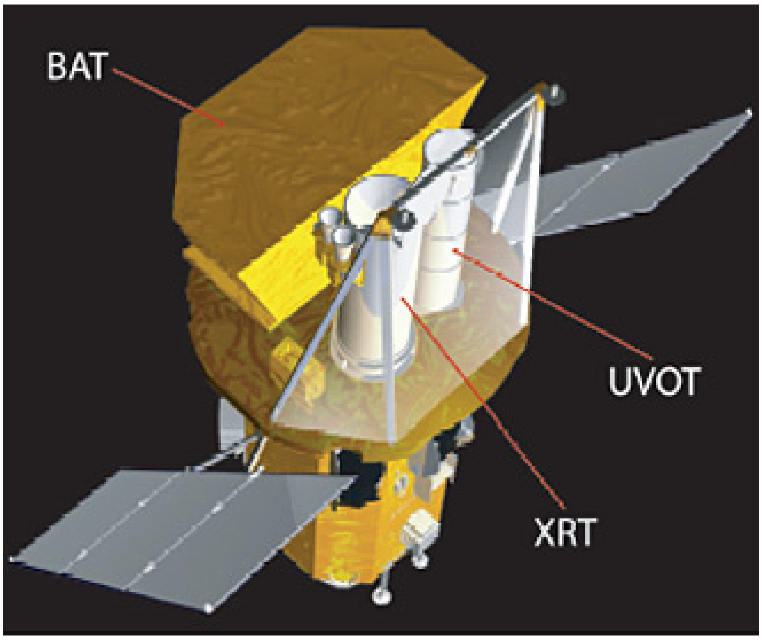

Figure 2.7 A rendered image of the *Swift* satellite and its three instruments BAT, XRT and UVOT. Courtesy of NASA Goddard.

telescopes to observe the afterglow. *Swift* data are public and available at the *Swift* data centre (`http://swift.gsfc.nasa.gov/docs/swift/sdc/`). The data reduction softwares are part of the HEASOFT Software, retrievable at `http://swift.gsfc.nasa.gov/docs/software/lheasoft/download.html`.

Nowadays the *Swift* mission accepts proposals for both ToO and non-ToO observations of non-GRB targets, and considers funding-only proposals related to GRB science.

2.2.1 BAT

The Burst Alert Telescope (BAT) is a highly sensitive, large field of view (1.4 steradian) coded aperture imaging instrument designed to provide GRB triggers with a position precision of ~ 1 to 4 arcmin (Barthelmy 2000). The energy range is 15-150 keV for imaging, with a non-coded response up to 500 keV. When detecting a burst, the BAT calculates an initial position, decides whether the burst merits a spacecraft slew and, if so, sends the position to the spacecraft. In order to study bursts with a variety of intensities, durations, and temporal structures, the BAT has a large dynamic range and trigger capabilities.

The BAT runs in two modes: burst mode, which produces burst positions, and survey mode, which produces hard X-ray survey data. In the survey mode the instrument collects count-rate data in 5-minute time bins for 80 energy intervals. When a burst occurs it switches into a photon-by-photon mode.

The burst trigger algorithm looks for excesses in the detector count rate above expected background and constant sources. It is based on algorithms developed for the HETE-II GRB observatory, upgraded based on HETE-II experience. The algorithm continuously applies a large number of criteria and the BAT processor continuously tracks hundreds of these criteria simultaneously. The burst trigger threshold is adjustable, ranging from 4 to 11 sigma above background noise.

Following the burst trigger, the on-board software checks for, and requires that the trigger corresponds to, a point source, thereby eliminating many sources of background. Time-stamping of events within the BAT has a relative accuracy of 100 microsec and an absolute accuracy of $\sim$ 200 microsec. Immediately after a GRB is detected and located by the BAT, the spacecraft slews to point both the UltraViolet and the X-ray telescopes at the GRB location. The spacecraft's $20 - 70$ s time-to-target means that about 1/3 of the GRBs is observed by the narrow field instruments still during the gamma ray emission. The sky location and lightcurve of the GRB are sent to the ground in near real time through the Tracking and Data Relay Satellite System (TDRSS) and distributed to the world-wide gamma ray burst community through the GCN-Notice system and on the web page `http://gcn.gsfc.nasa.gov/swift_grbs.html`.

2.2.2 UVOT

The UltraViolet and Optical Telescope (UVOT) is a diffraction-limited 30 cm (12" aperture) Ritchey-Chretien reflector, with seven filters (U, B, V, UVW1, UVM2, UVW2 and White) covering the wavelength range from 1700 to 6500 Å (Fig. 2.8) and sensitive down to magnitude 24 in the B-band in a 1000 s exposure.

Rapid response is required to observe GRB counterparts and determine their redshift while they are still bright. The UVOT is uniquely capable for afterglow studies because of the rapidity of the *Swift* slew and of its UV capability which is not possible from the ground. The UVOT also enables optimal ground based observations by providing a very accurate counterpart position ($\sim$ 0.5 arcsecs) and rapid optical images of the GRB field so that optical counterparts can be quickly identified and studied. Stars in the FOV of the UVOT provide an astrometric grid for the GRB field.

When a new GRB is triggered by the spacecraft, the UVOT goes through a predetermined program of exposure times and filter combinations. The initial images are immediately sent to the ground for use as a finding chart by ground-based observers, and for comparison to archival observations of the same patch of sky to detect a variable

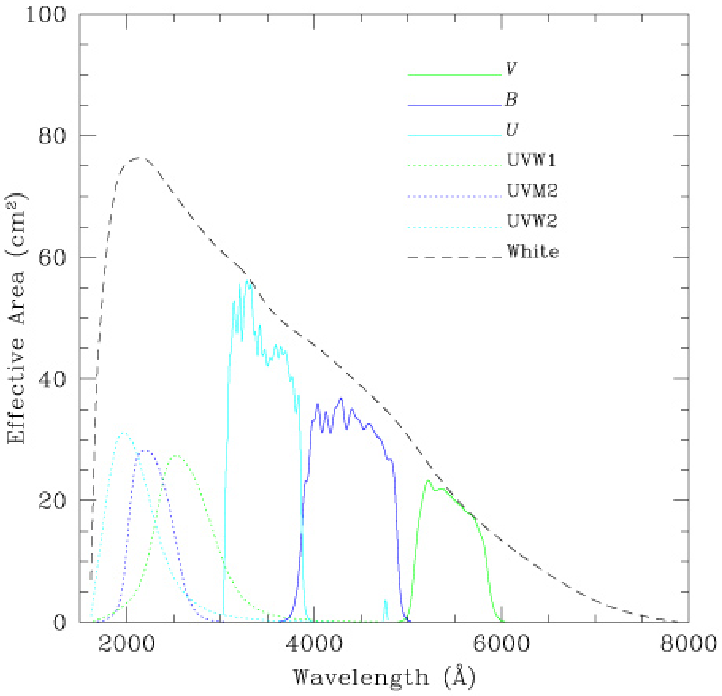

Figure 2.8 Effective area curves for the seven broadband filters of UVOT. From http://swift.gsfc.nasa.gov/ .

source that could be the optical counterpart. The filtered observations give the temporal behaviour as a function of wavelength. If the GRB is at a distance greater than $z \sim 1$, the filtered observations can also estimate the redshift of the GRB because the Lyman-α line (see Chapter 6) begin to absorbs the flux, starting from the U filters and affecting also the other filters as the redshift increases.

2.2.3 XRT

The *Swift* X-Ray Telescope (XRT) is designed to measure the fluxes, spectra, and lightcurves of GRBs and afterglows over a wide dynamic range covering more than 7 orders of magnitude in flux and the 0.2 – 10 keV range in energy (Burrows et al. 2000). The XRT can currently pinpoint GRBs to typically less than 5-arcsec accuracy within 10 s of target acquisition, allowing ground-based optical telescopes to begin immediate photometric and spectroscopic observations of the afterglow (see Fig. 2.9 for a comparison between BAT and XRT position error circles). GRB positions and X-ray spectra are transmitted in near real time through the TDRSS to the GCN network, in the same way said above for the BAT data. The XRT can study the X-ray counterparts of GRBs beginning 20-70 s from the burst discovery and may continue for days to weeks and months.

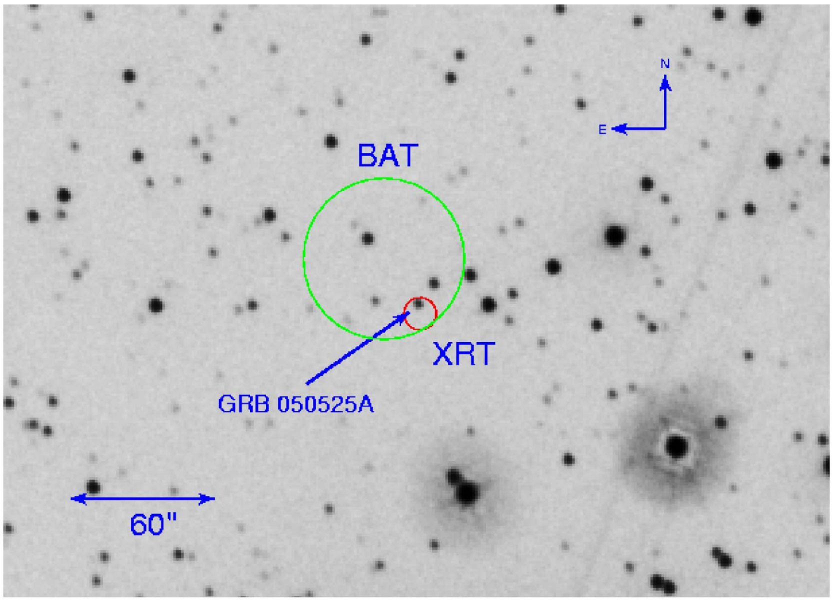

Figure 2.9 Image of the field containing GRB 050525a. The arrow marks the location of the optical afterglow. The BAT and XRT error circles are shown in green and red, respectively. From Blustin et al. (2006).

The XRT supports three readout modes to cover the dynamic range and rapid variability expected from GRB afterglows, and autonomously determines which readout mode to use. Imaging Mode produces an integrated image measuring the total energy deposited per pixel and does not permit spectroscopy, so is only used to position bright sources. Timing Mode sacrifices position information to achieve high time resolution and bright source spectroscopy through rapid CCD readouts. Photon-counting Mode uses sub-array windows to permit full spectral and spatial information to be obtained for source fluxes ranging from the XRT sensitivity limit of 2×10^{-14} up to 9×10^{-10} erg cm^{-2} s^{-1}.

The Window Timing (WT) mode is a high gain mode to achive high resolution timing (2.2 ms) with 1-D position information and spectroscopy. This mode is restricted to a 200 column window covering the central 8 arcmin of the FOV. The Photon-counting mode (PC) mode retains full imaging and spectroscopic resolution, but the time resolution is only 2.5 seconds. The instrument is operated in this mode only at very low fluxes. Fig. 2.10 shows an example of data obtained in these two different modes.

2.2.3.1 My involvement in the *Swift*-XRT Team

During the first year of my PhD thesis I became a Graduate Student Institutional Member of the *Swift* Team working with the XRT Italian Team at the Osservatorio Astronomico di

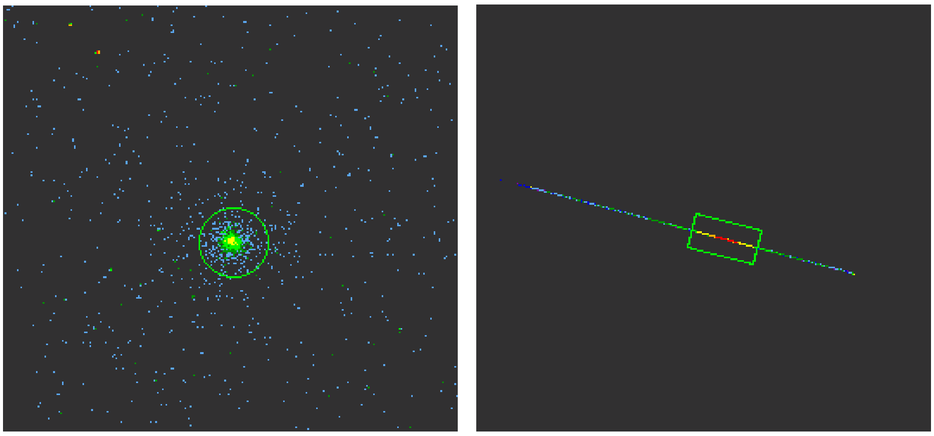

Figure 2.10 Examples of the 2-D (left side) and 1-D (right side) images resulting from data taken in PC and WT mode, respectively, for GRB 060418. The circle and the rectangle indicate the GRB position.

Brera-Merate (INAF-OAB). There, I have initially been trained in the XRT data reduction, I started some fruitful working collaborations that contributed to the achievement of the results presented in Chapters 3 and 4, and I supported the group acting as XRT-Burst Support Scientist (XRT-BSS) and Burst Advocate (BA).

Each team composing the *Swift* collaboration has periodically duty shifts during which its participants are BSS and/or BA, available 24h/24h. When BAT detects a possible GRB, the BSS receives an alert via sms. As soon as the alert is received, the *Swift* members in charge from the different groups give a first quick look at the data and participate in a teleconference where information is exchanged to confirm that the object detected is indeed a GRB and to write and send the first GCN to the scientific community. This first GCN is sent a few minutes after the alert reception, and is currently a pre-compiled text containing information on the main characteristics of the GRB: the detection time, the on-board calculated available position and error circles for each instrument, some preliminary information on the spectra and the flux, and an estimated magnitude in case of a detection by UVOT. The XRT-BSS is in charge of the quick XRT data reduction and of a more detailed analysis of the follow-up XRT observations, to be done everyday as long as the GRB is observed. She/he has to write a GCN reporting the XRT refined analysis results, including: the enhanced position (if any), the parameters resulting from the light-curve (shape, power-law indices...) and spectral fits (photon index, column density...), as well as a prediction on the decay and fluxes over a day time.

For the period of the shift, in Merate the XRT-BSS is also the BA. During the immediate response to a new burst the BA has to acknowledge that she/he has assumed responsibility for the new GRB, and she/he is the first author of the first GCN. The BA is expected to promptly establish regular, direct communication with the current *Swift* Observatory Duty Scientist (ODS), and inform the ODS of any issues relating to the scientific importance (or lack thereof) of the new burst and to the activities of the *Swift* follow-up team. The BA serves also as the *Swift* scientific interface to the *Swift* follow-up team and the general science community. She/He collects scientific inputs for the ODS which might pertain to the *Swift* operations or *Swift* observing schedules. The BA proposes an optimum observing strategy for each assigned bursts, to facilitate the preparation of a *Swift* pre-planned target list and, while the burst remains a viable target, she/he monitors the continuing *Swift* observations of the burst. She/he updates her/his proposal on a daily basis during the daily *Swift* Team teleconference, recommending also when no further data are valuable. After 1 day from the GRB detection, the BA is also in charge of the writing of a first GCN Report (`http://gcn.gsfc.nasa.gov/report_archive.html`) on the *Swift* data and their analysis results. She/He has also to write a final report once no further observation are planned.

Since 2005 I am also a member of the *Multiwavelength Italian Swift Team with International Co-Investigators* (MISTICI) whose principal aim is the photometric and spectroscopic follow-up observation of GRBs at optical-NIR wavelengths, through observational time obtained at ground based facilities such as the Very Large Telescope[5] (VLT) of the European Southern Observatory (ESO), the TNG and REM.

---

[5] http://www.eso.org/sci/facilities/paranal/instruments/overview.html

Chapter 3

The onset of the afterglow and the prompt optical-NIR emission by REM observations.

The early stages of GRB afterglow light curves display a rich variety of phenomena at all wavelengths and contain significant information which may allow determining the physical properties of the emitting fireball. The launch of the *Swift* satellite, combined with the development of fast-slewing ground-based telescopes, has hugely improved the sampling of the early GRB afterglow optical/NIR light curves. To date there are several published early afterglow light curves at these wavelengths whose detections started before the afterglow began its regular power law decay. To explain the early behaviour of most of them different mechanisms have been proposed, i.e. reverberation of the prompt emission radiation, reverse and refreshed shocks and/or energy injection and, lately, large angle emission (e.g. Panaitescu 2007; Kumar & Panaitescu 2008). Examples of early light curves are: GRB 990123: Akerlof et al. 1999; GRB 021004: Kobayashi & Zhang 2003; GRB 021211: Fox et al. 2003; Li et al. 2003; GRB 041219A: Fan et al. 2005; Vestrand et al. 2005; GRB 050730: Pandey et al. 2006; GRB 050801: Roming et al. 2006; Rykoff et al. 2006; GRB 050820A: Vestrand et al. 2006; GRB 050904: Boër et al. 2006; Wei et al. 2006; GRB 060206: Woźniak et al. 2006; Monfardini et al. 2006; GRB 060210: Stanek et al. 2007.

Panaitescu & Vestrand (2008) tried to find a common scenario producing all the different observed behaviours. They classify the optical afterglows in four classes according to the temporal behaviour of the early optical emission: fast-rising with an early peak, slow-rising with a late peak, flat plateau, and rapid decay since the first measurements. They conclude that all the four shapes can be explained by the (forward or reverse) shock coming from a beamed outflow whose kinetic energy has a smoother angular distribution then a top-hat. A wide range of post-peak decays is obtained varying the observer location and the structure of the outflows. They find also a peak flux-peak epoch correlation for the fast- and slow-rising optical afterglows that could provide a way to use them as standard candles. These authors do not consider the optical emission arising from the prompt GRB phase, notwithstanding the strong influence it can have in some cases, as for example for GRB 080319B (see Sect. 3.3.3). Indeed the early optical emission is produced by the afterglow emission starting during the prompt phase, or shortly after, but a counterpart emission tracking the prompt gamma-ray could also be present. The interplay and relative importance of the afterglow and prompt components give rise to the different observed lightcurve shapes.

Since many processes are at work in the early afterglows, it can be difficult to model them so as to determine the fireball characteristics. The simplest case is a light curve shaped by the forward shock only. This case is particularly interesting because, while the late-time light curve is independent of the initial conditions (the self-similar solution), the time at which the afterglow peaks depends on the initial fireball Lorentz factor, thus allowing a direct measurement of this fundamental parameter (Sari & Piran 1999)

The following sections report REM observations of the optical-NIR early light curves. Different shapes are sampled and their interpretations to retrieve informations on the fireball characteristic and the emitting mechanism are discussed.

3.1 GRB 060418 and GRB 060607A: the fireball Lorentz factor determination

I present here the NIR early light-curves of GRB 060418 and GRB 060607A afterglows observed with the REM robotic telescope (see Chapter 2) at La Silla ESO Observatory. They show the onset of the afterglow and its decay as simply predicted by the fireball forward shock model without being strongly affected by the presence of flares or other peculiar features. It has been therefore possible for the first time to obtain a direct determination of the initial fireball Lorentz factor. Part of these results is reported in Vergani (2007), Molinari et al. (2007) and Malesani et al. (2007).

GRB 060418 and GRB 060607A were detected by *Swift* at 03:06:08 UT (Falcone et al.

2006a) and 05:12:13 UT (Ziaeepour et al. 2006), respectively. The BAT light curve of the former ($T_{90} = 52 \pm 1$ s) showed three overlapping peaks (Cummings et al. 2006). For the latter, the light curve is dominated by a double-peaked structure with a duration $T_{90} = 100 \pm 5$ s (Tueller et al. 2006). The *Swift* XRT started observing the fields 78 and 65 s, respectively, after the trigger. For both bursts a bright previously uncatalogued fading source was singled out. The XRT light curves show prominent flaring activity, superposed on the regular afterglow decay. For GRB 060418 a prominent X-ray peak, also visible in the BAT data, was observed at about 128 s after the trigger (Falcone et al. 2006b) while the XRT light curve of GRB 060607A was characterised by at least three flares (Page et al. 2006). UVOT promptly detected bright optical counterparts for both events. The redshift is $z = 1.489$ for GRB 060418 (Dupree et al. 2006; Vreeswijk & Jaunsen 2006) and $z = 3.082$ for GRB 060607A (Ledoux et al. 2006b).

The REM telescope reacted promptly to both GCN alerts and began observing the field of GRB 060418 64 s after the burst (39 s after receiving the alert) and the field of GRB 060607A 59 s after the burst (41 s after receiving the alert). For both targets a bright NIR source was identified (Covino et al. 2006a,b). ROSS could not observe these two GRBs due to maintenance work. REM followed the two events down to the sensitivity limits adopting two different observing strategies. In the former case multi-colour $z'JHK'$-band observations were carried out while in the latter case only the H filter was used to get a denser sampling of the light curve in just one band. All the photometric data are reported in Tables 3.1 and 3.2. To reduce the REM data I used the procedure described in Sect. 2.1.2. Thanks to the brightness of the two afterglows it has been possible in both cases to obtain the afterglow photometry of each single dithered frame of the initial observations, increasing significantly the sampling of the light curve (a point every ~ 10 s).

3.1.1 Light curve modelling

Figures 3.1 (GRB 060418) and 3.2 (GRB 060607A) show the NIR and X-ray light curves of the two afterglows.

The NIR light curves of the two events display a remarkable similarity. Both present an initial sharp rise, peaking at 100–200 s after the burst. The NIR flux of GRB 060418 decays afterwards as a regular power law. The NIR light curve of GRB 060607A shows a similar, smooth behaviour up to ~ 1000 s after the trigger, followed by a rebrightening lasting ~ 2000 s.

To evaluate quantitatively the peak time, the NIR light curves have been fitted using

Table 3.1 Observation log for GRB 060418. The time t_0 indicates the BAT trigger time, 2006 April 18.12926 UT.

* Nysewander et al. (2006a).

Mean time (UT)	$t - t_0$ (s)	Exp. time (s)	Filter	Magnitude
Apr 18.12974	40	5	z	$15.3 \pm 0.3^*$
Apr 18.13371	479	100	z'	13.26 ± 0.06
Apr 18.14215	1114	100	z'	14.70 ± 0.09
Apr 18.15722	2416	100	z'	15.58 ± 0.12
Apr 18.13264	292	100	J	12.33 ± 0.05
Apr 18.13975	906	150	J	13.82 ± 0.06
Apr 18.15323	2071	300	J	14.94 ± 0.07
Apr 18.13014	76	10	H	11.98 ± 0.16
Apr 18.13032	92	10	H	11.46 ± 0.07
Apr 18.13050	107	10	H	11.00 ± 0.19
Apr 18.13067	122	10	H	10.92 ± 0.12
Apr 18.13085	137	10	H	11.01 ± 0.02
Apr 18.13538	529	150	H	12.24 ± 0.03
Apr 18.14527	1383	150	H	13.57 ± 0.04
Apr 18.16008	2663	150	H	14.89 ± 0.22
Apr 18.18578	4883	150	H	15.48 ± 0.10
Apr 18.19649	5809	150	H	15.40 ± 0.12
Apr 18.20720	6734	150	H	15.60 ± 0.10
Apr 18.21791	7659	150	H	15.83 ± 0.15
Apr 18.13121	168	10	K'	10.23 ± 0.04
Apr 18.13139	184	10	K'	10.26 ± 0.03
Apr 18.13157	200	10	K'	10.38 ± 0.03
Apr 18.13175	215	10	K'	10.48 ± 0.05
Apr 18.13192	230	10	K'	10.49 ± 0.05
Apr 18.14652	1491	300	K'	13.14 ± 0.09

a smoothly broken power-law (Beuermann et al. 1999)

$$F(t) = \frac{F_0}{[(t/t_{\rm b})^{\kappa\alpha_{\rm r}} + (t/t_{\rm b})^{\kappa\alpha_{\rm d}}]^{1/\kappa}} \tag{3.1}$$

where F_0 is a normalisation constant, $\alpha_{\rm r(d)}$ is the slope of the rise (decay) phase ($\alpha_{\rm r} < 0$) and κ is a smoothness parameter. The time at which the curve reaches its maximum is $t_{\rm peak} = t_{\rm b}(-\alpha_{\rm r}/\alpha_{\rm d})^{1/[\kappa(\alpha_{\rm d}-\alpha_{\rm r})]}$. We obtain for GRB 060418 and GRB 060607A, respectively, peak times of 153 ± 10 and 180 ± 6 s. Any other suitable functional forms provide comparable results. The complete set of fit results is reported in Table 3.3.

The X-ray data have been taken with the *Swift* XRT, and I carried out the data

Table 3.2 Observation log for GRB 060607A. The time t_0 indicates the BAT trigger time, 2006 June 7.21682 UT.

Mean time (UT)	$t - t_0$ (s)	Exp. time (s)	Filter	Magnitude
Jun 7.21767	73	10	H	14.60 ± 0.20
Jun 7.21794	97	10	H	13.35 ± 0.10
Jun 7.21811	111	10	H	12.91 ± 0.07
Jun 7.21829	127	10	H	12.57 ± 0.06
Jun 7.21848	143	10	H	12.33 ± 0.05
Jun 7.21866	159	10	H	12.01 ± 0.05
Jun 7.21883	174	10	H	12.18 ± 0.05
Jun 7.21902	190	10	H	12.10 ± 0.05
Jun 7.21919	205	10	H	12.07 ± 0.05
Jun 7.21937	220	10	H	12.21 ± 0.05
Jun 7.21955	236	10	H	12.21 ± 0.05
Jun 7.21973	251	10	H	12.31 ± 0.05
Jun 7.21991	267	10	H	12.40 ± 0.05
Jun 7.22008	282	10	H	12.40 ± 0.05
Jun 7.22027	298	10	H	12.55 ± 0.06
Jun 7.22045	314	10	H	12.72 ± 0.06
Jun 7.22062	328	10	H	12.59 ± 0.06
Jun 7.22080	344	10	H	12.82 ± 0.07
Jun 7.22098	359	10	H	12.84 ± 0.07
Jun 7.22128	385	30	H	12.95 ± 0.05
Jun 7.22169	421	30	H	12.96 ± 0.05
Jun 7.22209	455	30	H	13.10 ± 0.05
Jun 7.22251	492	30	H	13.23 ± 0.05
Jun 7.22292	527	30	H	13.25 ± 0.05
Jun 7.22400	620	150	H	13.40 ± 0.04
Jun 7.22606	798	150	H	13.96 ± 0.06
Jun 7.22812	976	150	H	14.32 ± 0.07
Jun 7.23033	1167	150	H	14.94 ± 0.08
Jun 7.23223	1331	150	H	14.63 ± 0.07
Jun 7.23427	1508	150	H	14.69 ± 0.08
Jun 7.23635	1687	150	H	14.55 ± 0.07
Jun 7.24047	2043	150	H	14.49 ± 0.07
Jun 7.24253	2221	150	H	14.68 ± 0.08
Jun 7.24459	2399	150	H	15.05 ± 0.09
Jun 7.24767	2665	300	H	15.46 ± 0.08
Jun 7.25113	2964	300	H	15.73 ± 0.10
Jun 7.25493	3293	300	H	15.58 ± 0.09
Jun 7.25886	3632	150	H	15.48 ± 0.13
Jun 7.37574	13730	6000	H	17.23 ± 0.23

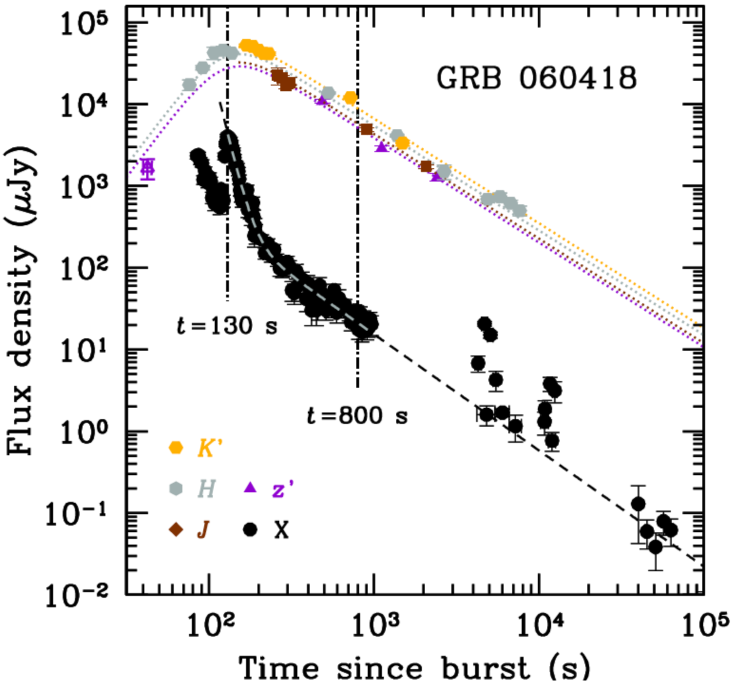

Figure 3.1 NIR and X-ray light curves of GRB 060418. The dotted lines show the fits of the NIR data using the smoothly broken power law (see Sect. 3.1.1), while the dashed line shows the best-fit to the X-ray data. The vertical lines mark the epochs at which we computed the SED (Fig. 3.3).

Table 3.3 Best fit values of the light curves of the first hour of observations for GRB 060418 and the first 1000 s for GRB 060607A (1σ errors), using the smoothly broken power-law described in Sect. 3.1.1 with $t_{\rm peak} = t_{\rm b}(-\alpha_{\rm r}/\alpha_{\rm d})^{1/[\kappa(\alpha_{\rm d}-\alpha_{\rm r})]}$. The relatively large χ^2 of the fits is the consequence of small-scale irregularities present throughout the light curve (see Figs. 3.1 and 3.2).

GRB	$t_{\rm peak}$ (s)	$t_{\rm b}$ (s)	$\alpha_{\rm r}$	$\alpha_{\rm d}$	κ	χ^2/d.o.f.
060418	153^{+10}_{-10}	127^{+18}_{-21}	$-2.7^{+1.0}_{-1.7}$	$1.28^{+0.05}_{-0.05}$	$1.0^{+0.4}_{-0.4}$	33.3/16
060607A	180^{+5}_{-6}	153^{+12}_{-12}	$-3.6^{+0.8}_{-1.1}$	$1.27^{+0.16}_{-0.11}$	$1.3^{+0.9}_{-1.1}$	28.5/19

reduction using the standard *xrtpipeline* task and the packages of the HEASOFT Software (see Sect. 2.2). Pile-up corrections both in WT and PC mode were taken into account when required, following Romano et al. (2006). As for many other GRBs observed by *Swift*, the early X-ray light curves of both events show several, intense flares superimposed on the power-law decay. In particular, for GRB 060418 a bright flare is active between ∼ 115 and 185 s. Excluding flaring times, the decay is described by a power law with decay slope $\alpha_{\rm X} = 1.42 \pm 0.03$. The X-ray light curve of GRB 060607A is more complex and

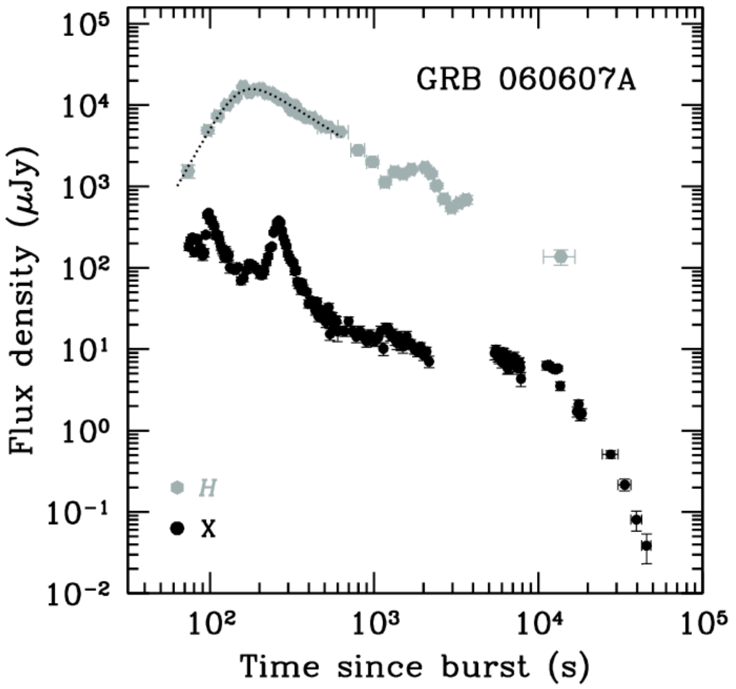

Figure 3.2 H-band and X-ray light curves of GRB 060607A. The dotted line shows the fit to the NIR data using the smoothly broken power law defined in Sect. 3.1.1.

presents two large flares within the first 400 s. After that the flux density decreases with a shallow power law (with small-scale variability) until steepening sharply at $t \sim 10^4$ s.

By comparing the X-ray and NIR light curves of both bursts, it is evident that the flaring activity, if any, is much weaker at NIR frequencies. It is thus likely that the afterglow peak, visible in the NIR, is hidden in the X-ray region.

This can be confirmed by considering the NIR/X-ray spectral energy distribution (SED; Fig. 3.3). A detailed explanation about how the SEDs are built and interpreted is presented in Chapter 4. We constructed the SED for GRB 060418. At $t = 800$ s, when both the NIR and X-ray light curves are decaying regularly, the SED is described by a synchrotron spectrum, with the cooling frequency (see Sect. 1.2.2) lying at $\nu_{\rm c} \sim 3 \times 10^{15}$ Hz (determined as the frequency where the optical spectral decay meets the X-ray branch, see Fig. 3.3). The spectral slopes at NIR and X-ray wavelengths are $\beta_{\rm NIR} = 0.65 \pm 0.06$ and $\beta_{\rm X} = 1.03 \pm 0.04$, respectively. A small amount of extinction in the host ($A_V = 0.3$ mag assuming the SMC extinction curve) was included in order to make $\beta_{\rm NIR}$ consistent with the synchrotron expectation $\beta_{\rm NIR} = \beta_{\rm X} - 0.5$. The situation is clearly different at early times, when X-ray flaring is active: the X-ray component is softer ($\beta_{\rm X} = 1.27 \pm 0.03$) and much brighter than the extrapolation of the NIR emission (even including the dust correction). This implies a

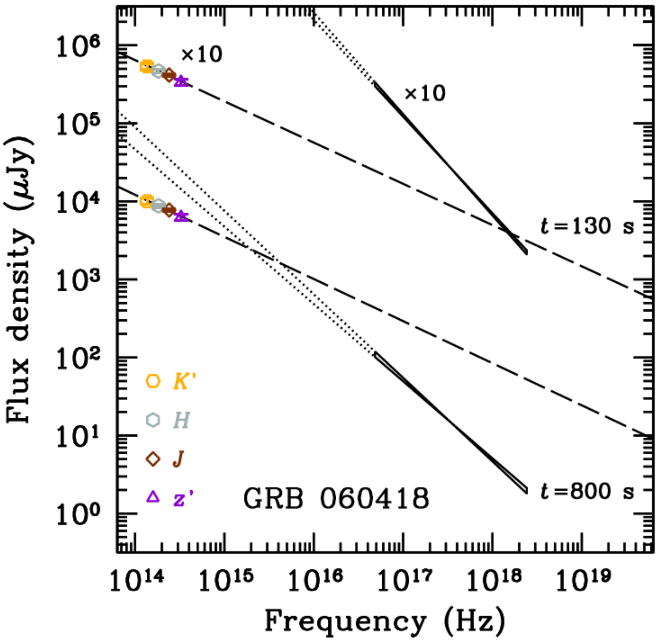

Figure 3.3 SED of the GRB 060418 afterglow at 130 and 800 s after the trigger. NIR data have been corrected for Galactic and host extinction ($A_V = 0.74$ and 0.3 mag, respectively). The dashed lines indicate the optical spectral slopes. The X-ray spectral slopes lie inside the solid (then dotted) lines.

different origin for the X-ray emission. For GRB 060607A, the light curve is complicated by several flares. Due to the lack of multicolour data, a detailed analysis is not possible.

3.1.2 Determination of the Lorentz factor Γ_0

The spectral and temporal analysis is in agreement with the interpretation of the NIR afterglow light curves as corresponding to the afterglow onset, as predicted by the fireball forward shock model (Sari & Piran 1999; Mészáros 2006). According to the fits, the light curves of the two afterglows peak at a time $t_{\rm peak} > T_{90}$ as expected in the impulsive regime outflow ('thin shell' case). In this scenario the quantity $t_{\rm peak}/(1+z)$ corresponds to the deceleration timescale $t_{\rm dec} \sim R_{\rm dec}/(2c\Gamma^2_{\rm dec})$, where $R_{\rm dec}$ is the deceleration radius, c is the speed of light and $\Gamma_{\rm dec}$ is the fireball Lorentz factor at the deceleration time. It is therefore possible to estimate the Lorentz factor Γ at $t_{\rm dec}$ (Sari & Piran 1999), which is expected to be half of its initial value Γ_0 (Panaitescu & Kumar 2000; Mészáros 2006). For a homogeneous surrounding medium with particle density n, we have

$$\Gamma(t_{\rm peak}) = \left[\frac{3E_\gamma(1+z)^3}{32\pi n m_{\rm p} c^5 \eta t^3_{\rm peak}}\right]^{1/8} \approx 160 \left[\frac{E_{\gamma,53}(1+z)^3}{\eta_{0.2} n_0 t^3_{\rm peak,2}}\right]^{1/8}, \tag{3.2}$$

where $E_\gamma = 10^{53} E_{\gamma,53}$ erg is the isotropic-equivalent energy released by the GRB in gamma rays, $n = n_0$ cm^{-3}, $t_{\rm peak} = 100\, t_{\rm peak,2}$ s is the peak time in the observer frame, $\eta = 0.2\, \eta_{0.2}$ is the radiative efficiency and $m_{\rm p}$ is the proton mass. I used $E_\gamma \sim 1.1 \times 10^{53}$ erg for GRB 060607A (Tueller et al. 2006) and $E_\gamma = 9 \times 10^{52}$ erg for GRB 060418 (Golenetskii et al. 2006b). Substituting the measured quantities and normalising to the typical values $n = 1$ cm^{-3} and $\eta = 0.2$ (Bloom et al. 2003), I inferred for both bursts $\Gamma_0 \approx 400\, (\eta_{0.2} n_0)^{-1/8}$. This value is very weakly dependent on the unknown parameters n and η, and therefore provides a robust determination of Γ_0.

One possible caveat concerns the density profile of the surrounding medium. In principle, the temporal and spectral properties of the afterglow can be used to distinguish among the different cases (see also Chapter 4). For $\nu < \nu_{\rm c}$, before $t_{\rm dec}$, the flux is expected to rise as t^3 for the homogeneous (ISM) case, while it evolves slower than $t^{1/3}$ in a wind environment. The measured NIR values for GRB 060418 and GRB 060607A seem therefore consistent with the ISM case (see also Jin & Fan 2007). For GRB 060418, however, no closure relation is satisfied for $t > t_{\rm peak}$. In fact, irrespective of the density profile, the temporal and spectral slopes in the X-ray region (which lies above $\nu_{\rm c}$) should verify $\alpha_{\rm X} = 3\beta_{\rm X}/2 - 1/2$ (see Sect. 1.2.2), which is clearly not the case given the observed values. Such a discrepancy has been observed in many other cases (see Chapter 4) and may be due to radiative losses and varying equipartition parameters (see e.g. Panaitescu et al. 2006; Zhang et al. 2006). An estimate of Γ at $t_{\rm peak}$, and consequently of Γ_0, in the case of a wind environment with a wind-shaped profile $n(r) = Ar^{-2}$ (Chevalier & Li 2000), where A is a constant, would be:

$$\Gamma(t_{\rm peak}) = \left[\frac{E_\gamma (1+z)}{8\pi A m_{\rm p} c^3 \eta t_{\rm peak}} \right]^{1/4} . \tag{3.3}$$

Using the same values as above for E and z, and assuming $A/(3 \times 10^{35}$ cm$^{-1}) = A^* = 1$, $\Gamma_0 \approx 150$ is found in both cases.

The determination of $t_{\rm peak}$ is in principle affected by the choice of the time origin t_0, which we set to the BAT trigger time (Lazzati & Begelman 2006; Quimby et al. 2006). These authors have however shown that this effect is small, and mostly affects the rise and decay slopes rather than the peak time (especially when $t_{\rm peak}$ is larger than the burst duration, as for GRB 060418 and GRB 060607A). The measurement of Γ_0 is thus not very sensitive to the exact choice of t_0.

For both bursts, no reverse shock emission is detected. The lack of such flashes has already been noticed previously in a set of *Swift* bursts with prompt UVOT observations (Roming et al. 2006). Among the many possible mechanisms to explain the lack of this component, strong suppression (or even total lack) of reverse shock emission is naturally expected if the outflow is Poynting-flux dominated (Fan et al. 2004; Zhang & Kobayashi 2005). Nevertheless, Jin & Fan (2007) showed that for GRB 060418 and GRB 060607A the reverse shock emission might be too weak to be detected.

The optical afterglow of GRB 030418 showed a peaked light curve similar to the GRB 060418 and GRB 060607A ones, explained by Rykoff et al. (2004) as due to a decreasing extinction. The peaks of both bursts are too sharp to match this interpretation. Furthermore, a very large extinction would be implied, which contrasts with the UVOT detection in the rest-frame UV (Schady & Falcone 2006; Oates et al. 2006). The peak of GRB 030418 might have been indeed the afterglow onset. In that case, assuming $z = 1$, $\Gamma_0 \sim 100$ is inferred using Eq. 3.2.

The measured Γ_0 values are well within the range envisaged by the standard fireball model ($50 \lesssim \Gamma_0 \lesssim 1000$; Piran 2000; Guetta et al. 2001; Soderberg & Ramirez-Ruiz 2002; Mészáros 2006). They are also in agreement with existing measured lower limits (Lithwick & Sari 2001; Zhang et al. 2006) or values determined using a possible thermal component of the prompt emission (Pe'er et al. 2007). Although the values for Γ_0 are comparable for GRB 060418 and GRB 060607A, prompt optical detections have shown very different shapes, so this value should not be taken as common to every GRB.

We point out that our measurements are valid also in the scenario of a structured outflow observed off-axis, proposed by Panaitescu & Vestrand (2008): in this case the value of Γ that is obtained would correspond only to the Lorentz factor of the region of the outflows moving towards the observer.

3.1.3 Determination of the fireball characteristics

Using $\Gamma_0 = 400$ it is also possible to derive other fundamental quantities characterising the fireball of the two bursts. In particular, the isotropic-equivalent baryonic load of the fireball is $M_{\rm fb} = E/(\Gamma_0 c^2) \approx 7 \times 10^{-4}\, M_\odot$, and the deceleration radius is $R_{\rm dec} \approx 2ct_{\rm peak}[\Gamma(t_{\rm peak})]^2/(1+z) \approx 10^{17}$ cm. This is much larger than the scale of $\sim 10^{15}$ cm where the internal shocks are believed to power the prompt emission (Meszaros & Rees 1997; Rees & Meszaros 1994), thus providing further evidence for a different origin of the prompt and afterglow stages of the GRB.

The detection of the peak allows the measurement of another important quantity, the afterglow bolometric fluence $\mathcal{F} = \int F_\nu(t,\nu)\,\mathrm{d}\nu\,\mathrm{d}t$. The integration over the frequency domain requires also the knowledge of the spectral shape. The multiwavelength coverage of GRB 060418, coupled with the X-ray monitoring, allows the determination of the peak frequency as a function of time, and the spectrum can be safely extrapolated.

The integral computation gives $\mathcal{F} = 2.2 \times 10^{-6}$ erg cm^{-2} (Malesani et al. 2007). This is the first case for which such a measurement has been performed. For comparison, the bolometric fluence of the prompt emission, computed thanks to the broad-band *Wind*/Konus[1] measurement (Golenetskii et al. 2006b), is $\mathcal{F}_{\rm GRB} = 1.6 \times 10^{-5}$ erg cm^{-2}. This implies an afterglow-to-prompt fluence ratio of 16%. In principle, external shocks are more efficient in dissipating the fireball energy than internal collisions (which have a low Lorentz factor contrast). This result thus implies that, at least for GRB 060418, external shocks are not much efficient in radiating the dissipated energy (but see also Eichler & Jontof-Hutter 2005). This is consistent with the observed regime of slow cooling inferred by the SED modeling.

3.2 GRB 070311: a direct link between the prompt emission and the afterglow

As introduced in Sect. 1.2, the prompt emission of GRBs is mostly thought to be produced in internal shocks of relativistic shells ejected by the progenitor at different times, whereas the late multi-band afterglow is interpreted as the synchrotron emission of electrons swept up by the fireball expanding through the surrounding ISM. The short timescale variability observed in flares superimposed on the X-ray/optical afterglow of several bursts, recently made evident by *Swift* (see Sect. 1.1.2.1), has been interpreted as evidence for prolonged activity of the inner engine through internal shocks (e.g. Zhang et al. 2006; Chincarini et al. 2007). Yet, it is not clear whether this applies to all the observed bursts and, in particular, whether the bursts exhibiting single γ-ray pulses with no short timescale variability at late times could also be entirely interpreted as external shocks.

In fact, the case of a single fast rise exponential decay (FRED; Fishman & Meegan 1995) profile can still match the expectations of a single shell sweeping up the ISM (Fenimore et al. 1996). In this scenario, the kinetic energy of a single ultrarelativistic shell is converted into internal energy of the swept-up ISM; the shocked electrons radiate via synchrotron emission and inverse Compton scattering. In the simplest case of a thin shell ploughing into the ISM and emitting for a short time, the expected time profile of the γ-ray prompt emission is that of a single pulse with fast rise and slow decay. The cooling timescale of

---

[1] Konus is a GRB monitor launched on the GGS-Wind spacecraft in November 1994. It covers the energy range from 10 to 770 keV. http://heasarc.gsfc.nasa.gov/docs/heasarc/missions/wind.html

electrons is in most cases negligible with respect to the hydrodynamical timescale (Sari 1997). As a consequence, the rise time is determined by the emission time given by the crossing time of the shell by the reverse shock, while the decay time is dominated by the angular spreading timescale. This can lead both prompt γ-ray emission and late X-ray/optical flares to a common origin within the external shock scenario: the main fireball would be responsible for the prompt emission, while a second shell would produce the rebrightening when impacting the leading blastwave in a refreshed shock.

This external shock scenario can explain the observations of GRB 070311, as illustrated in the following sections (based on Guidorzi et al. 2007c).

3.2.1 Multiwavelength Data

GRB 070311 triggered the INTEGRAL/IBAS on 2007 March 11 at 01:52:50 UT and it was localised at RA = $05^{\mathrm{h}}\ 50^{\mathrm{m}}\ 09.86^{\mathrm{s}}$, Dec. = $+03^\circ\ 22'\ 29.3''$, with an error radius of 2.5 arcmin (Mereghetti et al. 2007).

The γ-ray prompt emission in the 20–200 keV energy band lasted about 50 s, with a peak flux of 0.9 ph $\mathrm{cm}^{-2}\ \mathrm{s}^{-1}$ (1 s integration time) and a fluence of $(2 \div 3) \times 10^{-6}$ erg cm^{-2} (Mereghetti et al. 2007; Sazonov et al. 2007).

The REM telescope reacted promptly and began observing 55 s after the GRB trigger time (see Sect. 3.2.1.1), discovering a bright fading IR counterpart within the *INTEGRAL* error circle at RA = $05^{\mathrm{h}}\ 50^{\mathrm{m}}\ 08.21^{\mathrm{s}}$, Dec. = $+03^\circ\ 22'\ 30.3''$ (J2000; Covino et al. 2007), corresponding to Galactic coordinates (l, b) of (202.766°, −11.998°).

The *Swift* narrow field instruments, XRT and UVOT, began observing at 7004 s after the trigger time. The XRT found an uncatalogued fading source at the position RA = $05^{\mathrm{h}}\ 50^{\mathrm{m}}\ 08.43^{\mathrm{s}}$, Dec. = $+03^\circ\ 22'\ 30.0''$ (J2000), with an error radius of $3.8''$ and at a distance of $3.3''$ from the optical counterpart (Guidorzi et al. 2007b). No source was detected corresponding to the optical and X-ray afterglows by UVOT down to $V = 19.5$ and $B = 20.5$ (3σ) from 197 s exposures (Holland 2007).

The 2.2 m telescope of Calar Alto[2] (CAHA) equipped with the Calar Alto Faint Object Spectrograph (CAFOS) observed the afterglow in the R filter at 0.72 and 1.73 days after the burst.

Because of the low Galactic latitude, the Galactic reddening along the direction to the GRB is large: $E_{B-V} = 0.763$ mag (Schlegel et al. 1998). The Galactic extinction in

---

[2] http://www.caha.es/

each filter has been estimated through the NASA/IPAC Extragalactic Database extinction calculator[3]: $A_V = 2.53$, $A_R = 2.04$, $A_I = 1.48$, $A_J = 0.69$, $A_H = 0.44$, $A_K = 0.28$ mag.

3.2.1.1 γ–ray data

Figure 3.4 shows the 18–200 keV background-subtracted time profile of GRB 070311 as recorded by *INTEGRAL* (Sazonov et al. 2007). The onset of the GRB appears to occur about 45 s before the trigger time. Hereafter, all times will be given relative to the onset time, i.e. 45 s prior to the trigger time. From 75 to ∼125 s the signal drops below the sensitivity of the instrument. Interestingly, between ∼125 and 225 s there is a hint of the presence of a faint γ-ray tail. Although this feature is detected at a $\sim 2.5\sigma$ confidence level (see thick cross in Fig. 3.4), and thus should be regarded as tentatively detected, it is interesting to see how it fits into the overall picture together with near infrared, optical and X-ray observations of GRB 070311, as addressed below.

The integrated spectrum in the 18–200 keV band is well fit by a power law with a photon index of $\Gamma_\gamma = 1.3 \pm 0.1$ and a fluence of $(3.0 \pm 0.5) \times 10^{-6}$ erg cm^{-2} (20–200 keV). The spectrum shows no statistically significant high-energy cut-off. The peak energy lies above 80 keV during the prompt emission. There is also an indication of spectral softening in the course of the burst, with Γ_γ evolving from 0.8 ± 0.2 during the rise phase to 1.45 ± 0.15 during the peak and decay of the emission (Sazonov et al. 2007). The conversion factor from rate to flux units in the 18–200 keV band is $(1.2 \pm 0.2) \times 10^{-9}$ erg cm^{-2} count^{-1}.

3.2.1.2 Infrared/optical data

REM began observing the field of GRB 070311 55 s after the burst trigger (36 s after the reception of the alert), following the event for ∼1 hour.

For the first ∼500 s the REMIR observations were performed using only the H filter with increasing exposure times, then all the NIR filters were used in rotation. A similar observing strategy was adopted in the optical. R band observations lasted ∼1400 s for a total of 40 consecutive images. During the following ∼2700 s, VRI images were acquired in rotation but the optical transient was already below the instrument detection limits for the V and I filters.

For both the optical and NIR data sets, the reduction and the analysis were performed following standard procedures reported in Sect. 2.1.2. The photometric calibration for the NIR was accomplished by applying average magnitude shifts computed using the 2MASS

---

[3] http://nedwww.ipac.caltech.edu/forms/calculator.html

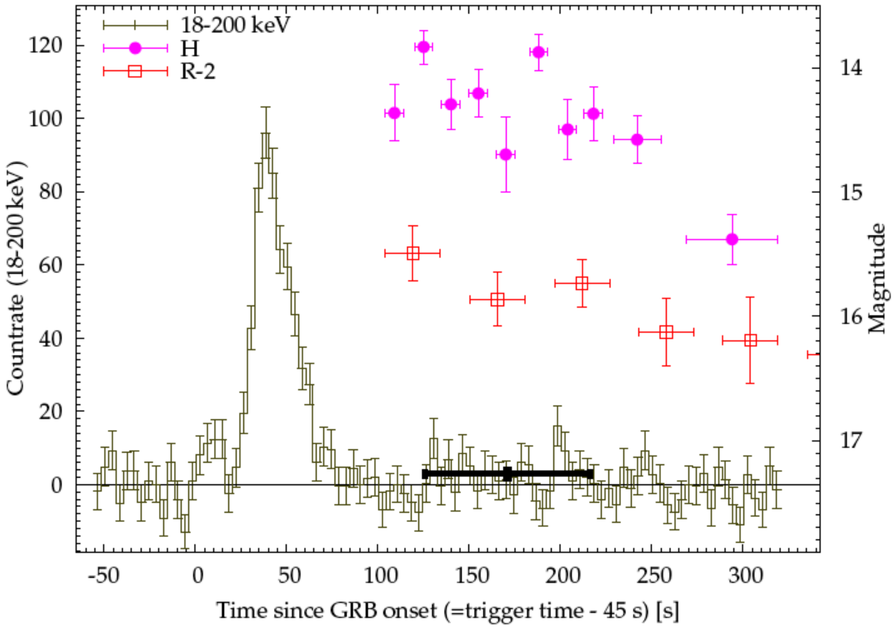

Figure 3.4 Histogram of the *INTEGRAL* 18–200 keV background-subtracted γ-ray profile of GRB 070311 (integration time of 4 s; left axis). The thick cross shows a grouped bin of the γ-ray profile, $\sim$2.5 σ above the background. REM H (filled circles) and R (empty squares) magnitudes of the NIR/optical afterglow are also reported, on the right axis.

catalogue. The optical data were calibrated using instrumental zero points, checked with observations of standard stars in the SA95 Landolt field (Landolt 1992), or with the SDSS[4] in the case of the z' filter.

Further observations were acquired with CAFOS. The photometric calibration was performed observing the standard field PG0942 (Landolt 1992) at a similar airmass as the GRB field.

REM and CAFOS photometry is reported in Table 3.4. Figure 3.4 shows the REM HR prompt measurements together with the γ-ray time profile, while Fig. 3.5 shows the $KHJz'R$ light curves.

Hereafter, the magnitudes shown are not corrected for Galactic extinction, whilst fluxes, flux densities and all the best-fit models are. When the models are plotted together with magnitudes, the correction for Galactic extinction is removed.

---

[4] http://www.sdss.org

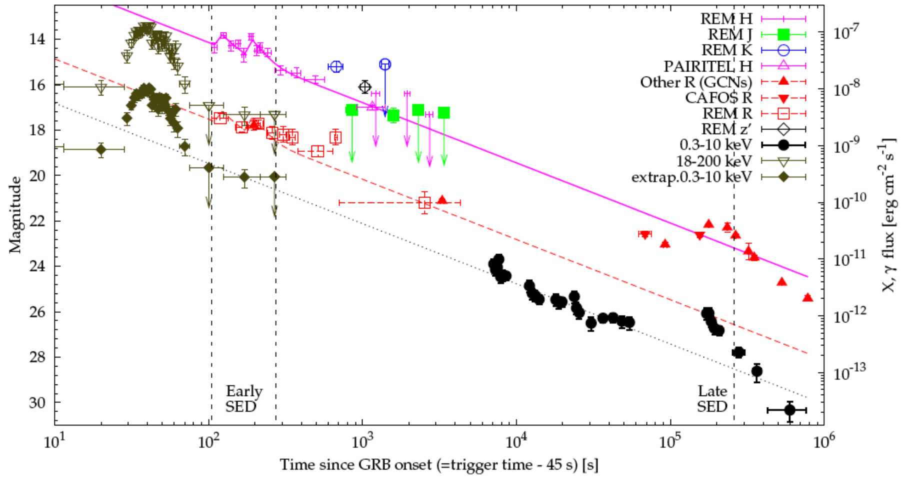

Figure 3.5 Panchromatic light curves of the prompt and afterglow emission of GRB 070311: the flux in the 18–200 keV band by *INTEGRAL* (empty upside down triangles) and in the 0.3–10 keV band of the late afterglow by *Swift*/XRT (filled circles) are given on the right axis. Filled diamonds show the γ-ray flux extrapolated to the 0.3–10 keV band (see Sect. 3.2.2.2). Magnitudes in J (filled squares), H (crosses), K (empty circles), z' (empty diamond) and R (empty squares) filters by REM and R by CAFOS (filled upside down triangles) are given on the left axis. A single H point from PAIRITEL (Bloom 2007; empty triangle) and other R points from GCN circulars (Cenko 2007; Dai et al. 2007; Garnavich et al. 2007; Halpern & Armstrong 2007b,c,a,d; Jelinek et al. 2007; Kann et al. 2007a; Wren et al. 2007; filled triangles) are also shown. Upper limits are at 3-σ confidence level. The solid (dashed) line shows the best-fit power law ($\alpha = 1.06 \pm 0.08$) and two pulses superposed on the H (early R, i.e. $t < 10^4$ s) filter curve (see Sect. 3.2.2.2). The dotted line shows the same power-law component renormalised to the first part ($t < 10^5$ s) of the X-ray curve ($\alpha_{\mathrm{x}} = \alpha_H = \alpha_R$). The two earliest vertical dashed lines show the time interval used to extract an early SED (Fig. 3.12), while the third vertical line shows the epoch of a late SED (Fig. 3.13).

3.2.1.3 X–ray data

The XRT began observing GRB 070311 on 2007 March 11 at 03:49:34 UT, 7004 s after the *INTEGRAL* trigger, and ended on 2007 March 19 at 22:38:54 UT, with a total net exposure of 81.8 ks in photon counting (PC) mode spread over 8.8 days. Table 3.5 reports the log of the XRT observations.

The XRT data were processed using the FTOOLS software package (v. 6.1) distributed within HEASOFT (see Sect.2.2), using the task *xrtpipeline* (v.0.10.4) applying calibration with standard filtering and screening criteria. Data were acquired only in PC mode (see Sect.2.2.3) due to the faintness of the source. Events with grades 0–12 were selected. The

Table 3.4 REM $KHJz'R$ and CAFOS R photometry of GRB 070311.

Start Time (s)	End Time (s)	Exposure (s)	Mag[a,b]	Instr/Filter
554	704	150	15.20 ± 0.24	REM/K
1281	1431	150	>15.10	REM/K
59	69	10	14.36 ± 0.23	REM/H
75	85	10	13.83 ± 0.14	REM/H
90	100	10	14.29 ± 0.20	REM/H
105	115	10	14.21 ± 0.19	REM/H
120	130	10	14.70 ± 0.30	REM/H
138	148	10	13.88 ± 0.15	REM/H
154	164	10	14.50 ± 0.24	REM/H
168	178	10	14.37 ± 0.22	REM/H
184	210	26	14.58 ± 0.19	REM/H
224	274	50	15.38 ± 0.20	REM/H
303	353	50	15.48 ± 0.22	REM/H
372	522	150	15.77 ± 0.15	REM/H
1099	1249	150	>16.4	REM/H
1826	1976	150	>16.4	REM/H
2536	2836	300	>17.3	REM/H
735	885	150	>17.10	REM/J
1462	1612	150	17.35 ± 0.31	REM/J
2188	2338	150	>17.10	REM/J
3198	3498	300	>17.24	REM/J
917	1067	150	16.1 ± 0.3	REM/z'
59.2	89.2	30	17.49 ± 0.22	REM/R
105.6	135.6	30	17.86 ± 0.21	REM/R
151.8	181.8	30	17.73 ± 0.19	REM/R
197.9	227.9	30	18.12 ± 0.27	REM/R
244.1	274.1	30	18.19 ± 0.35	REM/R
290.3	320.3	30	18.31 ± 0.35	REM/R
336.5	597.0	180	18.91 ± 0.24	REM/R
613.0	643.0	30	18.32 ± 0.34	REM/R
659.2	4295.6	1530	21.20 ± 0.50	REM/R
62174	74783	8400	22.57 ± 0.12	CAFOS/R
149180	160924	10810	22.60 ± 0.08	CAFOS/R

[a] Values are not corrected for Galactic extinction.

[b] Errors at the 68% confidence level and upper limits (3 σ) are given.

Table 3.5 XRT observation log of GRB 070311.

Sequence	Obs Mode	Start Time (UT)	End Time (UT)	Exposure (s)	Start Time[a](s)	End Time[a](s)
00020052001	PC	2007-03-11 03:49:34	2007-03-11 17:08:03	18780	7004	54913
00020052002	PC	2007-03-13 00:49:40	2007-03-13 13:46:56	9697	169010	215646
00020052003	PC	2007-03-14 00:49:36	2007-03-14 13:53:56	9465	255406	302466
00020052004	PC	2007-03-15 00:47:36	2007-03-15 14:01:54	9954	341686	389344
00020052005	PC	2007-03-16 01:06:34	2007-03-16 23:41:55	9028	429224	510545
00020052006	PC	2007-03-17 01:08:59	2007-03-17 22:21:55	14574	515769	592145
00020052007	PC	2007-03-17 23:45:20	2007-03-18 22:32:56	6283	597150	679206
00020052008	PC	2007-03-19 00:04:45	2007-03-19 22:38:54	3711	684715	765964

[a] Since *INTEGRAL* trigger time.

XRT analysis was performed in the 0.3–10 keV energy band.

Source photons were extracted from a circular region with a 20 pixel radius (1 pixel = $2.36''$; Fig. 3.6) and point spread function (PSF)-renormalised. The background was estimated from four circular regions with a total area of 11.5×10^3 pixel^2 away from any source present in the field. When the count rate dropped below $\sim 10^{-2}$ counts s^{-1}, `XIMAGE` has been used with the tool `SOSTA`, which corrects for vignetting, exposure variations and PSF losses within an optimised box, using the same background region.

The resulting 0.3–10 keV light curve is shown in Fig. 3.7. It was binned so as to achieve a minimum signal to noise ratio (S/N) of 3, except for the last two bins (with a S/N of 2.8 and 2.6, respectively), as well as a minimum of 20 total counts.

The spectral analysis is presented in Sect. 3.2.4

3.2.2 Early light curve fitting

The decays in different energy bands have been analyzed as homogeneously as possible.

The 18–200 keV pulse were first fitted adopting the FRED profile by Norris et al. (1996):

$$F(t) = \begin{cases} A\ \exp\left[-\left(\dfrac{t_{\rm max}-t}{\sigma_{\rm r}}\right)^{\nu}\right] & , \quad t < t_{\rm max} \\ A\ \exp\left[-\left(\dfrac{t-t_{\rm max}}{\sigma_{\rm d}}\right)^{\nu}\right] & , \quad t > t_{\rm max} \end{cases} \tag{3.4}$$

where $t_{\rm max}$ is the peak time, $\sigma_{\rm r}$ and $\sigma_{\rm d}$ are the rise and decay times, respectively, A is the normalisation and ν is the peakedness (when $\nu = 1$ the profile is a simple exponential, when $\nu = 2$ it is a Gaussian). The best-fit parameters for the γ-ray pulse are: $t_{\rm max} = 39.0 \pm 0.8$ s,

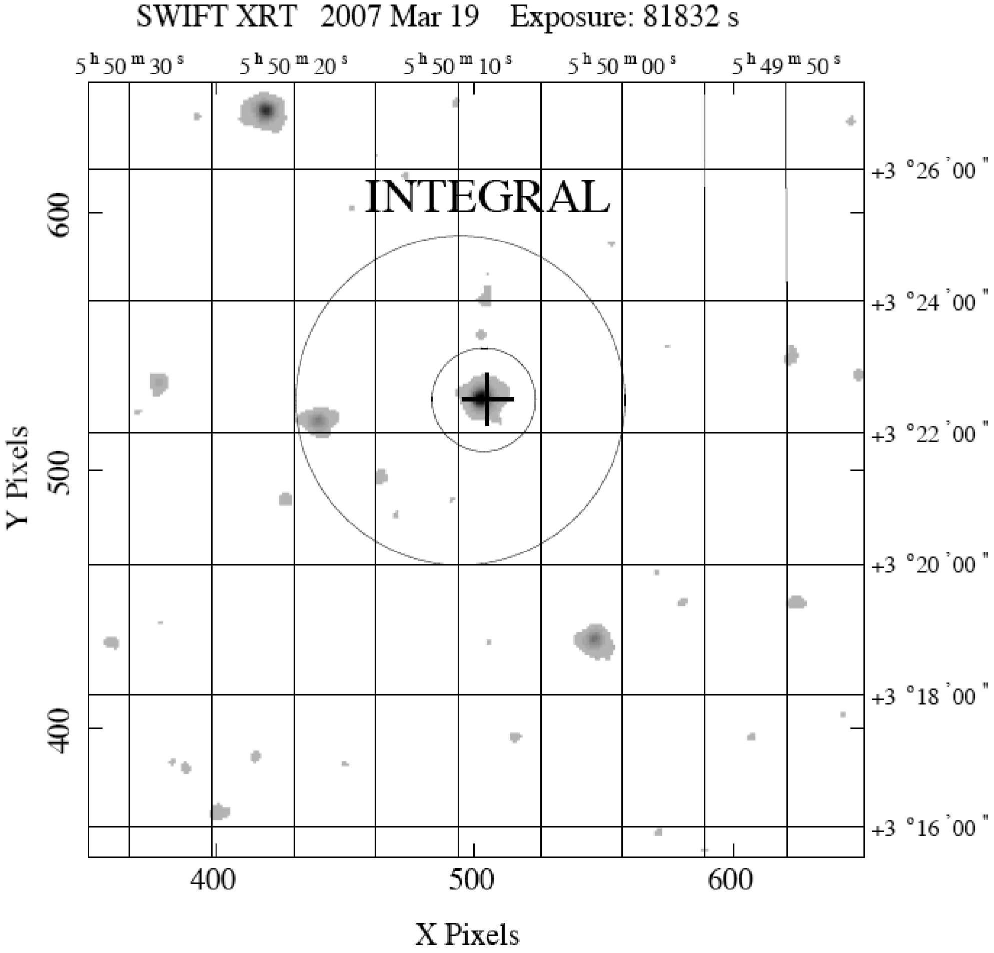

Figure 3.6 XRT image of the field of GRB 070311 obtained from 82 ks PC data. The large circle shows the *INTEGRAL* position with an error radius of 2.5arcmin (90% CL). The cross shows the optical afterglow position discovered by REM. The small circle is a 20 pixel radius region centred on the XRT afterglow.

$\sigma_{\rm r} = 8.5 \pm 1.0$ s, $\sigma_{\rm d} = 15.0 \pm 1.7$ s. The peakedness was found to be $\nu = 1.08 \pm 0.13$, starting with an initial value of $\nu = 1$. The result is shown by the solid line in Fig. 3.8. The flux density at 88 keV has been calculated, which corresponds to the energy at which the flux density equals the average flux density in the 18–200 keV band assuming $\beta_\gamma = 0.3$ (Sazonov et al. 2007).

Considering the NIR/optical data, the H light curve, which is the one best monitored at early times, has been fitted first. We tried to fit the points up to ~300 s with a simple power law to test whether the fluctuations visible in Fig. 3.4 are statistical variations around a power-law decay. The resulting χ^2/dof is only 17.5/7 with a chance probability of 1.4% and a power-law index of $\alpha_H = 0.5 \pm 0.4$ (1 σ). This probability becomes smaller if the R and H points are combined.

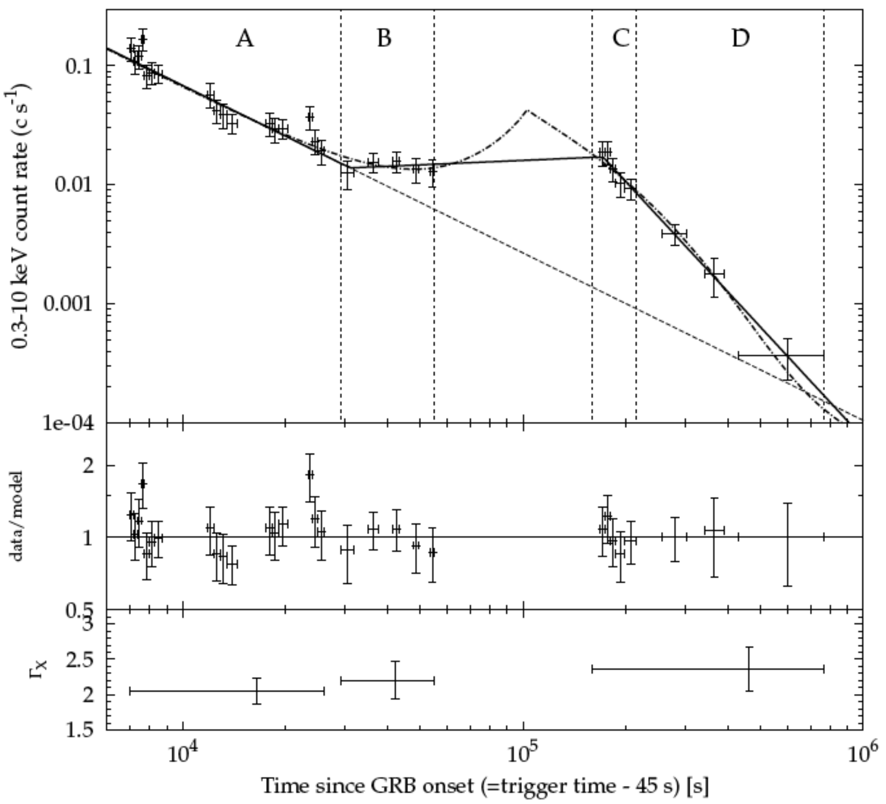

Figure 3.7 *Top panel*: X-ray afterglow light curve of GRB 070311 obtained with XRT in the 0.3–10 keV energy band. The solid line shows the best fit obtained with a double broken power law, while the dashed line shows the extrapolation of the initial power-law decay. The dashed-dotted line shows the best-fit combination of a FRED-like pulse superposed on a power law. A detailed description of these fits is given in Sect. 3.2.3. Labelled vertical slices correspond to four different regions where spectra have been extracted. *Mid panel*: fractional residuals with respect to the double broken power-law model. *Bottom panel*: photon index (vertical error bars are 1 σ).

A more detailed model is necessary, therefore two alternative approaches have been followed (the PAIRITEL point at $t = 1160$ s from Bloom 2007 was included in the H data set for this analysis). First, the early pulses have been fitted them in terms of two overlapping FRED-shaped pulses (PULSES model). Subsequently, a power-law continuum has been added, in the assumption that the afterglow contribution is not negligible at this time (PL+PULSES model). The choice of a FRED shape has been done because this fits well and also allows a better comparison with the results of the fit of the γ-ray pulse. Both H and R profiles were corrected for Galactic extinction. Given the less dense sampling of the H and R curve with respect to the γ-ray one, the peakedness was fixed to the best-fit value reported above for the γ-ray data.

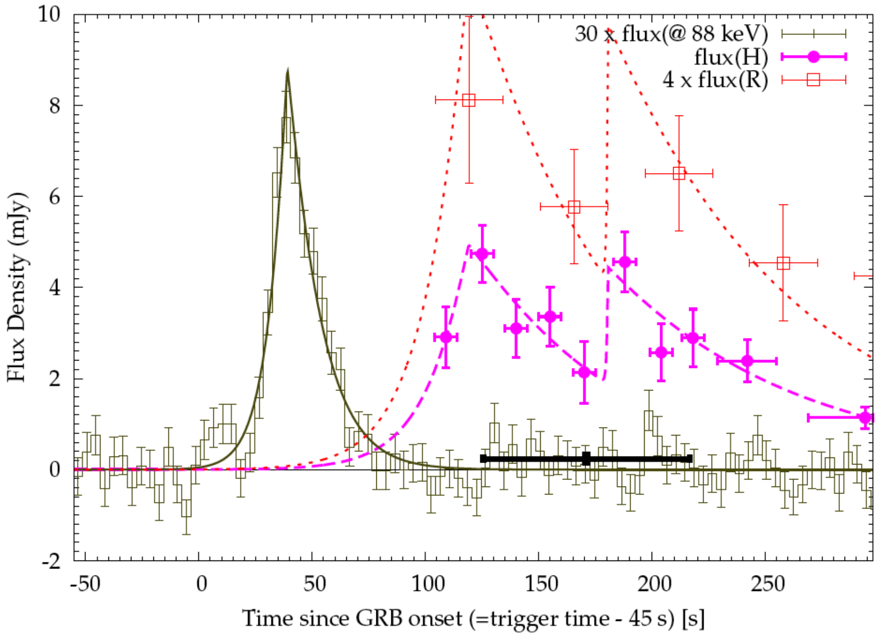

Figure 3.8 *INTEGRAL* background-subtracted γ-ray flux density at 88 keV (crosses; integration time of 4 s) magnified 30 times, REM H (filled circles) and R (empty squares; magnified 4 times) flux densities of the NIR/optical afterglow (corrected for Galactic extinction). Solid, dashed and dotted lines show the best-fit models of the γ-ray, H- and R-band pulses, respectively. The thick cross is the same as that in Fig. 3.4.

Best-fit parameters of the models are reported in Table 3.6.

3.2.2.1 PULSES **model**

The first H pulse peaks 80 s after the γ-ray peak. The pulse shape is different: the rise time of the H pulse is about twice as long, while its decay time is about 4 times longer. The flux density normalisation constant, $A_{\rm H1} = 4.9 \pm 0.3$ mJy, is about 17 times that of the γ rays at 88 keV. The second H pulse follows the first by $\sim$62 s. Because of the poor sampling of the rise, only the decay is better constrained and turns out to be about twice as long as the decay time of the first pulse, while the normalisation of the second pulse is about half as big: $A_{\rm H2} \simeq A_{\rm H1}/2$, so that the fluence during the decay is similar to that of the first pulse. The dashed line in Fig. 3.8 shows the sum of both pulses fitting the H points (filled circles).

To evaluate whether the R points that are simultaneous to the prominent pulses seen in H are consistent with being derived from the same profile as H within uncertainties, the best-fit model of the H curve has been integrated over the R time bins. The rescaling factor $f_{\rm best}$ that minimises the χ^2 between the measured R and the expected rescaled mean

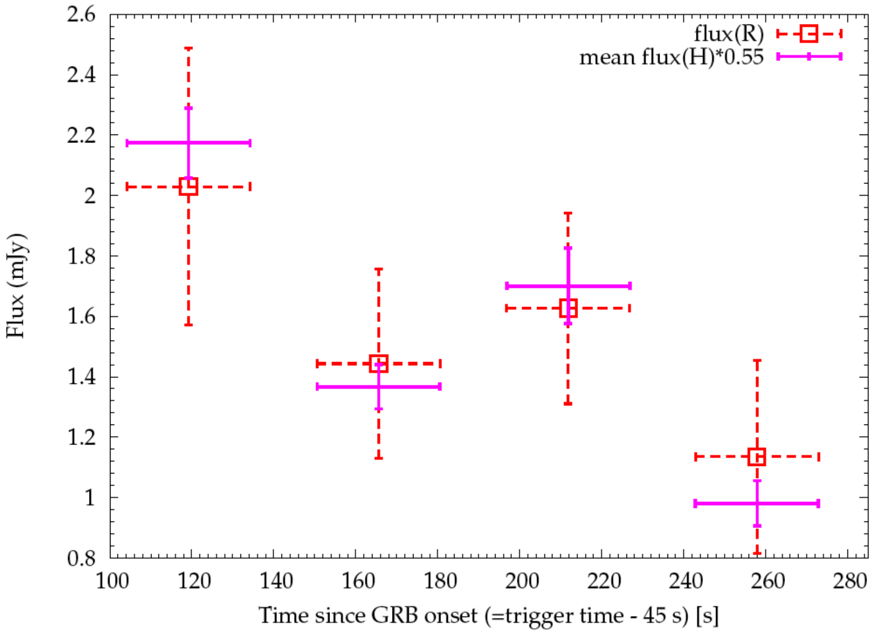

Figure 3.9 Early R optical flux (dashed squares) compared with the time-integrated flux expected from the best-fit model of the H curve rescaled by a factor of 0.55 ± 0.06, which minimises the χ^2.

H flux corresponds to $f_{\rm best} = 0.55 \pm 0.06$, yielding $\chi^2/{\rm dof} = 0.36/3$. The result is shown in Fig. 3.9. The time profile best-fitting the H pulses is consistent with the simultaneous R measurements. R points and the best-fit model are displayed in Fig. 3.8, both magnified by a factor of 4 for clarity.

3.2.2.2 PL+PULSES model

In contrast to the description of the PULSES model, here we assume that the contribution of the power-law continuum is not negligible from the very beginning of the NIR/optical observations. The result is shown in Fig. 3.5. For the same reasons as for the PULSES model, we first fitted the H profile. The power-law continuum turns out to have a slope of $\alpha_H = 1.06 \pm 0.08$ (solid line in Fig. 3.5). The same combination of pulses as that found for the PULSES model has been added, releasing gradually some of the parameters to obtain a better fit. Table 3.6 reports the best-fit values. The fit for the R filter was done by allowing just a scaling factor of the H profile. This turned out to be $f_{\rm best} = 0.55 \pm 0.07$, i.e. the same as that obtained with the PULSES model. The R best-fit profile is shown in Fig. 3.5 with a dashed line. The χ^2/dof of the best-fit model are acceptable: 6.0/7 and 12.1/8 for the H and R profiles, respectively.

The main differences with the results of the PULSES model concern the shorter rise times

Table 3.6 Best-fit parameters of the multi-band light curves of the afterglow of GRB 070311. Uncertainties are 1 σ. Values of frozen parameters are reported in square brackets.

Energy band/filter	Model	Component	α	$t_{\rm peak}^{\rm a}$ (s)	$\sigma_{\rm r}$ (s)	$\sigma_{\rm d}$ (s)	A (mJy)	ν
18–200 keV	PULSES	pulse	–	39.0 ± 0.8	8.5 ± 1.0	15.0 ± 1.7	$0.29 \pm 0.05^{\rm b}$	1.08 ± 0.13
H	PULSES	1st pulse	–	119.0 ± 2.2	18.2 ± 4.8	63.6 ± 5.2	4.9 ± 0.3	[1.08]
H	PULSES	2nd pulse	–	180.5 ± 9.4	0.5 ± 3.6	110 ± 15	2.6 ± 0.2	[1.08]
R	PULSES	1st pulse	–	[119.0]	[18.2]	[63.6]	2.7 ± 0.2	[1.08]
R	PULSES	2nd pulse	–	[180.5]	[0.5]	[110]	1.4 ± 0.1	[1.08]
H	PL+PULSES	pl	1.06 ± 0.08	–	–	–	$3.6 \pm 2.0^{\rm c}$	–
H	PL+PULSES	1st pulse	–	119.0 ± 0.1	[0.1]	27 ± 18	2.2 ± 1.0	[1.08]
H	PL+PULSES	2nd pulse	–	181.1 ± 0.6	[0.1]	41 ± 17	2.6 ± 0.8	[1.08]
R	PL+PULSES	pl	[1.06]	–	–	–	$2.0 \pm 1.1^{\rm c}$	–
R	PL+PULSES	1st pulse	–	[119.0]	[0.1]	[27]	1.2 ± 0.6	[1.08]
R	PL+PULSES	2nd pulse	–	[181.1]	[0.1]	[41]	1.4 ± 0.4	[1.08]
late R	PL+PULSE	pl	[1.06]	–	–	–	$11.0 \pm 0.9^{\rm d,e}$	–
late R	PL+PULSE	pulse	–	$19.1 \pm 0.3^{\rm f}$	$2.85 \pm 0.54^{\rm f}$	$7.4 \pm 0.7^{\rm f}$	$36 \pm 4^{\rm e}$	0.91 ± 0.34
0.3–10 keV	PL+PULSE	pl	1.47 ± 0.20	–	–	–	$1.3 \pm 0.1^{\rm d,g}$	–
0.3–10 keV	PL+PULSE	pulse	–	$10 \pm 3^{\rm f}$	$2.9 \pm 2.5^{\rm f}$	$6.6 \pm 0.9^{\rm f}$	$24 \pm 12^{\rm g}$	0.89 ± 0.56

[a] Time since GRB onset (corresponding to 45 s before the trigger time). [b] Flux density corresponding at 88 keV. [c] Flux at $t = 100$ s. [d] Flux at $t = 10^5$ s. [e] Units of μJy. [f]]Units of 10^4 s. [g] Units of 10^{-13} erg cm^{-2} s^{-1}.

which here were fixed to 0.1 s. This is a consequence of having increased the continuum component represented by the power law. The pulse shape is less constrained, for the same reason. The second pulse still has a longer decay than the first, while its peak intensity is now comparable with that of the first. The dotted line in Fig. 3.5 shows the best-fit power law of the X-ray data up to 10^5 s, obtained by fixing $\alpha_{\rm x} = \alpha_H = \alpha_R$. The fit is acceptable: $\chi^2/{\rm dof} = 24.3/21$.

We tentatively extrapolated the γ-ray flux to the 0.3–10 keV band, assuming the simple spectral power law with $\Gamma_\gamma = 1.3 \pm 0.1$ (Sect. 3.2.1.1). This assumption relies upon the fact that the peak energy is likely to lie above 80 keV because of the hardness of the photon index Γ_γ. The suppression factor due to the soft X-ray absorption measured in the X-ray spectrum has been applied. The result is shown in Fig. 3.5. Interestingly, the gamma-ray prompt emission flux extrapolated in the X-ray band matches the level of the single power law derived from fitting the early H and R continuum components, $\alpha = 1.06$.

It has to be noticed that the first J upper limit at 810 s, preceding the detection at 1537 s, is inconsistent with the assumption $\alpha_J = \alpha_H$. Comparing all the optical-NIR filters, a flux increase seems to appear still after the first two optical peaks, i.e. after ~600 s. This, combined with the detections in J and z', could be a hint of a third flare.

3.2.3 Late R/X-ray rebrightening

Together with the early optical/NIR flares possibly accompanied by a γ-ray tail, the late, bright and long rebrightening seen in X-ray and R band probably is the most intriguing feature of GRB 070311. Although such late brightenings or flares are not unprecedented, only a few bursts have exhibited them so far: e.g. GRB 970508 (Piro et al. 1998; Galama et al. 1998), the short GRB 050724 (Campana et al. 2006; Malesani et al. 2007), the $z = 6.3$ GRB 050904 (Cusumano et al. 2007; Watson et al. 2006c).

We also note the presence of the shallow decay phase preceding the X-ray brightening (or corresponding to its gradual onset). Due to the lack of contemporaneous coverage in the R band, a similar shallow decay phase is not observed in the optical bands. However, from Fig. 3.5 we infer that it must have taken place (e.g. some energy injection between $\sim 10^4$ s and $\sim 10^5$ s) to power the continuum component of the R-filter decay at late times, which is significantly above the extrapolation of the early data ($\sim$ 1 order of magnitude). The later R-band data therefore have been fitted separately from the early R light curve, adopting a combination of a power-law and a single pulse (Eq. 3.4). The power-law index was fixed to the value found in Sect. 3.2.2.2 for the early part of the R, i.e. $\alpha_R = 1.06$. The result is shown in Fig. 3.10 (thick dashed line).

The X-ray light curve was fit firstly with a double broken power law (solid line in Fig. 3.7), whose best fit parameters are the following: $\alpha_{\mathrm{x},1} = 1.4 \pm 0.1$, $\alpha_{\mathrm{x},2} = -0.1^{+0.7}_{-0.2}$, $\alpha_{\mathrm{x},3} = 3.1^{+0.5}_{-0.4}$, $t_{\mathrm{x,b1}} = 31 \pm 4$ ks, $t_{\mathrm{x,b2}} = 1.7^{+0.1}_{-0.4} \times 10^5$ s ($\chi^2/\mathrm{dof} = 16.8/24$), where $\alpha_{\mathrm{x},i}$ ($i = 1, 2, 3$) are the canonical initial, mid, and final decay slopes and $t_{\mathrm{x,b}i}$ ($i = 1, 2$) are the two break times, respectively. The last point lies near the extrapolation of the initial power-law decay (dashed line in Fig. 3.7). From the X-ray data alone it is not possible to determine whether the shallow and final steep decay phases are the result of a late rebrightening, after which the decay will resume the pre-break behaviour.

The dashed-dotted line in Fig. 3.10 represents the case when the X-ray late light curve is fit with the combination of two power laws, the second of which turns on between 6×10^4 and 2×10^5 s and models the rebrightening superimposed on the first power law. The best-fit indices are $\alpha^{(\mathrm{pp})}_{\mathrm{x},1} = 1.4 \pm 0.1$ and $\alpha^{(\mathrm{pp})}_{\mathrm{x},2} = 3.5 \pm 0.5$, respectively (1 σ confidence). For both components, the time origin was fixed to the GRB onset time. The time at which the second power law sets in cannot be estimated from the data; however, this is irrelevant for determining the power-law indices.

We then apply the same as model used for the R-band (thick solid line in Fig. 3.10). Initially α_{x} was fixed to $\alpha_{\mathrm{x}} = \alpha_R$ in analogy with Sect. 3.2.2.2, but it had to be released

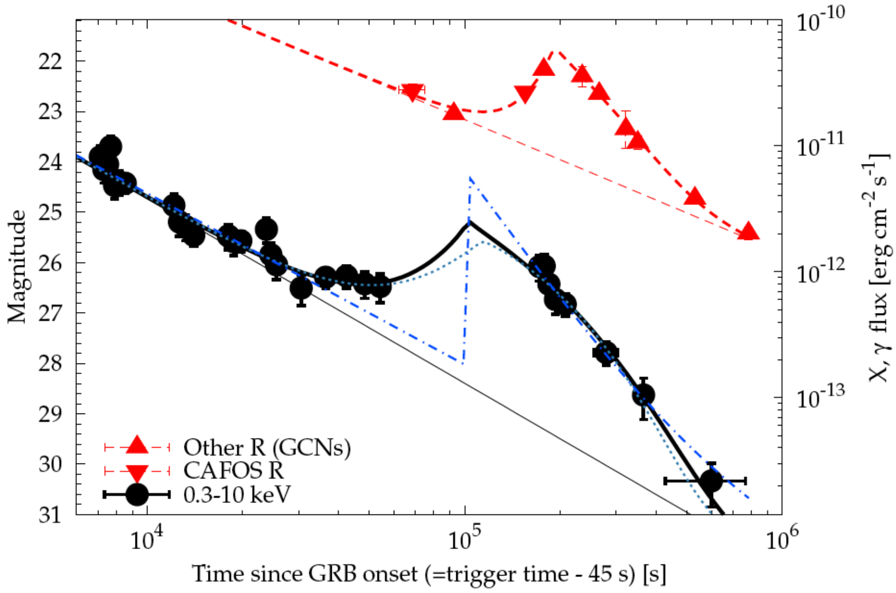

Figure 3.10 Late time rebrightening and corresponding best-fit models (power law and a pulse) seen in R filter (triangles, thick dashed line) and 0.3–10 keV band (circles, thick solid line). Thin lines show the corresponding power-law components alone. X-rays: the dotted line shows the rescaled version of the γ-ray prompt pulse combined with the underlying power law, while the dashed-dotted line represents the combination of two power laws (see text).

because of the badness of the fit and it turned out to be $\alpha_{\mathrm{x}} = 1.47 \pm 0.20$, more consistent with the broken-power-law fit described above. The X-ray coverage of the late rebrightening is not as detailed in catching the peak time as for the R filter, nonetheless from Fig. 3.10 it can be confidently affirmed that X-rays peak earlier than optical, which is rising or flattening during the beginning of the monitored X-ray decay. Best-fit parameters are reported at the bottom of Table 3.6.

Compared to the R band, the poorer coverage of the X-ray peak reflects in bigger uncertainties on the best-fit parameters of the X-ray profile. Interestingly, rise and decay times are similar and the ratios $\sigma_{\mathrm{d}}/\sigma_{\mathrm{r}}$ are 2.3 and 2.6 for the R filter and X-ray, respectively, i.e. the pulses resemble the typical shape of a prompt γ-ray pulse (Norris et al. 1996; for this GRB the prompt gamma-ray $\sigma_{\mathrm{d}}/\sigma_{\mathrm{r}}$ is 1.8). The peak intensities are 6.5 ± 0.9 and 18 ± 9 times the value of the corresponding underlying power-law at peak time for the R filter and X-ray band, respectively. The X-ray-R time lag amounts to $(9.1 \pm 3.3) \times 10^4$ s. More simply, the late R rebrightening peaks twice as late as the X-ray profile. A word of caution is needed regarding the evaluation of this temporal lag: the uncertainty could be larger than our estimate, which is constrained by the choice of the functional form used for fitting. Nevertheless, the evidence for a positive lag is apparent, regardless of the fits.

Notably, the ratios between the temporal parameters best fitting the pulse of the γ-ray prompt profile (Sect. 3.2.2.1), and the corresponding ones fitting the late X-ray rebrightening, are all comparable: $t_{\rm peak,lateX}/t_{\rm peak,\gamma} = 2600 \pm 800$, $\sigma_{\rm r,lateX}/\sigma_{\rm r,\gamma} = 3400 \pm 3000$, $\sigma_{\rm d,lateX}/\sigma_{\rm d,\gamma} = 4400 \pm 800$. We tried therefore also to fit the late X-ray rebrightening with a combination of the same power law obtained above and a scaled version of the γ-ray prompt pulse: $t_{\rm peak,lateX} = f_{\rm s,X}\,(t_{\rm peak,\gamma} - t_0)$, $\sigma_{\rm r,lateX} = f_{\rm s,X}\,\sigma_{\rm r,\gamma}$, $\sigma_{\rm d,lateX} = f_{\rm s,X}\,\sigma_{\rm d,\gamma}$. We left three parameters free to vary: the scaling factor $f_{\rm s,X}$, the time origin t_0 and the normalisation of the pulse. The choice of letting the time origin vary was motivated by the peak time of the γ-ray pulse being very sensitive due to its smallness. The result is shown in Fig. 3.10 (dotted line). The best-fit parameters are the following: $f_{\rm s,X} = 5700 \pm 700$ and $t_0 = -19.0 \pm 2.4$ s ($\chi^2/{\rm dof} = 19.3/27$). The potentially strong implications for the interpretation of this result are discussed in Sect. 3.2.6.

3.2.4 X-ray Spectral analysis

In order to detect possible spectral variations connected with changes in the X-ray light curve, we extracted the 0.3–10 keV spectra in four different time intervals, labelled “A”, “B”, “C” and “D”, corresponding to the initial steep decay, the beginning of the shallow phase, the end of the shallow phase (or the peak of the rebrightening, according to the alternative description of the X-ray light curve), and the final steep decay, respectively (see Fig. 3.7).

Source and background spectra were extracted from the same regions as the ones used for the light curve (Sect. 3.2.1.3), except for intervals “B” and “C”. For these intervals, due to their poor statistics, a 10 pixel radius circular region was used, to limit the background contamination.

The ancillary response files were generated using the task `xrtmkarf`. Spectral channels were grouped so as to have at least 20 counts per bin. For the spectral fitting the intervals “B” and “C” were coupled with at least one other interval. The fit was performed with `xspec` (v. 11.3.2). All the spectra can be successfully modelled with an absorbed power law with the `xspec` models WABS POW. Results of the best-fit parameters are reported in Table 3.7.

The Galactic neutral hydrogen column density along the GRB direction from 21 cm line radio surveys is $N_{\rm HI}^{\rm (Gal)} = 2.3 \times 10^{21}$ cm^{-2} (Kalberla et al. 2005). The X-ray absorption found from spectral fitting is approximately two times higher than that corresponding to

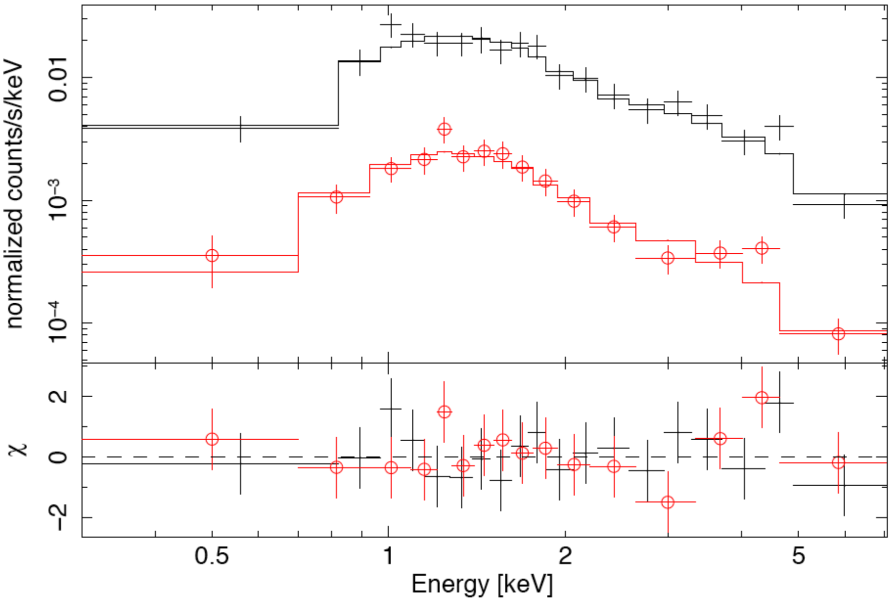

Figure 3.11 *Top Panel*: X-ray afterglow photon spectra of GRB 070311 obtained with XRT in the 0.3–10 keV energy band corresponding to the temporal interval A (crosses) and BCD combined (circles), respectively. Solid lines show the corresponding best-fit absorbed power laws. *Bottom Panel*: residuals with respect to the corresponding best-fit models.

Table 3.7 Best-fit parameters of the 0.3–10 keV spectrum of the X-ray afterglow. The model is an absorbed power law (`xspec` model: WABS POW).

Interval	Start time (s)	Stop time (s)	$N_{\rm H}$ (10^{21} cm^{-2})	$\Gamma_{\rm x}$	Mean flux (10^{-13} erg cm^{-2} s^{-1})	χ^2/dof
A	7004	26079	$4.5^{+1.3}_{-1.0}$	$2.05^{+0.27}_{-0.24}$	24 ± 4	11.0/16
BC	29217	215648	$5.0^{+1.9}_{-1.9}$	$2.5^{+0.6}_{-0.5}$	4.5 ± 1.5	12.4/9
BCD	29217	765966	$5.5^{+2.1}_{-1.7}$	2.5 ± 0.2	1.9 ± 0.1	10.3/13
CD	160010	765966	$4.4^{+2.1}_{-1.3}$	2.4 ± 0.4	1.1 ± 0.4	6.2/7

$N_{\rm HI}^{\rm (Gal)}$. For low Galactic latitudes ($b < 25°$) the $N_{\rm H}$ measured from X-rays is about twice as high as that derived from the radio, interpreted as being due to the presence of molecular gas (Arabadjis & Bregman 1999; Baumgartner & Mushotzky 2006). Therefore, it can be concluded that the $N_{\rm H}$ measured from the X-ray spectrum is consistent with the Galactic value expected in the direction of GRB 070311, although some intrinsic absorption cannot be excluded.

Comparing the best-fit parameters obtained for the different spectra, while the absorption seems constant, there is a 2.2σ suggestion for a softening of the photon index $\Gamma_{\rm x}$, from $2.05^{+0.27}_{-0.24}$ (interval A) to 2.5 ± 0.2 (intervals B, C, D merged together). The corresponding spectra are shown in Fig. 3.11, together with the best-fit models (the excess visible between 4 and 5 keV in the residuals of the spectrum with respect to the absorbed power law appears to be only $\sim 2\,\sigma$ significant). The change of the spectral index, $\Delta\beta_{\rm x} = \Delta\Gamma_{\rm x}$, is consistent with the canonical value of 1/2 expected in the standard synchrotron model when the cooling frequency crosses the observed passband (X-rays, in this instance; see Sect. 1.2.2 and Chapter 4). In this case, this passage would have occurred approximately between intervals A and BCD (Fig. 3.7).

3.2.5 Spectral energy distribution evolution [5]

Two spectral energy distributions were derived at different epochs (see Fig. 3.5). The early one comprises the NIR pulses seen at the beginning of the REM follow-up observations and lasts from 104 to 273 s. This SED consists of detections in two filters, H and R, and a 3-σ upper limit of 6.3 μJy in the 18–200 keV band. Given the substantial variability of the H curve, especially when compared with that of R, the mean H flux was derived by integrating the best-fit profile of the H curve described in Sect. 3.2.2.1 over this time interval. The simultaneous mean R flux was calculated assuming the best-fit rescaling factor ($f_{\rm best} = 0.55 \pm 0.06$) between H and R derived in Sect. 3.2.2 for the same time interval. The fit with a simple power law yields $\beta_{\rm NIR-opt} = 0.65 \pm 0.21$. The extrapolation of the fit to the γ-ray band is consistent with the upper limit (Fig. 3.12).

Interestingly, the spectral index is consistent with that at the end of the γ-ray pulse (Sect. 3.2.1.1), $\beta_\gamma = 0.45 \pm 0.15$, and might be indicative of an unbroken power law segment from NIR to γ at this epoch (see Chapter 1). However, because of the low Galactic latitude, the Galactic reddening along the direction to the GRB is large and makes the uncertainty on the Galactic extinction A_V quite large, $\delta A_V \geq 0.5$ mag. Should the Galactic extinction in V be larger (smaller) by 0.5, the corrected spectral index of the NIR/optical data alone would be $\beta_{\rm NIR-opt} = 0.3 \pm 0.2$ ($\beta_{\rm NIR-opt} = 1.0 \pm 0.2$). Thus, nothing conclusive can be said about the possible presence of extinction in excess of the Galactic one.

The late SED (Fig. 3.13) was extracted at 2.6×10^5 s, corresponding to the beginning of the decay following the late rebrightening in R and the final steep X-ray decay. This SED includes a single R measurement taken by Halpern & Armstrong (2007d) and the

---

[5] Many of the quantities and relations used in this section are introduced and discussed more in detail in Chapters 1 and 4.

XRT spectrum BCD (Sect. 3.2.4; Table 3.7) renormalised through the best-fit power-law segment of the X-ray light curve to the epoch of the R point (see Fig. 3.10). The SED was fit with an SMC-extinguished (Pei 1992; in the observer frame), X-ray photoelectrically absorbed broken power law with $\beta_{\mathrm{x}} - \beta_{\mathrm{opt}} = 0.5$. The N_{H} was fixed to the value already derived from the corresponding X-ray spectrum, i.e. 5.5×10^{21} cm^{-2}, consistent with being entirely Galactic (Sect. 3.2.4). We found $\beta_{\mathrm{opt}} = 1.0 \pm 0.2$. The break frequency turned out to be $\nu_{\mathrm{b}} = (3.0 \pm 0.9) \times 10^{17}$ Hz and $A_V = 0.80 \pm 0.15$ mag ($\chi^2/\mathrm{dof} = 9.6/12$). Figure 3.13 shows the SED: the dashed (dotted) line represents the best-fit model with optical extinction and X-ray absorption taken out (shown).

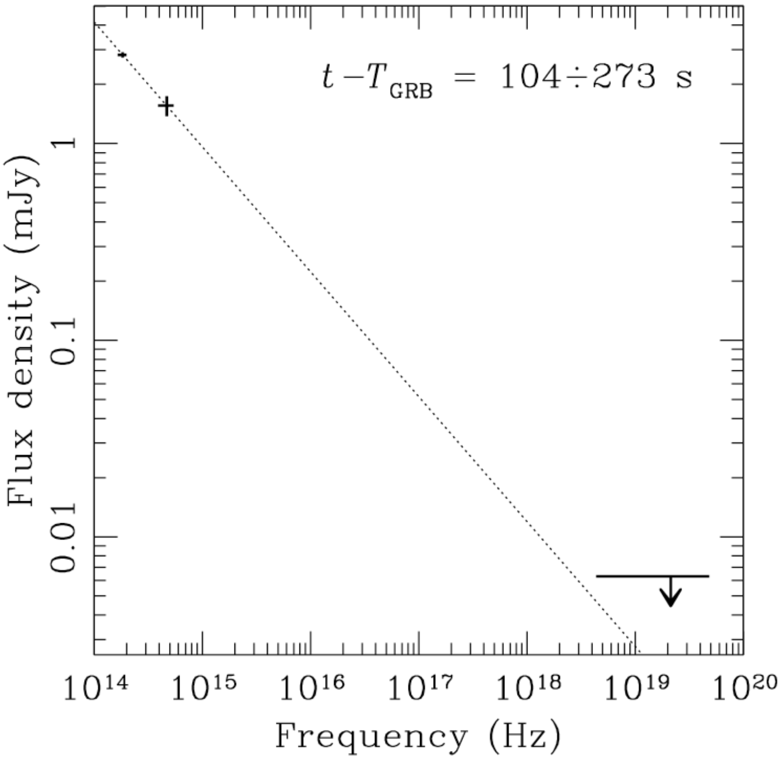

Figure 3.12 NIR-optical/γ-ray SED between 104 and 273 s after the GRB onset time. The dotted line shows the best-fit power law, with $\beta_{\mathrm{NIR-opt}} = 0.65 \pm 0.21$. The upper limit is at 3 σ.

If we interpret the break as the cooling break in the slow cooling regime (see Sect. 1.2.2 and Chapter 4), the electron power-law distribution index is $p = 2\beta_{\mathrm{x}} = 3.0 \pm 0.4$. The fact that β_{x} was around 1.0 at the beginning of the XRT observations (see Table 3.7; $\Gamma_{\mathrm{x}} = \beta_{\mathrm{x}} + 1$) can be explained if the cooling frequency crossed the X-ray band during the observations. When the cooling frequency is above the X-ray band, the temporal decay index α is calculated as $\alpha_{\mathrm{x}}^{\mathrm{ISM}} = 3\beta_{\mathrm{x}}/2$, $\alpha_{\mathrm{x}}^{\mathrm{wind}} = (3\beta_{\mathrm{x}} + 1)/2$, for the case of an ISM or wind profile medium, respectively. Considering $\beta_{\mathrm{x}} = 1.0$ we have, for the beginning of the

X-ray observations, $\alpha_{\rm x}^{\rm ISM} = 1.5$, $\alpha_{\rm x}^{\rm wind} = 2.0$. Since the pre-break temporal slope ranges from 1.0 to 1.4, depending on which model one assumes (Sects. 3.2.2.2, 3.2.3), the wind scenario is ruled out. After the cooling frequency crosses the X-ray band, the relation between the temporal and the spectral index is $\alpha_{\rm x} = (3\beta_{\rm x} - 1)/2$, independently from the medium profile, therefore for $\beta_{\rm x} = 1.5$ (see Table 3.7) we obtain $\alpha_{\rm x} = 1.75$. Considering the errors on the measured values of both $\alpha_{\rm x}$ and $\beta_{\rm x}$ (see Sects. 3.2.2.2, 3.2.3 and Table 3.7), this value could be still compatible with the pre-break slope. Also the optical decay $\alpha_R = 1.06 \pm 0.08$ is in agreement with that expected in the case of an ISM environment: $\alpha_R^{\rm ISM} = 3\beta_{\rm opt}/2 = 1.5 \pm 0.3$. Differently, the case of a wind environment is ruled out ($\sim 3\,\sigma$): $\alpha_R^{\rm wind} = (3\beta_{\rm opt} + 1)/2 = 2.0 \pm 0.3$.

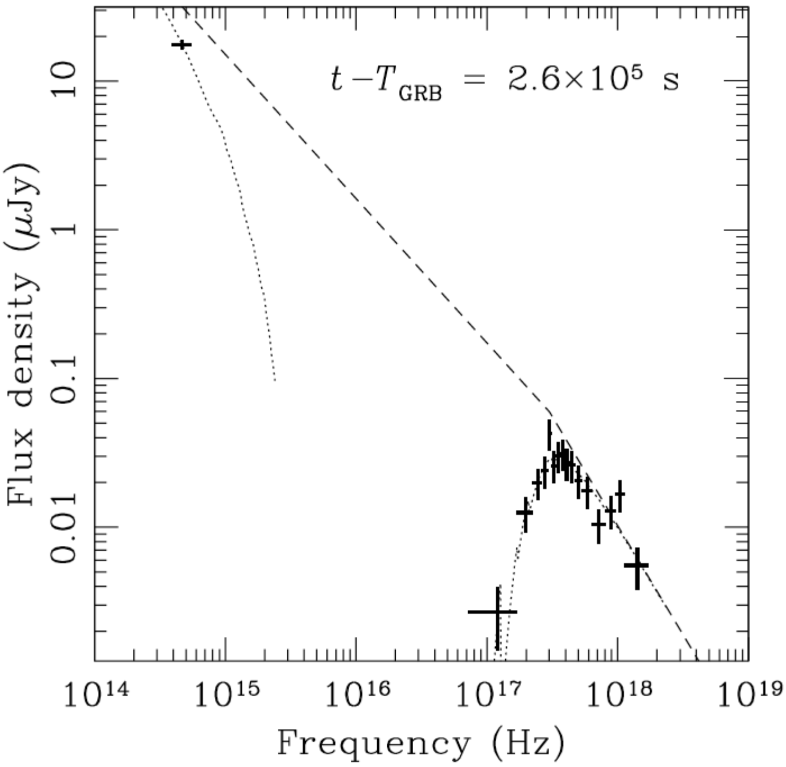

Figure 3.13 Optical/X-ray SED at 2.6×10^5 s, around the peak of the late rebrightening. The dashed (dotted) line shows the best-fit absorbed broken power law, corrected (not corrected) for the optical extinction and X-ray absorption. The $N_{\rm H}$ was fixed to 5.5×10^{21} cm^{-2} found from fitting the X-ray spectrum alone, while A_V is found to be 0.80 ± 0.15 mag, adopting an SMC profile (at $z = 0$).

Alternatively, if during the late rebrightening the bulk Lorentz factor has already decreased to $\Gamma < 1/\theta_{\rm j}$, where $\theta_{\rm j}$ is the jet opening angle, the afterglow should already have experienced an achromatic jet break (see Sect. 1.2.2): in this case, both optical and X-ray decay indices are simply equal to p. Notably, this is compatible with the measured values during the decay of the late rebrightening and this led Panaitescu (2007) to favour the jet interpretation for this burst. However, we believe that the late rebrightening is more likely to be due to an energy increase of the blastwave shock front that strongly affected the measured power-law slope, similarly to what was inferred in the case of GRB 050724 (Malesani et al. 2007; see Sect. 3.2.6 for details).

We tried also to fit the SED with a single absorbed power law. If we leave the slope free to vary, the fit is driven by the more numerous X-ray points, leading to $\beta \sim 1.5$ and $A_V = 6 \pm 3$ mag. However, if we correct the early SED for such an extinction, the intrinsic optical spectrum would be unphysically blue ($\beta_{\rm opt} = -3$). Otherwise, if we impose a single absorbed power law between optical and X-ray and fix $\beta_{\rm opt-x} = 1.0$, A_V becomes comparable with that found in the case of a broken power law. However, although the fit cannot be rejected ($\chi^2/{\rm dof} = 18/13$), the residuals of the X-ray points with respect to the model show a trend. Therefore, a simple absorbed power law does not seem to be a good representation of our data.

Because of the unknown redshift z of GRB 070311, we caution that the values of A_V computed in the fits above are calculated for $z = 0$ assuming a specific extinction law (SMC model), so they must be taken as indicative upper limits to the corresponding rest-frame values. The X-ray absorption in terms of $N_{\rm H}$ inferred from the X-ray data is consistent with the expected Galactic value. Due to the unknown redshift, it is not possible to set an upper limit to the possible intrinsic rest-frame $N_{{\rm H},z}$ absorption. For this reason, and because of the upper limits on A_V, nothing can be inferred on the amount of dust and gas along the line of sight to the GRB progenitor.

3.2.6 Interpretation of the results in the external shock context

The late rebrightening of GRB 070311 has $\Delta t/t \sim 1$ in both X-ray and R filter, so timescales arguments cannot be used against an external shock origin for it, in contrast to what has been observed for other GRBs (e.g. GRB 050502B: Burrows et al. 2005; Falcone et al. 2006c; GRB 050724: Barthelmy et al. 2005; Campana et al. 2006).

In addition, the FRED-like shape of the 18–200 keV prompt light curve and the lack of high variability (the high variability of the prompt emission is often used to argue against an external origin of the prompt emission of complex bursts; see Chapter 1; Sari & Piran 1997; but see also Dermer & Mitman 1999), indicate that the prompt emission of GRB 070311 is potentially consistent with an external shock origin (e.g., see Kumar & Panaitescu 2003).

These motivations and the analogies found between prompt and late afterglow, allow the interpretation of the observations of GRB 070311 in the light of an external shock origin. In this context the γ-ray pulse is thought to be produced during the deceleration of the shell against the surrounding medium: the time origin, moved to 19.0 ± 2.4 s before the GRB onset (see Sect. 3.2.3), would correspond to the explosion time in the detector frame, i.e. when the shell radii are negligible; then the shell would expand from this $t_{\rm expl}$ to $t_\gamma = 0$, when it would start emitting γ rays. The deceleration time $t_{\rm dec}$ would correspond to the peak time of the γ-ray pulse, i.e. 39.0 ± 0.8 s (see Fig. 3.8).

Two alternative explanations for the late rebrightening can be considered: either a *refreshed shock* by a second shell emitted after the first one, or a single shell whose forward shock encounters a *density bump*.

The fact that the spectral slope changes after the peak (Sect. 3.2.4) is consistent with the interpretation that the late rebrightening is due to a thin shell that caught up with the shock front of the blastwave at later times, as expected in the so-called refreshed-shock scenario (Rees & Meszaros 1998). In this picture, the fireball rebrightened and soon afterwards ($\sim 2 \times 10^5$ s) turned off. The decay is the result of two components: the pre-existing power law and the high-latitude radiation (see below) left over by the refreshed shock. This is the case when the energy of the impacting shell is lower than that of the fireball (as also suggested by the ratio between the radiated energy during the late flare and the prompt emission), so that no noticeable step in the power-law decay is observed, but it is still luminous enough to produce a peak on a short timescale.

According to the so-called "curvature" effect (Fenimore et al. 1996; Kumar & Piran 2000; Dermer 2004), the steepness of the fast decay phase of several X-ray afterglows, as well as of the γ-ray tail of single pulses, is due to high-latitude radiation Doppler-boosted in the observer fixed energy band. A relation is expected between temporal and spectral index: $\alpha = \beta + 2$ in its simplest form in the case of a thin shell emitting for a short time, where the time origin must correspond to the time of the GRB explosion as measured in the detector frame. Remarkably, for GRB 070311 both the decay of the γ-ray pulse and the longer decays in X-rays and R-filter of the late rebrightening are consistent with the high-latitude closure relation and *with the same time origin*, i.e. the GRB onset time: $\alpha_\gamma \sim \beta_\gamma + 2 = 2.3 \pm 0.1$ and $\alpha_{\rm x} = \beta_{\rm x} + 2 = 3.5 \pm 0.2$. This is proven by the measured slope of the second power law, $\alpha_{\rm x,2}^{\rm (pp)} = 3.5 \pm 0.5$, which describes the flare decay, in addition to the underlying power law with $\alpha_{\rm x,1}^{\rm (pp)} = 1.4 \pm 0.1$ (Sect. 3.2.3). Therefore, if we adopt the combination of a power law and either a pulse or another power law for the late rebrightening (Sect. 3.2.3), the slope of the bump decay is still consistent with a curvature effect: $\alpha_{\rm x,2}^{\rm (pp)} = \beta_{\rm x} + 2$. In addition, if the reference time is moved backwards to 19.0 ± 2.4 s before the GRB onset, the late brightening is well fit by a time-rescaled version of the prompt γ-ray pulse (Sect. 3.2.3). What is remarkable is that the peak time scales exactly in the same way as the pulse rise and decay times: $\Delta t_{\gamma,{\rm prompt}}/t_{\gamma,{\rm prompt}} = \Delta t_{\rm x,late}/t_{\rm x,late}$.

The 18–200 keV fluence of the prompt emission amounts to $(3.0 \pm 0.5) \times 10^{-6}$ erg cm^{-2} by integrating the best-fit model of Sect. 3.2.2.1, while the net 0.3–10 keV fluence of the late rebrightening is $(2.4 \pm 1.2) \times 10^{-7}$ erg cm^{-2}, i.e. lower by one order of magnitude. If we extrapolate the prompt spectrum to the XRT band as in Sect. 3.2.2.2 and correct for the X-ray absorption, the fluence of the late X-ray rebrightening becomes comparable with that of the prompt extrapolated to the same energy band. On the other hand, the late R hump has a time-integrated flux about one order of magnitude larger than the early pulses seen in the same filter. This difference might be explained with an increasing efficiency in converting the kinetic energy of the blastwave into radiation. This implies a change of the microphysical parameters of the afterglow, as suggested to explain the shallow decay phase of other GRBs (Ioka et al. 2006; Panaitescu et al. 2006). This can also be explained more simply as being due to the fact that the $\nu\, F_\nu$ broadband spectrum peaks at lower energies at later times, so that the energy release in the observed R filter during the late rebrightening is larger than during the prompt or soon after that.

Following Ioka et al. (2005), we can infer which scenarios could be compatible with the observed flux increase with respect to the regular power law decay, $\Delta F/F \approx 10$ (both in R and X; Sect. 3.2.3), and the observed $\Delta\, t/t \approx 1$: from their Fig. 1 (Fig. 3.14 in this section), the late hump of GRB 070311 is compatible with the refreshed shock scenario. Also the patchy shell model (Meszaros et al. 1998), characterised by an anisotropic emitting surface of the fireball, is not ruled out, while the scenario of a density bump causing the late rebrightening is ruled out, unless many clumps of matter are illuminated at the same time. Therefore, the bright flux of the rebrightening, $\Delta F/F \approx 10$, seems to disfavour the interpretation of a density medium enhancement as the cause of the observed flux increase (but see Dermer & Mitman 1999 and Dermer 2007). The interpretation of the late rebrightening as being due to a density bump seems also disfavoured by the crossing of the X-ray band by the cooling break $\nu_{\rm c}$, whereas the observed frequency must be below $\nu_{\rm c}$ for the decay to be affected by the effects of the density medium variation.

In both scenarios (refreshed shock produced by another shell or density bump), the scaling factor of the timescale of the late brightening with respect to the early pulse,

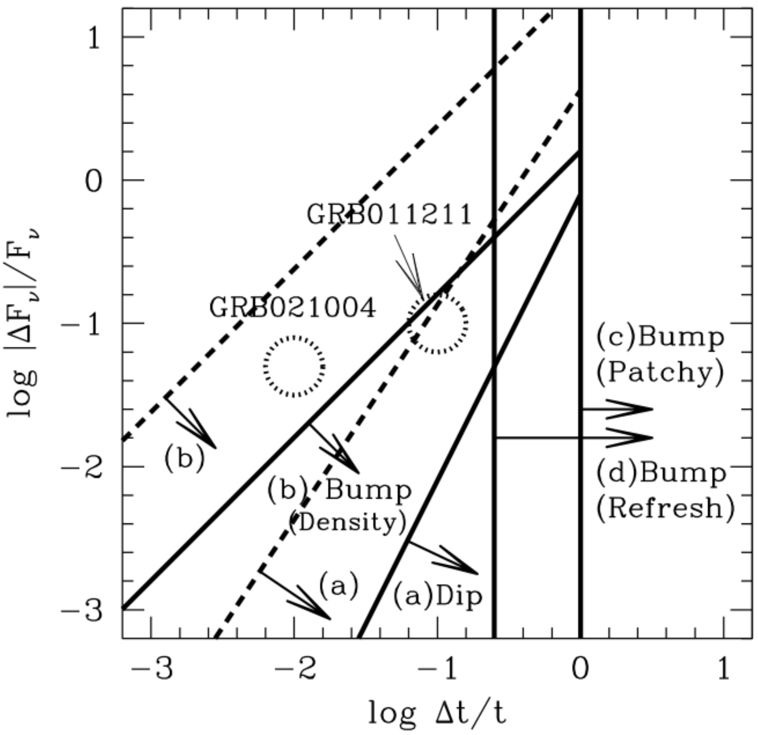

Figure 3.14 The kinematically allowed regions for afterglow variabilities are shown in the plane of the relative variability timescale $\Delta\, t/t$ and relative variability flux $\Delta F/F$ (from Ioka et al. 2005). For GRB 070311, $\Delta\, t/t \sim 1$ and $\Delta\, F/F \sim 10$.

$f_{\rm s} = 5700 \pm 700$, could result from the interplay of two factors: the increase of the visible portion of the emitting surface and the fact that the blastwave Lorentz factor has decreased by a factor of Γ_1/Γ_2 head on, thus stretching the timescale by $(\Gamma_1/\Gamma_2)^2$. Therefore, since $R_1 < R_2$, from $f_{\rm s} = R_2/R_1\,(\Gamma_1/\Gamma_2)^2$, it must be $\Gamma_1/\Gamma_2 < \sqrt{f_{\rm s}} = 75 \pm 5$.

The early NIR/optical pulses detected soon after the γ-ray pulse are consistent with both interpretations: they could be the result of density bumps swept up by the blastwave ($\nu_{\rm NIR/opt} < \nu_{\rm c}$), or of other shells emitted soon after the first one and catching up with the shock front 80 and 140 s after its deceleration.

The interpretation of the final steep X-ray decay following the flare as the post jet-break decay (Panaitescu 2007) seems unlikely: while the late X-ray flare might still be interpreted as a shallow-steep transition (Sect. 3.2.3), the identification as a flare cannot be questioned in the optical. Therefore, the steep decay after the peak simply corresponds to the declining part of the flare and not to a jet break.

Finally, we note that the early (late) NIR/optical pulses do not peak contemporaneously with the corresponding γ-ray (X-ray) pulses, but are delayed by a factor of ~3 (~2) in time. A clear interpretation of this effect is lacking.

3.3 Other REM early time observations

This sections is dedicated to the presentation of other early afterglow light curves detected by REM. Since I was only marginally involved in these works, I will discuss the main results only.

3.3.1 GRB 071010A

GRB 071010A was detected by *Swift* on Oct. 10, 2007 at 03:41:12 UT (Moretti et al. 2007). The BAT light curve shows a broad peak and has a T_{90} duration of 85 ± 5 s (Krimm et al. 2007). There are no XRT rapid observations because they were delayed by 34 ks due to technical problems (Guidorzi et al. 2007a). Early-time REM data, together with those of the TAROT telescope[6] (Bringer et al. 1999), GROND (Greiner et al. 2008a), Gemini-N telescope equipped with NIRI[7] and the Keck-I telescope equipped with LRIS[8] are reported in Tab. 3.8 and Fig. 3.15 and have been presented in Covino et al. (2008). A more complete analysis and discussion is given in this last paper. The redshift of the GRB 071010A is $z = 0.98$ (Prochaska et al. 2007).

Table 3.8 Optical/NIR early-time observations of GRB 071010A. The reference time t_{GRB} is Oct. 10, 2007 at 03:41:12 (Moretti et al. 2007). Data are not corrected for dust absorption. For the TAROT data, the "clear" magnitudes are calibrated against the R filter. Data are sorted according to wavelength and according to time for each filter.

Mean date (UT)	$t - t_{\mathrm{GRB}}$ (day)	Exp time (s)	Airmass	Filter	Instrument	Magnitude
2007 Oct 10.15742	0.00381	10×5	2.3	J	REM+REMIR	14.72 ± 0.18
2007 Oct 10.16498	0.01137	30×5	2.5	J	REM+REMIR	15.08 ± 0.13
2007 Oct 10.16737	0.01376	240	2.5	J	GROND	15.16 ± 0.11
2007 Oct 10.17856	0.02495	60×5	3.0	J	REM+REMIR	15.64 ± 0.13
2007 Oct 10.26426	0.11053	30×9	2.0	J	GEMINI_N+NIRI	16.90 ± 0.05
2007 Oct 11.15218	0.99856	1200	2.2	J	GROND	17.76 ± 0.10
2007 Oct 10.15519	0.00158	10×5	2.3	H	REM+REMIR	14.43 ± 0.15
2007 Oct 10.16038	0.00677	30×5	2.4	H	REM+REMIR	14.02 ± 0.10
2007 Oct 10.16737	0.01376	240	2.5	H	GROND	14.38 ± 0.05
2007 Oct 10.17049	0.01688	60×5	2.8	H	REM+REMIR	14.52 ± 0.10
2007 Oct 10.27297	0.11936	60×12	2.1	H	GEMINI_N+NIRI	16.12 ± 0.05
2007 Oct 10.82059	0.66698	60×30	2.1	H	TNG+NICS	16.62 ± 0.04

continued on next page

---

[6] http://tarot.obs-hp.fr/

[7] http://www.gemini.edu/sciops/instruments/niri/?q=sciops/instruments/niri

[8] https://www.keckobservatory.org/instrumentation.php

continued from previous page

Mean date (UT)	$t - t_{\rm GRB}$ (day)	Exp time (s)	Airmass	Filter	Instrument	Magnitude
2007 Oct 11.15218	0.99856	1200	2.2	H	GROND	16.94 ± 0.05
2007 Oct 10.15632	0.00271	10×5	2.3	K	REM+REMIR	13.42 ± 0.20
2007 Oct 10.16270	0.00909	30×5	2.4	K	REM+REMIR	13.39 ± 0.12
2007 Oct 10.16737	0.01376	240	2.5	K	GROND	13.66 ± 0.07
2007 Oct 10.17455	0.02094	60×5	2.8	K	REM+REMIR	14.04 ± 0.14
2007 Oct 10.28911	0.13550	30×6	2.3	K	GEMINI_N+NIRI	15.31 ± 0.05
2007 Oct 11.15218	0.99856	1200	2.2	K	GROND	16.10 ± 0.05
2007 Oct 10.15523	0.00161	31	2.3	clear	TAROT	17.57 ± 0.15
2007 Oct 10.15564	0.00203	29	2.3	clear	TAROT	17.20 ± 0.10
2007 Oct 10.15793	0.00432	90	2.3	clear	TAROT	16.52 ± 0.10
2007 Oct 10.15904	0.00543	90	2.3	clear	TAROT	16.39 ± 0.10
2007 Oct 10.16023	0.00661	91	2.3	R	TAROT	16.60 ± 0.10
2007 Oct 10.16138	0.00777	90	2.4	clear	TAROT	16.68 ± 0.10
2007 Oct 10.16249	0.00888	89	2.4	clear	TAROT	16.82 ± 0.10
2007 Oct 10.16367	0.01006	89	2.5	R	TAROT	16.97 ± 0.10
2007 Oct 10.16484	0.01123	90	2.5	clear	TAROT	17.00 ± 0.10
2007 Oct 10.16595	0.01234	91	2.5	clear	TAROT	17.10 ± 0.10
2007 Oct 10.16714	0.01353	90	2.5	R	TAROT	17.03 ± 0.10
2007 Oct 10.16829	0.01468	90	2.6	clear	TAROT	17.20 ± 0.10
2007 Oct 10.16940	0.01579	90	2.6	clear	TAROT	17.16 ± 0.10
2007 Oct 10.17059	0.01698	91	2.6	R	TAROT	17.27 ± 0.12
2007 Oct 10.18639	0.03278	365	3.3	clear	TAROT	17.91 ± 0.12
2007 Oct 10.19298	0.03936	365	3.6	clear	TAROT	17.98 ± 0.12
2007 Oct 10.20107	0.04745	100×1	1.7	R	Keck_I+LRIS	18.15 ± 0.06
2007 Oct 10.20351	0.04990	100×1	1.7	R	Keck_I+LRIS	18.25 ± 0.04
2007 Oct 10.28570	0.13209	120×1	2.2	R	Keck_I+LRIS	18.94 ± 0.04
2007 Oct 10.28884	0.13523	30×1	2.3	R	Keck_I+LRIS	18.98 ± 0.04
2007 Oct 10.29230	0.13869	30×1	2.3	R	Keck_I+LRIS	18.97 ± 0.04
2007 Oct 10.29375	0.14014	30×1	2.4	R	Keck_I+LRIS	18.98 ± 0.04
2007 Oct 10.29530	0.14169	30×1	2.4	R	Keck_I+LRIS	19.00 ± 0.04

From the data set, an early-time behaviour similar to that of GRB 060418 and GRB 060607A is evident. The fit performed using a Beuermann function up to 0.4 d results in $t_{max} = 420^{+124}_{-85}$ s, $\alpha_r = -0.88^{+43}_{-62}$ and $\alpha_d = 0.71^{+03}_{-04}$ for the time of the maximum and the rising and decaying power-law indices, respectively.

The maximum during the early afterglow evolution can then be interpreted as the afterglow onset in the thin-shell case as for GRB 060418 and GRB 060607A (see Sect. 3.1.2), since the prompt duration was much shorter than the peak of the afterglow emission. A

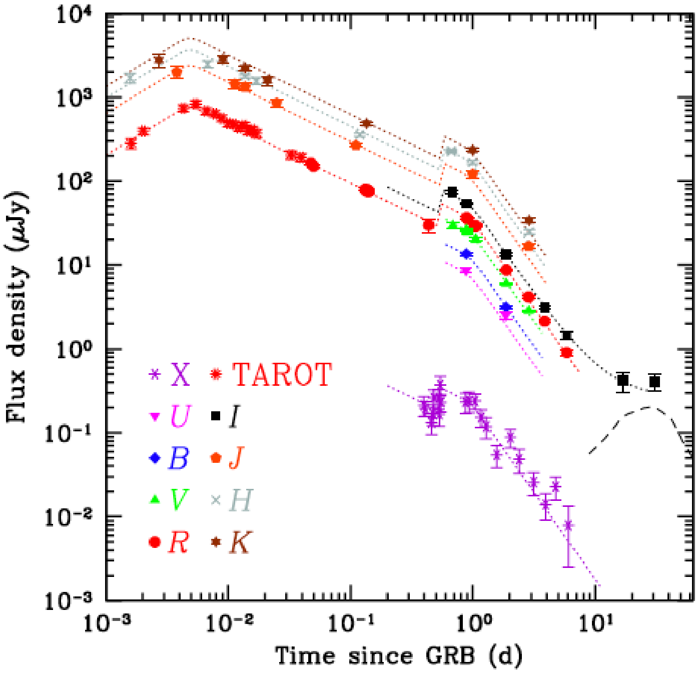

Figure 3.15 Lightcurve of GRB 071010A. The early-time points are from REM, TAROT and GROND robotic telescopes. Late time point ($t > 0.2$ days since GRB) data set description and discussion can be found in Covino et al. (2008).

$\Gamma_0 \sim 150$ is found for GRB 071010A for a uniform ISM and $\Gamma_0 \sim 40$ in the case of a wind-shaped density profile. These are lower than the values inferred for GRB 060418 and GRB 060607A due to the late occurrence of the maximum, but still within the theoretical expectations for the external-shock scenario.

The observed maximum cannot be related the to reverse shock emission in this case either. The reverse shock should be in general a short-lasting phenomenon, and in the thin-shell case it should peak slightly before the deceleration time, just before the afterglow onset, and dominate it in case the typical synchrotron emission is close enough to the optical band. The rapid decay of $f \sim t^{-2.1}$ predicted for the reverse shock emission (Sari & Piran 1999; Kobayashi & Zhang 2007) is inconsistent with the much milder decay observed after the optical flux peak of GRB 071010A.

Table 3.9 Light-curve data obtained by the REM telescope for GRB 060908. The time delay from the burst onset was updated as $T_0 = T_{\mathrm{BAT}} - 12.96\,\mathrm{s}$. Upper limits are at 3σ.

band	T-T$_0$ (s)	bin half size (s)	mag
V	633	10	16.88 ± 0.26
	783	10	17.50 ± 0.42
	1034	30	17.71 ± 0.29
	1385	30	18.04 ± 0.35
R	61	5	14.02 ± 0.04
	80	5	14.43 ± 0.06
	100	5	14.83 ± 0.06
	119	5	15.00 ± 0.08
	138	5	15.38 ± 0.10
	157	5	15.48 ± 0.12
	176	5	15.60 ± 0.12
	195	5	15.73 ± 0.12
	214	5	15.74 ± 0.13
	233	5	15.71 ± 0.14
	248	10	16.14 ± 0.14
	277	10	16.25 ± 0.15
	306	10	16.32 ± 0.16
	336	10	16.35 ± 0.16
	365	10	16.63 ± 0.21
	394	10	16.67 ± 0.20
	423	10	16.63 ± 0.18
	452	10	16.58 ± 0.20
	481	10	16.73 ± 0.21
	510	10	16.93 ± 0.26
	542	10	17.11 ± 0.25
	571	10	16.95 ± 0.23
	601	10	17.34 ± 0.34
	695	10	17.08 ± 0.28
	724	10	17.48 ± 0.36
	753	10	17.36 ± 0.33
	825	30	17.65 ± 0.27
	894	30	17.49 ± 0.24
	964	30	17.64 ± 0.27
	1211	65	18.36 ± 0.36
	1420	136	18.37 ± 0.34
	2864	25	18.29 ± 0.40
	3100	201	18.77 ± 0.40

continued on next page

continued from previous page			
band	T-T_0 (s)	bin half size (s)	mag
	3787	334	19.03 ± 0.43
I	740	85	17.17 ± 0.37
	1105	30	17.52 ± 0.34
	1456	30	17.55 ± 0.32

The detection of the (late) afterglow in the U band eliminates also for this GRB the possibility that the a smooth rising phase is produced by a decreasing extinction in the presence of a radially decreasing circumburst density (see Sect. 3.1.2).

This GRB would be classified by Panaitescu & Vestrand (2008) as a fast rising (see page 44). For this group of afterglows, these authors find a correlation between the 2eV peak flux scaled at $z = 2$ and the peak time. Our data are consistent with the correlation.

The late time data are analyzed and discussed in Covino et al. (2008). Here we just point out that, similarly to GRB 070311 (see Sect. 3.2.6) the rebrightening observed at $\sim$ 0.6 days at both optical and X-ray frequencies can be explained by a FRED pulse superposed on the underlying afterglow. The relatively long duration of the pulse, as compared to the time of occurrence, $\Delta t/t \approx 1$ (as for GRB 070311, see Sect. 3.2.6), is compatible with an origin of the emission at the external shock radius.

3.3.2 GRB 060908

GRB 060908 was detected by the *Swift* satellite on Sept. 8, 2006 at 08:57:22 UT (Evans et al. 2006). The event was observed by all the three on-board instruments BAT, XRT and UVOT. The T_{90} is 19.3 ± 0.3 s (Palmer et al. 2006). The onset of the GRB, T_0, occurred before the trigger time T_{BAT} as pointed out by the BAT team. An onset time $T_0 = T_{BAT} - 12.96$ s is found.

The optical afterglow was detected from ground by the PROMPT telescope[9] showing a bright, rapidly fading source (Nysewander et al. 2006b). The optical afterglow was then confirmed at coordinates RA: 02:07:18.3 and DEC: +00:20:31 (J2000, 0.5 arcsec error) with the REM telescope by Antonelli et al. (2006) about 7 min after the burst. Rol et al. (2006) derived a redshift $z = 2.43$. REMIR could not observe this GRB due to maintenance work. REM-ROSS data are reported in Tab.3.9.

Fig. 3.16 (Covino et al. 2008, in prep.) shows the early-time lightcurve of GRB 060908 as observed by REM as well as *Swif*t-XRT and -UVOT, together with later points taken

---

[9] http://www.physics.unc.edu/ reichart/prompt.html

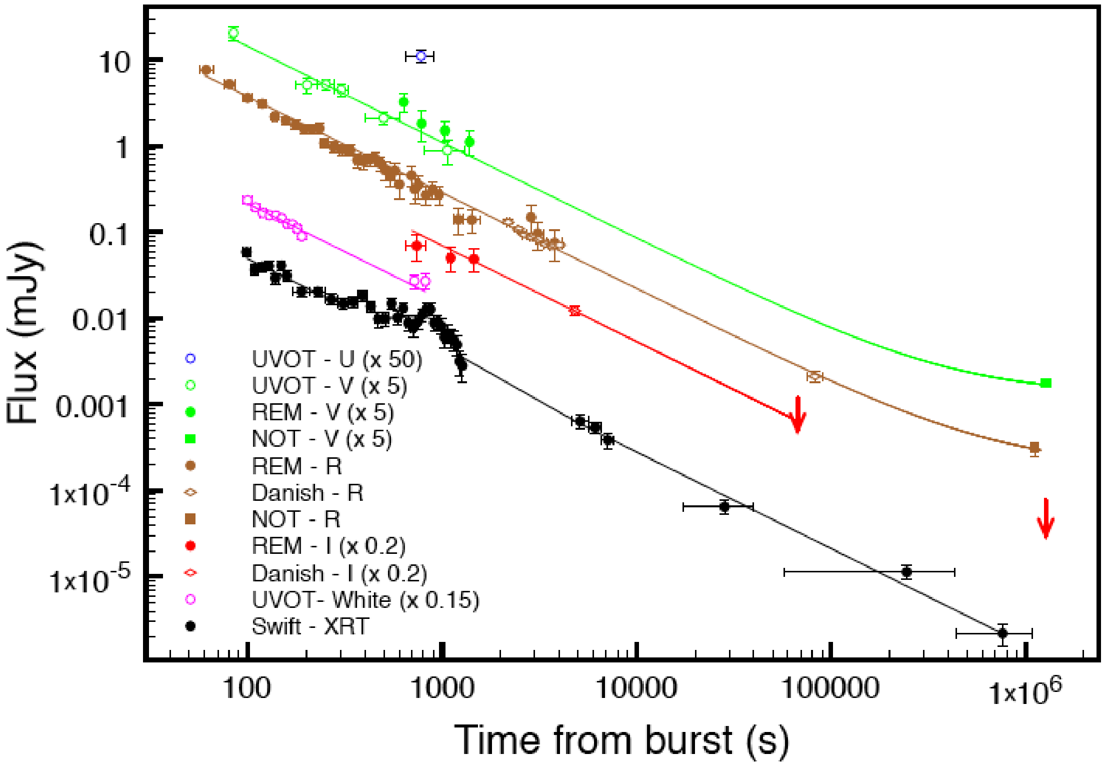

Figure 3.16 X-ray and optical lightcurve of GRB 060908 as observed by the *Swift*-XRT, *Swift*-UVOT, REM, Danish and NOT telescope. The lightcurves were fitted with a simple power-law with index ~ 1.12 for both the X-ray and optical data. The time delay from the onset of the burst was corrected as $T_0 = T_{\rm BAT} - 12.96\,{\rm s}$

by the 2.5m Nordic Optical Telescope[10] (NOT) equipped with the ALFOSC and located at the Canarian island of La Palma, and by the Danish 1.54 m telescope[11] at La Silla, Chile. In this case, even though the data monitor the afterglow from just $\sim 60\,{\rm s}$ from the the starting of the GRB, there is a lack of any initial rising phase. The fit of the lightcurve in the different band results in a simple power-law with index $\alpha \sim 1.12$ for both the X-ray and optical data. The afterglow onset should therefore have happened before the beginning of the observation. Assuming a thin shell case also for this GRB, it is possible to set an lower limit on the initial fireball Lorentz factor of $\Gamma_0 > 700$.

In the Panaitescu & Vestrand (2008) classification, GRB 060809 is a clear example of afterglow decaying since the first observation. The authors suggest that, in a scenario of a structured outflow observed from different location, this class of optical light curve would correspond to an observer location within the aperture of the brighter outflow core, with higher Lorentz factor and therefore with a shorter deceleration time-scale. We

---

[10] http://www.not.iac.es/

[11] http://www.eso.org/sci/facilities/lasilla/telescopes/d1p5/

want to check if the peak flux - peak time anti-correlation found by these authors for the afterglow with a rising phase could be valid also for this class of optical light curve. Our first observation is at $t = 61$s, the corresponding flux emission at 2eV predicted by the Panaitescu & Vestrand (2008) relation if $t_{peak} = 61$s would be $F_{2eV} \sim 500\,$mJy. The 2eV observed flux is much lower, $F_{2eV} \sim 10\,$mJy. If we suppose a regular decay and a $t_{peak} < 61\,$s, things are even worse because the peak flux - peak time correlation is steeper than the observed power-law index $\alpha \sim 1.12$. Assuming the correlation as true, this result could indicate that the afterglows with an optical light curve decaying since the first measurement are not produced in the same way as the afterglows with a rise, unless GRB 060908 is an outlier. It would be interesting to perform the same check on many other GRBs to figure out if the correlation holds.

3.3.3 GRB 080319B: the naked-eye GRB

GRB 080319B triggered the *Swift*-BAT at 06:12:49 UT (Racusin et al. 2008a) on 19 March 2008. The extreme brightness of the burst at high energies, in the X-ray afterglow, and in the optical/UV afterglow led to a huge set of follow-up observations, many automatically triggered on robotic facilities, but also from wide field cameras looking at the GRB field because of having been triggered by GRB 080319A that is only at ∼ 10° distance from GRB080319B. The peak optical flux during the burst was $V = 5.4\,$mag (Karpov et al. 2008). During the first 40 s the prompt optical emission would thus have been detectable with the naked eye. The fluence measured by the Wind-Konus satellite corresponds to an isotropic energy release of $E_\gamma = 1.3 \times 10^{54}\,$erg (Golenetskii et al. 2008), given the burst redshift $z = 0.937$ (Vreeswijk et al. 2008; Cucchiara & Fox 2008).

TORTORA observed the field of GRB 080319B before, during and after the gamma-emission with 0.13 s time resolution, producing therefore an amazing data set, unique for both the early monitoring and resolution of the optical lightcurve. The REMIR and ROSS cameras started the observations 51 s from the trigger and continued to monitor the event up to more than 3000 s (see Fig. 3.17).

The TORTORA data set has been used by Bloom et al. (2008), Kumar & Panaitescu (2008), Wozniak et al. (2008) and Racusin et al. (2008a), in the last case complemented also by REMIR and ROSS data. TORTORA, REM and VLT data obtained by the MISTICI are presented and interpreted in Guidorzi et al. (2008, in preparation).

The comparison of TORTORA and BAT/Konus-Wind data (Fig. 3.18) evidences that the optical and the gamma-ray lightcurves are partially correlated, suggesting that both

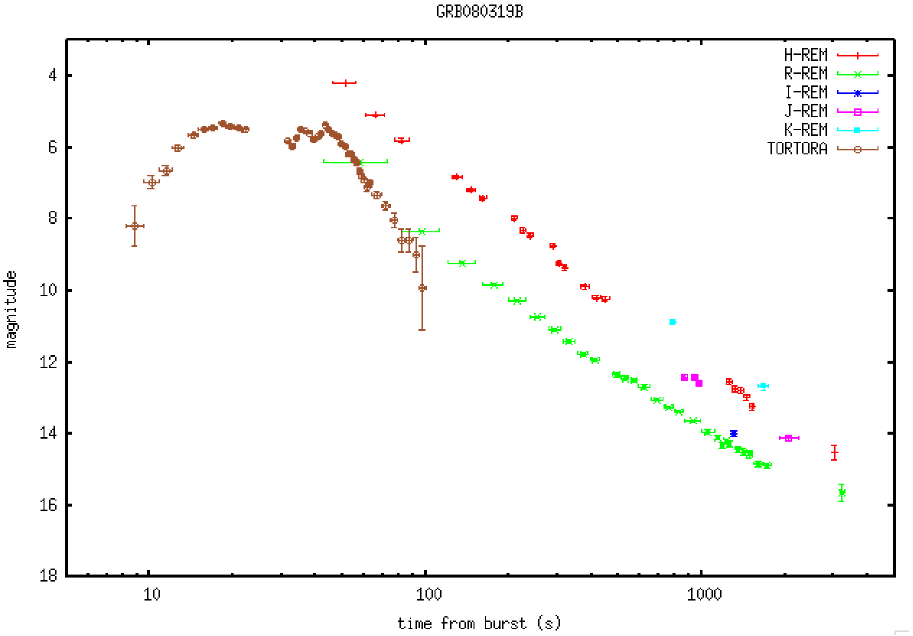

Figure 3.17 REMIR (H,J,K), ROSS (R,I) and TORTORA (V) data for GRB 080319B.

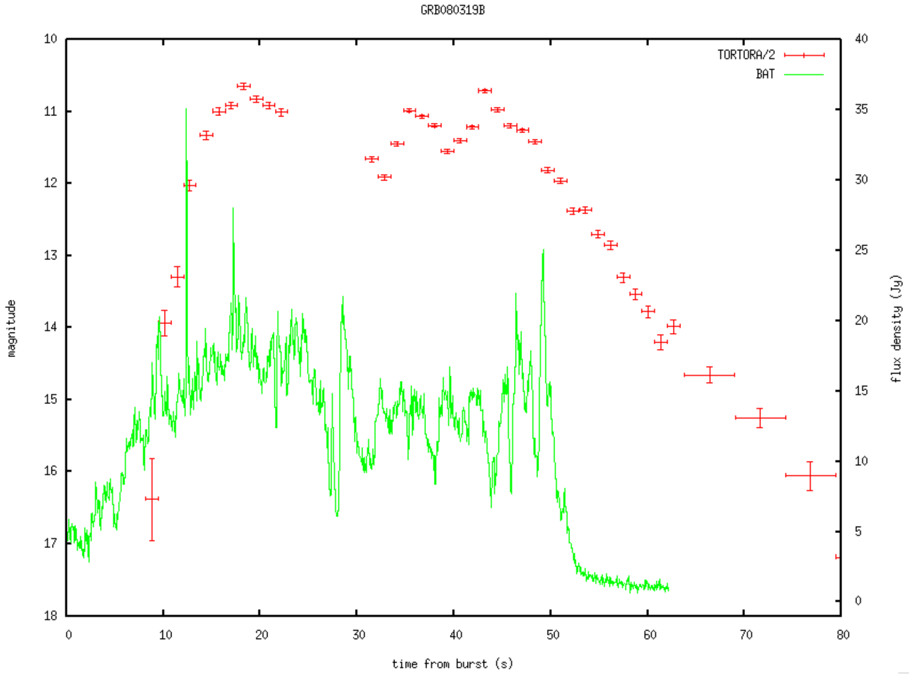

Figure 3.18 Prompt gamma-ray (BAT, green) and optical (TORTORA, red, scaled) lightcurves of GRB 080319B.

emissions originated from the same physical region. The initial step rise, the rapid decline (at $t > 43\,\mathrm{s}$) and the unchanged (instead of growing) widths of the optical pulses indicate that the optical emission did not arise from a reverse shock. Considering that the optical flux density of the prompt emission is $\sim 10^4$ larger than the extrapolation of the gamma-

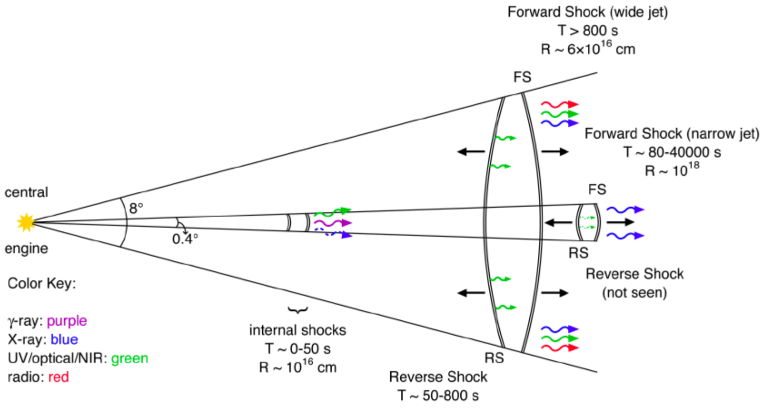

Figure 3.19 Diagram from Racusin et al. (2008a) showing spectral and temporal elements of their two-component jet model. The prompt gamma-ray emission is due to the internal shocks in the narrow jet, and the afterglow is a result of the forward and reverse shocks from both the narrow and wide jets. The dashed arrows correspond to emission that is not observed due to its faintness (optical case) or to the lack of temporal coverage (X-ray case).

ray spectrum into the optical band, the gamma and optical emission cannot be due both only to the synchrotron emission. This suggests that different radiation mechanisms must dominate in each regime. Kumar & Panaitescu (2008) and Racusin et al. (2008a) proposed that the synchrotron emission should dominate at optical wavelengths, while the gamma-rays are produced by synchrotron self-Compton, therefore implying that most of the energy in this burst was emitted at GeV energies.

The optical light curve decay at $50 - 1000\,$s monitored by TORTORA and REM has been explained by Kumar & Panaitescu (2008) as large-angle emission released during the burst and arriving at observer later due to the spherical curvature of the emitting surface. Racusin et al. (2008a) suggest to interpreted the whole data set considering the emission as coming from a two component jet, with a narrow jet highly relativistic ($\Gamma \sim 1000$) and a wide jet, less energetic and with a lower Lorentz factor, as illustrated in Fig. 3.19. In this scenario TORTORA and 50-800 s REM data monitor the light curve produced by the emission of the reverse shock associated with the interaction of the wide jet with the external medium, while the REM data after 800 s are associated with the forward shock of the wide jet.

3.4 Discussion

The REM early light curve data presented in this Chapter show the multifaceted picture of the GRB early afterglow light curves. It is evident that a typical GRB early afterglow light curve does not exist, due to the different mechanisms involved in the early time emission. GRB 060418, GRB 060607A and GRB 071010A optical/NIR observations display the onset of the afterglow as expected in the fireball model. The values obtained for these GRBs (in particular for GRB 060418) for fireball properties such as the Lorentz factor, the external shock radius and the afterglow bolometric fluence, are in agreement with the fireball model predictions. Nonetheless the picture is more varied, as illustrated by the examples of GRB 060908, for which we have no evidence of an early rise preceding the regular decay observed by REM, or GRB 080319B, where the onset of the afterglow seems to be hidden by the strong optical emission coming from the prompt phase. This last GRB and GRB 070311 testify that optical-NIR observations can be useful also to investigate the prompt emission mechanism. For GRB 070311 we showed how it is possible in some cases to explain the prompt emission as well as late rebrightenings as due to external shocks only. The results on GRB 080319B show how complicated can be to find a consistent explanation for both the prompt and the afterglow emission at different frequencies. This is also indicated by GRB 060418 and GRB 060607A (and many other examples in Chapter 4), for which the early afterglow X-ray emission does not follow the external shock predictions of the fireball scenario. On the other hand, the comparison between observations at different frequencies may allow to disentangle the different processes at work.

The GRB studies reported here underline the importance of GRB early afterglow analysis, and therefore of rapid multi-wavelength follow-up instruments, to retrieve fundamental properties on the GRB physics and test the GRB models.

Chapter 4

The early afterglow spectral energy distribution

All evidences are that long-duration GRBs are associated with the death of massive stars that explode as type-Ic supernovae (see Sect. 1.3). Therefore, they likely occur in the same regions where their massive progenitors were born and evolve rapidly (see however Hammer et al. 2006, Sect. 1.3.2). If these regions are similar to the giant molecular clouds in our Galaxy, then long-duration GRBs explode inside dense, dusty environments. The huge energy emitted in the γ-ray band during the prompt emission phase is almost unaffected by absorption. On the other hand, emission at optical or X-ray wavelengths is significantly affected by matter along the line of sight (gas and dust). By studying afterglow spectra, it is possible to infer the properties of the intervening matter, both in the proximity of the explosion and elsewhere along the line of sight. Furthermore, the study of the afterglow spectra and light curves allows the investigation of the explosion physics. In fact both issues must be handled together, since absorption modifies the observed spectrum, thus affecting the comparison with models; conversely, the properties of the intervening matter can be probed effectively only with an estimate of the intrinsic spectrum.

The standard model predicts that the afterglow radiation is produced by synchrotron emission during the slowing down of a relativistic fireball which impacts against the surrounding material (see Sect. 1.2.2). This model has proven successful in explaining the overall properties of afterglows, predicting, as observed, power-law shapes for both the light curves and the spectra (Meszaros & Rees 1997) that can be formalised by $F_\nu \propto \nu^{-\beta} t^{-\alpha} \propto \nu^{-(\Gamma-1)} t^{-\alpha}$ with β the spectral slope, $\Gamma = \beta + 1$ the power law photon index and α the temporal slope (see Sect. 1.2.2). Well-defined relations are set between the decay and spectral power-law indices, the so-called closure relations (see Tab. 4.1),

	$\nu_m < \nu < \nu_c$				$\nu_m < \nu_c < \nu$	
	k	$k = 0$	$k = 2$	Jet	k	Jet
$\beta(p)$	$\frac{p-1}{2}$	$\frac{p-1}{2}$	$\frac{p-1}{2}$	$\frac{p-1}{2}$	$\frac{p}{2}$	$\frac{p}{2}$
$\alpha(\beta,k)$	$\frac{6\beta(4-k)+2k}{4(4-k)}$	$\frac{3\beta}{2}$	$\frac{3\beta+1}{2}$	$2\beta + 1$	$\frac{3\beta-1}{2}$	2β
$p(\beta)$	$2\beta + 1$	$2\beta + 1$	$2\beta + 1$	$2\beta + 1$	2β	2β

Table 4.1 Table reporting the relations between the spectral slope β and the electron index p, and the closure relations between the temporal slope α and β (see Starling et al. 2008). The second column illustrates the case when the observed frequency ν lies between the peak frequency ν_m and the cooling frequency ν_c, while the third column refers to the case when ν is above both ν_m and ν_c. The parameter k varies depending on the medium profile ($k = 0/2$ represents a homogeneous/wind medium, respectively). The columns indicated by "Jet" refer to the post jet break scenario (see Sect. 1.2.2).

which have been tested observationally. These relations follow from the dynamics of the decelerating fireball using the Blandford-McKee solution (Blandford & McKee 1976), assuming an adiabatic expansion, and magnetic field and electrons comprising a constant fraction of the total energy.

The wealth of accumulated data, in particular after the launch of *Swift*, has challenged this scenario and highlighted a complex situation, which has led many authors to introduce several new ingredients, among which are energy injection, radiative losses, non-standard density profiles, angular structure, and varying microphysical parameters (Zhang et al. 2006; Panaitescu et al. 2006; Granot et al. 2006). The introduction of these effects has been more or less capable to explain the new data, but has somewhat reduced the predictive power of models, and the theoretical picture is not yet fully established. On the other hand, most of these solutions are still based on the idea that the observed spectrum is due to synchrotron emission. Independently from the details, the broad-band spectral shape can thus be computed from robust first principles, and from optical through X-ray frequencies it has the shape of a broken power law (see Sect. 1.2.2). The break frequency is interpreted as the cooling break frequency ν_c, that is the frequency of electrons whose radiative cooling time is equal to the dynamical timescale of the blastwave. In this case, a robust prediction is that the low- and high-energy spectral indices β_1 and β_2 differ by exactly 0.5 ($F_\nu \propto \nu^{-\beta}$): $\beta_1 = (p-1)/2$ and $\beta_2 = p/2$, where $p \approx 2$ is the index of the electron energy distribution (e.g. Sari 1998). The position of the break frequency can however vary significantly from burst to burst and it evolves with time for each case.

To gather information on the physics of the afterglows and of the intervening absorbing material, I collaborated with the *Swift*-XRT team at the Osservatorio Astronomico di Brera-Merate on a program to build the optical-to-X-ray spectral energy distribution (SED) of *Swift* GRBs with known redshift (Tagliaferri et al. 2006). Previous SED studies, on pre-*Swift* GRBs, have been presented in Galama & Wijers (2001); Stratta et al. (2004); Starling et al. (2007, 2008) and (only for the optical SED) Kann et al. (2006). With respect to those works, thanks to *Swift* it is possible to extend the study to much earlier epochs with the aim to check if there is evolution in the properties of both the absorbing material and the afterglow emission.

One study of the SED of *Swift* detected GRB afterglows has been published by Schady et al. (2007): their sample is composed by seven GRBs whose afterglow was detected by both XRT and UVOT, and chosen to have a spectroscopic redshift $z < 1.75$. Our overall sample would include all the *Swift* long-duration GRBs with spectroscopic redshift and an adequate X-ray and optical coverage. I present here the preliminary results on 22 of them (see Tabs. 4.3, 4.4 and figures in Appendix A), that is more than twice than the largest sample of published pre-*Swift* or *Swift* afterglow SEDs from X-rays to optical frequencies. The average redshift of the GRBs considered is $\langle z \rangle = 2.32$, slightly larger the the overall *Swift* sample (see Sect. 1.1.3). In Tab. 4.3 are reported for each GRB the times at which the SED have been built, the associated optical and X-ray spectral and power-law indices, and the estimated rest frame hydrogen column density. Tab. 4.4 presents for each GRB the inferred extinction and p values, as well as the position of the ν_c, the medium profile and some comments on the SED results when necessary.

As said above, this are preliminary results: we decided to report them even if the information is still incomplete. Some quantities are indicated without errors (for example the power-law slopes) and the analysis on the fit goodness is missing. For the moment the errors on the optical extinction A_V are considered approximately as the 30% of the A_V value.

4.1 The intervening matter: absorption and dust-to-gas ratio

The ISM intervening material affects the observed GRB spectrum by selectively extinguishing the radiation. At X-ray frequencies, the absorption is due to metals (either in the gas or dust phase), which affect mostly the low-energy range (particularly below

≈ 0.5 keV). At optical and ultraviolet wavelengths, the spectral shape is modified by dust. GRBs are very interesting sources for probing the interstellar medium in the Universe, for a number of reasons. First, they are very bright. Second, the intrinsic spectral shape is simple enough to allow a reliable determination of the absorption amount. They are also observable across a wide range of wavelengths allowing to probe complementary aspects of the ISM. An accurate study of the GRB host dust properties is of great importance to make a proper use of GRBs as cosmological probes, for example to understand the presence of selection effects, to measure the GRB host star formation rate and to characterise galaxy evolution. Absorption within our own Galaxy along a particular line of sight can be estimated and removed, but absorption which is intrinsic to the GRB host galaxy as a function of wavelength is unknown, and is especially difficult to determine given its dependence on metallicity and the possible existence of dusty intervening systems whose extinction curves cannot be disentangled from that of the host galaxy.

Extinction in the optical/UV range due to dust grains is typically modelled using either Milky Way (MW), Large Magellanic Cloud (LMC) or Small Magellanic Cloud (SMC) extinction curves (e.g. Pei 1992) because they can be measured in detail and so are well known. Alternatively, the Calzetti attenuation law (SB) derived empirically from UV observations of starburst and blue compact galaxies (Calzetti et al. 1994) is also used (see Fig. 4.1).

The dust content is parametrized by the optical extinction A_V, defined as the difference between the observed V-band magnitude and the V-band magnitude that would be observed in the absence of dust. The amount of dust present along GRB lines of sight is usually determined by fitting the photometric afterglow spectrum with an absorbed power law. This procedure, however, is strongly sensitive to the adopted extinction law, which is poorly known for the high-redshift ISM surrounding GRB sources. All previous studies on GRBs do not favour the presence of a MW-like dust along GRB lines of sight (Jensen et al. 2001; Stratta et al. 2004; Kann et al. 2006; see also Vergani et al. 2004), while SMC- or SB-like extinction curves are favored, in particular because of the scarce or null signature of the 2175 Å bump (but see also Ellison et al. 2006; Krühler et al. 2008; Elíasdóttir et al. 2008). This makes it even more difficult to estimate the amount of total absorption, since a featureless extinction curve can be hardly disentangled from a power-law shape unless good-quality photometry is available.

Here a complementary approach is presented to determine the dust content along GRB sight lines, by modelling the combined optical and X-ray spectral energy distribution,

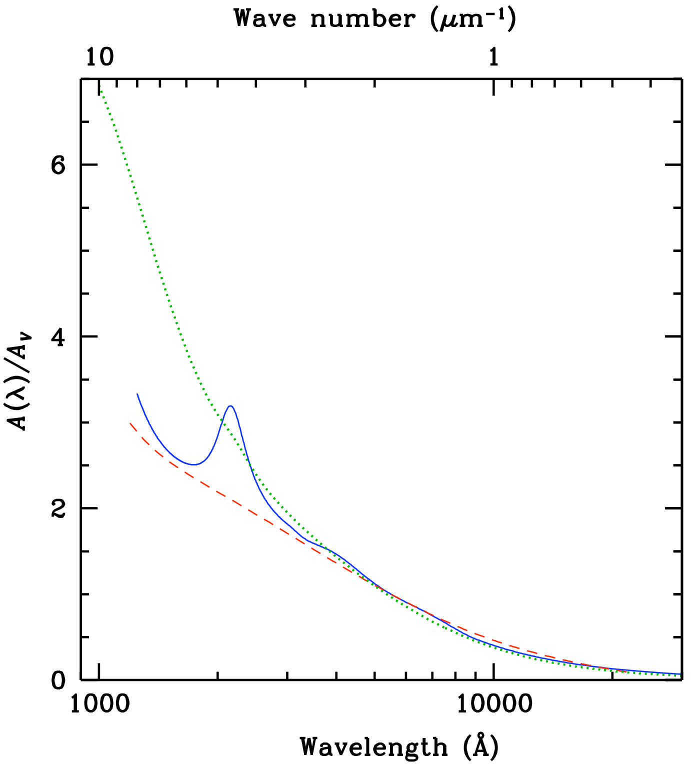

Figure 4.1 Plot representing the Milky Way (blue curve), Small Magellanic Cloud (green dotted curve) extinction curves and the Calzetti attenuation law (red dashed line), which are the ones we have employed in this study.

under the basic assumption that it is described by a synchrotron spectrum. This kind of analysis is potentially suffering from a selection bias, namely the requirement that the burst is detected at optical wavelengths. Dusty afterglows more frequently escape detection and, even if detected, they may lack detailed photometric and spectroscopic studies. *Swift* provides rapid and precise GRB triggers, allowing a much more efficient follow up, therefore effectively reducing this bias.

To build the optical-to-X-ray SED, optical and *Swift*-XRT data were interpolated (or extrapolated) at a common time (from a few minutes to hours after the GRB). Optical data have been taken from the MISTICI group VLT and TNG data and from the literature (including the GCNs, after rejecting clearly discrepant or miscalibrated points). Appropriate epochs with the best available spectral coverage have been chosen. The selection of GRBs with measured (spectroscopic) redshift avoids degeneracy in the modeling of the dust properties.

We concentrated mainly on the X-ray data obtained during the first two *Swift* orbits after a burst, from ~ 100 s up to 2–3 h (although we looked at the full light curve and

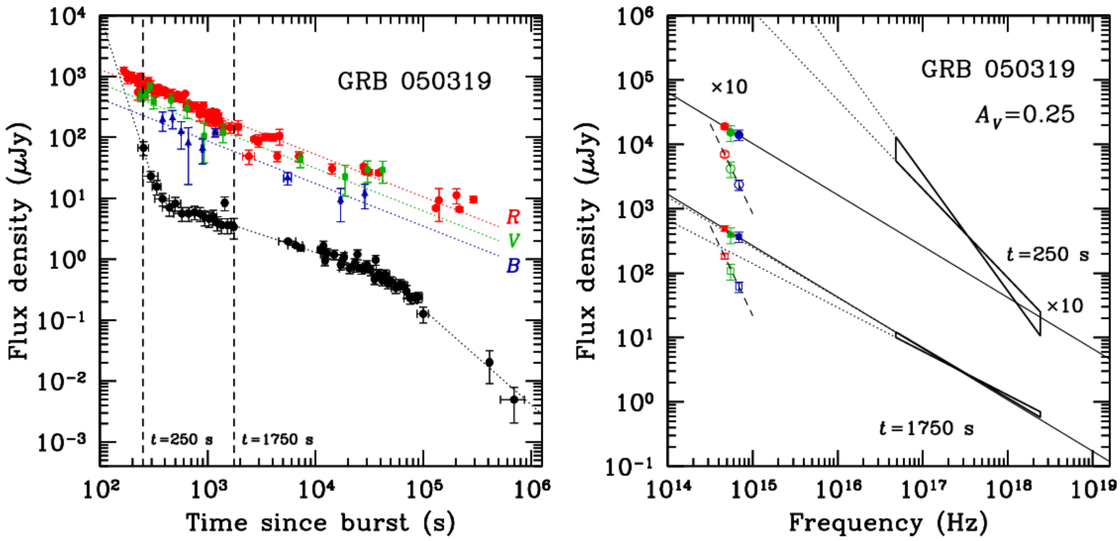

Figure 4.2 Left: optical (Red: R band; Green: V-band; Blue: B-band; all corrected for the MW extinction) and X-ray light curves (black filled dots) of GRB 050319 (for references see Appendix A). The vertical dashed lines mark the epochs at which we computed the SED (observer frame). Right: SED of GRB 050319 at the two epochs marked in the left panel. Empty symbols are not corrected for the host extinction, while filled symbols are. The solid and dotted lines indicate the extrapolation of the optical and X-ray spectra, respectively. The values of the SED at 250 s have been multiplied by 10 for better reading.

in some cases extracted also SEDs at later times). In these early phases, the X-ray light curves are characterised by a complex behaviour (e.g. Tagliaferri et al. (2005b); Nousek et al. (2006); O'Brien et al. (2006), see Fig. 4.2–4.3) that follows the usual steep-flat-steep sequence, often with superimposed flares. When relevant and possible, spectra for each of these phases were accumulated. The X-ray spectral slope $\beta_{\rm X}$ has been computed through fits to the XRT spectra assuming an absorbed power-law model and considering the absorption both in the Milky Way and local to the GRB. This model always provided a good fit to the data. It should be noticed, on the other hand, that Butler & Kocevski (2007a,b) showed that the curved shape of the early X-ray spectra could be reproduced using a Band model instead of an absorbed power law (Band et al. 1993, the same model that is used to fit the prompt gamma-ray emission). Of course this has consequences on the N_H determinations leading to different results (see page 97).

The dust extinction has been computed by requiring either that:

a) the optical and X-ray spectra lie on the same power-law component ($\beta_{\rm opt} = \beta_{\rm X}$) or that *b)* the cooling frequency ν_c lies between the two bands, so that $\beta_{\rm opt} = \beta_{\rm X} - 0.5$.

To choose among the two possibilities, the relative normalizations of the optical and X-ray components have been compared: for example, in case *a)* it is also necessary that the optical flux matches the extrapolation of the X-ray spectrum. If both solutions do not work, this would imply either a more complex spectral shape or a peculiar extinction curve. In our sample, however, all cases but one fit the simplest model (i.e. the synchrotron spectrum). Note that the extinction has not been found fitting the optical data, but was imposed as a correction to match the constraint from the X-ray slope. To model the extinction, both the SMC extinction curve and the SB law have been adopted. This method has the advantage of being less sensitive to small errors in the photometric data, since the overall extinction is constrained by the knowledge of the intrinsic slope.

As an example, Figs 4.2 and 4.3 show the light curves and SEDs of GRB 050319 and XRF 050416A[1]. In the X-ray band, GRB 050319 shows the canonical steep-flat-steep behaviour (Fig. 4.2, left panel; Cusumano et al. 2006). At optical wavelengths the behaviour is described by a single power law. We focus at first on the late SED (taken during the flat X-ray phase). The presence of dust is evidenced by the steep observed spectral index $\beta_{\rm opt} = 2.8$ (dashed line, right panel). However, if we set $A_V = 0.25$ mag the optical spectrum is much less steep and lies on the same power-law that describes the X-ray spectrum. This interpretation, i.e. that the two component are due to the same power law, is confirmed by the consistency of the temporal decay slopes in the two bands (for $t < 30$ ks). Fig. 4.3 shows the light curve and SED of XRF 050416A. Again, focussing on the later SED, the dust effect is evident, but the cooling frequency was in this case lying between the optical and X-ray bands, at $\nu \sim 2 \times 10^{16}$ Hz. In both cases the earlier SEDs show a much harder optical-to-X-ray spectral index: this characteristic, common to many GRBs, will be discussed in Sect. 4.2.

Figure 4.4 shows the distribution of the inferred A_V values with the two adopted extinction curves (see also Tab. 4.4) The average values are $\langle A_V \rangle = 0.26$ and 0.43 mag for the SMC and SB (Calzetti) curves, respectively, with very large dispersions. The SB extinction curve is flatter, so that on the average a larger A_V is needed in order to obtain the same reddening. In a few of the cases for which the presence of dust is needed, we could find no solution adopting the SB curve. The analysis does not support the existence of "grey" dust (called "grey" because its extinction affects all the optical bands in a similar

---

[1] For $t > 10^6$ s, the light curve data of XRF 050416A is contaminated by the host galaxy flux and the possible rising of a SN associated to the GRB (Soderberg et al. 2007).

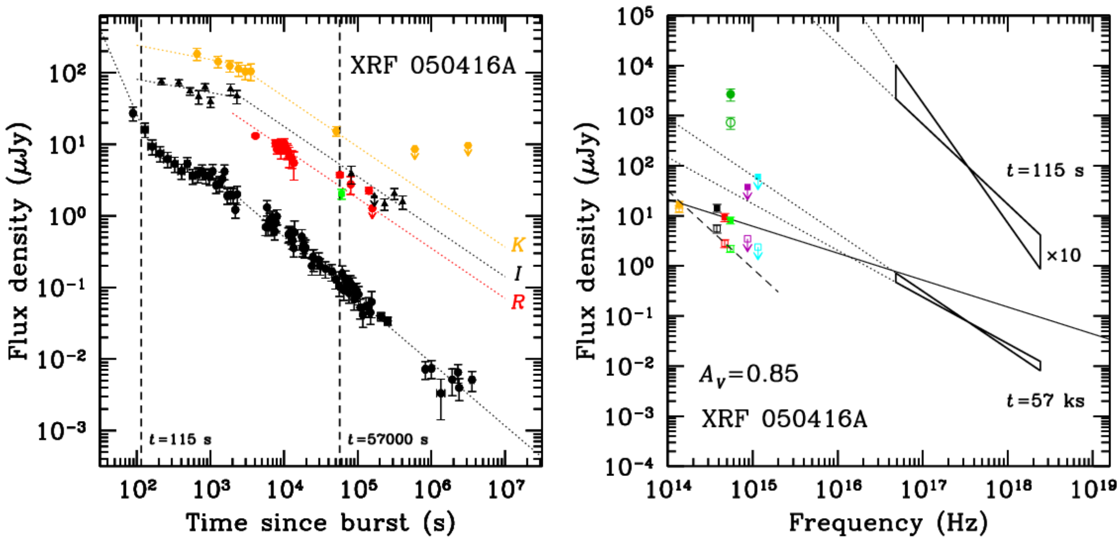

Figure 4.3 Optical (Yellow: K-band; Black: I-band; Red: R band; all corrected for the MW extinction) and X-ray light curves (left panel) and SED (right panel) of XRF 050416A (for references see Appendix A). The style and symbol convention is the same as in Fig. 4.2. The values of the SED at 115 s have been multiplied by 10 for better reading.

way). In particular a flat law $A(\lambda) \sim \text{const}$ (Maiolino et al. 2001) was never required.

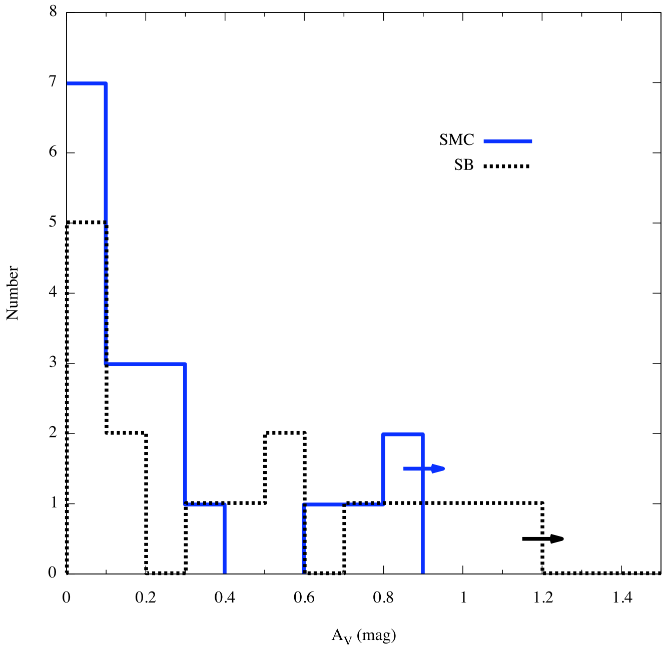

Figure 4.4 Distribution of the rest-frame A_V measured for our sample, assuming an SMC or starburst (SB) extinction curve.

The average A_V is consistent with pre-*Swift* values (Kann et al. 2006), indicating that also with the extended *Swift* sample the space of extinguished afterglows is not yet probed, although sampling much earlier phases than before. However, the bursts in the sample all have a measured redshift, so they could still suffer from some selection effect against faint (and more likely extinguished) afterglows.

The low amounts of optical extinction found towards GRBs are unexpected if GRBs are located in dusty star-forming regions and can be at odds with the high values for the absorption columns measured at X-ray frequencies. This discrepancy has first been noticed by Galama & Wijers (2001) in the analysis of X-ray and optical spectra of eight GRBs. They found evidence for high column densities of gas in the GRB environment that are comparable with those observed in giant molecular clouds. However, they found the optical extinction to be $10 - 100$ times smaller than expected given the gas column densities. Stratta et al. (2004) found that the ratio of gas column densities to visual extinction is much larger than for the MW, the LMC or SMC. The same result has been found by Starling et al. (2007) at least for some of the GRBs in their sample. These results are not yet satisfactorily explained. One possible factor reducing the visual extinction could be dust destruction caused by the high energy radiation field of the GRB, or from neighbouring hot stars, via sublimation of dust grains due to UV emission (Waxman & Draine 2000), sputtering (Draine & Salpeter 1979) or dust grain heating and charging (Fruchter et al. 2001). Another possibility is the presence of dust with different properties than the one monitored in the local universe, in particular dominated by large grains (and thus producing a grey extinction curve as for example the one found by Maiolino et al. 2001 in active nuclei) since the destruction of smaller grains is more efficient (Perna & Lazzati 2002; Perna et al. 2003). However, as noticed above, the presence of dust producing a flat extinction curve is not supported from the SED study presented here. Another explanation could be the expected young age of the stellar population implying that there has been not enough time for dust formation (Watson et al. 2006a; Campana et al. 2007). The discrepancy could also mean that the gas-to-dust ratio in galaxies span a far larger range than the one retrieved from the studies of local galaxies and that GRB lines of sight tend to be more gas rich or dust poor than random lines of sight. This last case has been demonstrated for four core-collapse SN remnants in the LMC observed by *Spitzer*[2] (Williams et al. 2006). More recent studies found no correlation between the extragalactic soft X-ray absorbing column densities and the host galaxy HI column densities, and indicate that the absorption of the X-ray afterglows is due also to regions

---

[2] http://www.spitzer.caltech.edu/spitzer/index.shtml

closer to the GRB site (a few pcs) in addition the ones affecting the UV/optical afterglows (Watson et al. 2007). There are evidences that these regions have been highly enriched in low atomic number metals ejected before the GRB explosion (Campana et al. 2008), explaining therefore the high X-ray absorption measured.

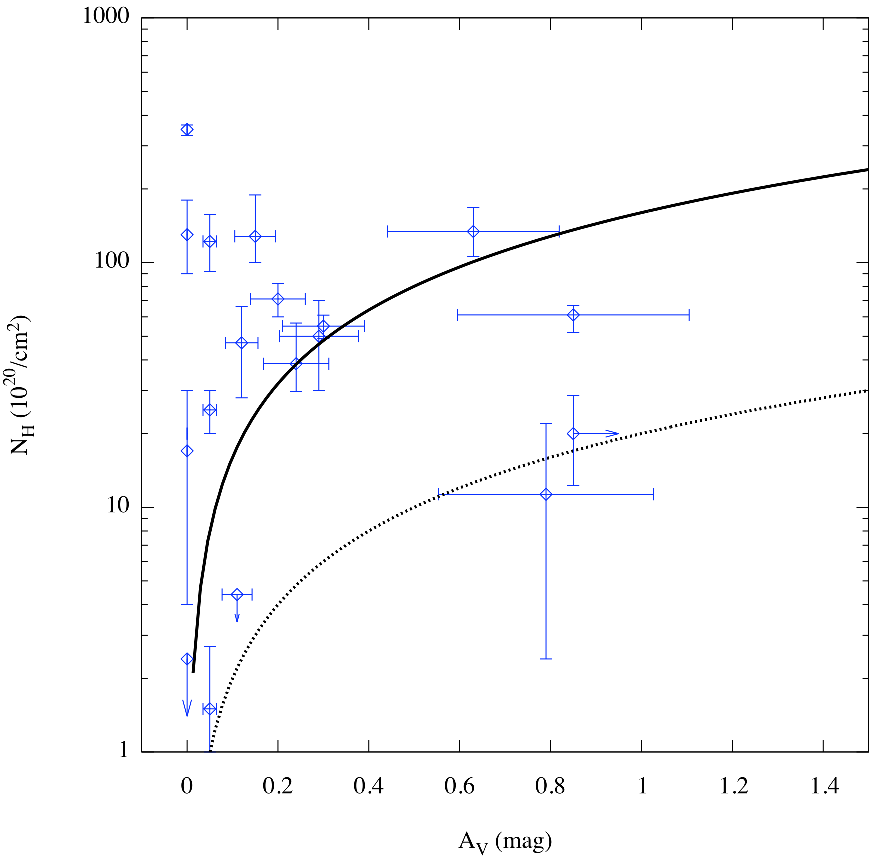

Figure 4.5 Rest-frame A_V and N_{H} (assuming a SMC extinction curve). The solid line shows the SMC gas-to-dust ratio, and the dashed line shows the same ratio when normalized to Solar metallicity.

The results of the study presented here confirm the discrepancy. Fig. 4.5 shows a comparison between the rest-frame A_V (using the SMC extinction curve) and the Hydrogen column densities N_{H} as measured from the X-ray spectra (assuming Solar abundances). The (logarithmic) average is $N_{\mathrm{H}}/A_V = 2.2 \times 10^{22}\,\mathrm{cm}^{-2}\ \mathrm{mag}^{-1}$. The average values for the MW and the SMC are $N_{\mathrm{H}}/A_V = 1.8 \times 10^{21}\,\mathrm{cm}^{-2}\ \mathrm{mag}^{-1}$ (Predehl & Schmitt 1995) and $N_{\mathrm{H}}/A_V = 1.6 \times 10^{22}\,\mathrm{cm}^{-2}\ \mathrm{mag}^{-1}$ (Weingartner & Draine 2000), respectively. The solid line represents the dust-to-gas ratio as measured in the SMC. Taken at face value, the column densities are on the average larger than expected from this relation. The N_{H} values have been computed assuming Solar metallicity, while the SMC has a lower value ($\approx Z_{\odot}/8$). The dashed line shows the relation expected after normalizing the SMC gas-to-dust ratio to Solar metallicity, further exacerbating the discrepancy.

It should be noticed that, contrary to all previous studies, Schady et al. (2007) found a higher dust-to-gas ratio, with a better agreement with values observed in the MW, LMC and SMC. 5 of the 7 GRBs in their sample are included in the work presented here. The dust-to-gas ratio values we found for this subsample are different but almost all consistent within $2\,\sigma$with their results (see Tab. 4.2[3] and Fig: 4.6) and do not show a trend towards lower values with respect to Schady et al. (2007). The differences could be due to the fact that the SEDs of Schady et al. (2007) are built differently from ours, imposing a simultaneous fit from X-ray to optical frequencies. Also the time at which the SEDs are built is different, in particular the SEDs from Schady et al. (2007) are built at 1 or 2 h from the trigger time. Different $N_{\rm H}$ values may be found depending on the time at which the spectra are extracted, in particular because of the presence of flares or of emission not belonging to the afterglow phase.

There is no evidence of a significant time evolution trend of $N_{\rm H}$ when comparing the Schady et al. (2007) values to ours (see Tab. 4.2), while a possible decrease of A_V with time is not excluded. Early time evolution of $N_{\rm H}$ has been claimed by Starling et al. (2005a); Rol et al. (2007); Campana et al. (2007). On the other hand Butler & Kocevski (2007a,b) evidenced that this could be artificial: if the early X-ray spectra exhibit a log-log curvature like that of GRBs, with E_{peak} evolving in time and typically crossing the XRT bandpass during the early X-ray afterglow (as they show), then the evolution in the spectral curvature could be mistaken for variations in $N_{\rm H}$. Indeed it would be interesting to compare SEDs built at different times for one GRB to check for $N_{\rm H}$ or A_V evolution. Unfortunately this is not an easy task: at early time light curves are contaminated by many different processes not yet fully understood, while late time light curves and spectra are very often poorly sampled.

It will also be interesting to compare the gas and dust properties found from the SED to those found from a dedicated analysis of the GRB host galaxy itself. This will be a dedicated project in itself beyond the scope of this chapter.

---

[3] The comparison has been made using the Schady et al. (2007) values corresponding to the spectral model we found for each GRB from our SEDs. It should be noticed that the cooling frequency could have varied from Schady et al. (2007) SED times and ours. In any case, these authors affirm that the $N_{\rm H}$ and A_V values they find do not change significantly depending with the continuum spectral shape adopted (power-law or broken power-law).

Name		$t(s)$	$N_{\rm H}(10^{20}{\rm cm}^{-2})$	A_V
GRB050318	This work	5382	$11.3^{+1.1}_{-0.9}$	0.79 ± 0.24
	Schady et al. (2007)	3600	$15.6^{+4.4}_{-1.2}$	0.53 ± 0.06
GRB050525A	This work	18600	25 ± 5	0.05 ± 0.02
	Schady et al. (2007)	3600	$13.9^{+4.8}_{-5.1}$	0.26 ± 0.04
GRB050824	This work	20000	17 ± 13	0
	Schady et al. (2007)	7200	$11.6^{+4.6}_{-3.7}$	$0.16^{+0.06}_{-0.04}$
GRB051111	This work	22000	71 ± 11	0.2 ± 0.06
	Schady et al. (2007)	7200	$100.4^{+27.0}_{-27.9}$	0.42 ± 0.13
GRB060418	This work	800	25 ± 6	0.3 ± 0.09
	Schady et al. (2007)	7200	$28^{+9.7}_{-8.5}$	0.17 ± 0.02

Table 4.2 Comparison of time t, $N_{\rm H}$ and A_V values of our SED analysis to those of Schady et al. (2007).

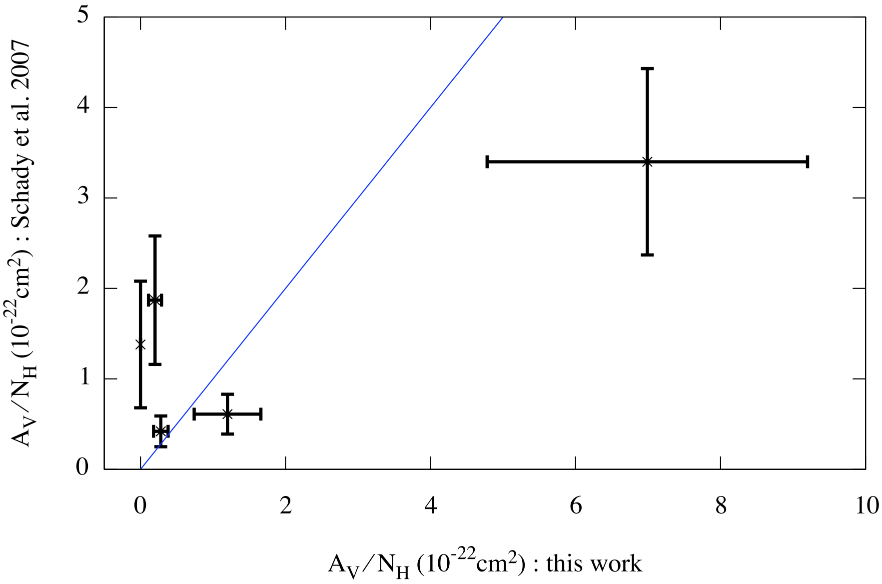

Figure 4.6 Comparison between the dust-to-gas values inferred from our work and those found by Schady et al. (2007). The blue line represents $(A_V/N_H)_{this\,work} = (A_V/N_H)_{Schady\,et\,al.\,2007}$.

4.2 GRB physics

Provided that the synchrotron spectrum assumption is valid, it is possible, using the optical through X-ray spectra and the relations of Tab. 4.1, to measure the underlying parameters of the blast wave, such as: the index of the input power law energy distribution of electrons, p; the index k of the density profile of the circumburst medium, $n(r) \propto r^{-k}$; and in some cases also the cooling break frequency ν_c, as shown above for XRF 050416A (Fig. 4.3).

The first, interesting result is that the synchrotron spectrum fits remarkably well. In the analyzed sample, only one case (GRB 050904) could not be modeled with a single synchrotron spectrum. In particular, there is no need to introduce an inverse Compton component (which is in any case expected to contribute only at later times, see Harrison et al. 2001). Thus, in contrast to the complexity in the temporal domain, a simple spectral model works well for most afterglows. Figure 4.7 shows the distribution of the spectral indices in the optical and X-ray ranges, as well as the inferred electron distribution power law index p. The observed optical slopes span a broad range, but after dust correction they cluster around the typical value $\beta_\mathrm{opt} \approx 0.7$, with a dispersion similar to that in the X-rays.

Some theoretical studies of particle acceleration by ultra-relativistic shocks indicate that there is a nearly universal value of $p = 2.2 - 2.3$ (e.g. Kirk et al. 2000; Achterberg et al. 2001), while other studies conclude that there is a large range of possible values for p of $1.5 - 4$ (e.g. Baring 2004). From broadband modeling of individual bursts and from SED studies (e.g. Starling et al. 2008; Chevalier & Li 2000), quite a large range of values for p has been found, which could indicate that there is a large intrinsic scatter in the value of p. In particular, values of p below 2 have been found (Masetti et al. 2001; Stanek et al. 2001). This requires a cut-off at the high-energy end of the distribution of the electrons, and adaptations of the models have been made for such cases (Bhattacharya 2001; Panaitescu & Kumar 2001) but are still under debate.

We found a spread of values of p clustered around the "canonical" value: $\langle p \rangle = 2.2 \pm 0.2$. 3/22 bursts have $p < 2$. The average value found is higher than the $\langle p \rangle = 1.92$ and $\langle p \rangle = 2.04$ obtained by Panaitescu & Kumar (2002) and Starling et al. (2008), respectively. The large dispersion challenges the hypothesis of an universal value, as also found by Starling et al. (2008).

It has been possible also to check the closure relations between the temporal and spectral decay indices α and β (see Tab. 4.1), and to determine the medium profile. Of the 22 analyzed cases, 4 are fitted by a homogeneous ISM model (and not by a wind), while

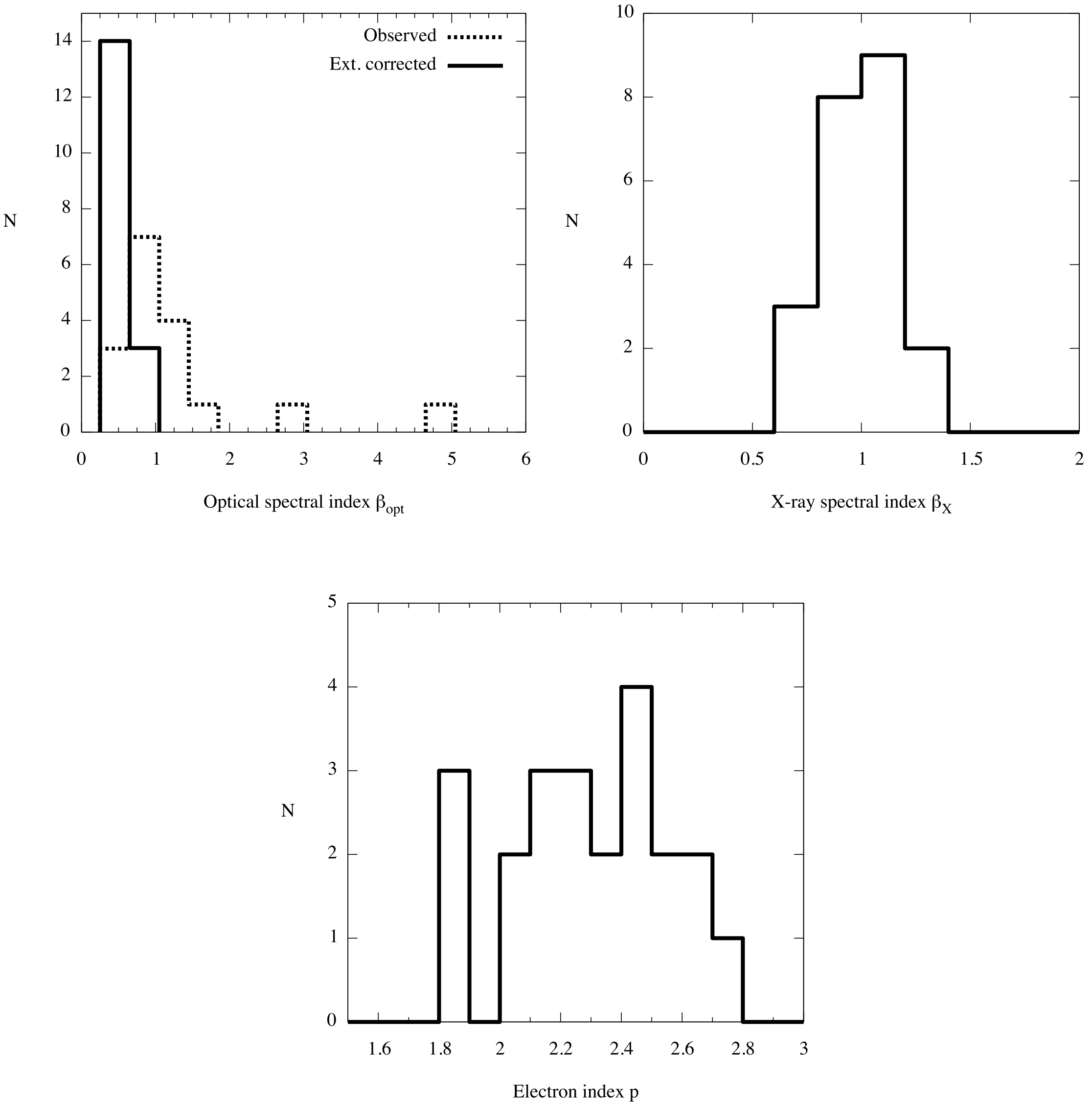

Figure 4.7 Top panels: distributions of the optical (left) and X-ray (right) spectral indices. Bottom panel: distribution of the electron power-law index.

3 are fitted by a wind (and not by a homogeneous ISM); for 14, the available data do not permit to discriminate between the two solutions, while for 1 no case works. The fact that there is evidence of a homogeneous ISM can be at odds with the belief of a Wolf-Rayet star progenitor for long GRBs (see Sect. 1.3), even if recent models of rotating WR stars may solve this issue (see Sect. 1.3.2 and references therein). For a few bursts, the SED shows the cooling frequency to be close to or inside the XRT range ($\nu_c \approx 0.1$–0.5 keV). This suggests the possibility to test afterglow models by measuring the time dependence (if any) of ν_c (see also Butler & Kocevski 2007a,b). For more than half of the GRBs in the sample, the closure relations do not work at any SED time considered. These relations are

a consequence of the fireball deceleration assuming an adiabatic expansion with therefore no radiative losses, no energy injection and assuming that the electric and magnetic field keep a constant fraction of the total energy. It is evident that some of these conditions should be relaxed, especially during the flat phase of the X-ray light curve (see also Zhang et al. 2006.

During the X-ray flares and during the inital steep decay phases, the optical-to-X-ray spectral index $\beta_{\rm OX}$ can be extremely hard (see the early SEDs of GRB 050319 and XRF 050416A in Figs. 4.2 and 4.3). This is a confirmation also from the spectral point of view that the X-ray radiation is not (or not only) afterglow emission during these phases, but is likely of internal origin, as already suggested on the basis of temporal properties (e.g. Zhang et al. 2006; Chincarini et al. 2007). In this case, care must be used when determining the optical "darkness" of a GRB, since the standard $\beta_{\rm OX}$ criterium (Jakobsson et al. 2004) may be violated even for low-redshift, unextinguished afterglows. There are also hints that the X-ray and optical emission do not belong to the same component but have different origins, not only at early times.

This work underlines the necessity of caution in building and interpreting the SEDs and the need of very well sampled multiwavelength spectra and light curves from very early to very late time. While the launch of *Swift* and the development of many robotic facilities assure now an excellent sampling of the early time afterglow, the need for an important amount of observing time at large telescopes (strongly increased because of the number of triggered GRBs) make the late time monitoring less well-sampled. When building and trying to interpret the SEDs many factors play a role and the use of the X-ray-to-optical SEDs as a source of information is less straightforward than expected even for well monitored GRBs, as for example GRB 080319B (Racusin et al. 2008b; Bloom et al. 2008). The possibility that the GRB jet is structured introduces a further source of complication because the different components of the jet dominate at different times and frequencies throughout the SED evolution. It is anyway evident that the SEDs point out that there is still significant work to be done on the models explaining the GRB phenomenon and the SEDs are an essential step to conceive and validate them.

GRB	z	t_1	t_2	t_3	α_{X1}	α_{X2}	α_{X3}	β_{X1}	β_{X2}	β_{X3}	α_{opt1}	α_{opt2}	α_{opt3}	β_{opt1}	β_{opt2}	β_{opt3}	N_{H} (10^{20} cm^{-2}) rest frame
GRB050126	1.29	58900			1.00			1.26 ± 0.22			N/A			N/A			11^{+65}_{-11}
GRB050315	1.95	140	41700		4.5	0.71		1.7 ± 0.4	0.7 ± 0.1		N/A	0.57		N/A	0.63		50 ± 20
GRB050318	1.44	5382			1.17			1.1 ± 0.1			1.17			4.8			$11.3^{+10.7}_{-8.9}$
GRB050319	3.24	253	1743	2×10^5	5.54	0.58	1.56	1.60 ± 0.22	0.69 ± 0.06	0.80 ± 0.08	0.7	0.7	0.7	2.8	2.8	2.8	$38.6^{+18.0}_{-8.9}$
GRB050401	2.9	1100			0.58			0.90 ± 0.05			0.82			1.37			366^{+47}_{-46}
GRB050408	1.24	30000			0.8			1.1 ± 0.1			0.9			1.68			134^{+34}_{-28}
GRB050416A	0.65	800	57000		0.44	0.88		1.04 ± 0.4	1.04 ± 0.11		0.2	0.7		1.56	1.56		$61.1^{+5.6}_{-9.3}$
GRB050505	4.27	25000			1.17			0.90 ± 0.08			N/A			0.9			128^{+61}_{-28}
GRB050525A	0.61	1000	18600		0.95	1.51		1.0 ± 0.1	1.0 ± 0.1		1.1	1.75		0.81	0.81		25 ± 5
GRB050730	3.97	168	517	11000	1.7	N/A	1.6	0.56 ± 0.07	0.60 ± 0.06	0.82 ± 0.05	N/A	0.74	N/A	N/A	N/A	0.95	122^{+35}_{-30}
GRB050803	0.42	18000			1.5			0.8 ± 0.1			N/A			N/A			$20.0^{+8.6}_{-7.7}$
GRB050820A	2.61	125	4780		1.8	1.2		0.98 ± 0.17	1.17 ± 0.12		N/A	0.94		N/A	0.83		
GRB050824	0.83	20000			0.72			0.92 ± 0.18			0.57			0.77			17 ± 13
GRB050904	6.29	480	35000	2.9×10^5	2.03?			0.50 ± 0.07	0.7 ± 0.1	1.5 ± 0.1	N/A	0.92	1.85	0.8	0.8	0.8	255^{+90}_{-88}
GRB050908	3.34	8600			0.92			1.0 ± 0.3			0.82			N/A			
GRB050922C	2.2	490	50000		0.85	1.45		0.99 ± 0.06	1.18 ± 0.13		0.75	1.1		1.37	1.37		47 ± 19
GRB051111	1.55	22000			1.7			1.20 ± 0.17			0.93			1.3			71 ± 11
GRB060124	2.3	35000			1.21			1.08 ± 0.09			0.86			0.44			130^{+50}_{-40}
GRB060210	3.91	5000			0.8			1.14 ± 0.06			1.25			N/A			164 ± 30
GRB060223A	4.41	300			1.3			0.9 ± 0.3			N/A			N/A			350^{+15}_{-19}
GRB060418	1.49	130	800		8.45	1.42		1.27 ± 0.03	1.03 ± 0.04		-2.7	1.28		1.04	1.04		55 ± 6
GRB060614	0.13	60000	150000		1.03	2.13		0.84 ± 0.07	0.84 ± 0.07		1.11	2.48		0.81	0.81		1.4 ± 1.2

Table 4.3 In columns 1 and 2 the 22 GRBs for which the SED has been built are reported, together with their redshift. Columns 3 to 5 refer to the times at which a SED has been built. Columns 6 to 8 and 9 to 11 report the α and β indices of the X-ray emission at each time, respectively, while in columns 12 to 14 and 15 to 17 the same indices are shown for the optical-NIR emission (corrected for the MW extinction, not corrected for extragalactic absorption). In the last column the rest-frame N_{H} (MW subtracted) values inferred from the X-ray spectra are indicated, an empty space means that there is no significant excess of N_{H} at rest frame compared to the MW N_{H} towards the GRB direction.

GRB	$A_{V(SMC)}$	$A_{V(SB)}$	p	dust	ν_c	k	Comments
GRB050126			2.52	unc.	likely below X-rays	unconstrained	closure relations not satisfied
GRB050315	0.29	0.75	2.4	yes	above X-rays	unconstrained	t_1 tail of the prompt, closure relations not satisfied for t_2
GRB050318	0.79	*NO*	2.2	yes	below optical	unconstrained	
GRB050319	0.24	*NO*	2.4	yes	above X-rays	wind	$t_1$not afterglow emission, closure relations not satisfied for t_2
GRB050401			1.8	unc.	close to X-ray	unconstrained	puzzling NIR data, closure relations not satisfied
GRB050408	0.63	1.05	2.2	yes	between optical and X-rays	unconstrained	closure relations not satisfied
GRB050416A	0.85	0.95	2.1	yes	between optical and X-rays	homogeneous	t_1 not afterglow emission, at t_2 closure relations not satisfied
GRB050505	0.15	0.83	1.8	yes	between optical and X-rays	unconstrained	closure relations not satisfied
GRB050525A	0.05	0.18	2	yes	between optical and X-rays	unconstrained	
GRB050730	0.05	0.15	2.6	yes	above X-rays	wind	t1 and t2 not standard afterglow, flare removed for t3
GRB050803	> 0.85	> 1.1	2.6	yes, large	likely above X-rays	likely wind	
GRB050820A	0.11	0.31	2.3	yes	between optical and X-rays	homogeneous	t1 may be the tail of the prompt
GRB050824	0	0	2.54	no	above X-rays	unc	closure relations not satisfied
GRB050904			2.4	unc.	above X-rays?	unconstrained	the X-ray light curve has multiple flares: it is not possible to point out the afterglow
GRB050908	0	0	2	no*	below optical	unconstrained	
GRB050922C	0.12	0.45	2.2	yes	between optical and X-rays	unconstrained	closure relations not satisfied
GRB051111	0.2	0.56	2.4	yes	between optical and X-rays	unconstrained	closure relations not satisfied
GRB060124	0	0	2.16	no	between optical and X-rays	homogeneous	energy injection may be needed
GRB060210	?	?	2.3	likely but unc.	likely between optical and X-rays	no solution works	closure relations are not satisfied, X-ray and optical emission produced by different components?
GRB060223A	0	0	1.8	no*	unconstrained	homogeneous	
GRB060418	0.3	0.5	2.1	yes	between optical and X-rays	unconstrained	X-rays at t_1 are not afterglow emission, closure relations not satisfied for t_2
GRB060614	0.07	< 0.1	1.7	yes	above X-rays	unconstrained	at t_2 achromatic post jet break scenario

*: even dust is not required by our data interpretation, but its presence cannot be excluded due to the poor optical coverage.

Table 4.4 Results on the intervening matter and the GRB physics from the SED analysis. In Columns 2 and 3 the SMC and SB estimated A_V values are reported. Column 4 gives the values of the electron index p. In columns 5, 6 and 7 are shown the results on the dust presence, the position of the cooling frequency ν_c and the density medium profile. Column 8 contains some comments and considerations on the SED results.

Chapter 5

Short GRB afterglows and host galaxies: the case of GRB 050724 and GRB 070707

The knowledge of the short/hard class of GRBs (see Sect. 1.1.1) has substantially improved in the last 3 years with the first detections of X-ray, optical and radio afterglow emission. The recent results have also challenged the standard division of GRBs into two families based on duration and spectral hardness, fostering the search for new classification schemes (see Sect. 1.1.1).

Despite this progress, the study of short GRB afterglows is still at its first steps, and only in a few cases are detailed observations available. Typically, the sampling of the afterglow light curves is poor and broad-band data are lacking, also due to the intrinsic faintness of these events (Berger et al. 2007). In fact, in the few cases where the short GRB redshifts are known, the isotropic equivalent gamma-ray energies inferred range between $10^{49} - 10^{51}$ erg, that is 2-3 orders of magnitude smaller than for long GRBs. In general, the late afterglows of short/hard GRBs have shown an overall similarity with those of long-duration GRBs. On the other hand, while for almost all the long GRBs detected by *Swift* an X-ray afterglow has been detected, only $\sim 1/3$ of the short GRBs with immediate XRT follow-up recorded a counterpart detection. This lack can partly be explained by the fainter gamma-ray flux, but an intrinsic faintness of the afterglow emission itself is needed to justify some of the measured upper limits. For several short GRBs the BAT data show a bright X-ray tail that follows the prompt gamma-ray emission and lasts for ~ 100 s, with an energy comparable to that emitted in the gamma-rays (Barthelmy et al.

2005; Villasenor et al. 2005). The origin of this component it is not yet clear and it does not seem to correspond to the afterglow onset. This kind of prompt light curve shape (a short spike followed by a long, soft pulse) can make the T_{90} (see Fig.1.4) of the GRB longer than 2 s. For example, a burst like GRB 050724 (discussed in the next sections) would be classified as long, if only its temporal properties would be considered, since it has a soft emission in the 15–25 keV energy band lasting > 100 s. On the other hand, as shown in the following sections, the lack of SN association and its early type host galaxy clearly distinguish it from the long GRB population.

The discovery of the afterglows allowed also the first host galaxy associations. So far, a dozen short GRBs were localized with sub-arcsecond precision and host galaxies have been firmly detected with small offset. Only in a few cases (e.g. GRB 061201: Stratta et al. 2007; GRB 080503: Perley et al. 2008a) no host galaxy was found down to $R \geq 26$–28 after the optical afterglow had faded. For other short GRBs, a putative host galaxy was proposed with magnitude $R \sim 23$–26. Spectroscopy of the brightest four of these galaxies indicates that they lie at $0.4 \leq z \leq 1.1$. A comparison with typical field galaxy magnitudes suggests that the rest of the sample lies at $z \geq 1$ (Berger et al. 2007). Up to now all the short GRB redshifts are those of the putative host galaxies: there is no redshift measured through the afterglow spectra absorption lines. The afterglow spectra collected are all almost featureless: it is not clear if this is only due to the poor signal-to-noise ratio or if it is directly connected to the nature of the afterglow and its environment. The unambiguously localized hosts are both early- and late-type galaxies, with very different star formation rates and masses (Nakar 2007). This in contrast with long GRB host galaxies that typically are dwarf field starburst galaxies. Gorosabel et al. (2006) considered the stellar ages of the hosts of short and long GRB and rejected at 99.75% the hypothesis that the two distributions are drawn from the same population.

The tight upper limits on any associated SN (Hjorth et al. 2005b; Covino et al. 2006c; Kann et al. 2008) as well as the association with a broad variety of host Hubble types, from elliptical to moderately star forming galaxies, rule out the core-collapse mechanism as the main channel for short-GRBs production and strongly suggest that the explosion mechanism and/or progenitors of short GRBs are different from those of long GRBs.

The leading model for short GRBs involves the merging of a system composed of two collapsed objects, a double neutron star or a black hole/neutron star binary (Eichler et al. 1989). In those systems that evolve out of massive stars that were born in a binary system, the delay between formation and merging is dominated by the gravitational wave spiral-in time, ranging from tens of Myr to a few Gyr (Perna & Belczynski 2002), strongly dependent on the initial system separation. Short GRBs that develop in this way are expected to: (a) have a redshift distribution which broadly follows that of star formation and (b) drift away in some cases from the star-forming regions in which they were born, and merge outside, or in the outskirts, of galaxies (Belczynski et al. 2002).

A binary system of compact object can also be formed dynamically, through binary exchange interactions in the core of globular clusters (Grindlay et al. 2006). For such a formation mechanism, the delay between star-formation and merging is driven by the cluster core collapse time, which is comparable to the Hubble time (Hopman et al. 2006). Therefore, short GRBs originating from dynamically formed double collapsed object binaries should form at lower redshifts than short GRBs from the classes described above (Guetta & Piran 2005, 2006; Salvaterra et al. 2008).

All these merging models are natural candidates to be short GRB progenitors, also because the outcome of the coalescence is the same central engine as in long GRB models - a disk accreting onto a black hole. This similarity between the engines naturally explains the similarity between the observational properties of the two phenomena. In both scenarios the duration of the burst is determined by the lifetime of the disk. The difference is that in binary mergers the disk is expected to be consumed within a fraction of a second, while in the 'collapsar' model for long GRBs, in-falling matter from the collapsing star feeds the disk for much longer, enabling the production of a long duration GRB. On the other hand, there is also the possibility that a small fraction of the observed short bursts is not directly connected to GRBs but may be giant flares from soft gamma-ray repeaters in the local universe (distances up to $\sim 100\,\mathrm{Mpc}$; Hurley et al. 2005; Tanvir et al. 2005; Frederiks et al. 2007; Mazets et al. 2008).

The redshift determination, the GRB position relative to the host galaxy and the properties of the host galaxy are all crucial pieces of information for understanding short GRBs and discriminating among different models. It should be noticed that the sample of short GRB host galaxies collected up to now could be biased. In particular, if short GRBs originate from a compact binary merger, some of them are expected to take place far away from their origin host galaxy, at distances of at least 100 kpc up to thousands of kpcs. The circumburst gas density depends of course on the offset. If the merger site is outside of a field host, in the inter-galactic medium (IGM), the density is expected to be $\sim 10^{-6}\,\mathrm{cm}^{-3}$. If, on the other hand, the merger takes place within its host galaxy or in the intra-cluster medium of a galaxy cluster the density is expected to be $> 10^{-3}\,\mathrm{cm}^{-3}$.

Since the brightness of the afterglow depends on the external density, afterglows of bursts with large offsets should be fainter and even if they are detected, a safe association with a host can be difficult. Following the model by Belczynski et al. (2006), the lowest densities are expected for binaries born in small early type galaxies, because early type galaxies are the places where long-lived binaries (therefore binaries that had longer time to migrate from their birth place) can be found, and small galaxies have a smaller gravitational potential to retain the system. If compact binary mergers lead to short GRBs then the scenario illustrated above predicts a strong selection effect that biases the observed redshift and host-type distributions, favoring bursts with short-lived progenitors, implying higher redshifts and late-type hosts, so as to achieve conditions that are more favorable for the afterglow brightness and a safe galaxy association. A bias is expected also in favour early-type cluster galaxies over early-type field galaxies. Several short GRB afterglows have been detected only in X-rays and thus localized with a precision of a few arcseconds (whereas sub-arcsecond localizations are required to reveal their host unambiguously). Some proposed short GRB associations with bright, nearby galaxies, based on statistics on angular separation, might result from chance alignment.

Mergers of compact binaries are expected to be the first cosmological sources of gravitational waves to be detected by ground based observatories such as LIGO[1] and VIRGO[2]. Simultaneous detection of the gravitational wave signal from a compact merger and a short GRB will provide conclusive evidence that at least some short GRBs originate from compact mergers and would improve our understanding of both merger physics and short GRBs significantly. Gravitational waves can provide a unique view of the formation, and possibly the operation, of the inner engine powering the burst. A coincident detection could also be important in order to determine the cosmological parameters, as the gravitational wave signal of a binary merger enables an accurate determination of the luminosity distance, while the electromagnetic signal may provide an accurate measurement of the redshift.

In this chapter (based on Vergani 2008, Piranomonte et al. 2008 and Malesani et al. 2007) I present the study of two of the best sampled short GRBs (GRB 050724 and GRB 070707), bringing relevant information to the short GRB picture. I was deeply involved in the data acquisition, analysis and interpretation for GRB 070707 (see also Vergani 2008), while my participation in the work on GRB 050724 was more marginal; that is the reason why for this latter GRB I report only the main results and not a detailed analysis.

---

[1] The Laser Interferometer Gravitational-Wave Observatory; http://www.ligo.caltech.edu/

[2] http://wwwcascina.virgo.infn.it/

Table 5.1 Log of the observations of GRB 050724. All measurements were carried out using the FORS 1 instrument of the ESO VLT. Upper limits are at the 3σ confidence level. The magnitudes are not corrected for Galactic or intrinsic extinction.

Mean time (UT)	Exposure time (s)	$t - t_0$ (day)	Seeing (")	Magnitude	Filter / Grism
2005 Jul 25.01581	3×180	0.49210	1.0	21.18±0.03	I
2005 Jul 25.97533	3×180	1.45162	0.8	23.22±0.12	I
2005 Jul 27.98413	3×180	3.46042	0.8	25.53±0.33	I
2005 Jul 25.00747	3×180	0.48376	1.1	21.85±0.04	R
2005 Jul 25.98390	3×180	1.46019	1.0	23.66±0.09	R
2005 Jul 26.96903	1×60	2.44532	0.8	> 24.4	R
2005 Jul 27.97569	3×180	3.45198	0.8	> 24.8	R
2005 Aug 25.98876	8×120	32.46505	0.7	> 25.7	R
2005 Jul 24.99906	4×120	0.47535	0.9	22.49±0.03	V
2005 Jul 27.99267	3×180	3.46896	0.8	> 25.45	V
2005 Jul 26.99009	3×600	2.46638	1.1	—	300V

5.1 Observations and data analysis

GRB 050724 and its X-ray afterglow were detected by *Swift* (Covino et al. 2005). *Swift*-UVOT did not find any optical afterglow down to a 3σ limiting magnitude of $V = 18.84$ (Chester et al. 2005). Optical, NIR and radio counterparts have subsequently been found by Bloom et al. (2005); Castro-Tirado et al. (2005b); Gal-Yam et al. (2005); Cobb & Bailyn (2005); Cameron & Frail (2005). The afterglow is on a galaxy, 0.6" off its centre.

GRB 070707 was detected by the *INTEGRAL* satellite (Gotz et al. 2007; McGlynn et al. 2008). Konus-Wind also detected this burst (Golenetskii et al. 2007a), allowing the measurement of the broad-band fluence ($\sim 1.4 \times 10^{-6}$ erg cm^{-2} in the 20 keV–2 MeV band) and peak energy (~ 400 keV). There is no evidence of a soft tail. The *Swift* satellite began to observe this burst about 9 hr after the *INTEGRAL* trigger and found the X-ray counterpart (Beardmore et al. 2007), while *Swift*-UVOT did not detect any optical afterglow down to a 3σ limiting magnitude of $V = 19.7$ (Schady & Parsons 2007). The optical counterpart was found by Piranomonte et al. (2007), using the observation presented below.

The MISTICI collaboration observed GRB 050724 and GRB 070707 with the ESO-VLT using the FORS1, ISAAC and NACO cameras. Image reduction was carried out following

Mean time (UT)	Exp. time (s)	$t - t_0$ (days)	Seeing (")	Instrument (VLT)	Magnitude	Filter / Grism
2007 Jul 08.12988	10×120	0.45742	0.9	FORS1	23.05 ± 0.02	R
2007 Jul 09.07984	10×120	1.40738	1.0	FORS1	23.86 ± 0.05	R
2007 Jul 09.23005	1×180	1.55759	1.0	FORS1	24.07 ± 0.12	R
2007 Jul 10.14491	10×120	2.47245	0.7	FORS1	25.33 ± 0.08	R
2007 Jul 10.21523	$20 \times 3 \times 30$	2.54277	0.7	ISAAC	> 23.6	J
2007 Jul 11.13697	20×180	3.46721	0.5	FORS1	26.62 ± 0.18	R
2007 Jul 12.17370	17×300	4.50124	0.8	FORS1	26.81 ± 0.22	R
2007 Jul 15.21785	18×300	7.54539	0.6	FORS1	27.39 ± 0.22	R
2007 Jul 19.12752	20×300	11.45506	0.6	FORS1	27.21 ± 0.20	R
2007 Aug 15.07151	20×300	38.38355	0.6	FORS1	27.15 ± 0.29	R
2007 Sep 28.03125	$20 \times 3 \times 60$	81.95974	0.5	NACO	> 22.7	K
2007 Jul 09.32508	5×2400	1.65262	1.0	FORS1	—	300V+GG375
2007 Jul 13.15960	2×900	5.48714	0.8	FORS1	—	300V+GG375

Table 5.2 VLT observation log for GRB 070707. Magnitudes are not corrected for Galactic absorption. Upper limits are given at 3σ confidence level.

standard procedures as explained in Sect 2.1.2. In order to minimize systematic effects, we performed differential photometry with respect to a selection of local isolated and non-saturated standard stars. All the VLT/FORS spectra were acquired with the 300V grism, covering the 4000–9000 Å wavelength range (7 Å FWHM resolution). We always used a 1" slit. The extraction of the spectra was performed with the IRAF[3] software package. Wavelength and flux calibration of the spectra were obtained by using a helium-argon lamp and by observing spectrophotometric stars. The log of observations and magnitudes measured is presented in Table 5.1 for GRB 050724 and Table 5.2 for GRB 070707.

5.2 Information on short GRB properties from the afterglow and the energetics of the prompt emission

5.2.1 The afterglow light curves

Figs. 5.1 and 5.2 show the light curves of the two GRBs, with the MISTICI data represented by filled symbols. Both afterglow light curves can be interpreted as showing signatures of late time activity of the central engine.

The X-ray light curve of the GRB 050724 afterglow evidences a flare at about $t - t_0 \approx 50$ ks. There are reasons to believe that this is present at the same time in the optical light curve. First of all, we performed a SED at 41.8 ks, during the X-ray flare. The SED is consistent with a single power-law from the optical to the X-ray ranges, with the optical and X-ray data therefore belonging to the same component (see Chapter 4). Second, the early time optical upper limits clearly indicate that a continuous power-law decay of the light curve is excluded, and third, Berger et al. (2005) report a possible rise of the light curve ($F \propto t^{1.7}$) in the I band between 43 and 51 ks. An optical rebrightening simultaneous with an X-ray flare was also proposed by Watson et al. (2006b) to explain the steep optical decay of the short GRB 050709.

The optical light curve of GRB 070707 appears to have had an initial slow decay, which got significantly steeper beginning 1–2 days after the GRB. At late times, a constant flux was observed, indicating a dominant contribution from the host galaxy. Different functional forms can be used to fit the light curve, given the sparse coverage at early times. We used first a model comprising a broken power law behaviour, representing

---

[3] IRAF is distributed by the National Optical Astronomy Observatories, which are operated by the Association of the Universities for Research in Astronomy, Inc., under cooperative agreement with the National Science Foundation.

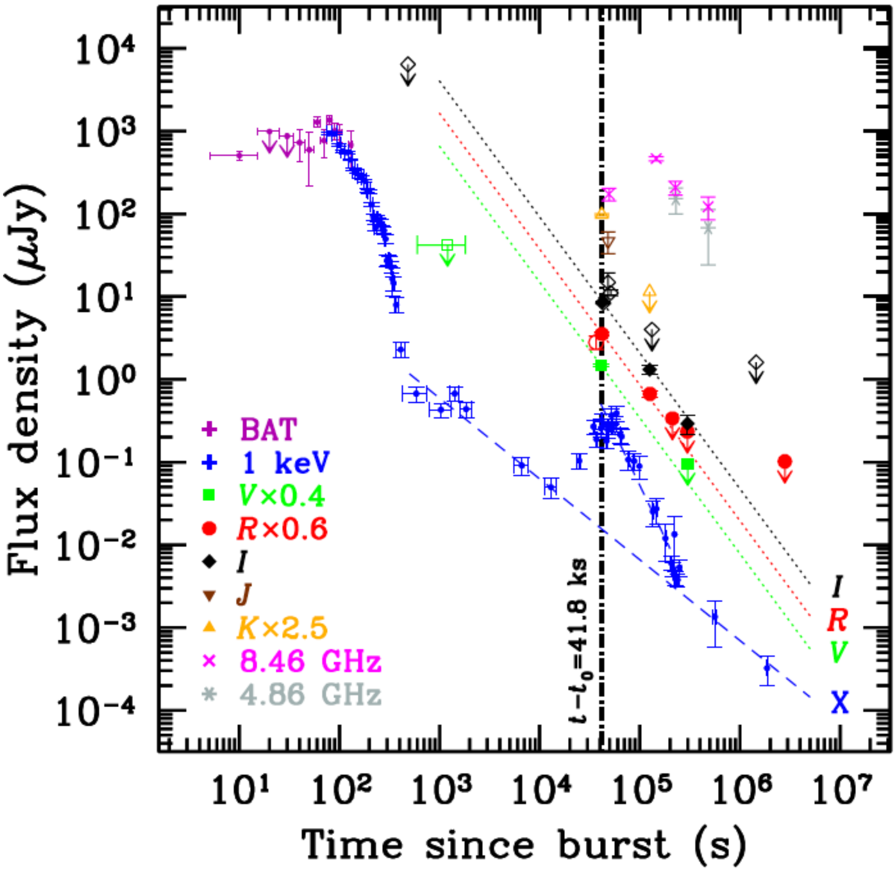

Figure 5.1 X-ray, optical and radio light curves of the afterglow of GRB 050724. Filled and empty symbols represent measurements from our data and from the literature, respectively (Berger et al. 2005; Chester et al. 2005; Torii 2005; Cobb & Bailyn 2005; Wiersema et al. 2005; Pastorello et al. 2005). The V-, R- and K-band data have been displaced vertically for graphical purposes (see legend). No correction for optical extinction has been applied. The X-ray data are taken from Campana et al. (2006); Grupe et al. (2006). Radio data are from Berger et al. (2005). The dotted and dashed lines show the best power-law fits to the optical and X-ray data, respectively. The vertical dot-dashed line marks the time at which we computed the SED.

the afterglow, plus a constant, representing the host. We adopted the usual Beuermann function (see Chapter 3; Beuermann et al. 1999) to model a transition from a shallow to a steeper decay: $F(t) = F_0/[(t/t_\mathrm{b})^{\kappa\alpha_1} + (t/t_\mathrm{b})^{\kappa\alpha_2}]^{1/\kappa}$, where α_1 and α_2 are the early- and late-time decay slopes, t_b is the break time, and κ is the smoothness parameter. Given the relatively low number of data points, we first froze $\kappa = 1$ in our fit. In Table 5.3 we report the best-fit parameters.

When κ was allowed to vary, the break time was only weakly constrained and the slope α_1 could also take negative values (i.e. the light curve could have also been initially rising

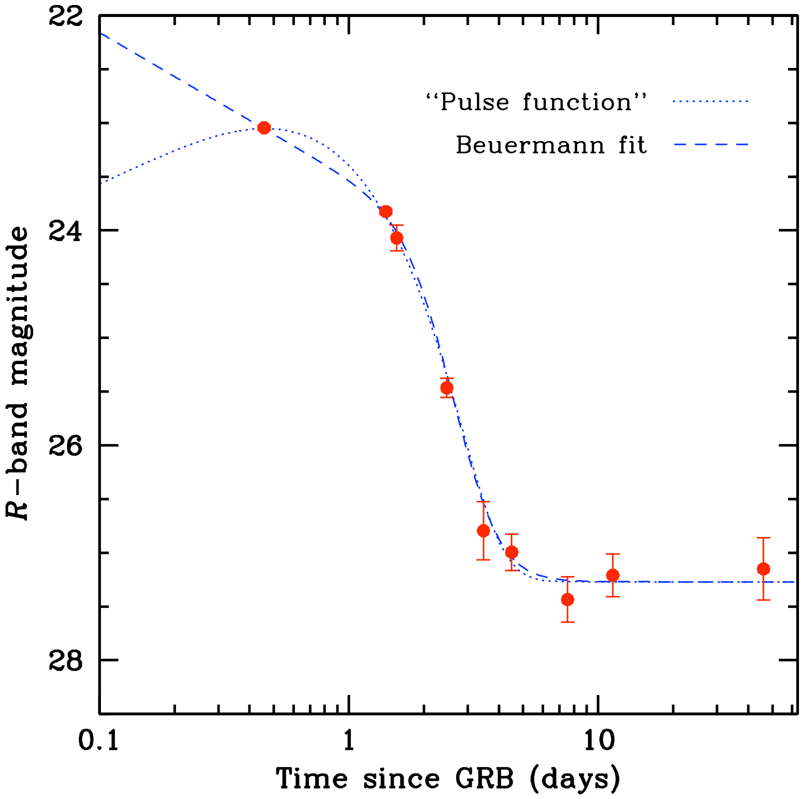

Figure 5.2 R-band light curve of the GRB 070707 afterglow. The dashed line represents the fit obtained using a Beuermann function (with $\kappa = 1$), while the dotted line shows the fit with the "pulse function" (see text).

and peak around 0.5 days). In any case the late time decay remained steep, with a lower limit $\alpha_2 \geq 3$ valid for any κ.

We then fitted the light curve using a "pulse function" model, consisting of a linear rise followed by an exponential decay $F(t) = F_1(t - t_0^*)e^{-(t-t_0^*)/\tau}$ providing a satisfactory fit to the data (also for $t_0^* = t_0 = 0$, i.e. the origin of time coincident with the high-energy event; see Table 5.3), with the peak of the pulse at $t_p \sim 0.58$ d.

The best fit models with the Beuermann function (with $\kappa = 1$) and the "pulse function" are shown in Fig. 5.2.

Unfortunately there is just one X-ray useful point for GRB 070707, nevertheless the hypothesis of a late internal shock is the only viable one for the moment to explain the light curve behaviour: as illustrated below, both a jet break interpretation and more generally a external shock interpretation are ruled out.

The steepening of the optical light curve could be interpreted as a jet break. However the index measured for GRB 070707 is too steep to be explained in terms of jetted emission. In fact this would require $\alpha_2 = p$ (Rhoads 1999), where p is the electron energy distribution

Table 5.3 Results of the GRB 070707 optical-light curve fitting with a Beuermann function (Beuermann et al. 1999), freezing the smoothness parameter $\kappa = 1$, and the "pulse function". Errors are at 1σ with all parameters free to vary.

	$\boldsymbol{\alpha_1}$	$\boldsymbol{\alpha_2}$	$\boldsymbol{t_\mathrm{b}}$ **(days)**	**Host $\boldsymbol{R}$ magnitude**	$\boldsymbol{\chi^2}$**/dof**
Beuermann	$0.44^{+0.08}_{-0.21}$	$5.3^{+0.9}_{-0.8}$	$1.82^{+0.13}_{-0.25}$	27.3 ± 0.13	1.96/4
Pulse function	$\boldsymbol{\tau}$**(days)**	$\boldsymbol{t_0^*}$ **(days)**	**Host $\boldsymbol{R}$ magnitude**	$\boldsymbol{\chi^2}$**/dof**	
	$0.52^{+0.07}_{-0.07}$	$-0.06^{+0.23}_{-0.29}$	27.3 ± 0.24	2.28/5	

index (see Chapt. 4). Such a steep decay could be marginally consistent with the post-break phase only by adopting a very soft electron energy distribution ($p > 3$). Such large p values have never been found in GRB afterglows, both from theoretical and empirical investigations, as illustrated in Sect. 4.2. Moreover, for GRB 070707 values of $p < 3$ are inferred based on the afterglow spectrum, in which case the analysis is more robust than when relying on the temporal behaviour. In addition, the magnitude of the steepening from the pre- to the post-break decay would be too large for a jet-break interpretation in GRB 070707.

The steepness of the observed decay might be difficult to reconcile with forward shock emission even considering only causality reasons. The fastest possible decay is the so-called high-latitude emission, which occurs when the fireball emission stops abruptly and the observers see photons coming from the wings of the emitting surface. In this case, $\alpha = 2 + \beta$, where β is the afterglow spectral index (Kumar & Panaitescu 2000). The observed upper limit in the J band (Tab. 5.2) allows us to derive $R - J < 1.8$ on Jul 10.2 UT, which corresponds to $\beta < 1.5$. This would make the high-latitude interpretation marginally viable. A stronger limit on β can be inferred by using the X-ray data. Assuming a synchrotron spectrum, the optical spectral index can never be softer than the optical-to-X-ray spectral index β_OX. For GRB 070707, the observed X-ray flux (Beardmore & Parsons 2007) implies $\beta_\mathrm{OX} = 0.75$. High-latitude emission from a source with such a spectrum cannot decay faster than $t^{-2.75}$, hence effectively ruling out such a possibility for GRB 070707.

When assuming a long-lived central engine the steep decay is not a problem anymore, because in this case the decay index should be computed after setting t_0 to the end of the extended activity phase (e.g. Zhang et al. 2006), corresponding for GRB 070707 roughly to the peak of the pulse at $t_p \sim 0.58\,\mathrm{d}$. The intrinsic decay slope would therefore be shallower than the observed value, eliminating the causality problem. The optical light curve of GRB 070707 might be produced, for example, by a large flare, as also argued above for GRB 050724 (Barthelmy et al. 2005; Malesani et al. 2007).

Flares explained by late engine activity are common features of long GRBs (Burrows et al. 2005; Zhang et al. 2006; Chincarini et al. 2007). The model to produce these late internal shocks has two variants. In the first, the colliding shells are ejected together with the main burst, and impact each other at late times because they a have small velocity difference. In the second case, the central engine remains active for a long time and emits fast shells at late times. The X-ray flare of GRB 050724 was spectrally hard, with the peak energy above the XRT range. In order to yield such a high value, the Lorentz factor contrast of the colliding shells has to be large (see Malesani et al. 2007). This in turn implies that the central engine remained active for a long time ($\approx$ 40 ks), which is not straightforward to achieve in short (but also long) GRB progenitor models (see Lee & Ramirez-Ruiz 2007 for a review).

5.2.2 The Amati relation

Amati (2006) found a correlation linking the peak energy (E_p) of long GRBs and their isotropic equivalent energy (E_{iso}), the so called “Amati relation”. This relation does not seem to be verified by short GRBs. Of the two GRBs presented here, only GRB 070707 has a measurement of E_p (Golenetskii et al. 2007a). To determine E_{iso} a measurement of the GRB redshift is needed. As explained in the following Section, we could only infer limits on the redshift of GRB 070707. Nevertheless, as illustrated in Fig. 5.3, GRB 070707 is a clear outlier of the “Amati relation” independently of its redshift, confirming the difference between long and short GRBs.

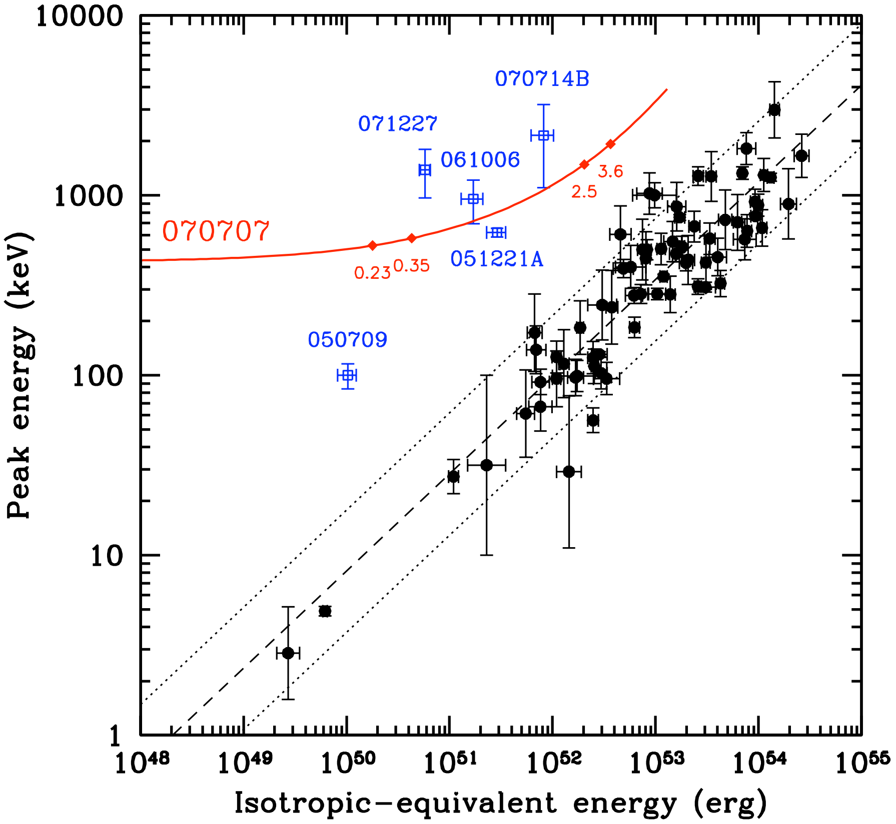

Figure 5.3 Location of GRB 070707 in the peak energy vs isotropic-equivalent energy plane. The thick solid line shows the position of GRB 070707 as a function of redshift, with the diamonds indicating specific values discussed in Sect. 5.3. Filled circles represent long-duration GRBs (from Amati et al. 2008), and the diagonal lines indicate the best-fit Amati relation (dashed) and the 2σ contours (dotted). Empty squares indicate other short-duration events with known redshift and peak energy (Amati 2006; Golenetskii et al. 2006a; Ohno et al. 2007; Golenetskii et al. 2007b).

5.3 Information on short GRB properties from their optical afterglow spectra and their host galaxies.

5.3.1 GRB 070707 optical afterglow spectrum

An optical spectrum of the afterglow of GRB 070707 has been taken about 1.7 days after the burst (see Table 5.2), consisting of five frames with a total exposure time of 200 minutes. The object was clearly visible only in the first two frames. As a consequence the total spectrum has a mediocre signal-to-noise ratio. Neither emission nor absorption lines are visible over a weak continuum in the 4200–9000 Å range. The detection of the continuum, on

Table 5.4 Properties of six galaxies in the field of GRB 070707 (see Fig. 5.4).

ID	RA (J2000)	Dec (J2000)	R magnitude	Redshift
G1	17:50:58.55	-68:53:35.0	21.05	0.3547
G2	17:50:58.40	-68:53:01.5	20.48	0.3780
G3	17:51:04.73	-68:54:27.0	20.17	0.3627
G4	17:51:00.67	-68:55:01.8	17.60	0.213
G5	17:50:58.97	-68:55:12.8	20.30	0.667
G6	17:50:57.18	-68:55:29.4	20.38	0.2394

the other hand, allows to put some constraints on the redshift of this event (see Sect. 6.2.1 for the definition of the following features). The most conservative limit on the redshift is given by the lack of Lyman limit suppression downwards of 4200 Å, which implies $z < 3.6$. The lack of observed Lyman-α forest provides a tighter constraint $z \leq 2.5$, although at such redshift the density of the IGM is relatively low, making this limit less robust.

The fact that the spectrum did not show any clear absorption feature is quite possibly due to the low signal-to-noise and/or the limited wavelength range covered. It is however interesting to note that a featureless spectrum has been reported also for the afterglow of the short GRB 061201 (Stratta et al. 2007) and, as stated at the beginning of this chapter, up to now there are no short GRBs with spectra containing meaningful features. If confirmed by further, better-quality observations, this fact may hint to a lower density of short GRB environments compared to long GRBs.

5.3.2 GRB 070707 field

Many galaxies are clearly visible in our VLT images of GRB 070707 (see Fig. 5.4). In order to check for the possible presence of a cluster (as claimed for example for GRB 050509B; Pedersen et al. 2005) we obtained optical spectra of six galaxies in the field and determined their redshifts (Table 5.4 and Fig. 5.4). These spectra were taken on 2007 Jul 9th and 13th (Table 5.2). The redshift gap between G1, G2 and G3 (0.3547–0.3780) is very large and corresponds to a velocity difference of 7000 km s^{-1} with a dispersion of 3500 km s^{-1}. This value is considerably higher than those measured in clusters of galaxies; therefore we consider very unlikely that these galaxies belong to a cluster. The object labelled as G6 is the closest to the position of the GRB, with a separation of 7.8". A qualitative analysis of the optical spectrum of galaxy G6 reveals that it is a starburst galaxy at $z = 0.2394$, as

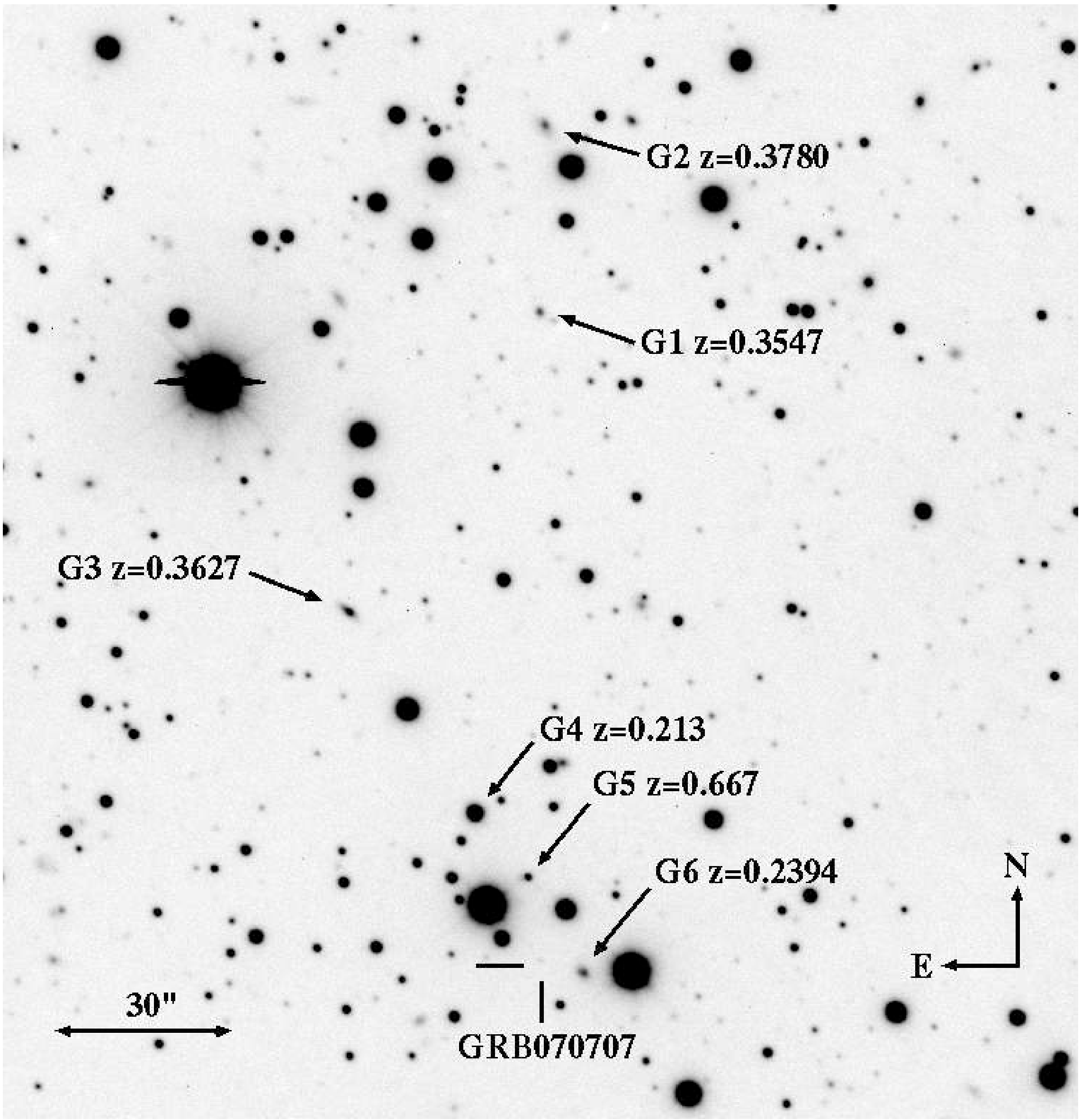

Figure 5.4 *R*-band image of the field of GRB 070707. The galaxies whose redshifts have been reported in Table 5.4 are marked, together with the position of GRB 070707. The field is about $3' \times 3'$ wide.

indicated by the presence of prominent nebular lines.

5.3.3 Host galaxies

Fig. 5.5 presents the spectrum and image of the host galaxy of GRB 050724. As stated in Sect. 5.1 and indicated in the lower panel of Fig. 5.5, the afterglow offset from the centre of the galaxy is only 0.6”, one of the safest GRB-host associations for short GRBs. The host spectrum is typical of an evolved galaxy with an old stellar population. The colors are consistent with those measured by Gorosabel et al. (2006), which analysed the host

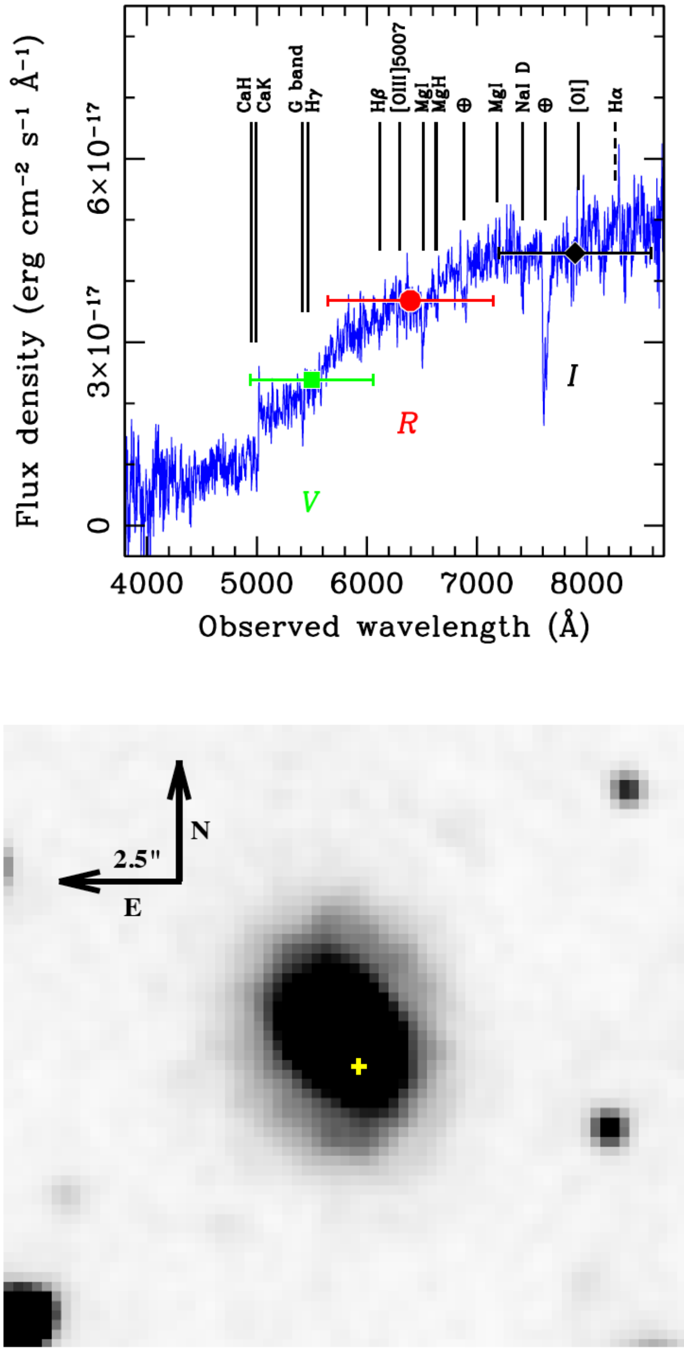

Figure 5.5 *Top panel*: spectrum of the host galaxy of GRB 050724 taken on 2005 Jul 26.99 UT with VLT+FORS1. The absorption lines at $z = 0.2582$ are indicated with solid lines. Telluric lines are indicated by the symbol $\oplus$. The spectrum has been rescaled by a factor of 2.3 to match our photometric measurements (dots). In this plot, no extinction correction has been applied. *Bottom panel*: image of the host galaxy of GRB 050724. The image was taken in the R band with VLT+FORS1 on 2005 Jul 30.1 UT. The cross marks the position of the optical afterglow. Extended emission is visible towards north-west and to the south of the galaxy. The intensity scale is non-linear to enhance the faint peripheral regions.

galaxy of GRB 050724 and found a best-fit age larger than 2.6 Gyr for the dominant stellar population. In the spectrum, no emission features are detected, but from several absorption lines a redshift $z = 0.2582 \pm 0.0003$ could be measured. We also obtain an upper limit to the Hα luminosity, $L < 2.8 \times 10^{40}$ erg s^{-1} (3σ, corrected for slit losses and Galactic extinction). Following Kennicutt (1998), this corresponds to a star formation rate (SFR) $< 0.17\ M_{\odot}$ yr^{-1}. The absolute magnitude of the galaxy is $M_B = -21.2$ ($L \approx 1.2 L_*$ assuming $M_B^* = -21$), computed from the measured V-band flux, so that the SFR per unit luminosity is $< 0.14\ M_{\odot}$ yr^{-1} L_*^{-1}. These results are consistent with previous determinations for this burst (Berger et al. 2005; Prochaska et al. 2006). The SFR per unit luminosity limit is ~ 50 times lower than the average value found in long-duration GRB hosts, both at low and intermediate redshift (Sollerman et al. 2005; Christensen et al. 2004).

Fig. 5.5 shows that a bulge is clearly prominent, but some faint structures are apparent towards north-west and, to a lesser extent, to the south. These may be due to weak spiral arms. The galaxy may thus be classified morphologically as an Sa spiral and not as an elliptical as reported by Berger et al. (2005). For L_* elliptical galaxies, the surface brightness profile is usually described by the de Vaucouleurs $r^{1/4}$ law. When applying this model, the residual images clearly show the spiral arm structure in all the bands, confirming the results of visual inspection (see Malesani et al. 2007 for a more detailed analysis).

It has been suggested that other short GRBs are associated with early-type galaxies, most noticeably GRB 050509B (Gehrels et al. 2005; Hjorth et al. 2005a; Castro-Tirado et al. 2005a; Bloom et al. 2006). On the other hand, a significant fraction of short GRB hosts shows moderate ongoing star formation and relatively young stellar populations (Fox et al. 2005; Covino et al. 2006c; Berger et al. 2007). In terms of progenitors, this implies that either more than one evolutionary channel leads to the production of short GRBs, or that there is a wide distribution of delay times between the birth of the progenitor system and the GRB explosion (Guetta & Piran 2006; Nakar 2007; Lee & Ramirez-Ruiz 2007). The models of merging of a binary compact object system introduced at the beginning of this Chapter are broadly consistent with this results.

The constant flux of the afterglow light curve of GRB 070707 observed at late time (see Fig. 5.6, Table 5.2 and Fig. 5.2), indicates a dominant contribution from the host galaxy.

From the fits of the afterglow light curve of GRB 070707 it is inferred that its host galaxy has a magnitude $R \sim 27.3$ (see Fig. 5.2 and Tab. 5.3). This is the faintest ever

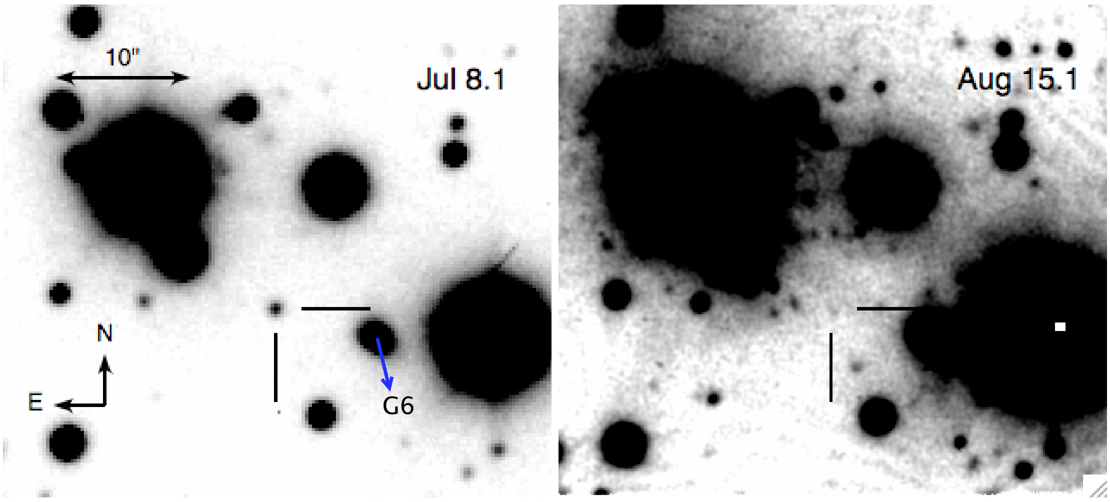

Figure 5.6 *Left panel*: R-band image ($\sim 1\dot{\rm d}$ from the trigger) of the optical afterglow of GRB 070707. The galaxy G6 is also indicated. *Right panel*: R-band image (taken a week later) of the host galaxy of GRB 070707 (see Table 5.2, Fig. 5.2 and Table 5.3).

detected for a short GRB, with magnitude comparable to those of long GRB hosts at high redshift (e.g. Wainwright et al. 2007; Fruchter et al. 2006).

Such a detection does not allow a detailed analysis. At the maximum allowed redshift $z = 3.6$, the host would have an absolute magnitude $M_{\rm AB} = -18.6$ (at rest-frame wavelength $\lambda \approx 1500$ Å). This is more than 2 magnitudes fainter than the Schechter luminosity at this redshift (e.g. Gabasch et al. 2004). It can thus be firmly set that $L < (1/6)L_*$ at any redshift, implying that the host is intrinsically faint. The late-time NIR upper limit ($K > 22.7$) implies $R - K < 4.6$ and hence rules out a bright, red host, such as an extremely red object (ERO) or a moderate-redshift elliptical. GRB 070707 hence confirms that short GRBs can explode inside faint and possibly extremely faint systems. Short GRB hosts indeed exhibit a wide range of luminosities. The hypothesis of the host as a globular cluster of G6 is discarded because the redshift of G6 would imply an absolute magnitude of $M_V \sim 13.2$, much brighter than a globular cluster.

The possibility to find short GRBs not spatially coincident with a host galaxy has been discussed by several authors (e.g. Bloom et al. 2007; Stratta et al. 2007; Levan et al. 2007).

In some cases, nearby, bright objects were proposed to be the short GRB host, based just on angular proximity. The case of GRB 070707 shows that caution is needed. Without deep VLT images (see Fig 5.6 to realize how faint the host is if observed deeply from an 8-m class ground-based telescope), it might have been tempting to associate GRB 070707 with the close-by galaxy G6, which is certainly not the GRB host. Many more galaxies of short GRBs may be just fainter than the fluxes probed by shallower exposures. While this is consistent with the suggestion that a substantial fraction of short GRBs resides at redshifts larger than $z \sim 1$ (Berger 2007), this may also indicate that some short GRBs go off inside low-luminosity galaxies at low redshift.

The existence of such faint short GRB host galaxies can also imply that space telescope observations may be needed in order to discriminate if a short GRB exploded 'inside' a galaxy or much farther away with a large offset. As explained at the beginning of this chapter, these kind of determinations are of capital importance when trying to collect information on short GRB progenitors and discriminate between the different possibilities.

Chapter 6

High resolution spectroscopy of GRB afterglows

Thanks to their exceptional brightness GRB afterglows can be used as powerful extragalactic background sources. Since GRBs can be detected up to very high redshifts and the GRB afterglow light enlightens all the matter along its way to us, they behave like distant lighthouses capable to unveil the properties of the universe at different redshifts. The intervening matter between the GRB and the observer absorbs selectively a part of the afterglow radiation (see Fig. 6.1), therefore the resulting spectra can be used to study the properties and evolution of galaxies and the IGM.

While only the most bright objects can be detected in emission, the study of absorption spectral features allows the detection of very small quantities of non-luminous matter, from column densities as small as 10^{12} to up to 10^{22} hydrogen atoms per cm^2, that is a 10 magnitude order of interval. Moreover the intensity of the absorption depends only on the physical properties of the gas involved and not on its distance. It is therefore possible to study gas between $z = 0$ and $z > 5$, depending on the wavelength spectral coverage.

Traditionally these kinds of studies have been performed since the end of the Sixties using quasar (QSO) spectra. QSOs are supermassive black holes in the center of galaxies accreting the surrounding matter. They are extremely luminous thanks to the conversion into radiation of the gravitational energy of the accreted matter. Up to now $\sim 100\,000$ QSOs have been discovered, with the highest redshift one being at $z = 6.43$. To obtain good quality GRB spectra is more difficult, due to the fading nature of these objects: to date, about 600 GRBs have been discovered while only some tens of suitable signal-to-noise (S/N) spectra are available. The community is putting in a lot of effort to increase this number aiming for quick systematic spectroscopy of well-localized GRBs. One of the results of this involvement has been the determination of the highest absorption redshift ever, that is the one of the host galaxy of GRB 080913 at $z \sim 6.7$ (Fynbo et al. 2008a).

QSOs are long-lasting sources that ionize, partially or totally, the gas over their entire host galaxy. Faint metal line systems along QSO sightlines probe mainly galaxy haloes, rather than their bulges or discs. Instead, GRBs are transient phenomena, affecting only smaller regions and, moreover, the star forming regions surrounding GRBs are probably much richer in enriched gas than the giant elliptical galaxies, which are the typical host of luminous QSOs (Savaglio 2006). Therefore, GRBs constitute a complementary tool to investigate the ISM of typical high redshift galaxies.

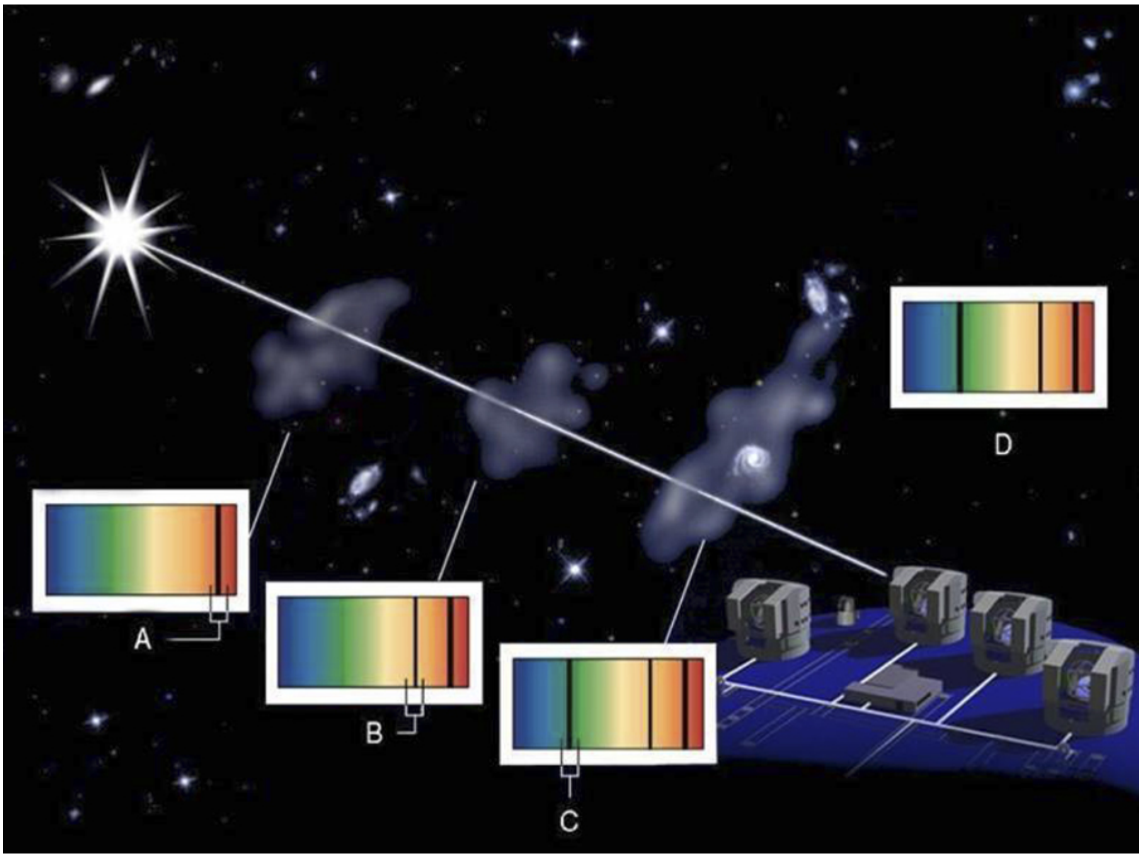

Figure 6.1 The light coming from an extragalactic source like a GRB or a QSO is observed at a telescope (D) after that the absorbers A, B and C left a signature in its spectrum. Figure from ESO Press Release 13/08.

6.1 The absorption line profile[1]

6.1.1 The Voigt profile

An absorption line profile can be described by its intensity as function of wavelength:

$$I(\lambda) = I_0(\lambda)(1 - e^{-\tau(\lambda)}) \tag{6.1}$$

where $I_0(\lambda)$ is the intensity of the continuum (i.e. of the GRB before absorption) and $\tau(\lambda)$ is the optical depth. The optical depth depends on two parameters: the quantity of atoms contributing to the absorption (measured by their density per surface unit N) and their cross section $\sigma(\lambda)$. We have therefore:

$$\tau(\lambda) = N\sigma(\lambda) \tag{6.2}$$

The absorption profile has a natural width different from zero due to the life time of the upper level of the transition. The cross section characterizing this transition (of frequency $\nu_0 = c/\lambda_0$) is given by (Mihalas & Auer 1970):

$$\sigma(\nu) = \frac{f}{4\pi\epsilon_0}\frac{\pi e^2}{m_e c} \times \phi(\nu) \tag{6.3}$$

where f is the line oscillator strength and $\phi(\nu)$ is the Lorentz function given by

$$\phi(\nu) = \frac{\frac{\Gamma}{4\pi}}{(\nu-\nu_0)^2 + (\frac{\Gamma}{4\pi})^2}. \tag{6.4}$$

Γ here is the attenuation coefficient of the line, taking into account the de-excitation process of the upper level. The typical width of the lorentzian is of the order of a few meters per second at 5000 Å, very small compared to the thermal width due to the Maxwell-Boltzmann distribution of the atoms, and also to the turbulent velocity dispersion and the instrumental width. In the absorber rest frame, the random movements of the atoms around the average velocity v_0 introduce a Doppler enlargement of the line profile. An atom with velocity v has therefore a cross section $\sigma(\nu')$ with $\nu' = \nu/(1-v/c)$ in the absorber rest-frame. The convolution of the lorentzian natural profile with a Gaussian profile (resulting from the Maxwellian distribution and from the Gaussian turbulent movements) gives

$$\tau(\nu) = \frac{N}{\sqrt{\pi}b}\int_{-\infty}^{+\infty} \sigma(\nu')e^{-(v-v_0)^2/b^2}dv \tag{6.5}$$

b is called the Doppler parameter. Last, the optical depth can be written as

---

[1] For a more detailed description see P. Petitjean PhD Thesis and Petitjean (1999).

$$\tau(\lambda) = 1.498 \times 10^{-2} \frac{Nf\lambda}{b} H(a,u) \tag{6.6}$$

where the Hjerting function $H(a,u)$ is given by:

$$H(a,u) = \frac{a}{\pi} \int_{-\infty}^{+\infty} \frac{e^{-y^2}}{(u-y)^2 + a^2} dy \tag{6.7}$$

with

$$\begin{cases} a = \frac{\lambda\Gamma}{4\pi b} \\ u = -c/b((1+v/c) - \lambda/\lambda_0). \end{cases}$$

The resulting profile is called *Voigt profile*.

6.1.2 The curve of growth

When the spectral resolution is not enough to resolve the absorption line profiles, it is still possible to retrieve some information on the line *equivalent width W*. In this case, the information given by N and b is incorporated in the single W quantity. The equivalent width is by definition proportional to the line area:

$$W_{obs} \equiv \int \frac{I_0(\lambda) - I(\lambda)}{I_0(\lambda)} d\lambda = \int (1 - e^{-\tau(\lambda)}) d\lambda \tag{6.8}$$

(W refers to the rest frame equivalent width: $W_{\mathrm{obs}} = (1+z) \times W$). The theoretical relation between the equivalent width of a line and the column density of the atom responsible for the absorption is given by the curve of growth (Unsöld et al. 1930; Wilson 1939). There is a relation between the projected density and the equivalent width for every transition. This depends on the Doppler parameter b. The curve of growth for the HI λ1215 transition (Lyman-α, often indicated as Ly-α) is drawn in Fig. 6.2 for different Doppler parameters ($b = 5$, 10, 20 and 40 $\mathrm{km\,s^{-1}}$). It is possible to differentiate three regimes:

- *linear regime:* When the projected density is weak ($< 10^{13}$ $\mathrm{cm^{-2}}$ for Ly-α), W is directly proportional to N. The Doppler parameter influences only the absorption profile shape but not its equivalent width ((1) in Fig. 6.2). The measurement of N is easy and robust, and we have:

$$W = \frac{\pi e^2 \lambda_0}{m_e c^2} N \lambda_0 f \tag{6.9}$$

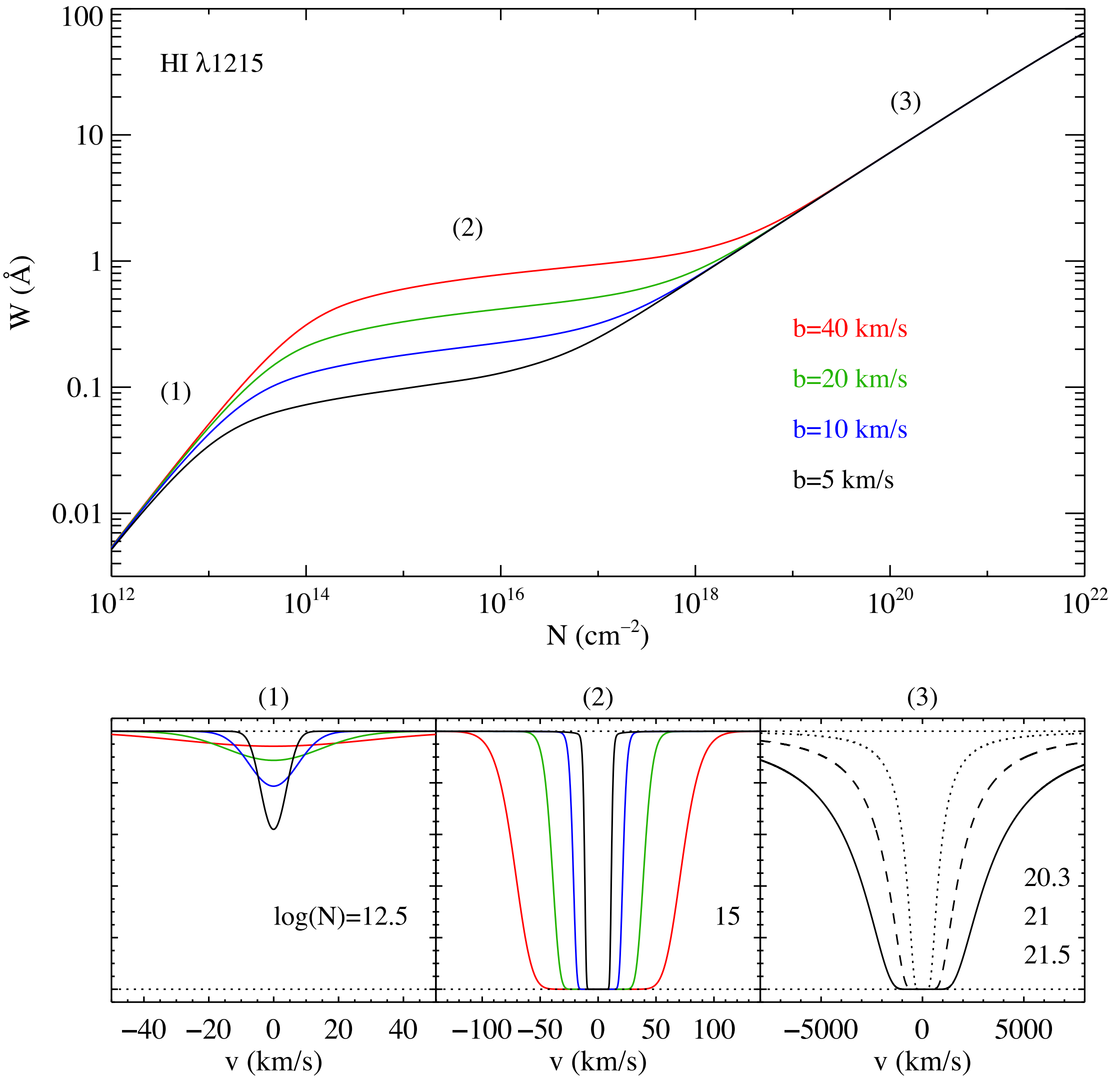

Figure 6.2 Curve of growth of HI λ1215 (Lyman-α). The different regimes are indicated by (1), (2) and (3), corresponding to the linear, the flat and the damped regime, respectively. In the lower panel the line profile corresponding to the three regimes is shown, for the different values of the Doppler parameter b indicated in the upper panel, and for values of the column density N varying from log(N)=12.5 to log(N)=21.5. From the upper panel it is easy to see that the so-called DLA systems ($N(HI) \geq 2 \times 10^{20}$ cm^{-2}) correspond to a rest frame equivalent width of about 10 Å. This make possible the search for DLA systems ($W_{\rm obs} > 30$ Å at $z \sim 2$) also inside low resolution spectra ($\sim$ 10 Å). Figure from P. Noterdaeme PhD thesis.

thus

$$N(\mathrm{cm}^{-2}) = 1.13 \times 10^{20} \frac{W(\mathrm{A})}{\lambda_0^2(\mathrm{A}) f} \tag{6.10}$$

- *The logarithmic (or saturated) regime:* This regime is characterized by a strong dependence of W on the Doppler parameter b for a given N. The column density measurement is therefore very uncertain and we have:

$$W \sim \frac{2b\lambda_0}{c}\sqrt{\ln \frac{\sqrt{\pi}e^2 N\lambda_0 f}{m_e cb}} \tag{6.11}$$

  thus $W \propto \sqrt{\ln N}$. The strong dependence of W and the profile shape on b for this saturated regime is well shown in Fig. 6.2, case (2).

- *The damped regime:* When the column density becomes very large, the Doppler parameter does not influence any longer either the shape of the profile and the equivalent width - column density relation.The line profile is totally dominated by the lorentzian component, with large wings on both side of a saturated core. The N determination is again reliable. We have:

$$W \sim \frac{\lambda_0^2}{c}\sqrt{\frac{e^2}{m_e c}Nf\Gamma}. \tag{6.12}$$

  As expected, this last relation is not dependent on b and, for Ly-α , it can be written as $N(\mathrm{cm}^{-2}) = 1.88 \times 10^{18} W^2$ (Å).

Most of the lines in a GRB spectrum can be well fitted by a Voigt profile (or a combination of Voigt profiles); it should be kept in mind that the N and b parameters of the Voigt profile are the result of densities and average dispersions of a portion of the line of sight. An absorption profile can be modelled as an entanglement of many components and the decomposition of the Voigt profile is not always unique. The use of several transitions of the same type allows the solution of the problem only up to a certain level.

6.2 Classification of the absorbers

Definitions

- The redshift z of a line is given by $z = \lambda_{obs}/\lambda_0 - 1$, where λ_0 is the wavelength at the absorber rest frame and λ_{obs} is the observed one, expressed in vacuum and in the heliocentric frame.

- All the lines belonging to the same absorber form a *system.* These lines can originate from different transitions of the same element or from different elements, but they are all at the same redshift.

- The lines of each system can span many tens or hundreds of kilometers per second. In this case, the systems can be decomposed in sub-systems called *components*. The decomposition of the overall profile of a system into components depends mostly on the observational resolution, the S/N and the saturation of the line. At low resolution the total profile of a system often appears as a single absorption that is not resolved and the decomposition is therefore not possible. At high resolution it is often possible to decompose a system even in tens of component (see Fig. 6.3 for a comparison between low and high resolution spectra).

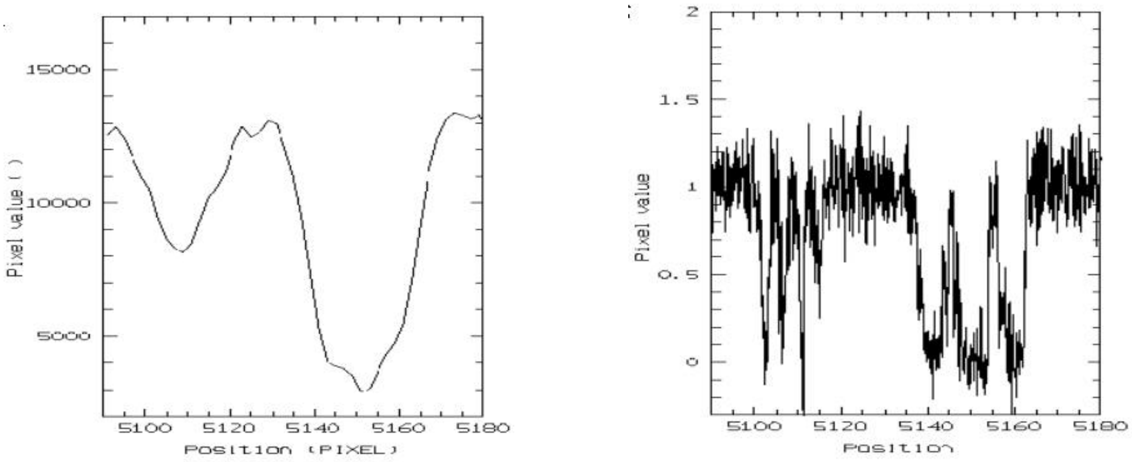

Figure 6.3 The left panel shows two CIV absorption signatures ($\sim 3000\,\mathrm{km/s}$ apart) in the afterglow spectrum of GRB 021004 observed with VLT-FORSI (resolution $R \sim 1000$). The right panel reports the VLT-UVES observation (resolution $R \sim 51500$) of the same systems clearly showing that each of them consists of several components. This information is completely lost in the low resolution spectrum.

Origins

- *The intervening absorbers,* $z_{abs} \ll z_{GRB}$: They are due to gas cosmologically distributed and found by chance along the line of sight (l.o.s.) linking the observer to the GRB. They are not associated with the GRB environment or its host galaxy.

- *The associated absorbers,* $z_{abs} \equiv z_{GRB}$: They correspond to the gas found in the GRB host galaxy and/or its halo, or belonging to the GRB environment itself. The physical, dynamical and chemical state of the medium in the star-forming region hosting the GRB progenitor can be modified by the GRB, through shock waves and ionizing photons. Strong fine structure lines are always observed in the high resolution spectra of these systems. The systems associated with random clouds of the ISM of the host galaxy along the line of sight show low ionization lines and ground state lines, implying distances from the GRB explosion site larger than a few hundred pc. The distinction between these two kinds of associated absorbers is not always clear cut. Vreeswijk et al. (2007) discovered large variations of FeII fine-structure lines in the spectra of GRB 060418 ($z = 1.48$) on rest frame time scales of a fraction of an hour, and interpreted them as due to ultraviolet (UV) pumping from the afterglow radiation field. Their detailed modeling of the observed variability suggests a distance of the FeII absorbing cloud from the GRB explosion site of ~ 1.7 kpc, comparable to the size of a typical galaxy at $z \sim 1.4$. This would imply that, at least in this case, the entire galaxy (or a significant fraction of it) is affected by the GRB explosion (see Cameron & Driver 2007 for typical galaxy sizes).

6.2.1 Classification according to the HI content

Hydrogen is the most abundant element in the Universe. The Ly-α hydrogen line has a strong oscillator strength and a wavelength $\lambda = 1215.67$ Å, useful to investigate the Universe at $z > 1.6$ from ground-based telescopes. Every system shows an HI absorption when this line is covered by the observed spectral range. The most common classification of the absorbers is therefore based on the hydrogen column density.

6.2.1.1 The Lyman-α forest

Fig. 6.4 shows a part of the VLT-UVES high resolution spectrum of GRB 050730. Several absorption lines are present at wavelengths shorter than the Ly-α absorption associated with the GRB. Most of these lines correspond to the Ly-α transition of the atomic hydrogen situated between the GRB and the observer, more precisely they are associated with hydrogen overdensities confined along filaments by the dark matter (Cen et al. 1994; Petitjean et al. 1995). All these lines together form the so-called *Lyman-α forest*. The gas inside the Lyman-α forest is strongly ionized, therefore the neutral gas responsible for the Ly-α absorptions represents only a small portion of the baryonic matter inside these absorbers. It has been shown indeed that the Lyman-α forest contains the bulk of baryonic gas in the Universe (e.g. Rauch et al. 1997).

6.2.1.2 The Lyman-limit systems

Some Ly-α absorptions correspond to neutral hydrogen column densities so high that all the ionizing photons, with wavelengths shorter than 912 Å (the Lyman series limit), are

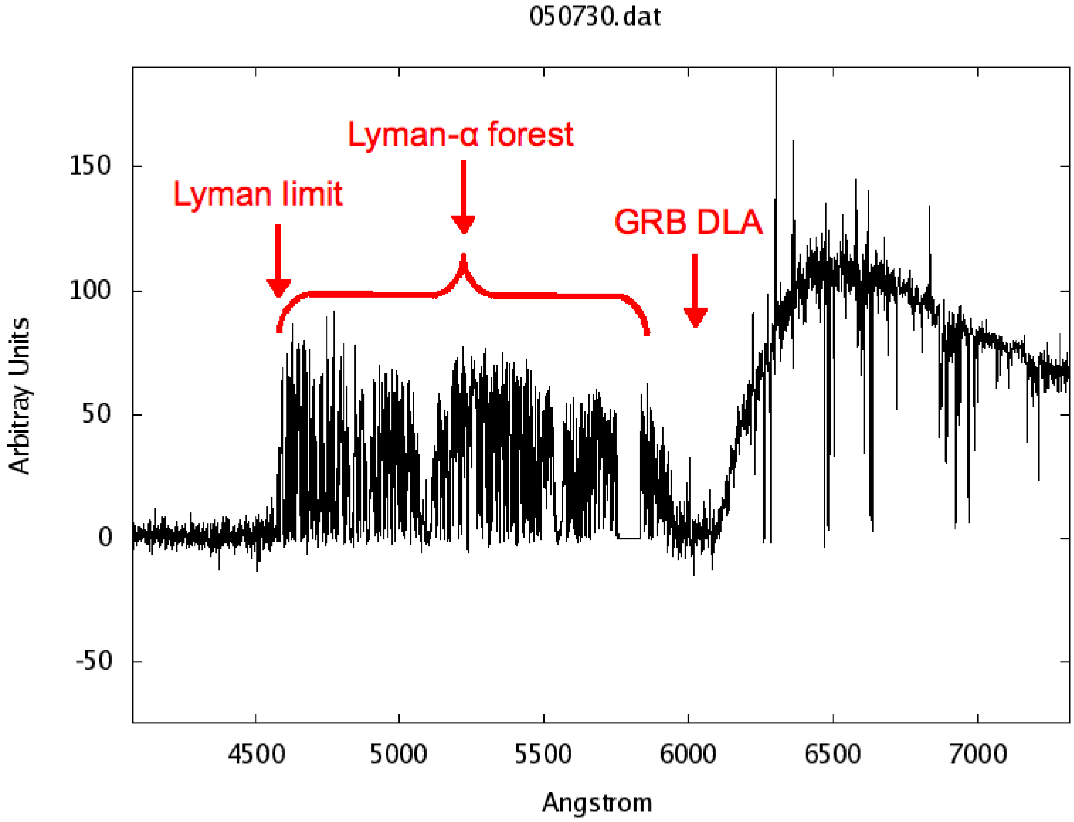

Figure 6.4 Part of the VLT-UVES high resolution spectrum of GRB 050730. The DLA absorption (see Sect. 6.2.1.3) associated with the GRB is clearly visible at ∼ 6000 Å, with the corresponding Lyman limit (see Sect. 6.2.1.2) at ∼ 4600 Å. The absorptions between the GRB Ly-α absorption and the Lyman limit break form the Lyman-α forest.

stopped by the hydrogen. The GRB afterglow (or QSO) spectrum shows a sudden break and its flux is null for wavelengths shorter than $\lambda = (1 + z_{abs}) \times 912$ Å. An example of this effect is illustrated in Fig. 6.4, with the Ly-α absorption at ∼ 6000 Å and the corresponding Lyman break at ∼ 4600 Å . These systems are called *Lyman-limit systems.* They correspond to column densities of $17 < logN(\mathrm{HI}) < 20.3$ (Péroux et al. 2003b) and originate probably in border region of forming galaxies (see Prochaska 1999 for a discussion on the origins of these systems).

6.2.1.3 The Damped Lyman-α systems (DLAs)

When the hydrogen column density is large enough, the optical depth becomes very high and the ionizing radiation is absorbed by a thin hydrogen layer. These systems have $N(\mathrm{HI}) \geq 2 \times 10^{20}\mathrm{cm}^{-2}$ (Wolfe et al. 1986) and are called *Damped Lyman-α systems.* DLAs are very interesting. They contain most of the neutral gas of the Universe and are associated with metal lines, found most of the time at wavelengths larger than the GRB Ly-α. They probably trace the interstellar medium of forming protogalaxies.

6.3 Abundances and Metallicity

Apart from using the DLAs to study the hydrogen content of the Universe and its evolution with time, the identification of such neutral hydrogen systems in the Universe allows the study of the element abundances (see Pettini 2004 for a review on this subject). Usually the abundances of elements of a certain astrophysical medium are compared to the solar composition as a reference. The standard notation to describe the abundance of an element X compared to another Y is:

$$[\mathrm{X/Y}] \equiv \log(\mathrm{X/Y})_{\mathrm{obs}} - \log(\mathrm{X/Y})_{\odot} \tag{6.13}$$

where $(\mathrm{X/Y})_{\mathrm{obs}}$ is the ratio between the observed column densities of X and Y, while $(\mathrm{X/Y})_{\odot}$ is the same quantity observed in the Sun.

Different elements are produced by stars with different masses and therefore different life duration. The so-called α elements (O, Ne, Mg, Si, S, Ca) are primarily produced by massive stars exploding into type II supernovæ. Iron, as well as the elements of the iron peak (e.g. Zn, Ni), are on the other hand mainly produced by type Ia supernovæ. From the study of the abundance ratio of two elements it could be possible therefore to retrieve information on the star population of a galaxy and on its star formation history.

Some refractory elements, such as iron or chrome, have a strong affinity with dust. A non-negligeable fraction of these elements can be in solid form and thus the abundance measurements, since they come from the observation of the gaseous state only, represent just a lower limit on the true abundance. It is therefore interesting to understand better how to infer the true abundance values from the observed ones (see for example Vladilo 1998, 2002).

The abundance of an element heavier than He compared to hydrogen is called **metallicity**. Its notation is [X/H] or Z. The neutral hydrogen content of the Universe is dominated by the DLAs. The DLAs average metallicity is therefore the best measurement of the chemical enrichment of the Universe at a particular epoch. To have a safe measure of Z using HI we need to be sure that the most significant fraction of hydrogen is in its neutral state, and that the measured column density of a particular state of the X element corresponds to a very significant fraction of that element as well. High resolution echelle spectroscopy of DLAs allows a precise measurement of these quantities. In fact, most of the hydrogen in DLAs is neutral and the UV photons with energy higher than the hydrogen ionization energy ($h\nu > 13.6\,\mathrm{eV}$) cannot penetrate deep inside the neutral hydrogen clouds, thus limiting the ionization state of the elements. The photons with energy $h\nu < 13.6\,\mathrm{eV}$ can penetrate the gas and most of the metals are observed in their first ionization state (FeII, SiII, ZnII), having a second ionization energy larger than 13.6 eV. Other elements as for example oxygen (O) have a first ionization energy $h\nu \geq 13.6\mathrm{eV}$ and are observed in their neutral phase. Moreover, the N(HI) measurement in DLAs is precise, because in this regime the line profile does not depend on the Doppler parameter but it is very sensitive to column density. Lastly, the high resolution and the large spectral coverage of these kind of spectra allow the observation of many transitions of the same element within the same spectra, thus improving the precision of the column density determination of each of them. Ideally, the metallicity is measured using OI, but its lines are often saturated and therefore not suitable for a precise determination of the column density. Zinc is the most used element because its absorption lines are outside the Lyman-α forest, they are optically thin and it is poorly depleted onto dust in the interstellar medium (Savage & Sembach 1996).

The average DLA metallicity (measured using QSO spectra) in the redshift interval $0.5 < z < 3$ is low (Pettini et al. 1994, 1997, 1999), about 1/20 of the solar one ($\langle Z \rangle \simeq -1.3$), with a large dispersion. In addition to the intervening DLA that can be detected along GRB l.o.s. (the study of which is at its beginning and will be introduced in Sect. 6.5), there is almost always a DLA associated with the GRB. The metallicities of the DLAs associated with the GRBs are on average higher than the QSO-DLA metallicities (Savaglio 2006; Fynbo et al. 2006a, 2008b). This difference arises naturally from two effects: i) the generally higher impact parameters (defined as the projected physical distance between the putative absorbing galaxy and the QSO/GRB sightline at the galaxy redshift) of QSO-DLAs relative to the DLAs associated with GRBs, and ii) the fact that GRBs explode in bright star forming regions (Fynbo et al. 2008b). These last authors indicate that the metallicity distribution of GRB-DLAs at $z \sim 3$ is consistent with the prediction that GRBs directly trace the star-formation rate and that the host metallicities follow a luminosity-metallicity relation.

While the knowledge of the galaxies associated with the DLAs detected through QSO spectra is very poor, GRBs allow the possibility to study quite easily the galaxies corresponding to the GRB-DLAs. Indeed, the fading nature of GRBs and the precise localization of the afterglow favour a detailed photometric and spectrometric investigation of the

GRB host galaxy once the afterglow has vanished.

In the following sections I will discuss different kinds of studies that can be performed using high resolution afterglow spectra. The first section, partly based on Piranomonte et al. (2008, submitted), is dedicated to the investigation of the DLA system associated with GRB 050922C, trying to disentangle its different components and their origins as well as retrieving information on the metallicity of the system. The second section is dedicated to the preliminary results of a study on the intervening systems along GRB lines of sight and their comparison to those of QSOs. This work is part of a larger project I am carrying out in collaboration with people at the Institute d'Astrophysique de Paris, the DARK Cosmology centre and ESO (Vergani et al. 2008, to be submitted).

6.4 High resolution spectroscopy of GRB 050922C

GRB 050922C was detected by *Swift* on 2005 September 22 19:55:50 UT (Norris et al. 2005) and, after 4 s, by Konus/Wind (Golenetskii et al. 2005). ROTSE[2] discovered a bright transient source at RA(J2000) = $21^{\mathrm{h}}09^{\mathrm{m}}33.1^{\mathrm{s}}$ and DEC(J2000) = $-08^{\circ}45'29.8''$, 172.4 s after the burst, which was promptly identified as the optical afterglow of GRB 050922C (Rykoff et al. 2005b) with a magnitude $R = 14.7$. The redshift of the GRB, $z \sim 2.2$, was determined by Jakobsson et al. (2005) using ALFOSC at the Nordic Optical Telescope at the Observatorio del Roque de los Muchachos in La Palma and was confirmed shortly after through TNG/DOLoRes spectroscopy (Piranomonte et al. 2005). The afterglow was then observed by UVES/VLT at high spectroscopic resolution ($R \sim 40000$) about 3.5 hours after the burst, when its magnitude was $R = 19.0$.

6.4.1 Observations and data analysis

In the framework of ESO program 075.A-0603 the MISTICI collaboration observed the afterglow of GRB 050922C with UVES mounted at the VLT-UT2 telescope. Table 6.1 gives the log of the observations. Both UVES dichroics, as well as the red and the blue arms, were used. This allowed us to achieve a particularly wide spectral coverage, extending from ~ 3200 Å to ~ 10000 Å. In order to maximize the signal to noise ratio the CCD was rebinned in 2×2 pixels. The data reduction was carried out by using the UVES pipeline (Ballester et al. 2006). Following Fiore et al. (2005) the total spectrum was rebinned to 0.1 Å to increase the signal-to-noise ratio. This resolution is still good enough to sample weak lines with at least 3-4 bins. The resolution element, set to two pixels, ranges then from

---

[2] http://www.rotse.net/

Table 6.1 Journal of observations.

Date	Dichroic	Central wavelength		Slit width	Seeing	Exposure	Time since GRB
(UT)		Blue arm	Red arm	(")	(")	(min)	(hr)
09/22/05 00:07:17	1	3460 Å	5800 Å	1	≤ 1	50	4.15
09/22/05 01:02:09	2	4370 Å	8600 Å	1	≤ 1	50	5.07

14 $\mathrm{km\,s^{-1}}$ at 4200 Å to 6.6 $\mathrm{km\,s^{-1}}$ at 9000 Å. The noise spectrum, used to determine the errors on the best fit line parameters, was calculated from the real-background-subtracted and rebinned spectrum using line-free regions. This takes into account both statistical errors and systematic errors in the pipeline processing and background subtraction.

The line fitting was performed using the MIDAS package FITLYMAN (Fontana & Ballester 1995). This uses a Voigt profile and yields independently the column density N and the Doppler parameter b for each absorption component. For each absorption system several lines, spread over the entire spectral range covered by the UVES observations, were fitted simultaneously, using the same number of components for each line, and the same redshift and b value for each component.

In all of the following figures showing plots from FITLYMAN (Fig. 6.5 - 6.8) the x-axis represents the velocity shift of the gas with respect to the zero, the y-axis represents the flux normalized to 1 for each element, the horizontal blue lines and dashed blue lines represent the flux level of the spectrum normalised to 1 and the zero point, respectively. The red line corresponds to the fit profile of the individual components and the magenta and green lines correspond to the polynomial approximation of the noise and the residual spectrum, respectively.

The spectrum exhibits a large number of absorption features, belonging to different absorption systems. The main system is due to the gas inferred to be in the host galaxy, at redshift $z = 2.1996$. We identified eight more intervening absorbers at $z < 2.1996$ (z =0.6369, 1.1076, 1.5670, 1.5693, 1.9891, 2.0086, 2.0778 and 2.1421). Sudilovsky et al. (2007) found one more intervening system at $z = 1.6911$, but we could not confirm that this is real because the CIV doublet is coincident with the SiIIλ1304 and OIλ1302, OI*λ1304 lines of the main system at $z = 2.1996$; moreover there is no Ly-α absorption at that redshift.

In this section I will discuss the results concerning the main system. The intervening systems are part of the discussion in Sect. 6.5.

6.4.2 The $z = 2.1996$ absorption system

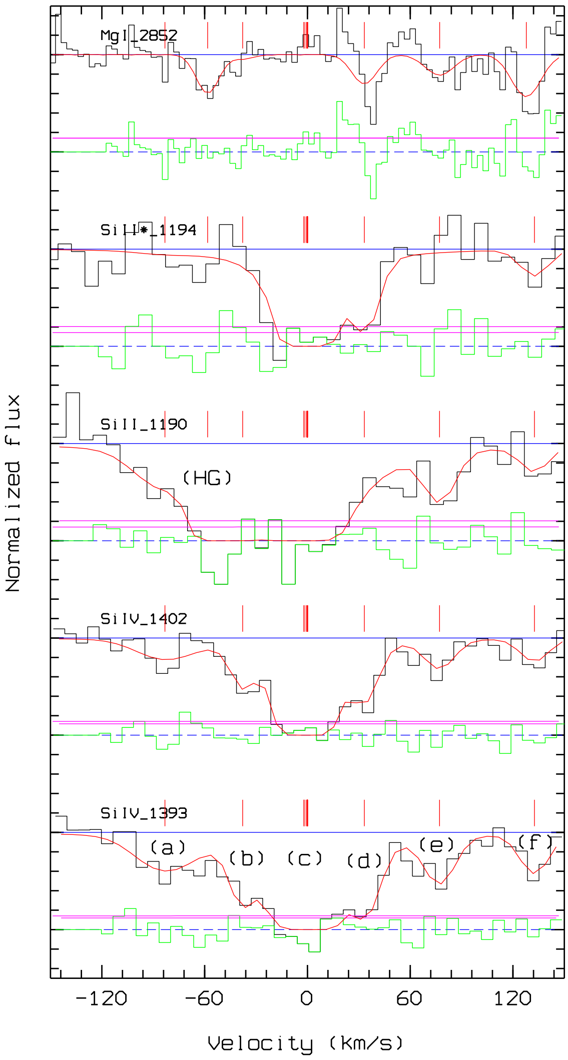

Figure 6.5 The UVES spectrum around the lines Si IV λ1393,1402, SiII λ1190, SiII* λ1194 and MgIλ2852. For MgI we clearly see the (HG) component. The zero of the velocity scale refers to the redshift of the host galaxy, $z = 2.1996$.

Considering the non-detection of higher redshift systems or Ly-α lines and the presence of a strong DLA at this redshift, the system at $z = 2.1996$ is most likely associated to the GRB host galaxy. Like most GRB host galaxy absorption systems (e.g. Fiore et al. 2005; D'Elia et al. 2007; Vreeswijk et al. 2007; Prochaska et al. 2006, 2008; D'Elia et al. 2008) it presents many components, spanning a rather large velocity range (~ 210 km s^{-1}). Interestingly, different components exhibit different transitions: some exhibit low-ionization lines, high-ionization lines and fine-structure lines, others exhibit low-ionization lines only. An example is given in Figure 6.5. Six components, labeled from (a) to (f), are identified for the SiIV and CIV doublets, spanning a velocity range from -75 to +140 $\mathrm{km\,s^{-1}}$. The adopted zero velocity is also indicated. Each component has a width between 10 and 25 $\mathrm{km\,s^{-1}}$. Component (c) has nearly zero velocity shift and shows strong fine-structure lines, high-ionization transitions and no detection for MgI. Fainter, but still significant SiII* lines are associated with components (d) and (f) too. On the other hand, the SiIIλ1190 component labeled (HG) at ~ -58.60 $\mathrm{km\,s^{-1}}$ is not present in either SiIV or SiII* transitions. This component shows the MgI absorption.

The complex line profile, and the fact that different components may exhibit different line transitions, made it impossible to fit the system with a single Voigt profile. Therefore we were forced to identify the different components, before we could derive the column densities through a fitting procedure. The main goal of this work is indeed to disentangle the relative contribution of the different components. We use the less saturated transitions to guide this identification. We identified 7 components for the $z = 2.1996$ system ((a) through (f), and (HG); see Fig. 6.5). The redshifts of components (a) to (f), and therefore their velocity shifts with respect to $z = 2.1996$ which has been taken as a reference, were determined using the CIV and SiIV lines. The redshift of the (HG) component was determined by using the SiII transitions. The redshifts were taken fixed when fitting all other lines belonging to each component with Voigt profiles. The Doppler parameter of a component is the same for every element. The column densities of non saturated and moderately saturated transitions of each component of the main absorption system at $z = 2.1996$ are given in Table 6.2. Strongly saturated lines could not be used for column density evaluation, and accordingly a "‡" symbol is given in the tables for the corresponding transitions.

To test the robustness of the results, in terms of the accuracy and stability, we performed many fits, using several combinations of line components. We found that the results presented in Table 6.2 provide a good compromise between increasing the statistical precision of the fit, obtained by increasing the number of components fitted simultaneously, and the stability/repeatability of the results. The latter is degraded when the number of fitted parameters is increased, because of the increasingly complex shape of the χ^2 hypersurface in the parameter space, which may contain many local minima. We verified that the total best-fit column density of each system is stable, within the statistical errors, changing the number of components in each system.

Table 6.2 Derived column densities for the $z = 2.1996$ system.

Transition	2.1996a	2.1996(HG)	2.1996b	2.1996c	2.1996d	2.1996e	2.1996f
km s^{-1}	-83.26	-58.60	-37.88	-0.39	+33.15	+77.54	+136.73
MgI	†	11.8±0.1	†	< 11.8	12.0±0.1	11.6±0.2	⋆
OI	-	15.4±0.3	-	‡	‡	-	-
OI*	-	-	-	15.1±0.1	14.0±0.2	<13.7	-
OI**	-	-	-	14.53±0.08	13.4±0.3	<13.7	-
MgII	†	14.6±0.3	†	14.8±0.6	13.6±0.3	13.4±0.3	11.3±0.5
CII	†	15.5±0.4	†	14.6±0.2	14.6±0.5	14.2±0.3	13.06±0.21
CII*	-	< 13.3	-	14.6±0.1	14.2±0.3	13.5±0.2	< 13.3
SiII	†	14.26±0.07	†	14.8 ± 0.1	13.9 ± 0.2	13.5 ± 0.2	12.9 ± 0.2
SiII*	-	< 13.0	-	14.28 ± 0.04	13.1 ± 0.1	13.1 ± 0.1	12.4 ± 0.3
AlII	†	12.90±0.05	†	14.0±0.3	12.1±0.2	12.15±0.07	10.6±0.5
AlIII	†	11.8±0.1	†	12.09±0.04	11.30±0.3	-	-
CIV	13.40±0.05	< 13.26	13.15±0.09	15.0±0.2	13.63±0.07	13.78±0.03	13.12±0.07
SiIV	13.07±0.07	< 13.17	13.2±0.1	14.3±0.2	13.3±0.1	13.06±0.06	12.76±0.09
NV	-	-	-	14.06±0.08	15.3±0.7	-	-
OVI	-	-	-	15.2±1.9	14.6±0.2	-	-
Fe	2.1996a	2.1996(HG)	2.1996b	2.1996c(1)/2.1996c(2)	2.1996d	2.1996e	2.1996f
km s^{-1}	-83.26	-58.60	-37.88	-13.3/+15.74	+33.15	+77.54	+136.73
FeII	-	13.67±0.04	13.75±0.03	13.3±0.1/13.73±0.04	-	14.3±0.4	-
FeII*	-	-	-	- /13.36±0.07	-	-	-

† This component is blended with the component (HG), so we cannot determine the relative column density.

‡ Saturated component.

⋆ The absorption feature is shifted to 5.5 km s^{-1} with respect to the (f) position and is not associated with the MgI absorption of component (f).

6.4.2.1 Low-ionization lines

Strong low-ionization lines were detected for all components. In four cases (MgII, CII, AlII and AlIII) reliable estimates of the ion column density for the (c), (d), (e), (f) and (HG)

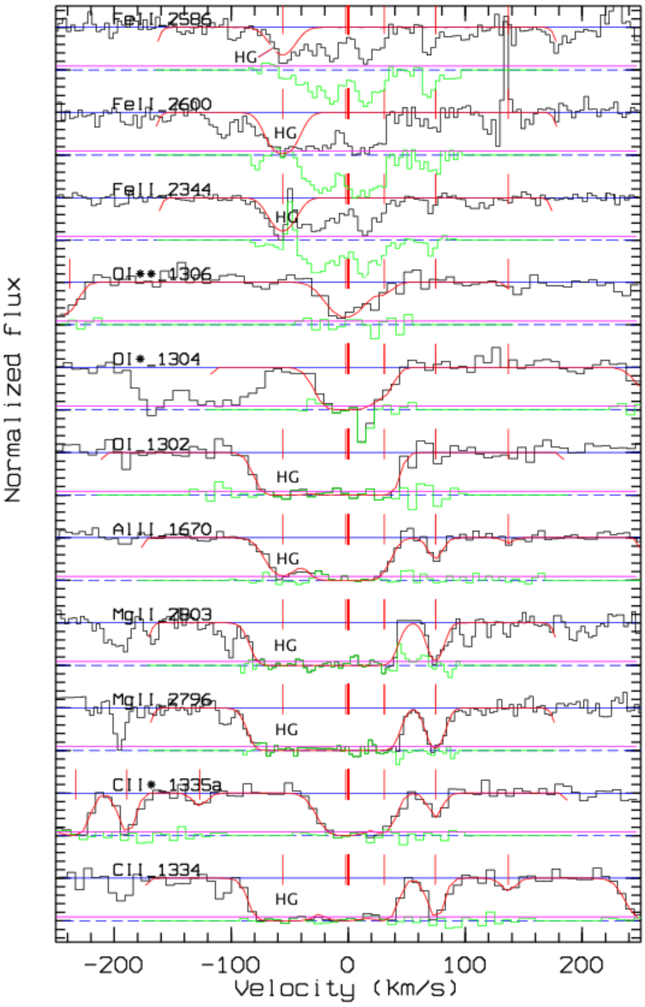

Figure 6.6 The (HG) component is present in all low-ionization lines. The column density determination for components (a) and (b) is difficult due to their blending with the (HG) one.

components were possible. In all cases, strong blending of the (a) and (b) components with the stronger (HG) one renders such an estimate difficult for these first two components. We observe the SiII (λ1190Å, λ1193Å, λ1260Å, λ1304Å, λ1526Å), CII (λ1334Å), MgII doublet (λ2796Å, λ2803Å), AlIIλ1670Å and the AlIII doublet (λ1854Å, λ1862Å). From Table 6.2 and Fig. 6.6 we can see that the host galaxy component (HG) is present in all low ionization lines (and absent in all the fine structure lines).

6.4.2.2 High-ionization lines

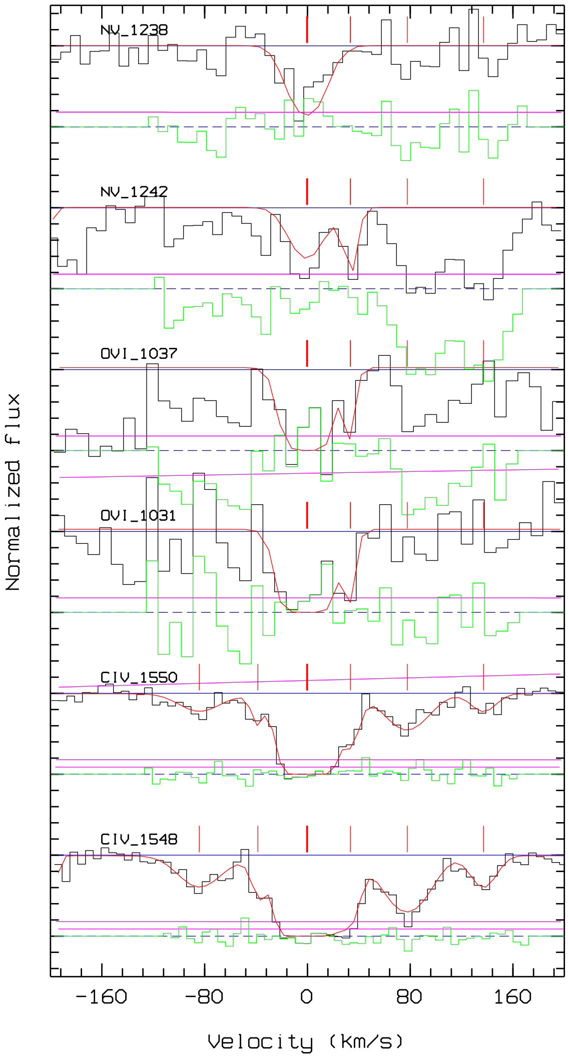

Figure 6.7 High-ionization absorption lines for the main system at z=2.1996.

Figure 6.7 shows all high-ionization lines (NV doublet, OVI doublet) identified together with CIV. Significant column densities of CIV and SiIV (see Fig. 6.5) are detected for all six components (a) to (f). NV and OVI are detected for components (c) and (d) only. Confusion with the Lyman-α forest made it difficult to search for faint OVI and NV lines for the other weaker components or to compute robust upper limits. No high-ionization lines were detected for component (HG).

6.4.2.3 The atoms MgI and OI

We detect significant amounts of both neutral Mg and O (see Table 6.2, Figs. 6.5 and 6.6). The first ionization energy of Mg lies below the 1 Ryd threshold, at 7.6 eV. This transition is not screened by H absorption and therefore Mg would be ionized easily by the strong radiation coming from the GRB. As a consequence, the presence of significant MgI implies large distances ($>$ 100 pc, Prochaska et al. 2006; Chen et al. 2007) of the gas clouds from the GRB site. MgI is detected for components (HG), (d) and (e) (see Table 6.2 and Fig. 6.5). These components are therefore likely to be associated with gas clouds which are little affected by the GRB radiation field. MgI of components (a) and (b) is difficult to constrain because of the blending with the HG component. MgI is not detected for component (c), which has very high-ionization and fine-structure lines, and for component (f). It should be noted that a line is present at 5.5 km s^{-1} from the position of MgI at the redshift of component (f), too big a shift for this line to be associated with the component.

6.4.2.4 Fine-structure lines

We detect several fine-structure lines associated with components (c), (d), (e) and (f) (see Figs. 6.5 and 6.6 for some examples). We identified the following lines arising from fine structure levels: SiII*λ1194 Å, SiII*λ1197 Å, SiII*λ1264 Å, SiII*λ1309 Å, SiII*λ1533 Å, CII*λ1335a Å, OI*λ1304 Å, OI**λ1306 Å. The redshifts of all these lines were fixed to those of the corresponding components in the CIV and SiIV systems.

We also detect three FeII fine-structure lines: FeII*λ1618Å, FeII*λ1621Å, FeII*λ2365Å. The redshift of both FeII and FeII fine-structure lines is shifted by about 20 km s^{-1} from that found for component (c) using the CIV and SiV systems (see Fig. 6.8 and Table 6.2). This suggests that additional structure is actually present in this absorption system. In the following we consider the FeII fine-structure lines as associated with component (c) without making further splitting in velocity. No FeII fine-structure transition is found for the other six components and, in particular, no fine-structure line was found at a redshift consistent with that of component (HG).

6.4.3 Fine-structure line excitation I: constraining the density of the gas

As shown in section 6.4.2.4, several fine-structure transitions have been found. Atomic fine-structure levels are caused by an energy split due to the interaction of the total electron spin and total angular momentum of the electrons. The transitions between these levels are not allowed, i.e. they cannot proceed through an electric dipole transition, and therefore

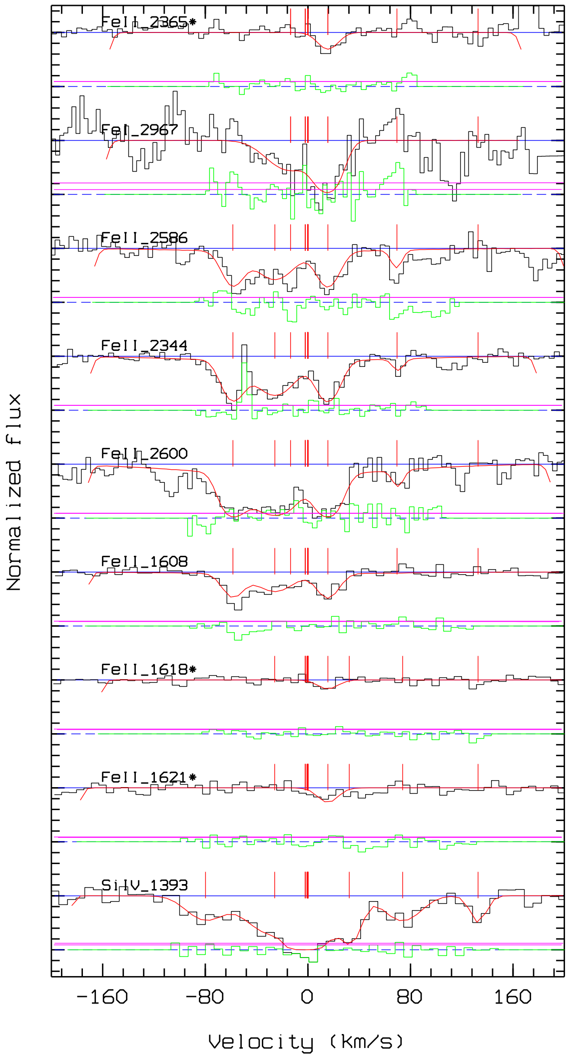

Figure 6.8 The UVES spectrum around some FeII and FeII* lines compared with SiIV $\lambda1393$. The zero of the velocity scale refers to the redshift of the host galaxy, $z = 2.1996$.

the corresponding transition probabilities are low. These levels can be populated (1) indirectly through excitation by ultraviolet photons, followed by fluorescence, (2) through collisions between the ion and other particles like free electrons, (3) and/or via direct photo-excitation by infrared photons. The first mechanism has been conclusively shown to be the preferred mechanism in two cases: GRB 060418 (Vreeswijk et al. 2007) and GRB 080319B (D'Elia et al. 2008). The latter mechanism is the less dominant one and we will not consider it. Whatever the case, the physical conditions of the interstellar medium can be probed through the detection of transitions from these energetically lower excited levels.

For GRB 050922C, fine-structure transitions are present in component (c), (d), (e) and

(f) (see Table 6.2). If the collisions with electrons are the dominant excitation mechanism, it is possible to put constraints on the electron density of the components where we find such transitions. A method to estimate the electron density is presented by Prochaska et al. (2006). We can compare our results on the SiII*/SiII and FeII*/FeII ratios with Fig. 9 of Prochaska et al. (2006), showing collisional excitation of the first excited state relative to the ground state for Si^+, Fe^+ and O^0. We can only use SiII and FeII because oxygen is saturated. From this comparison we find for SiII n_e in the range $(1.3-3)\times 10^2$ cm^{-3} for component (c), n_e in the range $(1.2-2)\times 10^2$ cm^{-3} for component (d), $n_e < 2\times 10^1$ cm^{-3} for component (e) and $n_e > 2\times 10^3$ cm^{-3} for component (f).

We have evaluated the electron density of component (c) also using the FeII transitions. This produces a result $n_e \sim (0.1-5)\times 10^5$ cm^{-3} inconsistent with the previous estimate. A possible reason for this inconsistency may be our simple description of a complex system (the excited transition lines are shifted by 20 km s^{-1} from the ground level lines).

6.4.4 Fine-structure line excitation II: constraining the radiation field

A competing mechanism that can be responsible for the presence of fine-structure levels is indirect UV pumping. If this is the dominant excitation mechanism, it is possible to constrain the GRB radiation field and the distance of the gas from the GRB. Prochaska et al. (2006), using the PopRatio code developed by Silva & Viegas (2001, 2002), analyzed the relation between the far UV radiation field intensity and the relative fraction of excited fine-structure states with respect to their ground levels (for OI, SiII and FeII, see their Figs. 7 and 8). In the following we make use of these figures to estimate the radiation field intensity from our column density data.

Using Fig. 7 of Prochaska et al. (2006), we find that our measured ratio log(SiII*/SiII) = -0.5 ± 0.1 for component (c) implies a radiation field intensity $G/G_0 = 2^{+3}_{-1}\times 10^5$ (90% confidence interval; $G_0 = 1.6\times 10^{-3}$ erg cm^{-2} s^{-1} is the Habing constant). We note that the SiII lines of this component are moderately saturated and therefore that additional systematic uncertainty may affect their column density determination. Fortunately, for this component we detect also FeII and FeII* transitions. The log(FeII*/FeII) is -0.5 ± 0.1, implying a radiation field intensity $G/G_0 = 6^{+4}_{-5}\times 10^6$, consistent with the SiII determination, within the rather large statistical errors. A similarly high value of G/G_0 is found for component (f) only, for which we find log(SiII*/SiII) = -0.5 ± 0.3, implying a radiation field intensity of $G/G_0 = 3^{+5}_{-0.4}\times 10^5$.

For component (d) and (e) the result is log(SiII*/SiII) = -0.8 ± 0.2 and -1.4 ± 0.4

respectively, implying radiation field intensities $G/G_0 = (8 \pm 1) \times 10^4$ and $G/G_0 = 1^{+0.7}_{-0.7} \times 10^4$, both significantly lower than for component (c). We note that the SiII lines of component (e) are certainly not saturated or blended with other components, while that of component (d) may be slightly blended and/or saturated.

The “smoking gun” of the UV pumping mechanism is time variability of fine structure lines (Vreeswijk et al. 2007; D’Elia et al. 2008). Unfortunately we have only one single observation of the GRB 050922C and therefore we cannot look for line variations. We note that components (c) and (f) experience the highest radiation field, which is relevant to the discussion of the following section.

6.4.5 Distances from the burst region

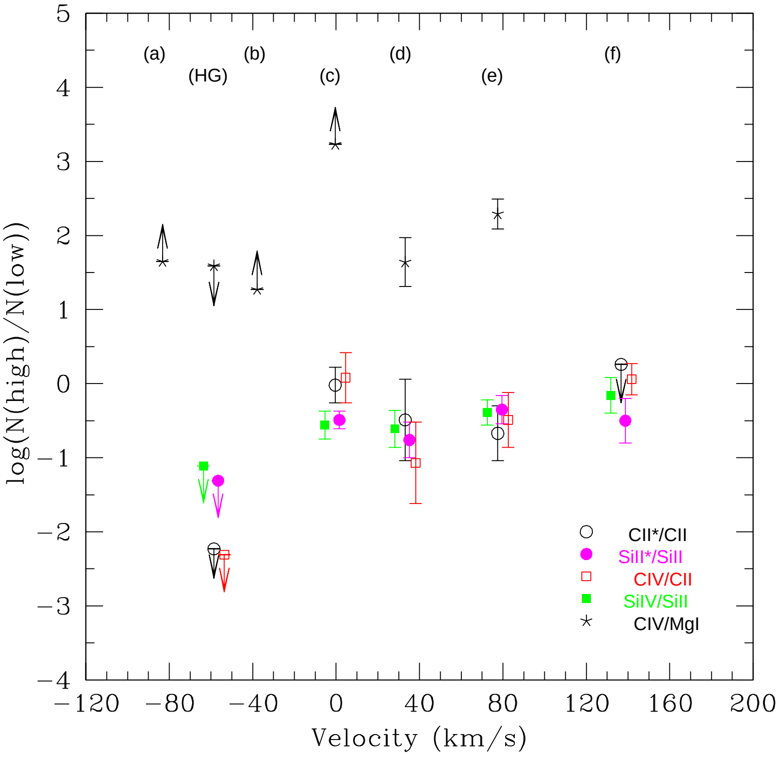

Figure 6.9 Several high- to low-ionization ion column densities ratios for the seven components of the $z = 2.1996$ system as a function of the velocity shift with respect to the redshift of the host galaxy. See text for details.

We plot in Fig 6.9 high- to low-ionization line ratios and fine structure to ground state line ratios for the seven components of the $z = 2.1996$ system. The different behaviour of component (HG) with respect to all the others is evident from this plot. The most natural explanation for this is to assume that the various components do not belong to the same physical region in the host galaxy. The strength of the high ionization lines and of the fine-structure lines, the absence of MgI absorption, the analysis of the ratio of the excited levels to ground levels suggest that components (c) and (f) are closer to the GRB site than the other components. To quantify better this suggestion we perform detailed time evolving photoionization calculations using the GRB light-curve to estimate the photoionization fractions (assuming an optically thin medium). We use the code initially developed by Nicastro et al. (1999) and updated by Krongold et al. (2008, in prep.). We assume a constant density profile throughout the cloud, and a plane parallel geometry. We studied gas densities between $10^2\,\mathrm{cm}^{-3}$ and $10^8\,\mathrm{cm}^{-3}$ (10^2, 10^4, 10^6 and $10^8\,\mathrm{cm}^{-3}$). The ionizing continuum was assumed to be a power law, $F(E) = E^{-\Gamma}$ photons $\mathrm{cm}^{-2}\ \mathrm{s}^{-1}$, with cutoffs at low and high energy. Our calculations require that component (c) is closer than ~ 200 pc to the GRB site, to reproduce the observed, quite large abundances of SiIV and CIV and the presence of OVI and NV. This is consistent with the results by Prochaska et al. (2008) who suggest that the presence of NV implies a distance of ~ 10 pc from the GRB site.

Also the presence of neutral elements in the spectra of GRB afterglows can place strong constraints on the distance of the gas from the GRB. For example, Prochaska et al. (2006) suggest that components showing MgI absorption should be located at distances greater than 100 pc from the GRB site. In the afterglow spectra of GRB 050922C we detect neutral MgI for three components: (HG), (d) and (e), see Fig. 6.5. In particular, the presence of MgI absorption, absence of high-ionization lines and excited transitions, suggest that the (HG) component is located further away from the GRB site, in a region not strongly affected by the GRB radiation field. Our time evolving photoionization calculations require a distance of at least 700 pc from the GRB site for this component. Components (d) and (e) do show fine-structure transitions. If the dominant excitation mechanism is UV pumping from the GRB radiation field, this suggests a distance ≤ 1 kpc from the GRB site (Prochaska et al. 2007). Our time evolving photoionization calculations require a distance $\gtrsim 300$ pc for both components, to be consistent with the observed C and Si line ratios. Component (d) exhibits also high-ionization absorption (NV, PV, OVI). The presence of these highly ionized ions, along with the presence of low ionized ones (O I, Mg I, Fe II), can be explained at a distance of ~ 300 pc from the GRB site if the density of this cloud is high enough, i.e. $> 10^5\,\mathrm{cm}^{-3}$.

For components (a) and (b) we do not have information on the abundance of neutral elements, because these transitions occur at wavelengths affected by the absorption of component (HG). The detection of CIV implies a distance to the GRB site closer than $\sim 700\,\mathrm{pc}$ for both components (a) and (b).

This scenario might be not longer true in the case of a structured jet like the one introduced in Chapter 3, and used by Starling et al. (2005b) to explain the possibility to observe neutral, low- and high- ionization lines in the high velocity system of GRB 021004. These authors consider a structured afterglow with a narrow jet and one slower, much wider jet of material which are both visible to us. The wider jet will ionize the material in its path to a much lesser degree than the inner jet. The fact that the afterglow has a surface area implies that there are several lines of sight along which the light can reach the observer. Therefore, for the same gas cloud, we would observe sightlines with different ionization degrees.

6.4.6 Metallicity of the main system

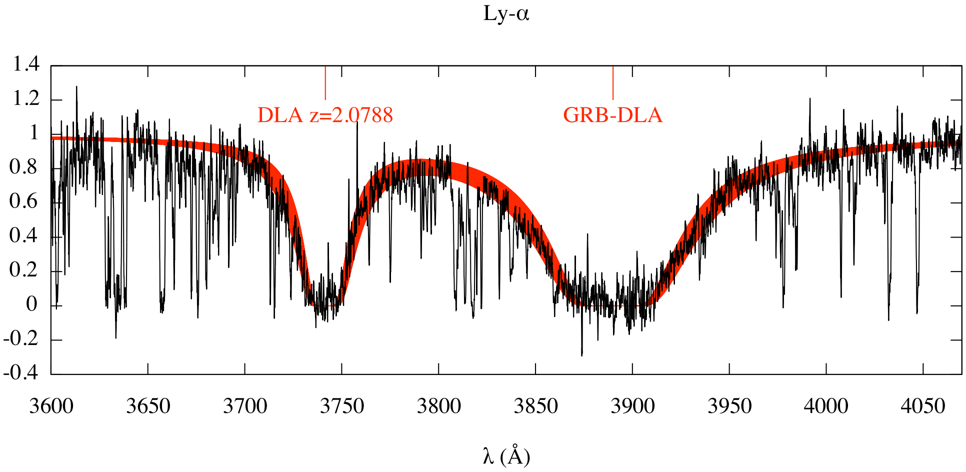

Figure 6.10 DLA associated with the GRB at $z = 2.1996$ (this system has been fitted together with the intervening Sub-damped Ly-α absorption at z=2.0778, see Sect. 6.5.6). The red area corresponds to the fit result including the column density error range.

Figure 6.10 shows the Ly-α absorption feature associated to GRB 050922C. Hydrogen absorption results in very broad lines with damped wings, reaching well beyond the velocity range of the heavier ions. Therefore it is clearly impossible to separate the seven components identified from the analysis of CIV and SiII, and we can only estimate the metallicity of the host galaxy in terms of the ratio [X/H] between the total absorption column of the X element with respect to that of hydrogen.

The hydrogen column density is $\log N_{\mathrm{HI}} = 21.5 \pm 0.1$ cm^{-2}, similar to the average value found by Jakobsson et al. (2006a) for a sample of *Swift* GRBs.

Since the OI lines are saturated we calculate the metallicity using Si. Its total column density in log scale is 15.3 ± 0.5 and therefore we have [Si/H]$= -1.7 \pm 0.5$. It should be considered, however, that we do not know how much hydrogen has been ionized by the GRB, even if it is probable that it is not significant compared to the high value inferred from the DLA Ly-α absorption. The total iron column density is of 14.9 ± 0.4, for a iron abundance of [Fe/H]$= -2.3 \pm 0.4$. This value compared to the silicon abundance can suggest dust depletion of iron, but the large error bars let them be statistically consistent.

6.4.7 Summary

Using the VLT high resolution spectrometer UVES, we have obtained a high signal to noise (~ 20) spectrum of the optical afterglow of GRB 050922C. The system associated to the GRB is identified at $z = 2.1996$. The spectrum shows that the ISM of this galaxy is complex, with at least seven components contributing to the main absorption system showing high- and low-ionization lines, fine-structure lines and neutral element absorption lines, thus suggesting wide ranges of distances to the GRB site and physical properties of the absorbing clouds. The analysis of the transitions and column densities found in each component allow us to put quantitative constraints on the distance of the absorbing clouds to the GRB site. In particular, we find that component (c) is likely to be the closest component, with a distance < 200 pc. Component HG is likely to be farthest component, with a distance > 700 pc.

We calculated the average metallicity of the GRB host galaxy by adding the column densities of all components. This turned out to be about 1/100 solar, even for an element like Silicon, which should not be strongly affected by dust depletion. This value is roughly consistent with what is found by absorption spectroscopy in other z=2-4 GRBs (Savaglio 2006; Prochaska et al. 2008) but is lower than the average found by emission line spectroscopy at z< 1 (Savaglio 2006; Savaglio et al. 2008).

The element transitions detected, the complexity of the components and the column densities measured are similar to the other high redshift GRB high resolution spectra present in the literature. We have no evidence of the high velocity components, suggested to be the signature of a WR wind, reported for GRB 021004 (Mirabal et al. 2003; Fiore et al. 2005; Starling et al. 2005b), GRB 030226 (Klose et al. 2004) and GRB 050505 (Berger et al. 2006).

6.5 Statistics and characteristics of Mg II absorbers along GRB lines of sight observed with VLT-UVES

As explained at the beginning of this Section, since GRBs can be detected up to very high redshifts the afterglow spectra can be used to study the properties and evolution of galaxies and the IGM, similarly to what is traditionally done using QSOs.

Even if the number of the available GRB lines of sight (l.o.s.) is much lower than those of QSOs, it is interesting to compare the information obtained using GRBs to what is known from the study of QSO l.o.s.. In particular, considering 14 GRB l.o.s. (for a Mg IIλ_{2796} total redshift path $\Delta z = 15.5, \langle z \rangle = 1.1$[3]), Prochter et al. (2006b) found that the number of strong intervening Mg II absorbers (rest equivalent width $W_r > 1\,\text{Å}$) is more than 4 times larger along GRB l.o.s. than what is expected for QSOs over the same path length with similar average redshift. This result has been confirmed by Sudilovsky et al. (2007). Dust extinction bias for QSO l.o.s., gravitational lensing, contamination from high-velocity systems local to the GRB and difference of beam sizes are among the possible causes of this discrepancy, but no convincing explanation has been found up to date (Porciani et al. 2007). Similar studies have been performed on the C IV intervening systems (Sudilovsky et al. 2007; Tejos et al. 2007). Their results are in agreement with QSO statistics.

A possible source of uncertainty is the inhomogeneity of the l.o.s. sample that can be observed with different telescopes and at different spectral resolution. We therefore decided to investigate the excess of strong Mg II absorbers using an homogeneous sample of high resolution VLT/UVES GRB spectra, doubling the number of l.o.s. compared to Sudilovsky et al. (2007). With these data, and thanks to their high quality, we also can extend the search of systems to lower equivalent widths and derive the properties of the absorbing systems.

A detailed explanation of the above-mentioned causes for the excess of strong Mg II absorbers is beyond the scope of this Chapter. My purpose is to check which of these hypothesis may be favoured or discarded by the observational results, as well as to try to

---

[3] For each spectrum, the redshift path δz for a given line is defined as the sum of the redshift ranges (associated with that line) for which the equivalent width detection limit of the spectrum (see page 150) is lower than the equivalent width limit chosen for the survey. The total redshift path Δz is the sum of the single δz. Depending from the GRB or QSO redshift, different distances in the Universe are sampled. It can be therefore important to specify also the average redshift $\langle z \rangle$ associated to the total redshift path. Instead of the redshift path, the comoving distance can also be used: this imply the choice of a cosmological model.

retrieve more information on these systems, and more generally on GRB l.o.s., to have a more complete picture.

6.5.1 Data

We consider here two samples. The first one is constituted by GRB lines of sight observed with UVES with sufficient signal-to-noise ratio. It is used to detect absorption systems with equivalent widths down to 0.1 Å and to derive physical properties of strong Mg II systems in order to reveal their nature. The second sample, enlarging the first one, is aimed at increasing the redshift path over which strong Mg II systems are observed and includes observations from the literature.

Our first sample (hereafter the *UVES sample*) includes ten GRB afterglows with available follow-up UVES high-resolution optical spectroscopy as of June 2008: GRB 021004, GRB 050730, GRB 050820A, GRB 050922C, GRB 060418, GRB 060607A, GRB 071031, GRB 080310, GRB 080319B and GRB 080413A. All GRBs were detected by the *Swift* satellite (Gehrels et al. 2004), with the exception of GRB 021004, which was detected by the *High-Energy Transient Explorer (SwiftIN-2)* satellite (Ricker et al. 2003).

Rapid-Response Mode (RRM) UVES observations began for each GRB afterglow with the minimum possible time delay: in some cases a sub-ten minute response was achieved. The only exception is GRB 021004, which occurred before the RRM was implemented and was observed as a ToO. A log of the observations is given in Table 6.3.

The observations were performed with a 1.0" slit and 2×2 binning providing a spectral resolution of $R \approx 43\,000$ (FWHM ~ 7 km s^{-1}) for a $\approx$2 km s^{-1} pixel size[4]. The UVES data were reduced by our collaborators with a customized version of the MIDAS reduction pipeline (Ballester et al. 2006). The individual scientific exposures were co-added and rebinned in the heliocentric rest frame.

Although the *UVES sample* has a smaller number of l.o.s. compared to the sample used by Prochter et al. (2006b) (10 l.o.s. instead of 14), the redshift path of the two samples is similar ($\Delta z = 13.9$ and 15.5 for the UVES and Prochter's samples respectively). Compared to previous studies, the *UVES sample* has 6 new l.o.s. (050922C, 060607A, 071031, 080310, 080319B and 080413A) corresponding to $\Delta z = 9.4$. Therefore more than half of the redshift path is new. In addition, the UVES sample is homogeneous (same resolution, same instrument, similar S/N). It also doubles the sample used by Sudilovsky

---

[4] Though the nominal spectral resolution of UVES in this mode is 43 000, we find that in some cases a higher resolution, up to ≈50 000, is achieved in practice, due to variations in the seeing conditions.

Table 6.3 GRB sample and log of UVES observations.

GRB (yymmdd)	UT[a] *Swift*	δt [b] (hh:mm)	t_{total} [c] (h)	ESO Program ID	z_{GRB}
021004	12:06:13	13:31	2.0	070.A-0599[d]	2.3295
050730	19:58:23	04:09	1.7	075.A-0603	3.9687
050820A	06:34:53	00:22	1.7	075.A-0385	2.6147
050922C	19:55:50	03:33	1.7	075.A-0603	2.1996
060418	03:06:08	00:10	2.6	077.D-0661	1.4900
060607A	05:12:13	00:08	3.3	077.D-0661	3.0748
071031	01:06:36	00:09	2.6	080.D-0526	2.6922
080310	08:37:58	00:13	1.3	080.D-0526	2.4272
080319B	06:12:49	00:09	2.1	080.D-0526[e]	0.9378
080413A	02:54:19	03:42	2.3	081.A-0856	2.4346

[a]: UT of trigger by the BAT instrument on-board *Swift*. Exception: GRB 020104, detected by *WXM* on-board *SwiftIN-2*.

[b]: Time delay between satellite trigger and start of the first UVES exposure.

[c]: Total UVES exposure time over all setups.

[d]: Also 070.D-0523.

[e]: Also 080.A-0398.

et al. (2007) for the Mg II statistics. Their l.o.s. are part of our sample.

The second sample we consider (the *overall sample*) is formed adding observations from the literature (see Tab. 6.6) to the *UVES sample* (see Sect. 6.5.2.2). The sample gathers observations of 26 GRBs for $\Delta z = 31.53$. It therefore doubles the statistics of Prochter et al. (2006b).

In the following we use solar metallicities from Morton (2003).

6.5.2 Mg II absorbers

6.5.2.1 The UVES sample

For each line of sight we searched by eye the spectrum for Mg II absorbers outside the Ly-α forest considering all Mg II components within 500 km s^{-1} as a single system. The systems are identified when the two absorption lines of the doublet are detected with an equivalent width that is larger than the 3 σ equivalent width detection limit. Table 6.4 summarizes the results. Columns 1 to 8 give, respectively, the name of GRB, its redshift, the redshift paths for $W_{\rm r,lim} > 0.3$ and 1 Å (see Eq. 6.14 and following description), the redshift of the Mg II absorber, the rest equivalent width of the Mg $\rm II_{\lambda2796}$ transition and the velocity difference relative to the GRB redshift. The last column gives comments on peculiar systems if need be. When a line is blended either with a sky feature or an absorption from another system, we fit at the same time the Mg II doublet and the intervening absorption. The sky lines at the position of an absorption are obtained from other spectra where other absorption features are not present. This helps decontaminating the absorption. The values obtained are reported into brackets.

Table 6.4 Characteristics of the Mg II absorbers in the *UVES sample*.

GRB	$z_{\rm GRB}$	$\Delta z_{\rm W>0.3}$	$\Delta z_{\rm W>1}$	$z_{\rm abs}$	$W_{\rm r}(2796)$(Å)	$v_{\rm ej}$ (km/s)	Remarks
021004	2.3295	1.675	1.787	1.3800	1.637 ± 0.020	~ 97000	
				1.6026	1.407 ± 0.024	~ 72000	
050730	3.9687	0.718	1.243	1.7732	0.927 ± 0.030	~ 157000	
				2.2531	$< 0.783\,(0.650)$	~ 120000	sky contamination (subtracted)
050820A	2.6147	1.655	1.845	0.6896	0.089 ± 0.007	~ 192000	
				0.6915	2.874 ± 0.007	~ 192000	
				1.4288	1.323 ± 0.023	~ 113000	
				1.6204	0.277 ± 0.024	~ 93000	
				2.3598	$< 0.424\,(0.306)$	~ 22000	bad S/N and contribution by $\rm FeII_{2600}$ at $z = 2.6147$ (subtracted)
050922C	2.1996	1.554	1.701	0.6369	0.179 ± 0.018	~ 175000	
				1.1076	0.677 ± 0.029	~ 118000	
				1.5670	$< 0.102\,(0.08)$	~ 62000	sky contamination (subtracted)
				2.0778	> 1 Å?	~ 12000	not covered by the spectrum
060418	1.4900	1.242	1.265	0.6026	1.293 ± 0.010	~ 124000	
				0.6559	1.033 ± 0.006	~ 116000	
				1.1070	1.844 ± 0.014	~ 50000	
060607A	3.0748	1.529	1.660	1.5103	0.204 ± 0.011	~ 135000	
				1.8033	1.854 ± 0.006	~ 107000	
				2.2783	0.343 ± 0.058	~ 64000	
071031	2.6922	1.509	1.789	1.0743	0.330 ± 0.016	~ 156000	
				1.6419	0.692 ± 0.014	~ 97000	
				1.9520	0.804 ± 0.016	~ 66000	
080310	2.4272	1.786	1.841	1.1788	0.047 ± 0.024	~ 127000	
				1.6711	0.421 ± 0.012	~ 73000	
				2.0685	?	~ 33000	not covered by the spectrum
080319B	0.9378	0.790	0.790	0.5308	0.614 ± 0.001	~ 69000	
				0.5662	0.083 ± 0.003	~ 63000	
				0.7154	1.482 ± 0.001	~ 36000	
				0.7608	0.108 ± 0.002	~ 29000	
080413A	2.4346	0.814	1.650	2.1210	0.768 ± 0.259	~ 29000	

The rest equivalent width detection limit (at any given statistical level) is calculated at each redshift along the spectrum using the following equation (Tytler & Fan 1994):

$$W_{\rm r,lim} \simeq \frac{U M_{\rm L}^{0.5}}{S/N} \Delta\lambda \,, \tag{6.14}$$

where $M_{\rm L}$ is the number of pixels the line is expected to cover, U is the number of rms-intervals defining the statistical significance of the detection limit, S/N is the signal-to-noise ratio at the corresponding wavelength and $\Delta\lambda$ is the FWHM of the spectrum. We will apply this detection limit to the Mg II$_{\lambda 2796}$ transition. Using $M_{\rm L} = 5$ and $U = 6$ (so that both transitions of the Mg II doublet are detected at more than 3 σ, since the oscillator strength of the λ2803 transition of the doublet is about a half of that of the λ2796 transition), it can be seen that for a typical signal-to-noise ratio of S/N $\sim$ 10 and a typical FWHM of $\Delta\lambda = 0.13$ Å ($R = 43000$ and $\lambda = 5600$ Å), the formula gives a detection limit of ~0.17 Å which is much smaller than the equivalent width limit we will use in our statistical studies below (1 and 0.3 Å).

We then can compute the redshift path over which a line of a given equivalent width would be detected in our data. Prochter et al. (2006b) limited their analysis to the redshift range 0.359 – 2 and compared their results to those of the SDSS QSO survey reported by Prochter et al. (2006a). However, the SDSS QSO survey extends to $z_{\rm max} \sim 2.3$ (Nestor et al. 2005) so that there is no reason to limit our analysis to $z = 2$ and we will use the same redshift limits as Nestor et al. (2005), $z_{\rm start} = 0.366$ and $z_{\rm max} = 2.27$ instead. As in all QSO surveys and following Prochter et al. (2006a), we will exclude along each l.o.s. the redshift range within a velocity of 3000 km s^{-1} from the GRB redshift in order to avoid contamination from any possible system ejected by the GRB system and therefore associated to it and not properly intervening.

Table 6.5 Number of Mg II systems and redshift path

$W_{\rm r}$	>0.3 Å (*all*)	>1 Å (*strong*)	$0.3 < W_{\rm r} < 1$ Å (*weak*)
$\langle z_{\rm abs}\rangle$	1.34	1.11	1.57
Redshift path	12.5	13.9	12.5
Number of Mg II systems (GRBs: UVES sample)	18 (± 4.2)	9 (±3)	9 (±3)
$n_{\rm exp}^{\rm MgII}$(QSOs: Nestor et al. 2005)	10.54 (±3.25)	4.81 (±2.19)	6.42 (±2.53)
$n_{\rm exp}^{\rm MgII}$(QSOs: Prochter et al. 2006)		3.99 (±2.00)	

Table 6.5 gives the mean redshift, $\langle z_{\rm abs}\rangle$, the total redshift paths and the number of systems detected in our sample over these redshift paths for different $W_{\rm r}$ limits or ranges: $W_r > 0.3$ Å (*'all systems'*) $W_r > 1.0$ Å (*'strong systems'*) and $0.3 \leq W_r \leq 1.0$ Å (*'weak systems'*). The total redshift paths for the *all* and *strong* samples are $\Delta z = 12.49$ and 13.92,

respectively, for 18 and 9 systems detected, corresponding to redshift number densities of $\partial n/\partial z = 1.44 \pm 0.35$, 0.65 ± 0.22 for *all*, *strong* Mg II systems, respectively.

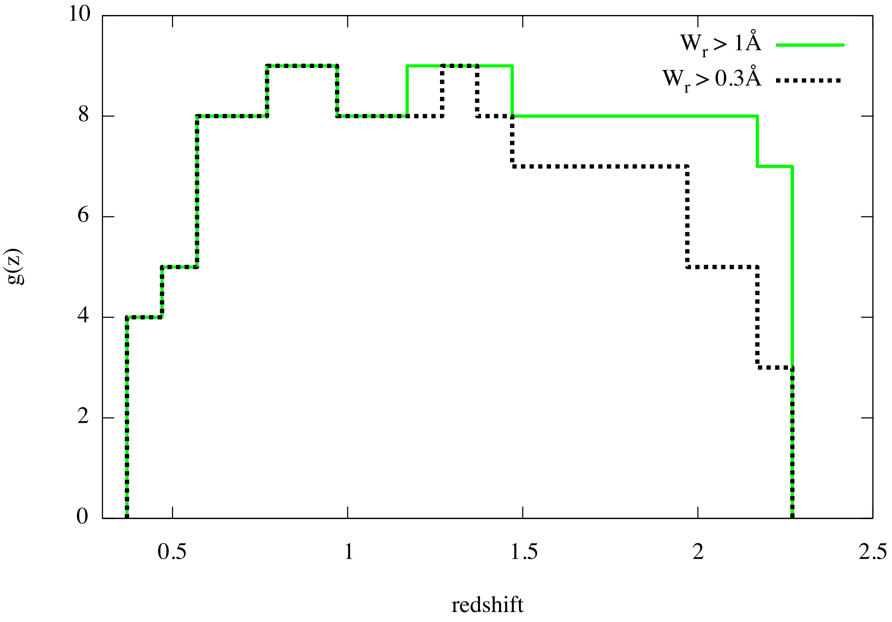

Figure 6.11 Redshift path density $g(z)$ of the *UVES sample* for $W_r > 0.3$ Å (black dashed line) and $W_r > 1.0$ Å (green line).

In Table 6.5 is also reported the number of Mg II absorbers that would be expected along lines of sight toward QSOs over the same redshift path, $n_{\rm exp}^{\rm MgII}$, for two QSO studies. To calculate these numbers, we determine the redshift path density of the UVES GRB sample, $g(z)$, defined as the number of l.o.s. along which a Mg II doublet of redshift z and with a rest equivalent width $W_0 \geq W_{lim}$ could have been discovered (see Fig. 6.11). We combine $g(z)$ with the number density, $\partial n/\partial z$, of QSO Mg II absorbers as observed by Nestor et al. (2005) and Prochter et al. (2006a) (for the strong systems only) in the SDSS survey:

$$n_{\rm exp}^{\rm MgII} = \int_{z_{\rm start}}^{z_{\rm end}} g(z) \frac{\partial n}{\partial z}\, dz. \qquad (6.15)$$

Both Nestor et al. (2005) and Prochter et al. (2006a) showed that the traditional parametrization of $\partial n/\partial z$ as a simple power law $n_0(1+z)^\gamma$ is not a good fit to the SDSS data. Therefore we will use their empirical fits to the redshift number density. Nestor et al. (2005) give

$$\partial n/\partial z = \int \frac{dn}{dW_{\rm r}}(z) dW = \int \frac{n^*(z)}{W^*(z)} e^{-W_r/W^*} dW, \qquad (6.16)$$

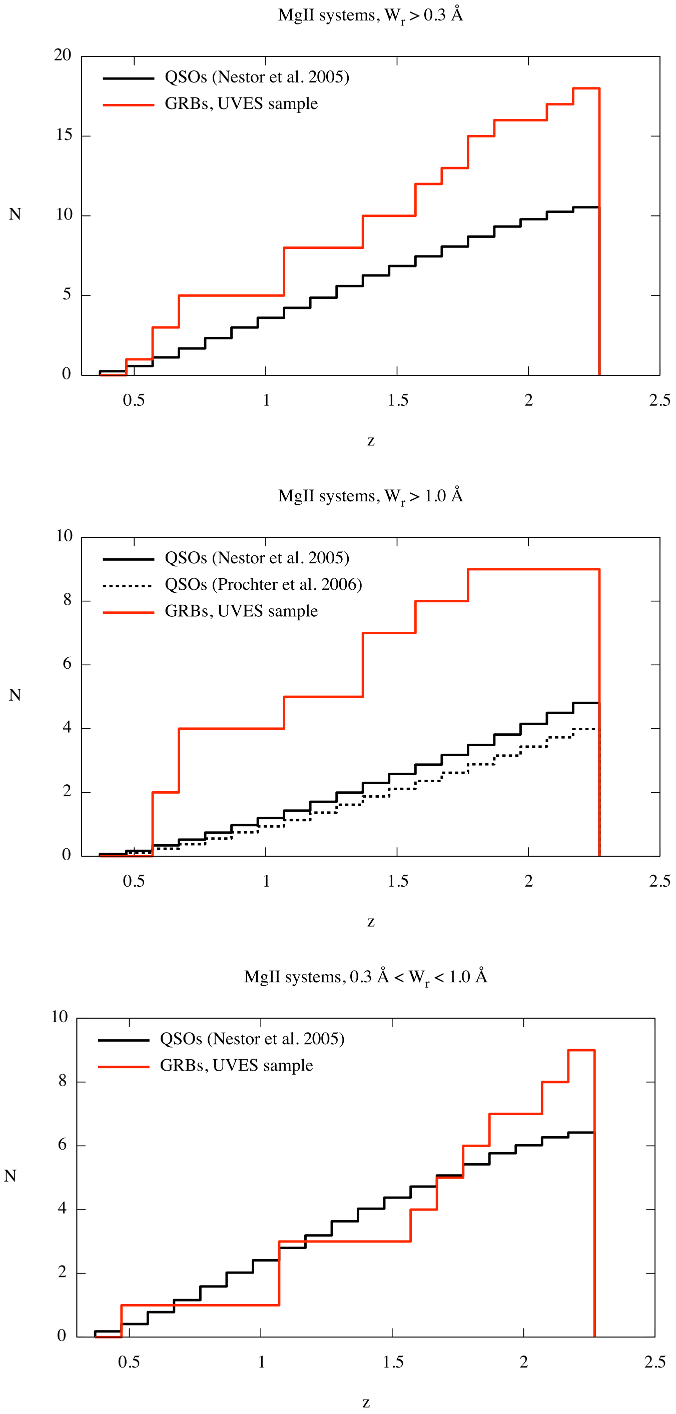

Figure 6.12 Comparison between the cumulative distribution of strong Mg II systems detected along the UVES GRB l.o.s. (red) and the one expected along QSO l.o.s. following Eq. 6.16 (black solid) or Eq. 6.17 (black dashed), for: top panel: *all*, middle panel: *strong*, bottom panel: *weak* systems.

where both n^* and W^* vary with redshift as power laws: $n^* = 1.001 \pm 0.132(1+z)^{0.226\pm0.170}$, $W^* = 0.443 \pm 0.032(1+z)^{0.634\pm0.097}$. Prochter et al. (2006b) derive for the strong MgII systems statistics only:

$$\partial n/\partial z = -0.026 + 0.374z - 0.145z^2 + 0.026z^3 \tag{6.17}$$

The results of the calculations for the different W_r ranges ($W_r > 0.3$ Å, $W_r > 1.0$ Å and $0.3 \leq W_r \leq 1.0$ Å) are shown in Fig. 6.12 and reported in Table 6.5. Errors are taken poissonian and scaled as $\sqrt{n_\mathrm{exp}^\mathrm{MgII}}$.

As a verification, we note from Fig. 13 of Nestor et al. (2005) that the number density, $\partial n/\partial z$, of $W_\mathrm{r} > 0.3$ Å systems is almost independent of the redshift. Multiplying the $\partial n/\partial z = 0.783$ value reported there by the UVES *'all systems'* $\Delta z = 12.49$ we obtain an expected total number of 9.78, consistent with the values reported in Table 6.5 for systems along QSO l.o.s. (e.g. 10.54).

The excess of *all* and *strong* Mg II systems along GRB l.o.s. compared to QSO l.o.s. is significant at more than 2σ (see Table 6.5), but this excess is more than a factor of ~ 2 lower than what was found by Prochter et al. (2006b). The number of weak systems is consistent within $\sim 1\sigma$ to that expected for QSO l.o.s..

6.5.2.2 The overall sample

In order to increase the statistics of strong Mg II systems, we added to the *UVES sample* both high and low resolution GRB afterglow spectra published in the literature. The total sample is composed of 26 l.o.s. (see Table 6.6 for details). Since this sample includes many low resolution spectra, we study the statistics of strong ($W_\mathrm{r} > 1$ Å) Mg II absorbers only, using the same redshift limits as in the previous Section. Three l.o.s. of this sample (GRB 991216, GRB 000926 and GRB 030429) were not used by Prochter et al. (2006b) even if available because the spectral resolution of the corresponding spectra was FWHM > 500 km s^{-1}. This limit corresponds to the spectral resolution needed to resolve the Mg II doublet. However, the low resolution does not prevent detection of strong systems, even though the doublet is blended. In addition, the total equivalent width of the doublets detected along the GRB 991216 and GRB 030429 l.o.s. is larger than 2 Å so that we are confident that $W_{\mathrm{r},2796}$ is larger than 1 Å. In any case, as detection of Mg II systems is more difficult at lower resolution, including these lines of sight will only minimize their number density.

The total number of strong Mg II systems is $N = 22$ and the redshift path is $\Delta z = 31.53$.

Table 6.6 GRB l.o.s. available from the literature.

GRB	$z_{\rm GRB}$	$z_{\rm start}$	$z_{\rm end}$	$z_{\rm abs}$	$W_{\rm r}(2796)$ (Å)	$\Delta v_{\rm ej}$ (km/s)	Reference [†]
991216	1.022	0.366	1.002	0.770	4.0 ± 0.8^a	~ 40000	3
				0.803	6.1 ± 0.7^a	~ 34000	
000926	2.038	0.616	2.008				1
010222	1.477	0.430	1.452	0.927	1.00 ± 0.14	~ 74000	2
				1.156	2.49 ± 0.08	~ 41000	
011211	2.142	0.366	1.932				3
020405	0.695	0.366	0.678	0.472	1.1 ± 0.3	~ 42000	4
020813	1.255	0.366	1.232	1.224	1.67 ± 0.02	~ 4000	5
030226	1.986	0.366	1.956				6
030323	3.372	0.824	1.646				7
030328	1.522	0.366	1.497				14
030429	2.66	0.620	1.861	0.8418	3.3 ± 0.4^a	~ 179000	15
050505	4.275	1.414	2.27	1.695	1.98	~ 176000	8
				2.265	1.74	~ 134000	
050908	3.35	0.814	2.27	1.548	1.336 ± 0.107	~ 147000	9
051111	1.55	0.488	1.524	1.190	1.599 ± 0.007	~ 45000	9,13
060206	4.048	1.210	2.27	2.26	1.6	~ 123000	10
060526	3.221	0.836	2.27				11
071003	1.604	0.366	1.578	0.372	2.48 ± 0.20	~ 170000	12

[†] 1: Castro et al. (2003); 2: Mirabal et al. (2002); 3: Vreeswijk et al. (2006); 4: Masetti et al. (2003); 5: Barth et al. (2003); 6: Klose et al. (2004); 7: Vreeswijk et al. (2004); 8: Berger et al. (2006); 9: Prochter et al. (2006b); 10: Chen et al. (2008); 11: Thoene et al. (2008); 12: Perley et al. (2008b); 13: Hao et al. (2007); 14: Maiorano et al. (2006); 15: Jakobsson et al. (2004).

[a] : The $W_{\rm r}$ values refer to both lines of the MgII doublet.

This leads to a number density $\partial n/\partial z = 0.70 \pm 0.15$. We use the $g(z)$ function of this enlarged sample to compute the total number of strong systems expected for a similar QSO sample following the same method as used in Sect. 6.5.2.1. We find $n = 10.41 \pm 3.23$ and $n = 8.62 \pm 2.94$, using Eq. 6.16, and 6.17, respectively, that is 2.1 ± 0.6 and 2.6 ± 0.6 times less than the number found along the GRB l.o.s. (see Fig. 6.13).

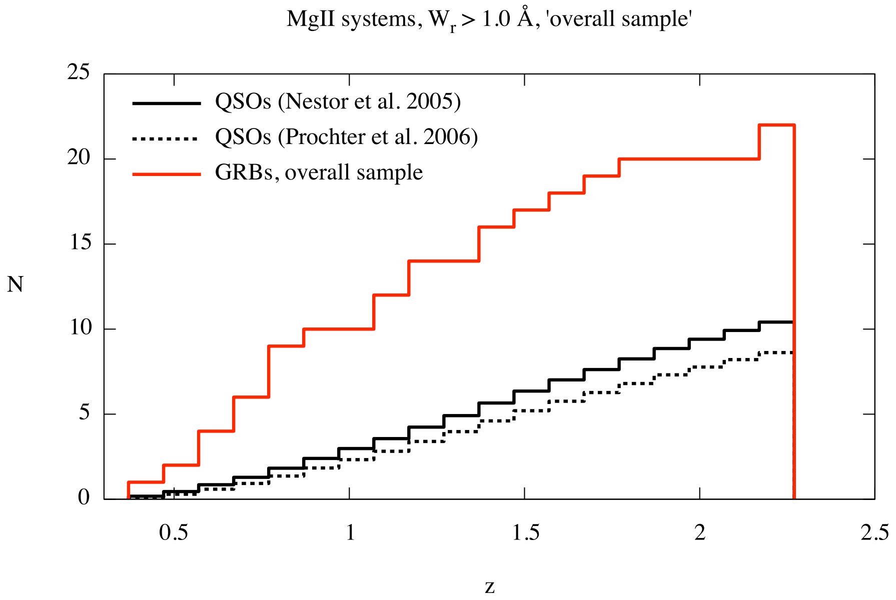

Figure 6.13 Comparison between the cumulative distribution of strong Mg II systems in the *overall sample* of GRB l.o.s. (red) and the one expected along QSO l.o.s. following Eq. 6.16 (black solid) or Eq. 6.17 (black dashed).

The excess of strong Mg II systems along GRB lines of sight for this enlarged sample is confirmed and statistically significant (more than 3σ). The excess found is higher than for the *UVES sample* but still a factor of ~ 2 lower that what previously reported by Prochter et al. (2006b) on a sample with a smaller redshift path. The redshift path of this sample is twice as large as that used by Prochter et al. (2006b).

6.5.3 Number density evolution

We divided both the UVES and the *overall sample* in three redshift bins ($0.37 < z < 1.00$, $1.00 < z < 1.63$, $1.63 < z < 2.27$) and calculated $\partial n/\partial z$ for each bin. Fig. 6.14 shows the number of systems per redshift bin scaled to the total number of systems expected along QSO l.o.s. and compared to the QSO number density evolution (Nestor et al. 2005). The function describing the QSO number density evolution has been obtained by using Eq. 6.16 and multiplying the $\partial n/\partial z$ by the average $g(z)$ value of the corresponding W_{lim}, to simplify the functional form. While the total number of systems and the number of weak systems have a comparable redshift evolution in GRB and QSO l.o.s., the strong systems appear to have a different evolution in GRBs. An excess of strong systems is seen in GRBs in the first two bins. We performed a KS test for each of the three cases to assess

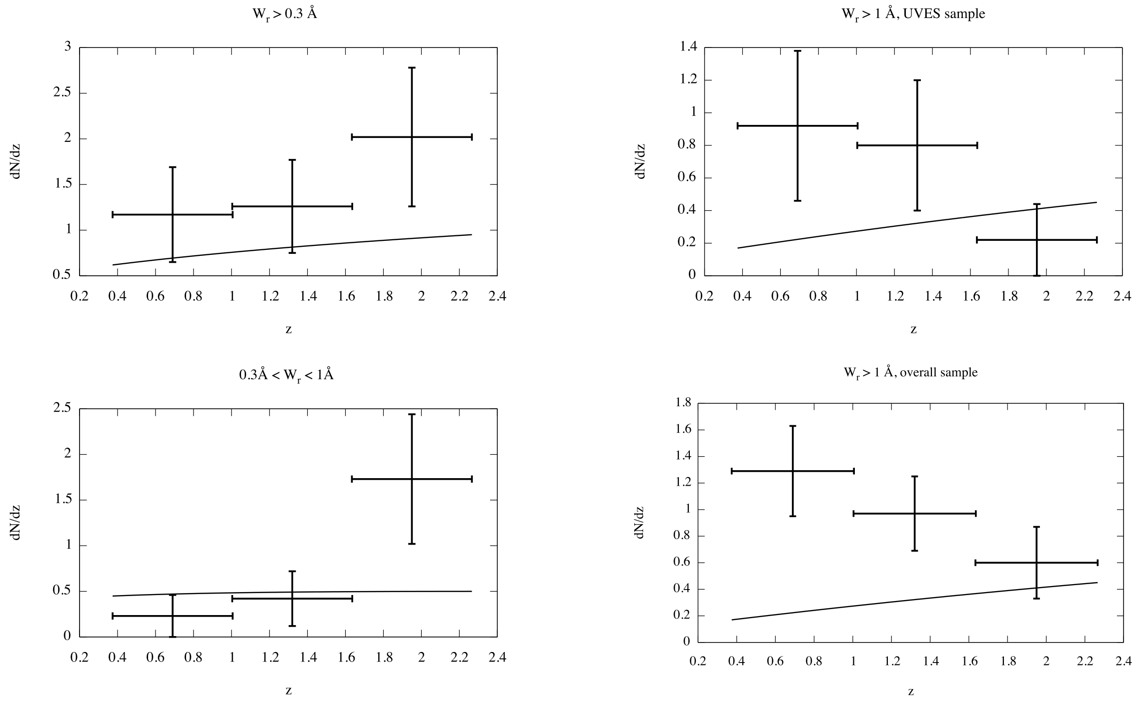

Figure 6.14 Number density evolution of Mg II systems detected along GRB l.o.s., scaled to the total number of systems expected along QSO l.o.s. (Nestor et al. 2005), for (left to right, top to bottom): *all*, *strong*, *weak* systems of the 'UVES sample'; *strong* systems of the 'overall sample'. The solid line represents the function describing the QSO SDSS results (Eq. 6.16).

the similarity of the redshift distribution of Mg II systems along GRB and QSO l.o.s.. In Fig. 6.15 we report the comparison between the normalized cumulative distributions of the number of systems per unit redshift for GRB and QSO l.o.s.. There is a 90.7% and 23.5% chance that the two *all* and *weak* Mg II absorber samples are drawn from the same population. The probability for the *strong* systems is 20.1% for the *UVES sample*, but it decreases to $\sim$ 2% when considering the 'overall sample'. This apparent excess of strong systems in the low-redshift bin could be an additional argument in favour of some lensing bias as the effect of lensing should be larger in case the deflecting mass is at smaller redshift.

6.5.4 Equivalent width distribution

We show in the top panel of Fig. 6.16 the comparison between the normalized $W_{\rm r}$ distribution of all Mg II systems with $W_{\rm r} > 0.3$ Å detected in the *UVES sample* and the one reported by Nestor et al. (2005) for the Mg II systems along the QSO l.o.s. in the SDSS

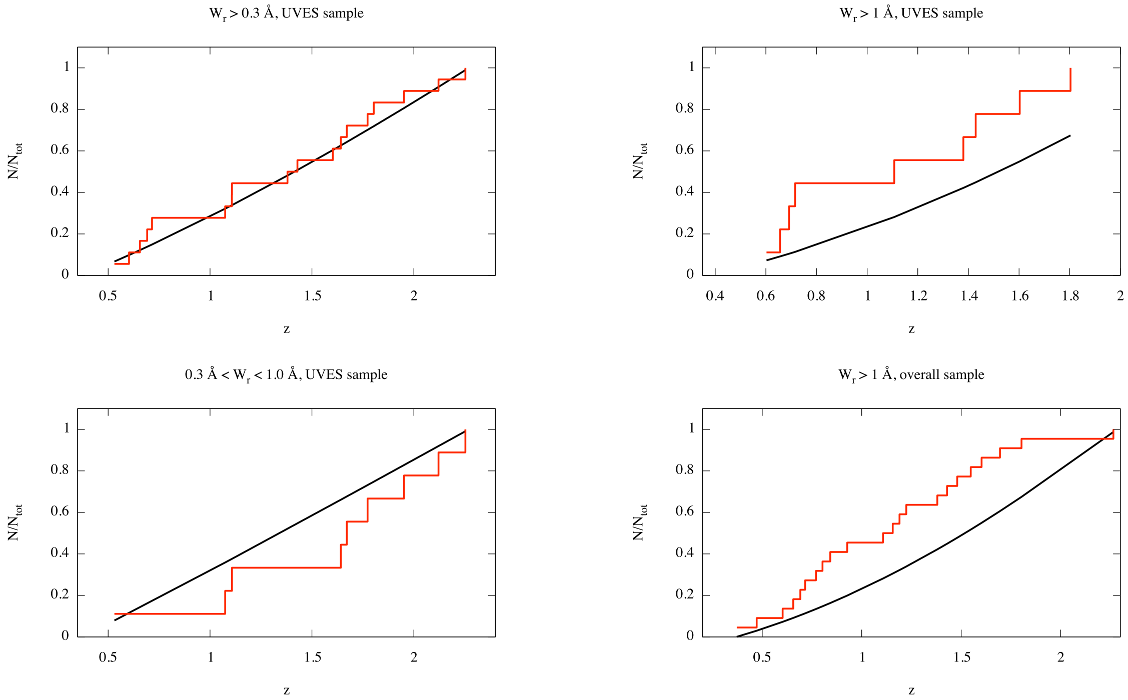

Figure 6.15 Normalized cumulative redshift distributions of Mg II systems detected (i) along GRB l.o.s. (red) and (ii) expected along QSO l.o.s. following Eq. 6.16 (black solid line; Eq. 6.17 give similar results) for (left to right, top to bottom): *all*, *strong*, *weak* systems of the 'UVES sample'; *strong* systems of the 'overall sample'.

survey.

Fig. 6.17 shows the corresponding W_r cumulative distributions. The KS tests give a 27.1% chance that the GRB and QSO distributions are drawn from the same population. Porciani et al. (2007) affirm that if the excess of Mg II systems is related to the beam size of the source, then the GRB and QSO Mg II W_r distributions should be different. In particular, the distribution of MgII equivalent widths along GRBs should be flatter than in QSOs. Our results do not favour this hypothesis and confirm what found by Porciani et al. (2007) in a similar study on the Prochter et al. (2006b) sample only.

In the following, we will use our high-quality UVES data to investigate in more detail the properties of the strong Mg II systems observed along GRB l.o.s..

6.5.5 The nature of strong Mg II absorbers towards GRBs

Both the results on the UVES homogeneous sample and those obtained using the enlarged sample confirm, although to a smaller extend, the excess of strong Mg II absorbers along GRB l.o.s. first reported by Prochter et al. (2006b). On the other hand, the number

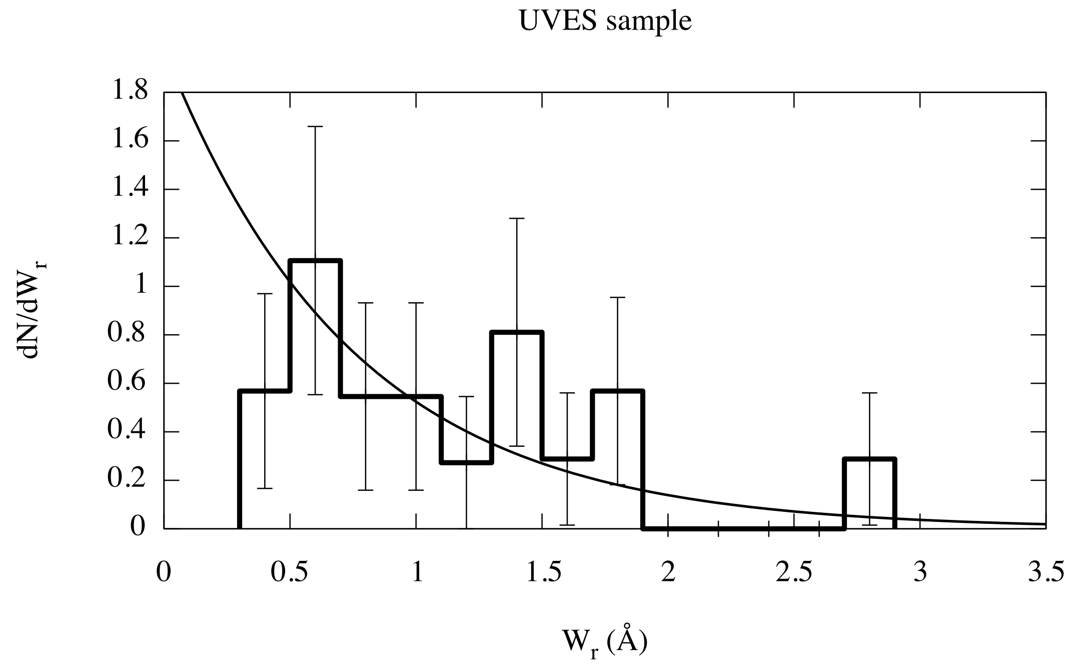

Figure 6.16 Normalized $W_{\rm r}$ distribution of the Mg II systems with $W_{\rm r} > 0.3$ Å detected in the *UVES sample*. The fully drawn curve represents the same function for QSO absorbers (Nestor et al. 2005).

density of weak systems seems to be the same along GRB and QSO lines of sight. It must be noted however that the limit of $W_{\rm r} = 1$ Å to define a "strong" system has no physical meaning. It corresponds to an observational limit: these systems are easily detected even in low-resolution data. To understand the reason of the discrepancy in the number density of "strong" systems it is therefore important to study in more detail these systems and to derive their physical characteristics. This is possible using the UVES data. In the following, we will not restrict our study to the arbitrarily defined 1 Å equivalent width. We will study also all systems with $W_{\rm r} > 0.6$ Å which is a limit frequently used in QSO absorption line studies.

The characteristics of all these systems are reported in Table 6.7. The GRB l.o.s. and the redshifts of the systems are in Columns 1 and 2, respectively. Column 3, 4 and 5, report the $W_{\rm r}^{MgII\lambda2796}$, $W_{\rm r}^{MgI\lambda2852}$ and $W_{\rm r}^{FeII\lambda2600}$ (when these lines are detected). In Columns 6, 7 and 8, the results of the measurements of the column densities (when they were possible) of Zn II, Si II and Fe II are shown. The values of the velocity spread by each systems, Δv (see Sect. 6.5.5.1 for a description on how this measurement has been

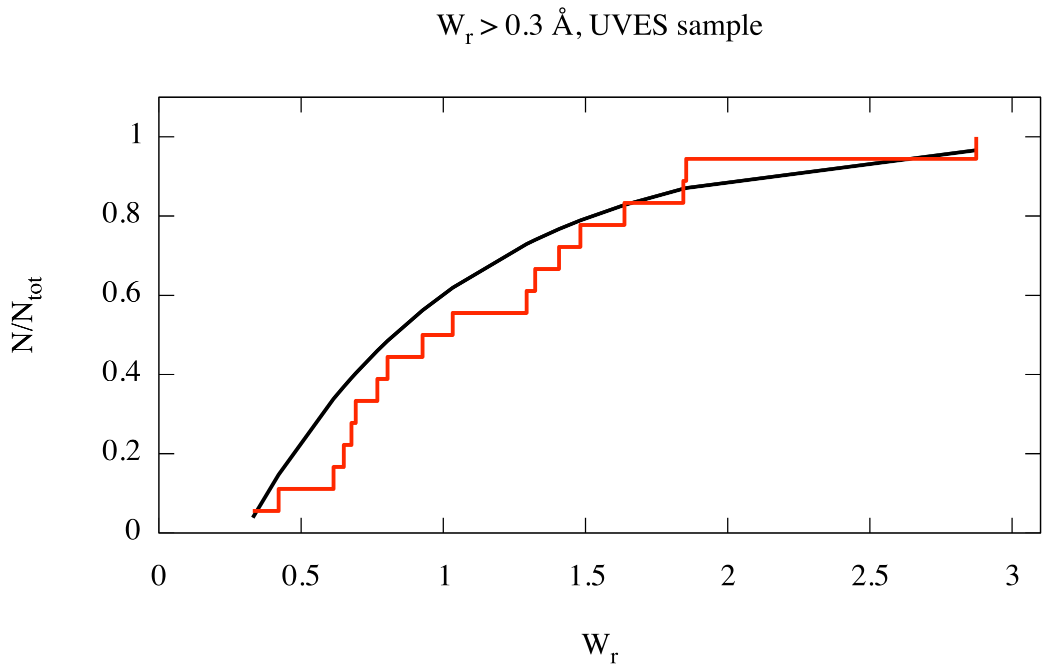

Figure 6.17 Cumulative $W_{\rm r}$ distribution of the Mg II systems with $W_{\rm r} > 0.3$ Å detected in the *UVES sample*. The black solid line represents the function (normalized) reported by Nestor et al. (2005).

performed), can be found in Column 9. Columns 10 and 11 report the values (or lower limits) inferred for the metallicity [X/H] and hydrogen column density $N_{\rm HI}$ of each system (the method to obtain these values is described in Sect. 6.5.5.1).

6.5.5.1 Velocity spread, metallicity and H I column density

To illustrate our discussion, the profiles of the doublet of the $W_{\rm r} > 1$ Å Mg II systems found in the UVES spectra are plotted on a velocity scale in Fig. 6.18. The profiles are complex, spread over at least 200 km s^{-1}, covering up to $\sim$ 600 km s^{-1} in some cases, and show a highly clumpy structure.

A key parameter to characterize an absorber is the corresponding H I column density. Unfortunately, the H I Lyman-α absorption line of most of the systems is located below the atmospheric cut-off and is unobservable from the ground. If we want to characterize the systems with their H I column density or at least an estimate of it, we have to infer it indirectly. For this we will assume that the systems are cosmological and that the physical state of the gas does not depend on whether the gas is in front of a GRB or a QSO. This

Table 6.7 Characteristics of Mg II systems with $W_{\rm r} > 0.6\,\text{Å}$ in the *UVES sample.*

GRB	$z_{\rm abs}$	$W_{\rm r}^{MgII\lambda2796}$ (Å)	$W_{\rm r}^{MgI\lambda2852}$ (Å)	$W_{\rm r}^{FeII\lambda2600}$ (Å)	$N_{\rm ZnII}$ cm^{-2}	$N_{\rm SiII}$ cm^{-2}	$N_{\rm FeII}$ cm^{-2}	Δv^{a} km s^{-1}	[X/H]^{b}	$N_{\rm HI}^{c}$ cm^{-2}
021004	1.380	1.637	0.190	0.972		15.19 ± 0.09	15.09 ± 0.05	170	−0.78	20.41
021004	1.603	1.407	0.366	0.737	12.78 ± 0.02		14.60 ± 0.03	164	−0.80	20.92
050730	1.773	0.927	0.184	0.396			14.04 ± 0.02	81	−1.24	>19.77
050730	2.253	0.650	0.132	0.392			14.47 ± 0.01	35	−1.77	>20.73
050820A	1.429	1.323	0.488	0.601			14.34 ± 0.03	271	−0.48	>19.31
050820A	0.692	2.874						436^{e}		
050922C	1.108	0.677	< 0.1	0.154			13.06 ± 0.05	45	−1.61	>19.16
060418	0.656	1.033	0.078	0.486			13.96 ± 0.02	136	−0.92	>19.37
060418	0.603	1.293	0.361	0.989			16.43 ± 0.04^{d}	76	−1.28	>22.2
060418	1.107	1.844	0.483	1.080	12.87 ± 0.03		14.69 ± 0.01	119	−1.00	21.21
060607A	1.803	1.854	> 0.226	0.825		14.36 ± 0.1	14.07 ± 0.03	333	−0.35	19.15
071031	1.642	0.692	< 0.1				12.71 ± 0.05	122	−0.98	>18.18
071031	1.952	0.804	< 0.1	0.352			13.86 ± 0.02	57	−1.46	>19.81
080319B	0.531	0.614	0.155	0.467			14.37 ± 0.01	49	−1.56	>20.42
080319B	0.715	1.482	0.303	0.697			14.00 ± 0.01	354	−0.31	>18.80
080413A	2.121	0.768	< 0.1	0.301		> 15.02	13.65 ± 0.07	60	−1.43	>19.6^{f}

[a] Velocities are measured following Ledoux et al. (2006b); [b] Metallicities inferred using the velocity-metallicity relation found by Ledoux et al. (2006b); [c] When only the iron column density is available, the $N_{\rm HI}$ value has to be considered has a lower limit due to possible dust extinction; [d] Line is saturated; [e] Velocity measured using the saturated Mg II lines (see page 162); [f] The equivalent width of the Lyman-α line measured from the UVES data is $W_{\rm r} = 1.4$ Å, which would imply $N_{\rm HI} \sim 18.6$.

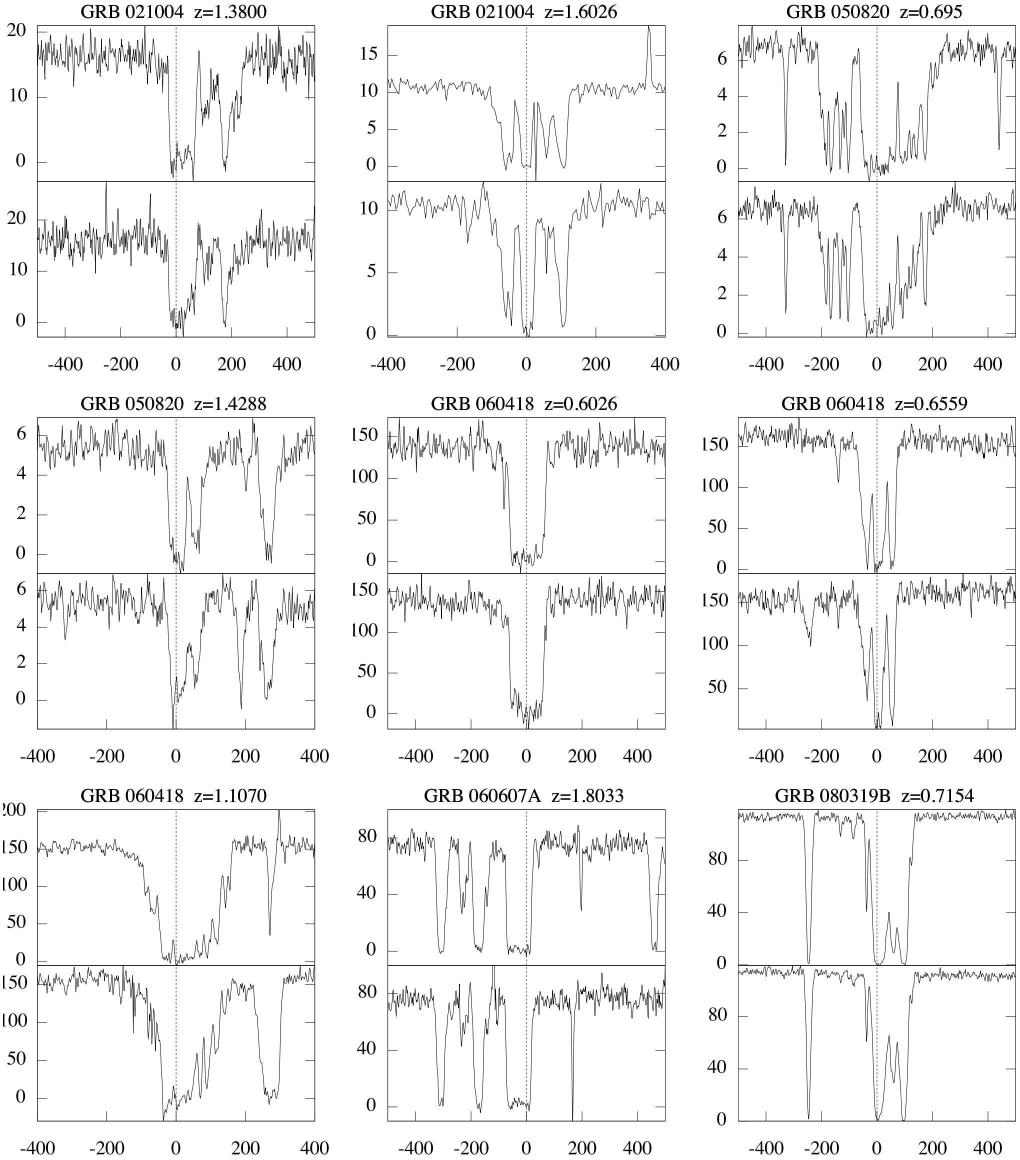

Figure 6.18 The $W_{\rm r} > 1.0$ Å Mg II absorption systems detected in the UVES spectra. the Mg II $\lambda2796$ (top) and $\lambda2803$ (bottom) absorption lines are displayed for each system on a relative velocity scale with 0 km s^{-1} centered at the redshift reported in Table 6.4.

is a reasonable assumption as we have no reason to believe that physics is different along the two types of l.o.s..

We measured the velocity spread of the strong Mg II systems in the *UVES sample* following Ledoux et al. (2006a). We therefore used a moderately saturated absorption line and measured the velocity difference between the points of the absorption profiles at which 5% and 95% of the absorption occurs. In case no moderately saturated absorption line is available, we used the mean value of the velocity widths calculated from a saturated line and an optically thin line. Note that this definition implies that the measured

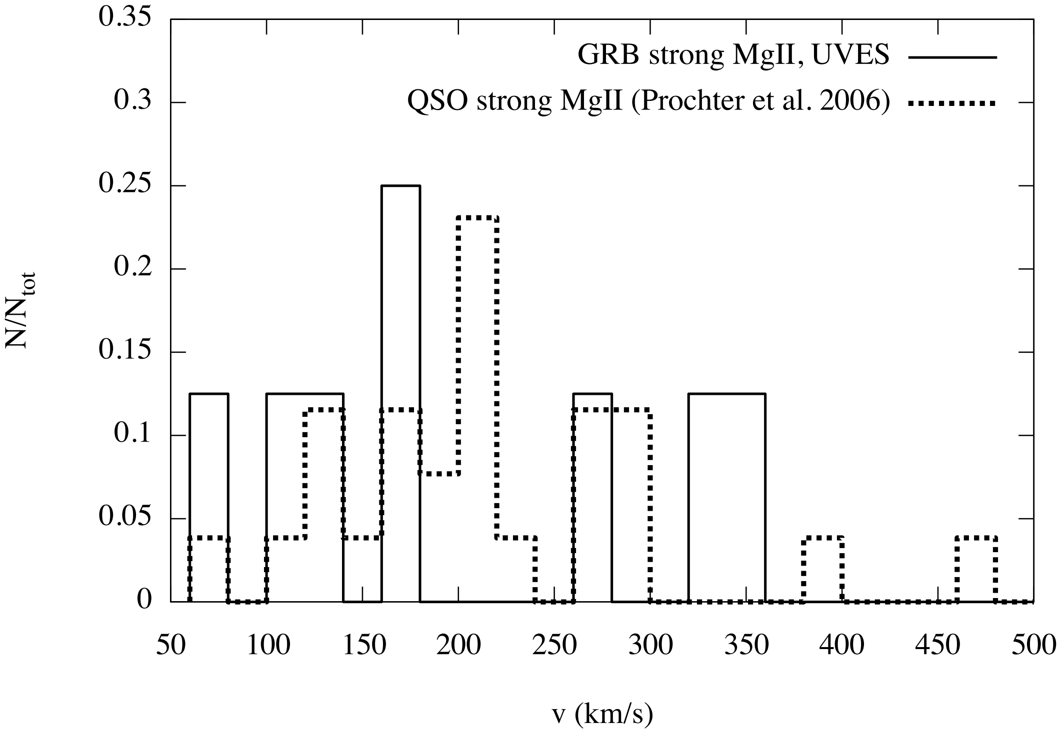

Figure 6.19 The solid line histogram represents the distribution of the velocities of the strong Mg II systems in the UVES sample calculated following Ledoux et al. (2006a). The thick dashed histogram refers to the 27 SDSS Mg II systems observed at high spectral resolutioin (Prochter et al. 2006a).

velocity spread is usually smaller than the spread of the Mg II profile, which is strongly saturated. Results are given in column 9 of Table 6.7. For the system at $z_{\rm abs} = 0.692$ toward GRB 050820A, the only available lines are the saturated Mg II lines. Therefore the corresponding velocity spread should be considered an upper limit.

The velocity-spread distribution is shown for UVES systems with $W_{\rm r} > 1$ Å in Fig. 6.19 together with the SDSS QSO distribution from 27 SDSS systems with $W_{\rm r} > 1$ Å observed at high spectral resolution (Prochter et al. 2006a). Although the statistics is small, the UVES and SDSS distributions are statistically similar. A KS test gives 65% chance that the two samples are drawn from the same population.

We use the velocity-metallicity correlation found by Ledoux et al. (2006b) to estimate the expected metallicity of the systems, assuming that the correlation is valid also for sub-DLA. This may be a strong assumption and we are aware that further investigation is needed. We then infer the hydrogen column densities dividing the zinc and/or silicon column densities measured in the UVES spectrum by the metallicity. When the two later species are not available, we use the iron column density. In that case the derived $N(\mathrm{H\,I})$ column density should be considered a lower limit because iron can be depleted onto dust-grains. The results are shown in Table 6.7. The error on the procedure should be of the order of 0.5 dex (see Ledoux et al. 2006). However, for one of the systems toward GRB 080413A the UVES spectrum covers also the H I Lyman-α line. The measured equivalent width of the line is $W_{\mathrm{r}} = 1.4$ Å. A simple curve of growth analysis leads to a column density of log $N(\mathrm{H\,I})\sim 18.6$, approximately independent of the Doppler parameter value. The difference is larger than the above quoted value for the errors. This means that these estimates should be considered with caution. We find that at least 4 of the 9 systems with $W_{\mathrm{r}} > 1$ Å could be DLAs. Out of the 16 systems in the table ($W_{\mathrm{r}} > 0.6$ Å) , 6 could be DLAs. In any case, and even if we consider that we systematically overestimate the column density by 0.5 dex, a large fraction of the systems should have log $N(\mathrm{H\,I}) > 19$.

We can now compare the observed characteristics of the systems seen along GRB l.o.s. with what is observed for strong Mg II systems in front of QSOs. Rao et al. (2006), using SDSS and HST data, derived the probability for a strong Mg II system to be a DLA. They found that $36 \pm 6\%$ of the systems with $W_{\mathrm{r}}^{\mathrm{MgII}\lambda2796} > 0.5$ Å and $W_{\mathrm{r}}^{\mathrm{FeII}\lambda2600} > 0.5$ Å are DLAs. From the results shown in Table 6.7, it can be inferred that at least 57% of the systems along GRB l.o.s. fulfilling the same conditions are DLAs. Rao et al. (2006) also found that $42 \pm 6\%$ of the systems having $W_{\mathrm{r}}^{\mathrm{MgII}\lambda2796}/W_{\mathrm{r}}^{\mathrm{FeII}\lambda2600} \leq 2$ and $W_{\mathrm{r}}^{\mathrm{MgI}\lambda2852} > 0.1$ Å are DLAs. In our sample we find that ALL the systems fulfilling this condition are DLAs. It must be noted that $W_{\mathrm{r}}^{\mathrm{MgI}\lambda2852}$ is pretty strong in systems towards GRBs (with $W_{\mathrm{r}}^{\mathrm{MgI}\lambda2852} > 0.3$ Å in five systems). On the other hand no DLAs are found for systems with $W_{\mathrm{r}}^{\mathrm{MgII}\lambda2796}/W_{\mathrm{r}}^{\mathrm{FeII}\lambda2600} > 2$, in agreement with the results by Rao et al. (2006).

We compare the number of DLA per unit redshift (n_{DLA}) found by Rao et al. (2006) to that of our sample. The n_{DLA} is defined as the product of the Mg II system number density by the fraction of DLA in a Mg II sample. Rao et al. (2006) found that 20% of the Mg II systems with $W_{\mathrm{r}} > 0.6$ Å are DLAs. Using the number density of such Mg II systems derived by Nestor et al. (2005), they found that $n_{\mathrm{DLA,QSO}} \sim 0.1$. Our redshift path being $\Delta z = 13.68$ for $W_{\mathrm{r}} > 0.6$ Å , we find that $n_{\mathrm{DLA,GRB}} \sim 0.44$ if we assume that six systems are DLAs in our sample. This means that the number of DLAs is four times larger along GRB lines of sight as compared to QSO lines of sight. We notice that even considering a more conservative case where three systems of the sample are DLAs, we obtain $n_{\mathrm{DLA,GRB}} > 0.22$, that is more than twice bigger than along QSO l.o.s..

The above estimate of log N(H I) can be considered as highly uncertain and the identification of a few of the systems as DLAs can easily be questioned. What is much less questionable is that 10 to 12 of the systems listed in Table 6.7 probably have log $N(\mathrm{H\ I}) > 19$. We can compare the number density of these sub-DLAs to the number density measured by Péroux et al. (2005). The number density of our sample is 0.88 (resp. 0.73) per unit redshift in the case that 12 (resp. 10) systems are counted, while the expected number density of systems along QSO l.o.s. is in the range 0.1−0.4 (Péroux et al. 2005). We can therefore conclude that the number density of DLAs and sub-DLAs toward GRBs is about twice larger than along QSOs.

All this indicates that GRBs favour lines of sight with not only an excess of strong Mg II systems but with an excess of (sub)DLAs. Since these systems are more likely to be located in the central parts of massive halos, this may again favour the idea that there exists a bias in GRB observations towards GRB with afterglows that are brighter because they are subject to some lensing amplification.

6.5.5.2 Dust

It has been proposed that a dust bias could possibly affect the statistics of strong Mg II systems (Fall & Pei 1993). Indeed, if part of the population of strong Mg II systems contains a substantial amount of dust, then the corresponding lines of sight could be missed in QSO surveys because of the attenuation of the QSO whereas for GRBs, being intrinsically brighter, the same lines of sight would not be missed.

The existence of a dust extinction bias in DLA surveys is still a debated topic among the QSO community although observations of radio selected QSO l.o.s. (Ellison et al. 2004) seem to show that, if any, this effect is probably small.

Table 6.8 Iron to Zinc or Silicon ratio and extinction estimate for 4 strong Mg II systems.

	z	N(FeII) (cm^{-2})	N(ZnII) (cm^{-2})	N(SiII) (cm^{-2})	[Fe/Zn]	[Fe/Si]	$N_{\mathrm{Fe}}^{\mathrm{dust}}$ (cm^{-2})	A_{V}
GRB021004	1.3800	15.09 ± 0.05		15.19 ± 0.09		-0.05 ± 0.10	14.18 ± 0.23	~ 0
GRB021004	1.6026	14.60 ± 0.03	12.78 ± 0.02		-1.03 ± 0.04		15.59 ± 0.02	< 0.2
GRB060418	1.1070	14.69 ± 0.01	12.87 ± 0.03		-1.05 ± 0.03		15.68 ± 0.03	< 0.2
GRB060607A	1.8033	14.07 ± 0.03		14.36 ± 0.10		-0.24 ± 0.10	13.94 ± 0.17	~ 0

We can use our UVES l.o.s. to estimate the dust content of strong Mg II systems from the depletion of iron compared to other species, as is usually done for DLAs. We have therefore searched for both Fe II and Zn II absorption lines (or Si II, in case the Zn II lines are not available) associated with the strongest Mg II systems present in the UVES spectra. Because the spectra do not always cover the right wavelength range, the associated column densities could be measured only for 4 out of the 9 systems (see Table 6.8). We estimated the depletion factor, and therefore the presence of dust, from the metallicity ratio of iron (a species heavily depleted into dust grains in the ISM of our Galaxy) to zinc (that is little depleted), [Fe/Zn] = log(Fe/Zn)−log(Fe/Zn)$_\odot$ (or [Fe/Si]). We also determine the iron dust phase column density ($N_{\rm Fe}^{\rm dust}$, reported in Column 8 of Table 6.8) using the formula given by Vladilo et al. (2006) and from this we infer an upper limit on the corresponding flux attenuation $A_{\rm V}$ from their Fig. 4 (see last column of Table 6.8). We used also the $A_{\rm V}$ estimate given by (Bohlin et al. 1978; Prochaska & Wolfe 2002):

$$A_{\rm V} = 0.5 \frac{N({\rm HI})}{10^{21}} \kappa \tag{6.18}$$

where κ represents the dust-to-gas ratio as:

$$\kappa = 10^{[{\rm X/H}]}(1 - 10^{[{\rm Fe/X}]}) \tag{6.19}$$

with X referring to Zn or Si if Zn is not available.

The results of this last method are consistent with those found with the procedure referring to Vladilo et al. (2006). It can be seen that although depletion of iron can be significant, the corresponding attenuation $A_{\rm V}$ is modest because the column densities of metallic species are relatively small owing to low metallicities. Indeed we find high dust depletion in two systems at $z_{\rm abs} = 1.107$ toward GRB 060418 (see also Ellison et al. 2006) and at $z_{\rm abs} = 1.6026$ toward GRB 021004. Their column densities are low however so that the inferred $A_{\rm V}$ does not exceed values typically found for QSO l.o.s. (see Vladilo et al. 2006; Prantzos & Boissier 2000).

We note that for GRB 021004 and GRB 060607A we could estimate the attenuation for ALL strong Mg II systems identified along the l.o.s.. Therefore our results do not support the idea that a bias due to the presence of dust in strong Mg II systems could be the explanation for the overabundance of the strong Mg II absorbers along GRB l.o.s.. On the other hand, the fact that 2 out of 4 of the selected systems have a dust depletion higher than the values usually found for QSO DLAs (Meiring et al. 2006) supports the fact that these systems probably arise in the central part of massive halos of galaxies where the probability to find cold gas is expected to be higher.

6.5.6 Sub-DLA absorbers

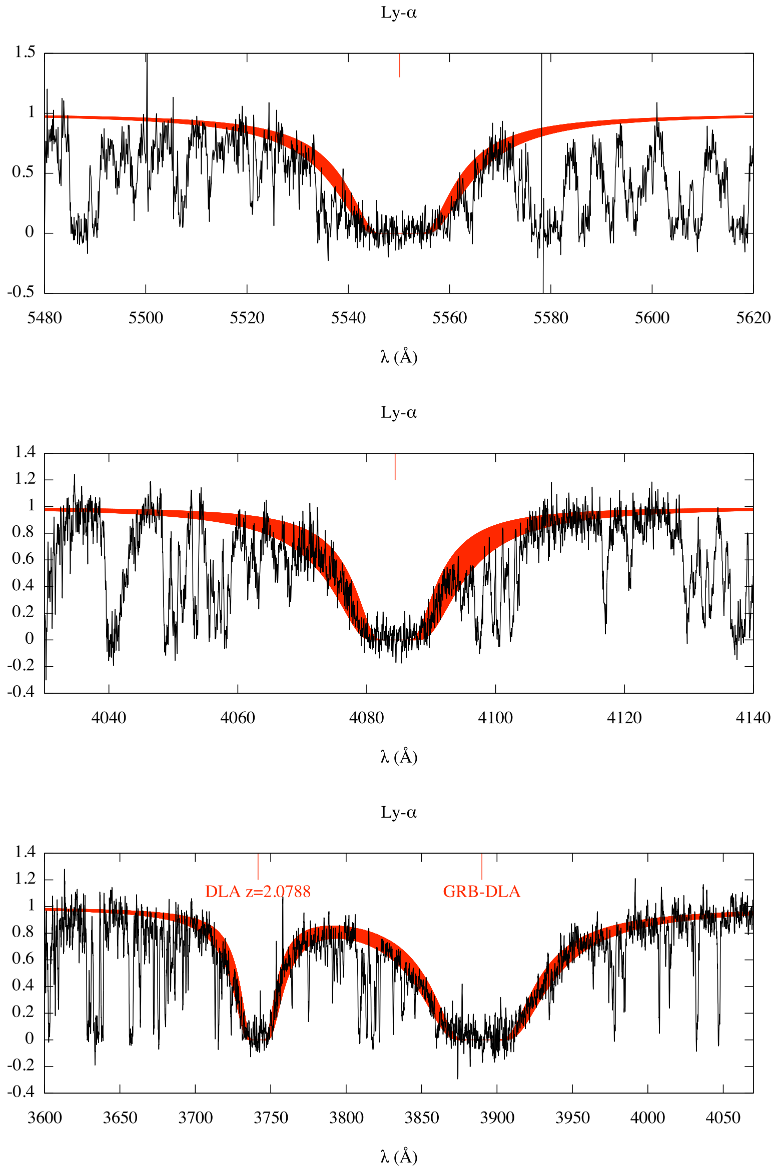

Figure 6.20 Foreground (sub-)DLAs. *Top panel*: Sub-damped Ly-α absorption along GRB 050730 l.o.s. at $z = 3.5655$. *Middle panel*: Damped Ly-α absorption along GRB 050820 l.o.s. at z=2.3598. *Bottom panel*: Sub-damped Ly-α absorption along GRB 050922C l.o.s. at z=2.0778 (this system has been fitted together with the DLA associated with the GRB at $z = 2.1996$). The red area correspond to the fit result covering the column density error range.

The UVES spectra often cover a substantial part of the Lyman-α forest in front of the GRB. It is therefore possible to search directly for strong H I Lyman-α absorption lines corresponding to DLAs or, more generally, sub-DLAs. This can only be performed for 8 of the 10 GRBs in the sample: the redshifts of GRB 060418 and GRB 080319B are unfortunately too low to allow the detection of the Lyman-α absorptions in the UVES spectral range. We exclude from our search the highest redshift DLA, which is believed to be associated with the close surrounding of the GRB (see for example the DLA at z=2.1996 along the l.o.s of GRB 050922C, that is the DLA associated to the GRB host, as illustrated in Sect. 6.4). We find additional (sub-)DLAs along the l.o.s. of GRB 050730, GRB 050820, GRB 050922C (Fig. 6.20) and GRB 060607A (Fig. 6.21).

The three former systems are simple with a single Lyman-α component. The system detected at 2.9374 toward GRB 060607A is more complex. The profile is made of two main clumps at $z = 2.9322$ and 2.9374. The latter is a blend of the four O I components (see top panel in Fig. 6.21). The constrains on the H I column densities come mostly from the red wing of the Lyman-α line and the structures seen in the Lyman-γ line. We find that the two main H I components at $z = 2.9374$ and 2.9322 have log $N_{\rm HI} = 19.4$ and 19.0 ± 0.1, respectively. These two sub-DLAs are separated by only $\sim$400 km s^{-1} and we consider therefore only the strongest component in the following. It is worth noting however that the limit on the O I component at $z = 2.9322$ is log $N(\text{O I}) < 12.6$ implying that the metallicity in the cloud could be as low as $[\text{O/H}] < -2.9$ which would be the lowest metallicity ever observed yet in such a system. Some ionization correction could be necessary however in case the oxygen equilibrium is displaced toward high excitation species by a hard ionizing spectrum.

Table 6.9 reports the column densities (columns 4, 5, 6 and 7) and abundances (columns 8, 9, 10 and 11) of the systems assuming that all elements are in their neutral or singly ionized state. The values are similar to those usually found for (sub-)DLAs along QSO l.o.s. (see for example Péroux et al. 2003a).

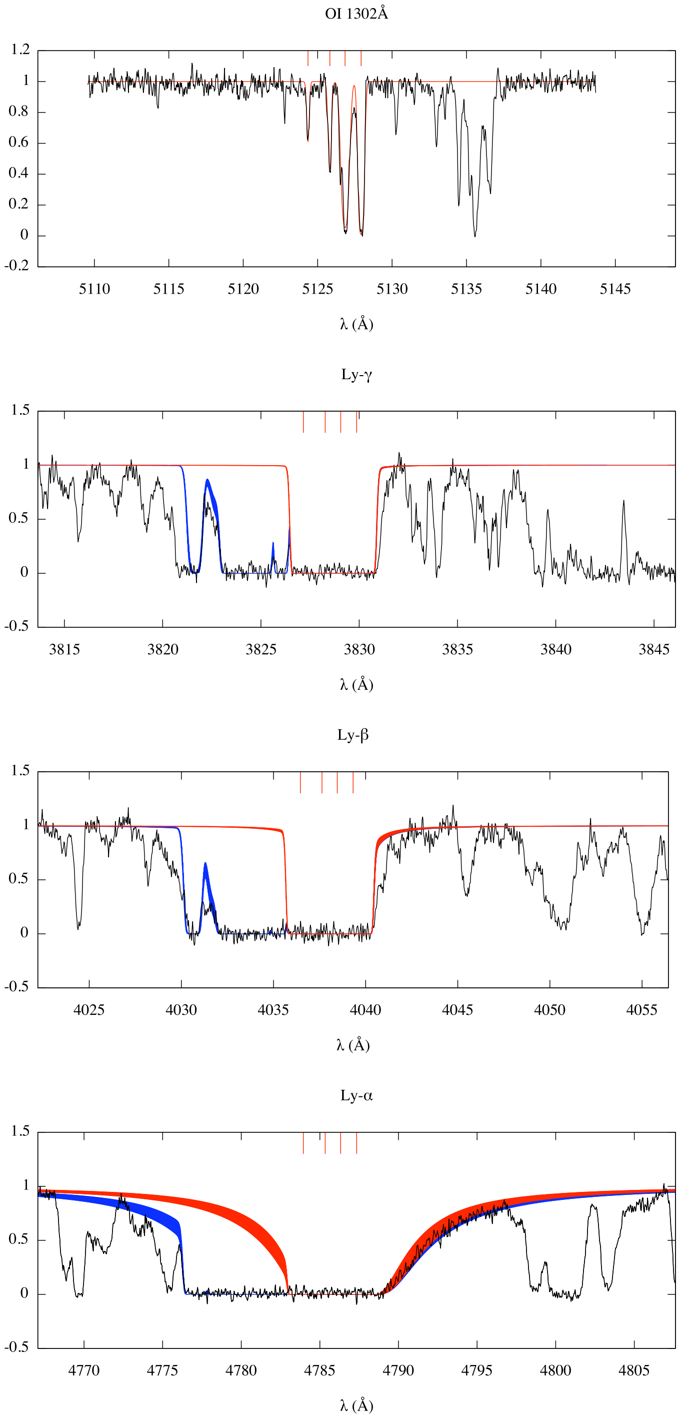

Figure 6.21 The Sub-DLA system along the l.o.s. of GRB 060607A at $z = 2.9374$. The top panel show the fit for the OI lines, while the following panels report the fit results of the Ly-γ, Ly-β and Ly-α absorption lines (from top to bottom, respectively). The red area represent the fit of the $z = 2.9374$ systems, covering for the HI lines the column density error range. In blue is shown the total fit including also the Sub-DLA system at $z = 2.9322$.

Table 6.9 Properties of the foreground damped Ly-α systems detected along the UVES GRB spectra.

	Δz [a]	z (Sub-)DLA	log N_{HI} (N in cm^{-2})	log N_{OI} (N in cm^{-2})	log N_{SiII} (N in cm^{-2})	log N_{FeII} (N in cm^{-2})	[Fe/Si]	[O/H]	[Si/H]	[Fe/H]
GRB021004	0.487	There are no intervening (Sub-)DLA along this l.o.s.								
GRB050730	0.542	3.5655	20.2 ± 0.1	N/A[b]	< 14.7	< 13.6			< -1.0	< -2.3
GRB050820A	0.529	2.3598	20.1 ± 0.2	N/A[b]	13.84 ± 0.02	14.11 ± 0.02	-0.22 ± 0.02		-1.5 ± 0.2	-1.7 ± 0.2
GRB050922C	0.468	2.0778	20.65 ± 0.15	> 15.30	14.38 ± 0.10	14.44 ± 0.03	0.11 ± 0.10	> -2.1	-1.83 ± 0.18	-1.72 ± 0.15
GRB060607A	0.596	2.9374[c]	19.4 ± 0.1	> 15.07	> 14.74[d]	14.16 ± 0.03	< -0.53	> -1.1	> -0.2	-0.7 ± 0.1
		2.9322[c]	19.0 ± 0.1	< 12.8	< 12.6	< 12.6		< -2.9	< -1.9	< -1.9
GRB071031	0.540	There are no intervening (Sub-)DLA along this l.o.s.								
GRB080310	0.501	There are no intervening (Sub-)DLA along this l.o.s.								
GRB080413A	0.503	There are no intervening (Sub-)DLA along this l.o.s.								

[a] Calculated from the Ly-β absorption line of the GRB to 3000 km/s from the GRB Ly-α, except for GRB 050730 where the z range ends at the beginning of the spectral gap at $\lambda = 5096$Å. [b] The line is blended with other lines in the Ly-α forest. [c] To calculate the DLA number density we counted the $z = 2.9374$ and $z = 2.9322$ systems as a single system. [d] Blended with the SiIV(1402Å) absorption line associated to the GRB.

The presence of these (sub-)DLA systems allow us to extend the search for strong systems along GRB l.o.s. to higher redshift. The redshift paths (see Column 2 of Table 6.9) have been calculated considering $z_{\rm start}$ as the redshift of an absorber for which the corresponding Lyman-α line would be redshifted to the same wavelength as the Lyman-β line of the GRB afterglow. We therefore avoid confusion with the Lyman-β forest. $z_{\rm end}$ is fixed at 3000 km/s from the GRB Lyman-α. The only exception to this rule is GRB 050730 for which there is a gap in the spectrum at about 3000 km/s from the GRB redshift and starting at $\lambda = 5096$ Å. We use this wavelength to fix $z_{\rm end}$. The corresponding total redshift path is $\Delta z = 4.17$. For the statistical study we consider the $z = 2.9374$ and $z = 2.9322$ systems along GRB 060607A as a single system. We have therefore 4 (Sub)DLA in a redshift path of $\Delta z = 4.17$. The resulting number density for systems with log $N_{\rm HI} > 19.0$ is 0.96 ± 0.48 for an average redshift of $\langle z \rangle = 2.08$. At this redshift a value of about 0.5 ± 0.2 is expected (Péroux et al. 2005). Taken at face value, the number density obtained for our sample is larger, but the statistics is too poor to claim that there is an excess of (Sub)DLA.

It is intriguing however to note that the four systems are in that half of the Lyman-α forest closer to the GRB, with ejection velocities of 25000, 22000, 12000 and 11000 km s^{-1} for GRB 050730, 050820A, 050922C and 060607A respectively. This may indicate that for these systems the excess is not of the same origin as the excess of Mg II systems and that part of the gas in these systems could have been ejected by the GRB. We did not find however any additional evidence to be able to further support this idea.

6.5.7 Summary

We used UVES observations of GRB afterglows obtained over the past six years to build an homogeneous sample of lines of sight observed at high spectral resolution and good signal-to-noise ratio to re-investigate the presence of Mg II systems in GRB spectra, extending the study to smaller equivalent widths. We use these data also to derive intrinsic physical properties of these systems. We detect 9 (resp. 9) intervening Mg II systems with $W_{\rm r} > 1$ Å (resp. $0.3 < W_{\rm r} < 1.0$ Å) over an absorption length of $\Delta z = 13.9$ (resp. 12.5) when about 3 (resp. 6) are expected from observations of QSO sightlines. The number of weak systems is similar in GRBs and QSOs while the number of strong systems is larger along GRB l.o.s.. We increase the redshift path for strong systems to $\Delta z = 31.5$ using intermediate resolution observations reported in the literature and find that the number density of strong Mg II systems is a factor of about 2 higher toward GRBs compared to QSOs. We therefore confirm the excess of strong Mg II absorbers along GRB l.o.s. compared to QSO l.o.s. However, the excess is less than what has been claimed (Prochter et al. 2006b) by a factor of about two. Possible explanations of this excess include: dust obscuration bias in QSO studies; difference of the beam sizes of the two types of background sources; gravitational lensing.

The equivalent width distribution of the Mg II systems is similar in GRBs and QSOs. This does not favour the different beam sizes hypothesis as the cause of the strong Mg II excess (Porciani et al. 2007). The dust extinction inferred for the strong GRB Mg II systems is consistent with what is observed in standard QSO (sub-)DLAs. It seems therefore that the dust bias explanation does not play an important role either.

We investigated in details the properties of strong Mg II systems observed with UVES extending the analysis to systems with $W_{\mathrm{r}} > 0.6$ Å and deriving an estimate of the H I column density. We find that the number density of (sub-)DLAs per unit redshift in the UVES GRB sample is probably two times larger than what is expected from QSO sightlines. As (sub-)DLAs are expected to be found in the central part of massive haloes, this supports the idea of a gravitational bias. In addition, we divided our sample in three redshift bins and found that the number density of strong Mg II systems is larger in the low redshift bin ($0.4 < z < 1.0$). All this supports further the idea that current sample of GRB lines of sight could be biased by a subtle gravitational lensing effect.

We searched the Lyman-α forest probed by the UVES spectra for the presence of damped absorption lines. We find four sub-DLAs with log N(H I) > 19.3 over a redshift path of $\Delta z = 4.3$. This is again twice larger than what is expected in QSOs. However the statistics is poor. It is intriguing that these systems are all located in the part of the Lyman-α forest which is closer to the GRB. It is therefore not excluded that part of this gas is somehow associated with the GRBs. In that case, velocities of the order of 10 to 15 000 km/s are required. We did not find however any additional evidence to be able to further support this idea.

A clear explanation to this excess of strong systems would come from a systematic search for the field galaxies associated to these systems, but these kind of studies have not been performed yet. Very recently Chen et al. (2008) have used HST images of seven GRB fields (4 with strong MgII absorbers and 3 without MgII absorbers) to show that indeed there is an excess of galaxies within 2 arcsec of the GRB los in the GRB fields showing strong absorbers in their spectra (see their figure 22), as it could be expected in the case of a lenses bias in GRB l.o.s.. The statistics is small however, and no clustering properties have been studied in these fields, or more generally in GRB fields, up to now.

Chapter 7

Conclusions and Future Prospects

It is evident that GRBs are a very interesting phenomenon from several points of view. First of all their physics and origins are still a challenge to understand, moreover thanks to their exceptional brightness they can be used as a precious tool to retrieve information on the high redshift universe. A clear example of some of the different aspects that can be investigated using GRBs is given in this thesis by GRB 060418, whose multiwavelength data has been used in three different chapters.

The launch of the *Swift* satellite contributed to important development in GRB studies. Thanks to its rapidity it has become possible to observe the GRB counterpart emission at X-rays and optical frequencies immediately after (and in some case at the same time of) the initial gamma-ray trigger.

Using Swift data combined with the ground based robotic telescope observations, such as those of REM presented in this thesis, it is possible to monitor the early afterglow stages and to retrieve information on the prompt and afterglow emission mechanisms. From one side, the observations confirm the general picture predicted by the classical fireball model, as shown for example by the detection of the afterglow onset and the inferred values of the fireball Lorentz factor, deceleration radius and fluence. On the other hand the data point out several issues still to be solved, as testified by the studies on the light curves of the GRBs observed by REM and by the results of the SED survey on a large sample of GRBs, discussed in Chapters 3 and 4, respectively. The mechanism of both the prompt and afterglow emissions still need a better and stronger characterization. The structure of the jet is still unknown and the nature of the different breaks present in the light curves is still debated. Several lines of evidence indicate a possible different origin for the X-ray emission compared to the optical one, in particular during the early afterglow phases and flares. The most popular hypothesis is that there is some energy injection due to a prolonged activity of the central engine, even if it is still not clear how it is possible to make it active for so long.

Considering the nature of the progenitors, many progresses have been done in the last few years, in particular thanks to the discovery of SN spectral signatures in long GRB afterglows and to the discovery of short GRB afterglows (and therefore host galaxies). While for short GRBs there are still very few data, the light curves and spectra of long GRBs challenge some aspects of the progenitor models. The fact that in many cases the GRB surrounding medium profile does not correspond to a wind profile (as expected for a WR progenitor) and the lack of wind termination shock signatures lead to more complicated and less predictive models of the GRB environment. Other possible issues come from the low A_{V} values of the extinction retrieved from the SED analysis and the hydrogen column density values inferred from the X-ray data that seem to be at odds with both the A_{V} and the HI column densities measured from the afterglow optical spectra.

Up to date, many works have focussed on single GRBs, or on narrow energy ranges. There is the need for the future to have more statistical, panchromatic observational and theoretical studies using data covering all the stages of the GRBs, from the prompt emission to the late afterglow light curve. This is now possible at high energy thanks to both the *Swift* and Fermi satellites. Although at lower frequencies this goal is very demanding in terms of ground based telescope time, it may be reached by joining together the efforts of the different groups of the science community.

As explained in Chapter 6 of this thesis, GRBs can be used as lighthouses to investigate the high redshift universe. GRB afterglow spectra are a very rich source of information. As illustrated by the spectrum of GRB 050922C, the spectral features associated to the GRBs show that the GRB environment and host galaxy ISM are complex. Thanks to the detection of fine structure lines it is possible to retrieve information on the gas density or on the GRB radiation field and distances of the gas clouds. The aim is to disentangle the clouds belonging to the GRB surroundings from those less affected by the GRB and more characteristic of the host galaxy. It will be then possible to retrieve information (gas density, metal and dust content) on the progenitor environment so as to have a better picture of the progenitor characteristics, and also on the host galaxy itself in order to study galaxy evolution. The latter point can be investigated also through the study of the intervening systems along GRB spectra. As pointed out in Chapter 6, there are evidences of an excess of strong MgII systems (but more generally of sub-DLAs) along GRB l.o.s. compared to QSOs l.o.s.. This could be due to a gravitational lensing bias of

GRB sightlines. A clear explanation to this excess of strong systems would come from a systematic search for the field galaxies associated to these systems, therefore the hope is to succeed in obtaining the relevant amount of observational time needed for this kind of study, leading at the same time to the solution of the excess puzzle and to the gathering of more information on those systems.

A very interesting possibility is the study of GRB host as tracer of the star formation in the universe. This require the knowledge of the GRB redshift distribution less biased and as complete as possible. A strong improvement in this sense should come in the future thanks to the X-shooter spectrograph[1] that will be mounted on the ESO-VLT. Its large spectral range coverage, from 3200 to 24000 Å, will allow the detection of useful features for redshift measurements also in what is commonly know as the 'redshift desert' region (between about $z = 1.5$ and $z = 2$) and the discovery of very high redshift systems ($z > 6$). It will also possible to collect much more information on the dust and metal content of GRB host galaxy as well as on the intervening systems, so as to add knowledge to the cosmic evolution picture.

---

[1] http://www.eso.org/sci/facilities/develop/instruments/xshooter/

Appendix A

In the following pages are shown the figures representing the light curves (upper panels) and SEDs (lower panels) of the sample of GRBs discussed in Chapter 4, with the following point color conventions: Yellow: K-band; Grey: H-band; Brown: J-band; Black: I-band; Red: R band; Green: V-band; Blue: B-band; Violet: U-band; Cyan: UVW1 UVOT filter; Pink: UVM2 UVOT filter; Purple: UVW2 UVOT filter. Arrows refers to upper limits. The X-ray light curve data are represented by big black filled dots. The empty (resp. solid) points in the SEDs represent data points not corrected for the host extinction, while filled (resp. dashed) symbols are. For GRB 050525A and GRB 060614, considered the very small amount of dust, we report only the SED already corrected for the dust extinction. The lines (solid, dotted or dashed) in the SED figures indicate the extrapolation of the optical and X-ray spectra. In the relevant cases a light grey dotted line in the lower panels (SEDs) connects the optical data to the X-ray ones to avoid possible misinterpretations. SEDs time are indicated as well as a possible scaling factor of the SED, applied for better reading.

The X-ray data have been reduced partly from myself and partly from the Italian Swift-XRT Team. In addition to data belonging to our group or GCN data, the optical and NIR points have been retrieved from:

GRB050319: Woźniak et al. (2005); Mason et al. (2006); Quimby et al. (2006).

GRB050401: Rykoff et al. (2005a); Watson et al. (2006a)

GRB050408: Foley et al. (2006); de Ugarte Postigo et al. (2007)

GRB050416: Soderberg et al. (2007)

GRB050505: Hurkett et al. (2006)

GRB050525A: Klotz et al. (2005); Blustin et al. (2006); Della Valle et al. (2006b)

GRB050730: Pandey et al. (2006)

GRB050820A: Cenko et al. (2006)

GRB050824: Sollerman et al. (2007)

GRB050904: Tagliaferri et al. (2005a); Boër et al. (2006); Haislip et al. (2006)

GRB051111: Butler et al. (2006)

GRB060124: Romano et al. (2006); Misra et al. (2007)

GRB060210: Stanek et al. (2007)

GRB060418: Molinari et al. (2007)

GRB060614: Della Valle et al. (2006a); Mangano et al. (2007)

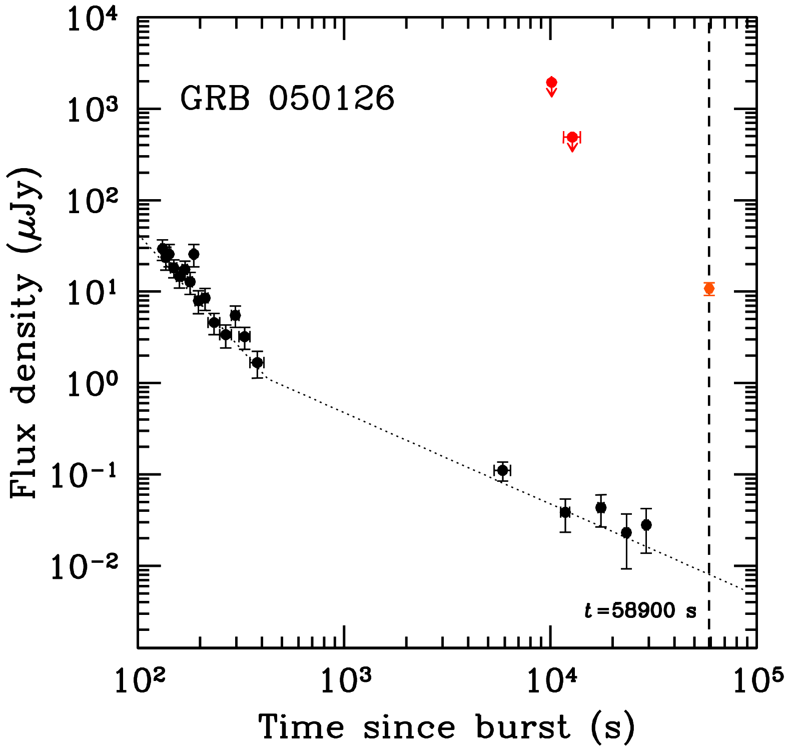

GRB 050126
Flux density (μJy)
Time since burst (s)
t =58900 s
10⁴
10³
10²
10¹
10⁰
10⁻¹
10⁻²
10²
10³
10⁴
10⁵

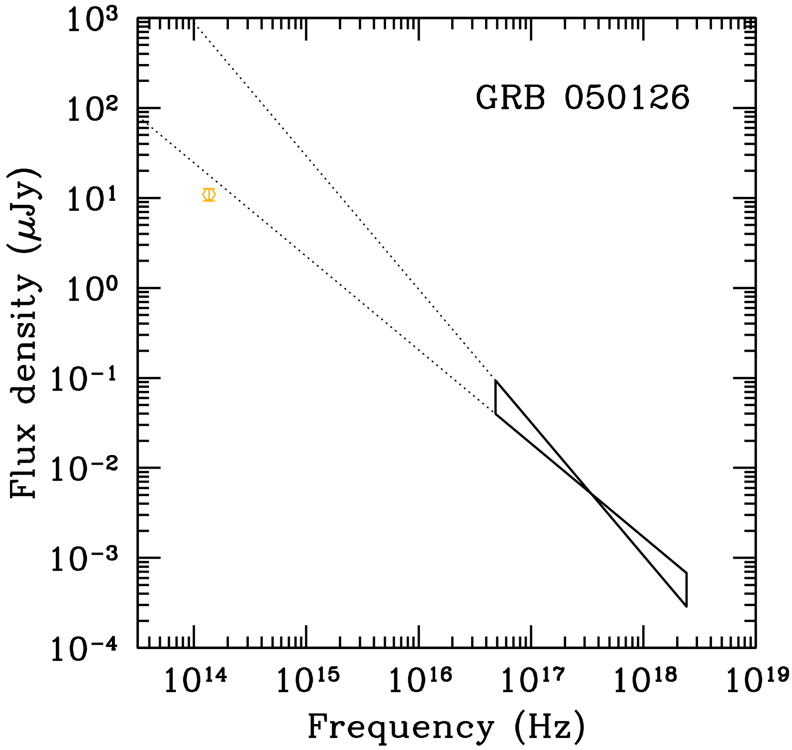

GRB 050126
Flux density (μJy)
Frequency (Hz)
10³
10²
10¹
10⁰
10⁻¹
10⁻²
10⁻³
10⁻⁴
10¹⁴
10¹⁵
10¹⁶
10¹⁷
10¹⁸
10¹⁹

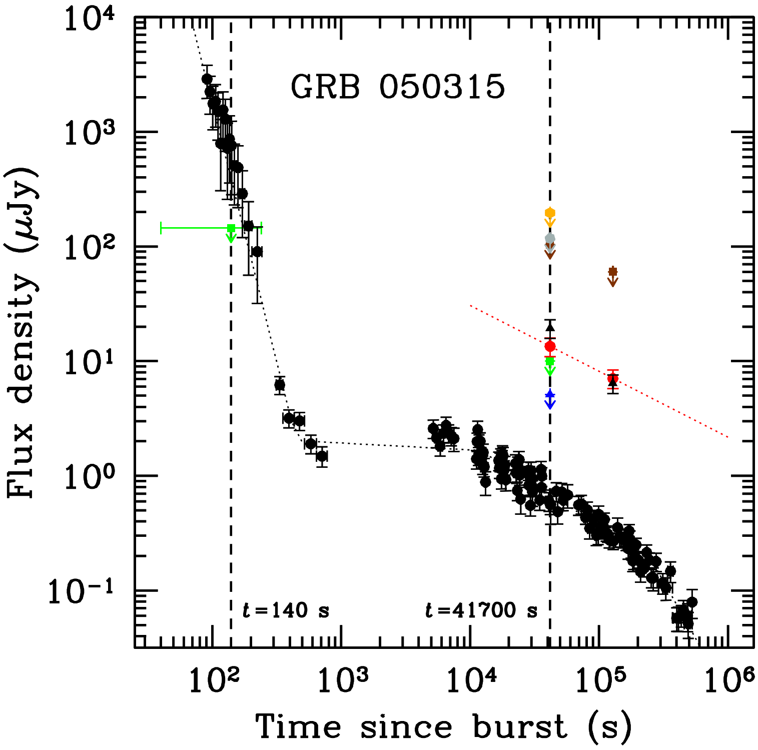
GRB 050315
Flux density (μJy)
Time since burst (s)
t = 140 s
t = 41700 s
10^{4}
10^{3}
10^{2}
10^{1}
10^{0}
10^{-1}
10^{2}
10^{3}
10^{4}
10^{5}
10^{6}

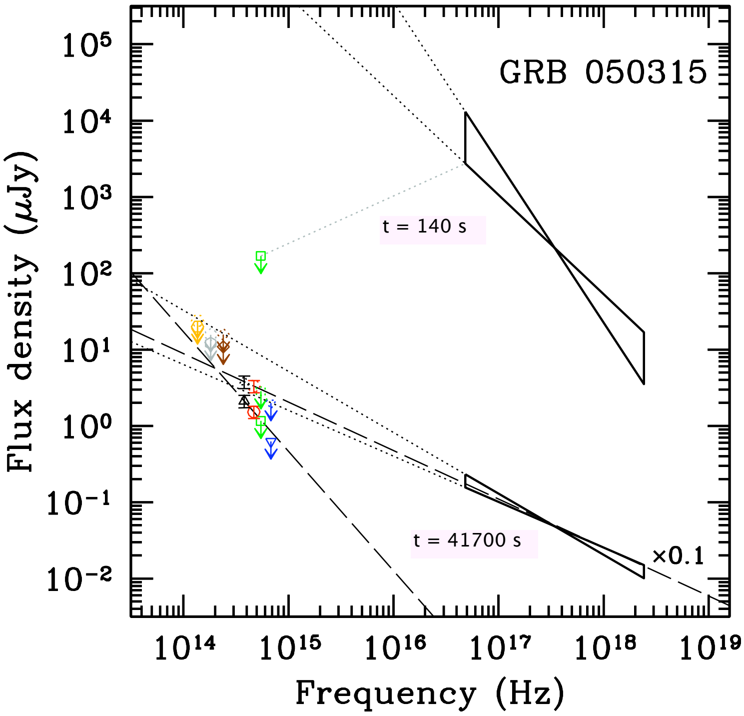
GRB 050315
Flux density (μJy)
Frequency (Hz)
t = 140 s
t = 41700 s
×0.1
10^{5}
10^{4}
10^{3}
10^{2}
10^{1}
10^{0}
10^{-1}
10^{-2}
10^{14}
10^{15}
10^{16}
10^{17}
10^{18}
10^{19}

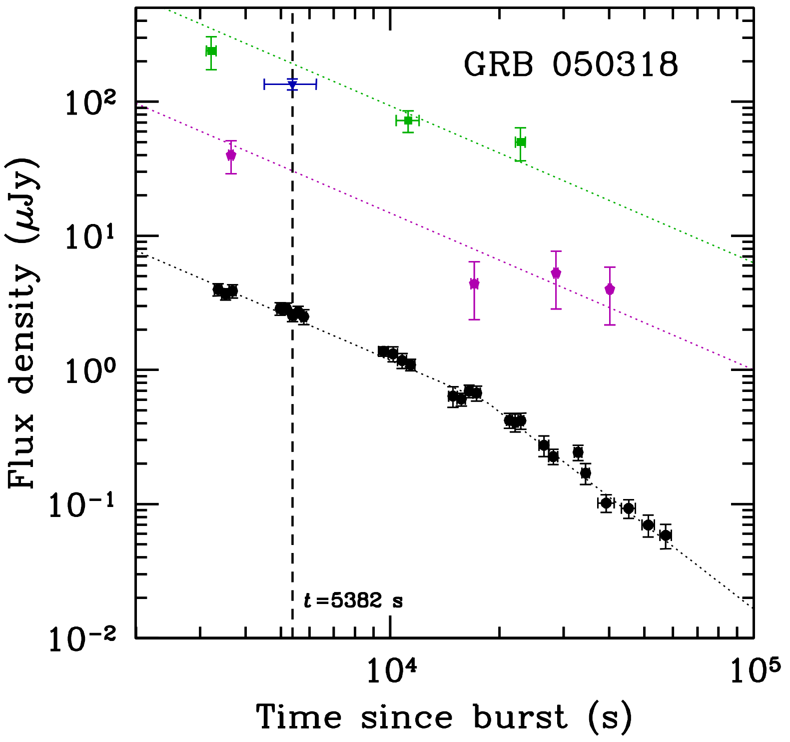
GRB 050318
Flux density (μJy)
10^{2}
10^{1}
10^{0}
10^{-1}
10^{-2}
$t=5382$ s
10^{4}
10^{5}
Time since burst (s)

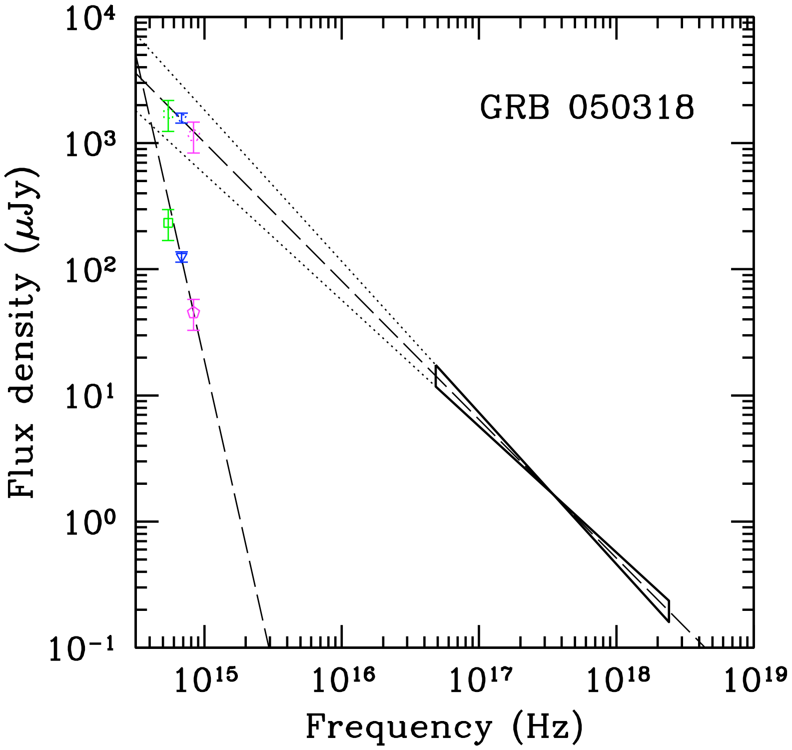
GRB 050318
Flux density (μJy)
10^{4}
10^{3}
10^{2}
10^{1}
10^{0}
10^{-1}
10^{15}
10^{16}
10^{17}
10^{18}
10^{19}
Frequency (Hz)

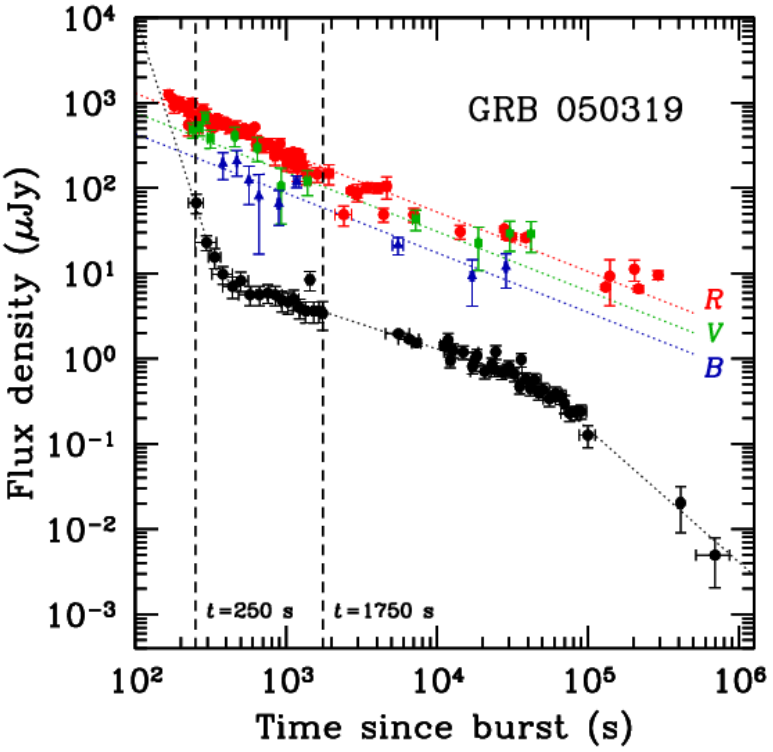
GRB 050319
Flux density (μJy)
Time since burst (s)
10⁴
10³
10²
10¹
10⁰
10⁻¹
10⁻²
10⁻³
10²
10³
10⁴
10⁵
10⁶
t=250 s
t=1750 s
R
V
B

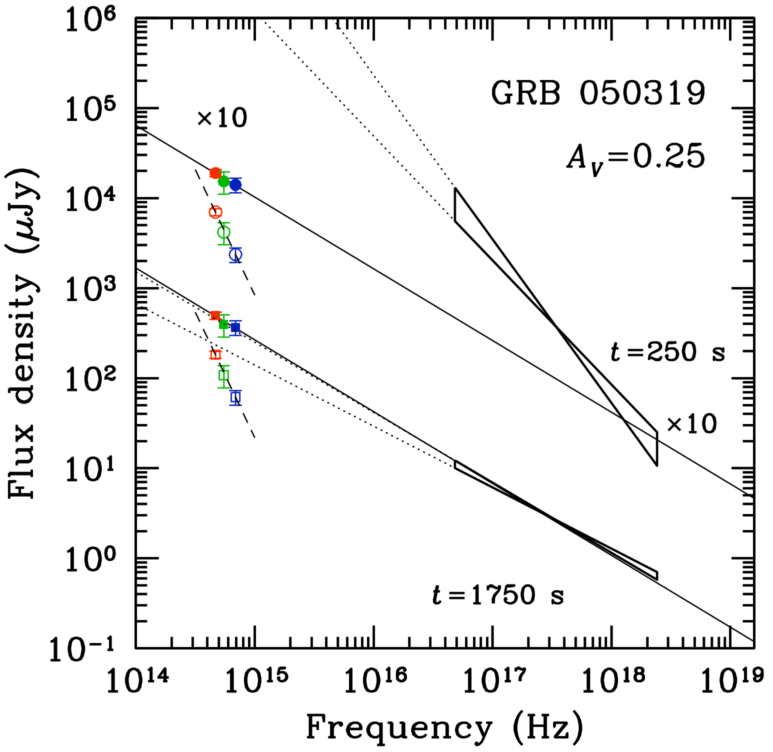
GRB 050319
A_V=0.25
×10
×10
t=250 s
t=1750 s
Flux density (μJy)
Frequency (Hz)
10⁶
10⁵
10⁴
10³
10²
10¹
10⁰
10⁻¹
10¹⁴
10¹⁵
10¹⁶
10¹⁷
10¹⁸
10¹⁹

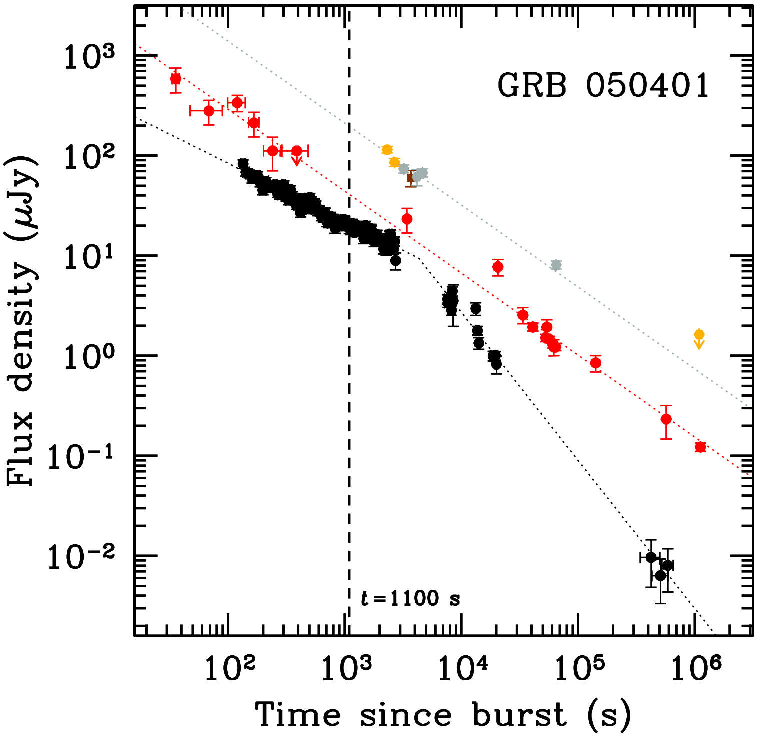
GRB 050401
Flux density (μJy)
10^3
10^2
10^1
10^0
10^{-1}
10^{-2}
t = 1100 s
10^2
10^3
10^4
10^5
10^6
Time since burst (s)

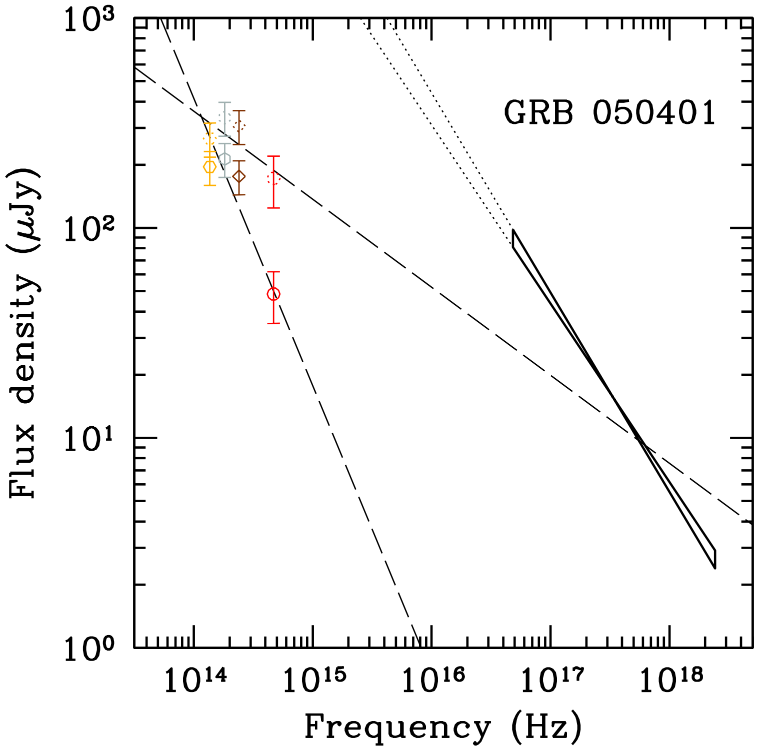
GRB 050401
Flux density (μJy)
10^3
10^2
10^1
10^0
10^{14}
10^{15}
10^{16}
10^{17}
10^{18}
Frequency (Hz)

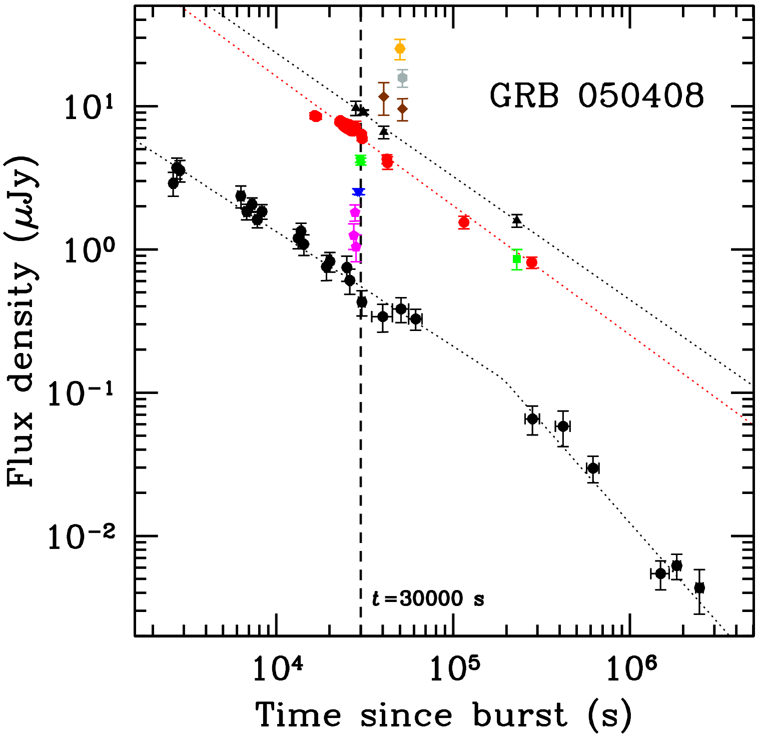
GRB 050408
Flux density (μJy)
Time since burst (s)
t = 30000 s
10¹
10⁰
10⁻¹
10⁻²
10⁴
10⁵
10⁶

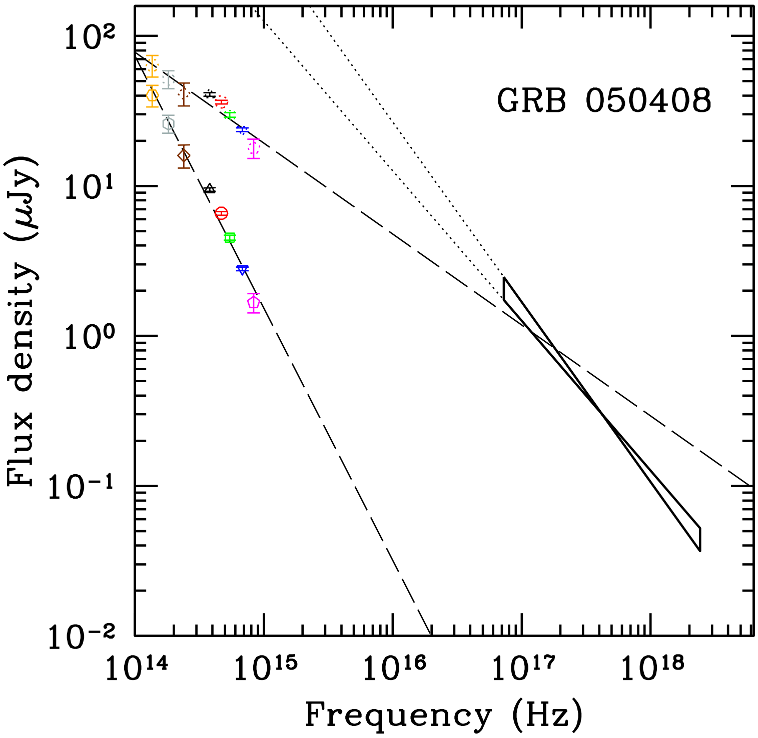
GRB 050408
Flux density (μJy)
Frequency (Hz)
10²
10¹
10⁰
10⁻¹
10⁻²
10¹⁴
10¹⁵
10¹⁶
10¹⁷
10¹⁸

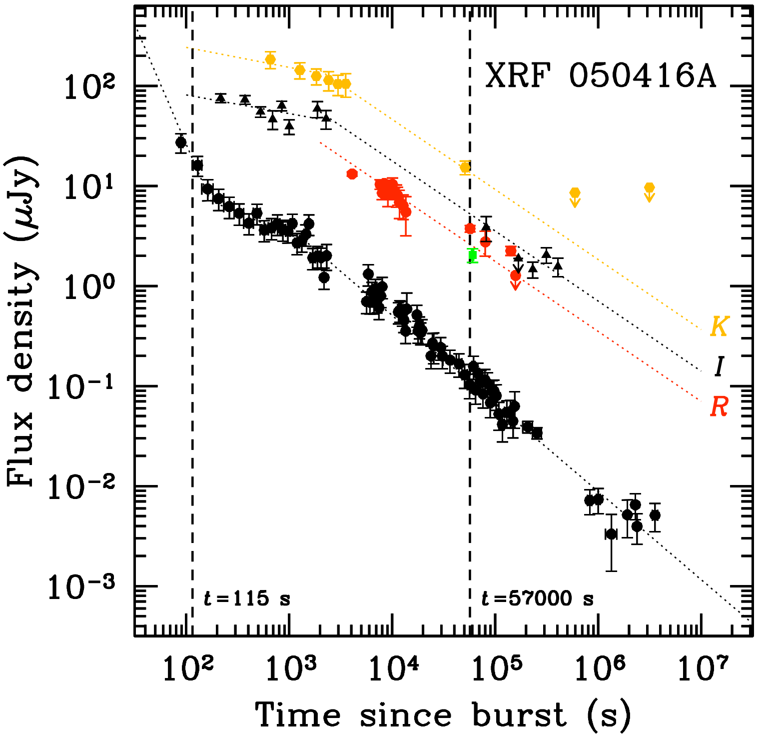
XRF 050416A
Flux density (μJy)
10^2
10^1
10^0
10^{-1}
10^{-2}
10^{-3}
Time since burst (s)
10^2
10^3
10^4
10^5
10^6
10^7
t=115 s
t=57000 s
K
I
R

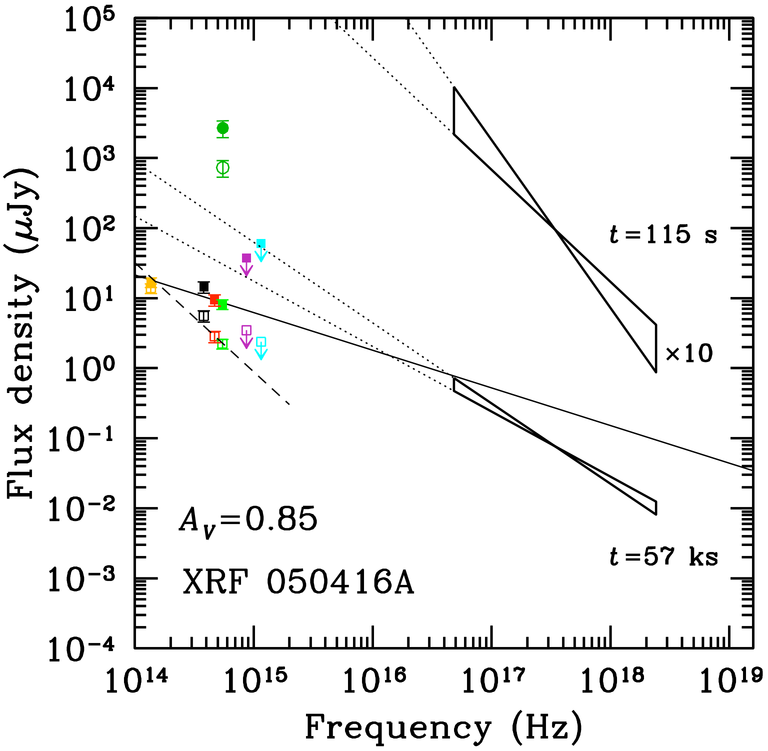
Flux density (μJy)
10^5
10^4
10^3
10^2
10^1
10^0
10^{-1}
10^{-2}
10^{-3}
10^{-4}
Frequency (Hz)
10^{14}
10^{15}
10^{16}
10^{17}
10^{18}
10^{19}
t=115 s
×10
t=57 ks
A_V=0.85
XRF 050416A

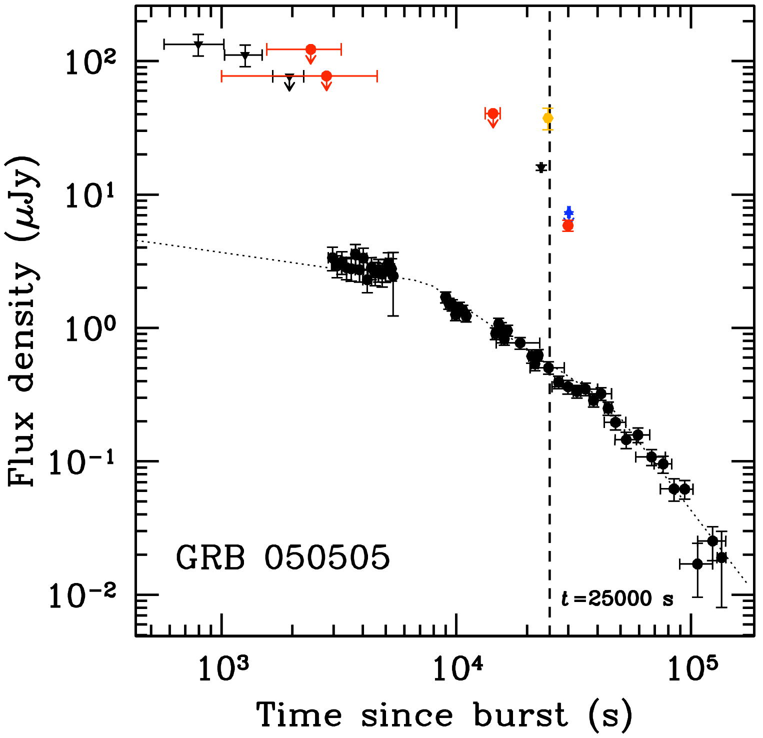
Flux density (μJy)
10^2
10^1
10^0
10^{-1}
10^{-2}
GRB 050505
t =25000 s
10^3
10^4
10^5
Time since burst (s)

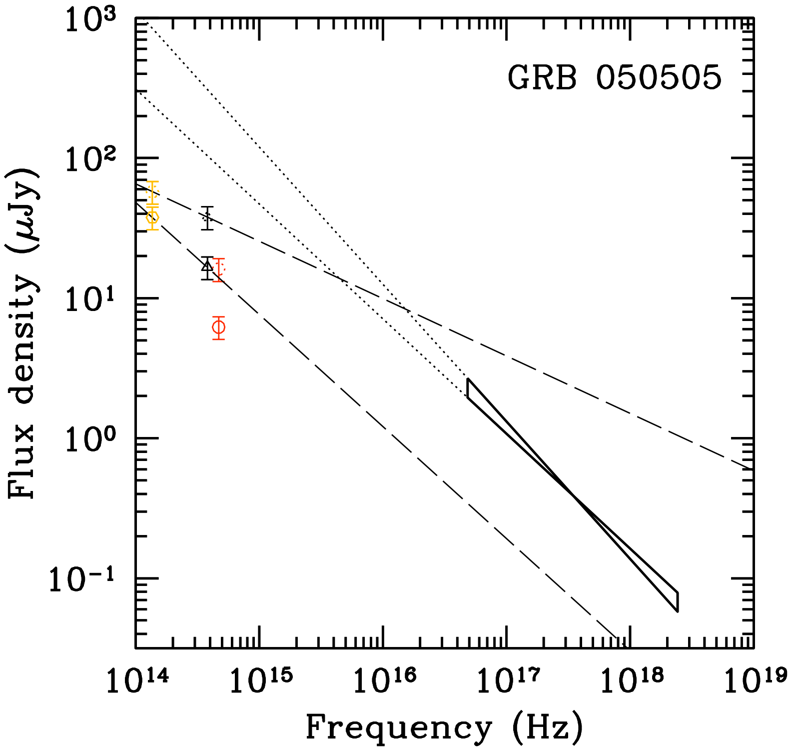
10^3
GRB 050505
Flux density (μJy)
10^2
10^1
10^0
10^{-1}
10^{14}
10^{15}
10^{16}
10^{17}
10^{18}
10^{19}
Frequency (Hz)

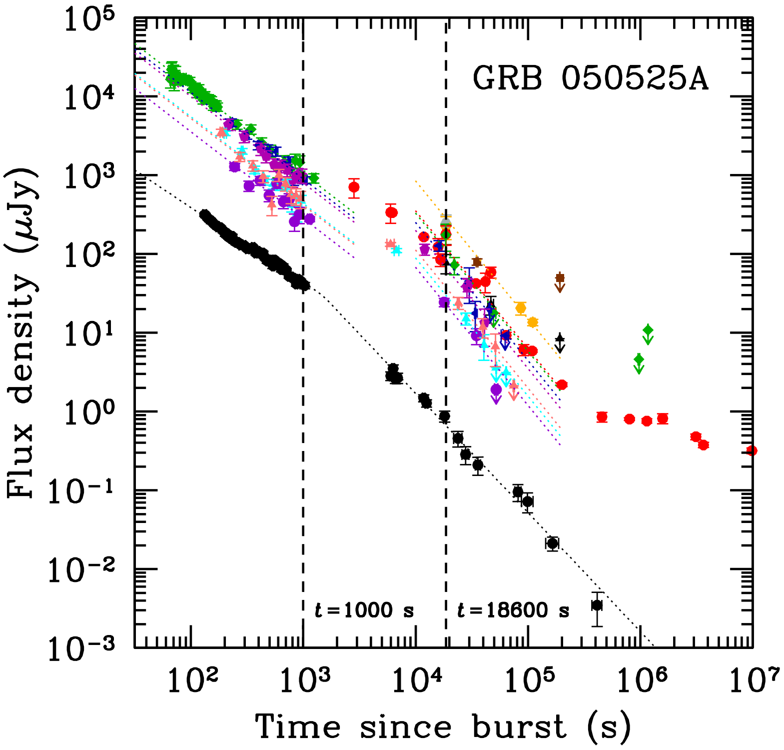
GRB 050525A
Flux density (μJy)
10^5
10^4
10^3
10^2
10^1
10^0
10^{-1}
10^{-2}
10^{-3}
Time since burst (s)
10^2
10^3
10^4
10^5
10^6
10^7
t = 1000 s
t = 18600 s

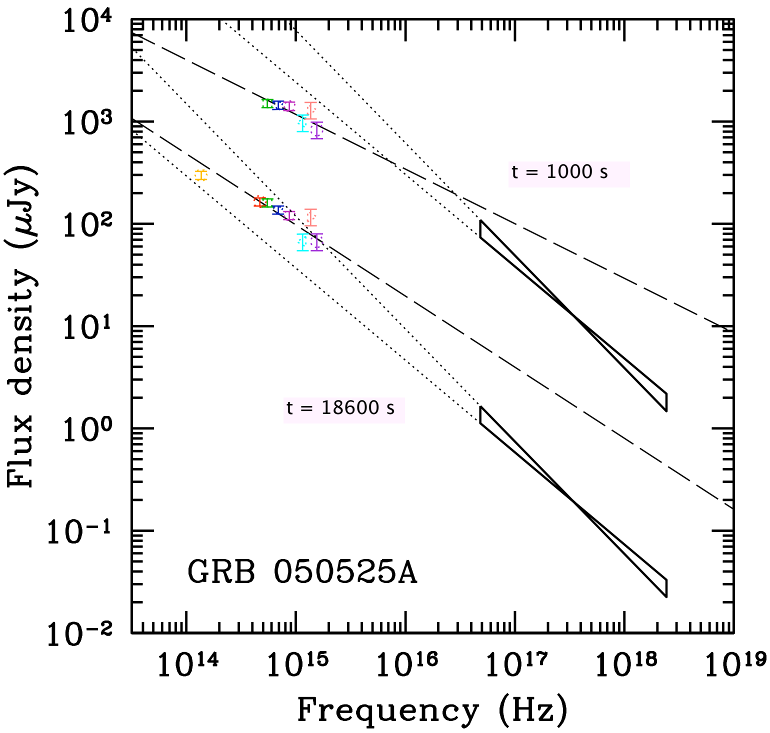
Flux density (μJy)
10^4
10^3
10^2
10^1
10^0
10^{-1}
10^{-2}
Frequency (Hz)
10^{14}
10^{15}
10^{16}
10^{17}
10^{18}
10^{19}
t = 1000 s
t = 18600 s
GRB 050525A

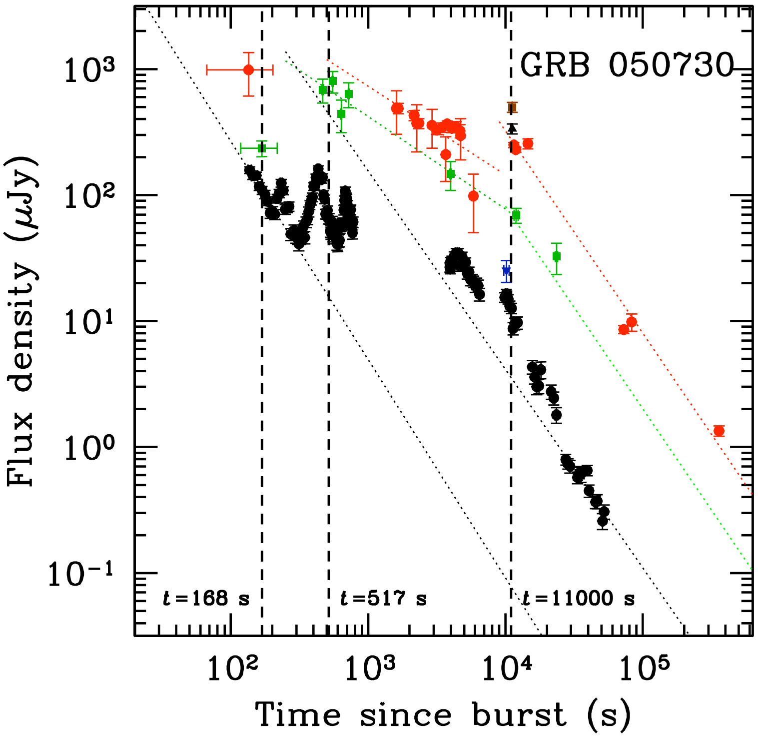
GRB 050730
Flux density (μJy)
Time since burst (s)
10^{3}
10^{2}
10^{1}
10^{0}
10^{-1}
10^{2}
10^{3}
10^{4}
10^{5}
t=168 s
t=517 s
t=11000 s

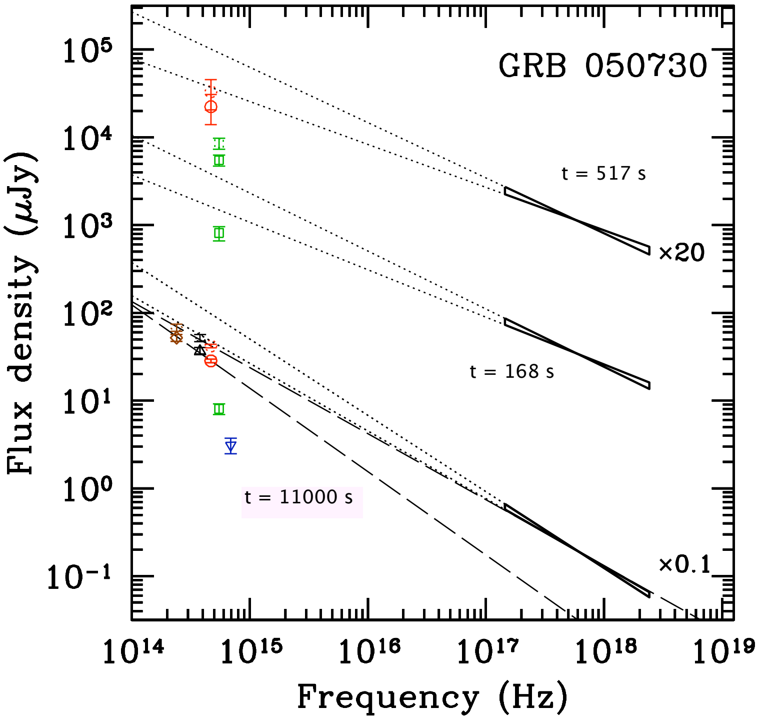
GRB 050730
Flux density (μJy)
Frequency (Hz)
10^{5}
10^{4}
10^{3}
10^{2}
10^{1}
10^{0}
10^{-1}
10^{14}
10^{15}
10^{16}
10^{17}
10^{18}
10^{19}
t = 517 s
×20
t = 168 s
t = 11000 s
×0.1

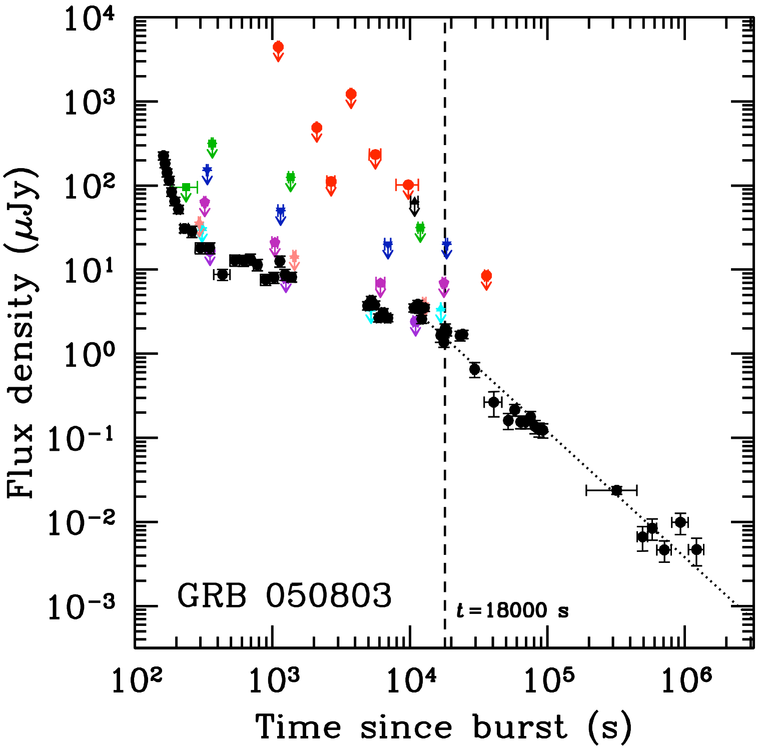
Flux density (μJy)
10^{4}
10^{3}
10^{2}
10^{1}
10^{0}
10^{-1}
10^{-2}
10^{-3}
GRB 050803
$t=18000$ s
10^{2}
10^{3}
10^{4}
10^{5}
10^{6}
Time since burst (s)

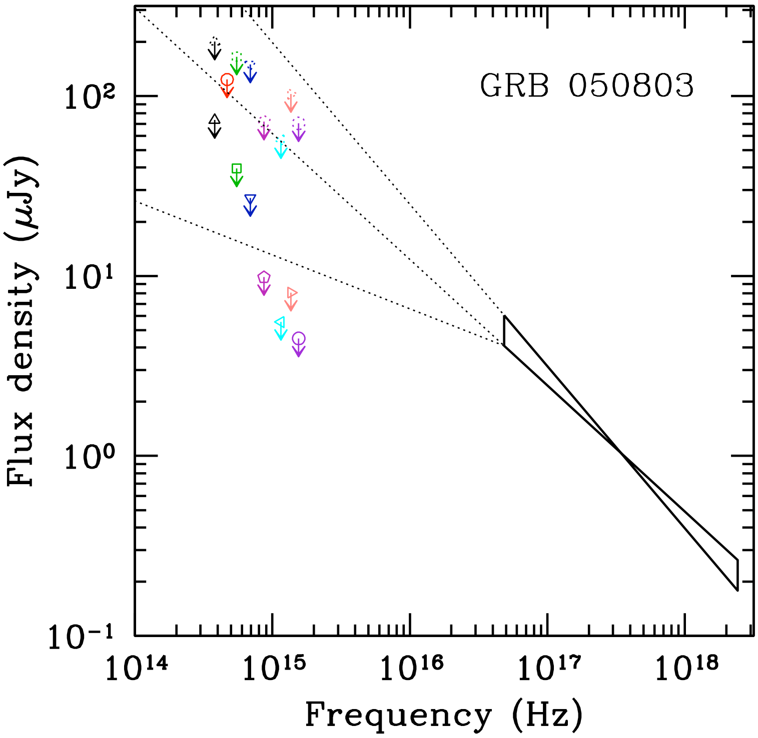
Flux density (μJy)
10^{2}
10^{1}
10^{0}
10^{-1}
GRB 050803
10^{14}
10^{15}
10^{16}
10^{17}
10^{18}
Frequency (Hz)

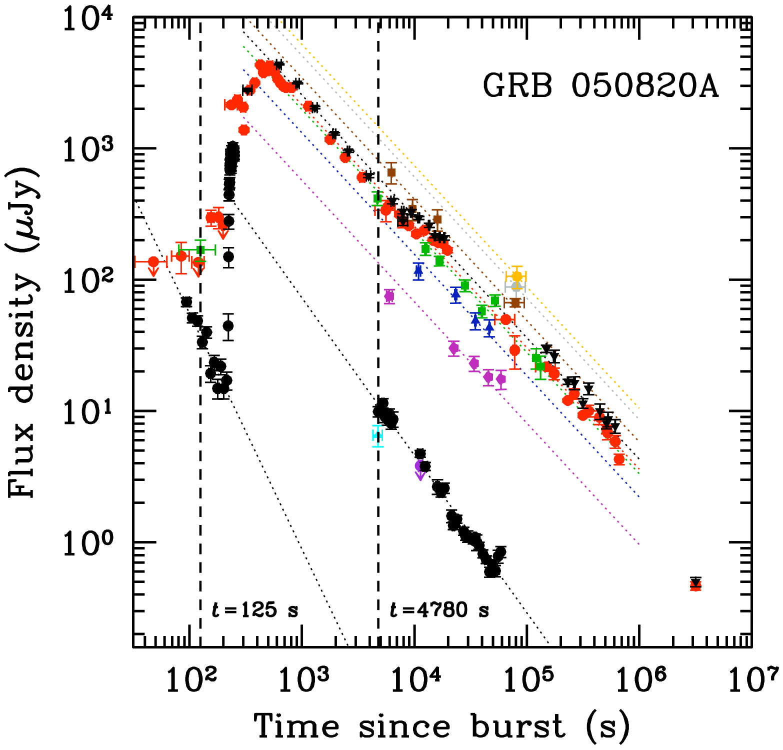
GRB 050820A
Flux density (μJy)
10⁴
10³
10²
10¹
10⁰
t=125 s
t=4780 s
10²
10³
10⁴
10⁵
10⁶
10⁷
Time since burst (s)

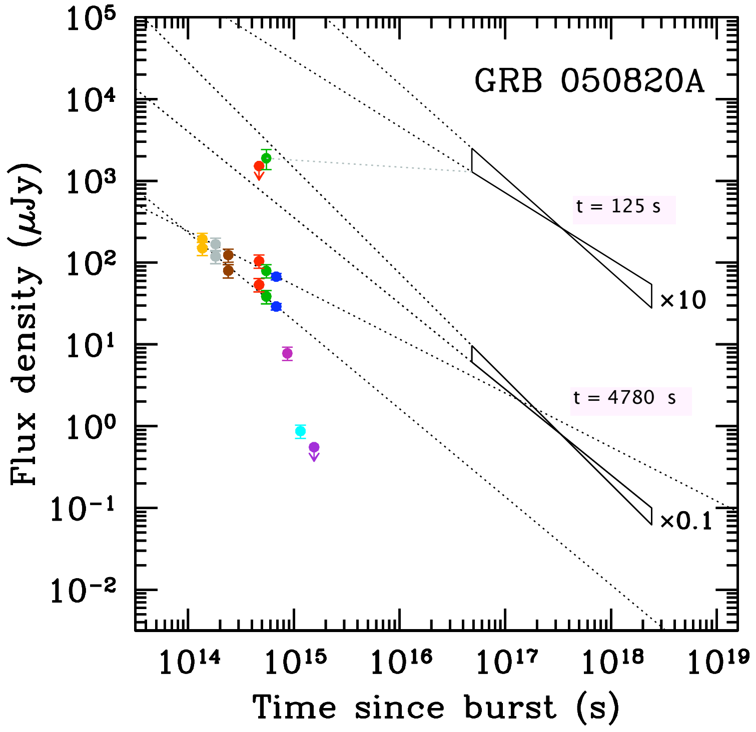
GRB 050820A
Flux density (μJy)
10⁵
10⁴
10³
10²
10¹
10⁰
10⁻¹
10⁻²
t = 125 s
×10
t = 4780 s
×0.1
10¹⁴
10¹⁵
10¹⁶
10¹⁷
10¹⁸
10¹⁹
Time since burst (s)

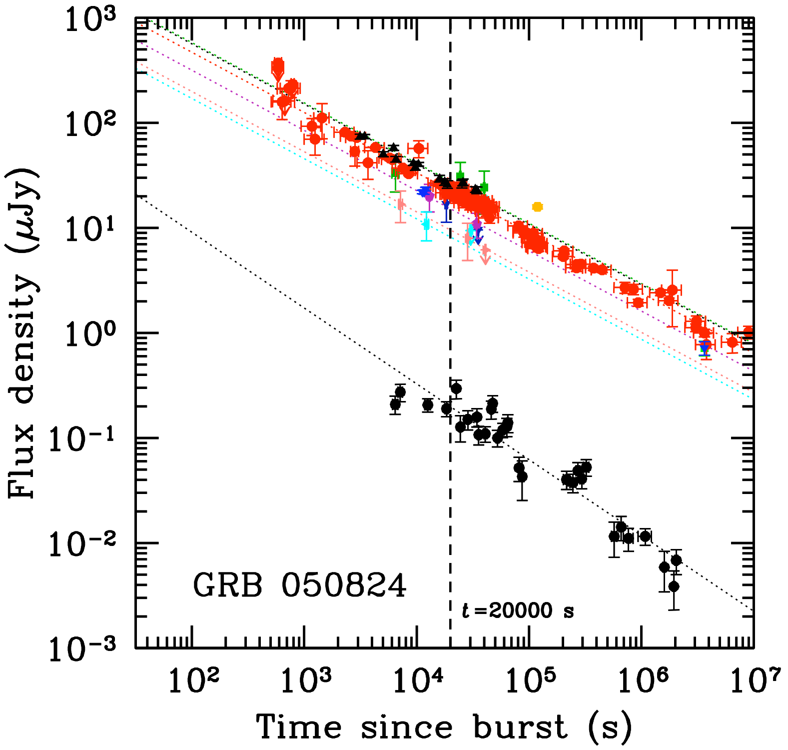
GRB 050824
t =20000 s
Flux density (μJy)
Time since burst (s)
10³
10²
10¹
10⁰
10⁻¹
10⁻²
10⁻³
10²
10³
10⁴
10⁵
10⁶
10⁷

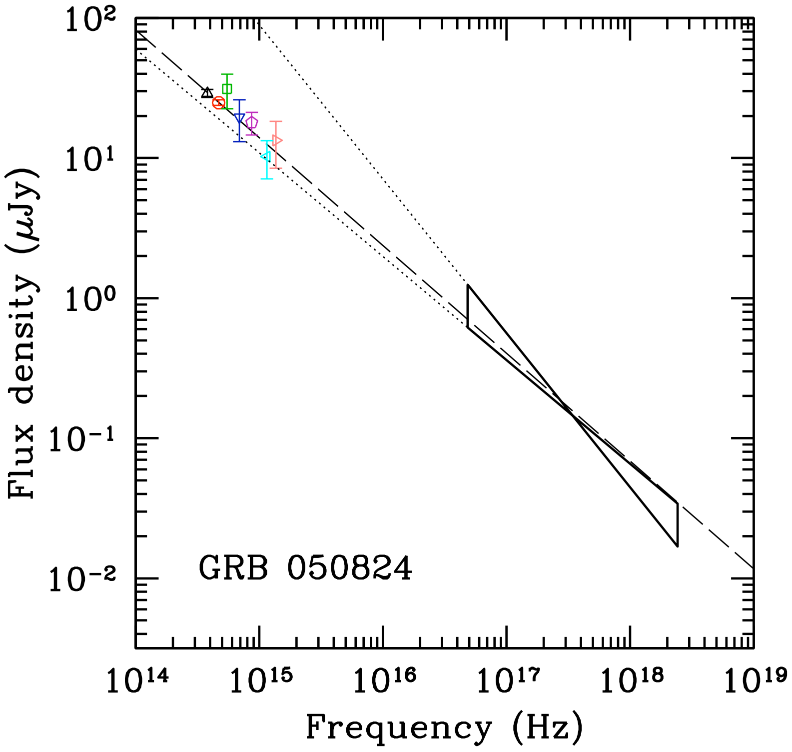
GRB 050824
Flux density (μJy)
Frequency (Hz)
10²
10¹
10⁰
10⁻¹
10⁻²
10¹⁴
10¹⁵
10¹⁶
10¹⁷
10¹⁸
10¹⁹

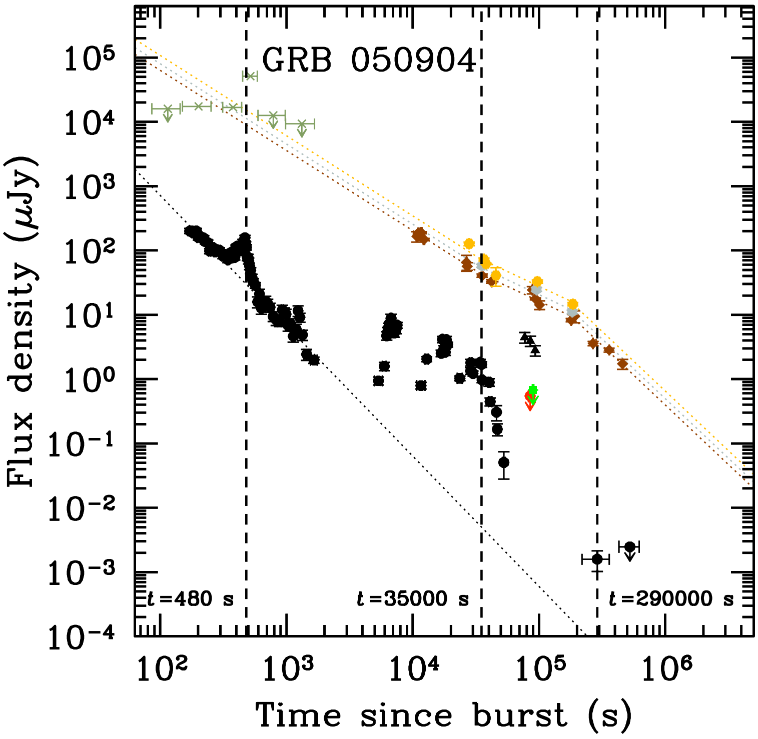
GRB 050904
t =480 s
t =35000 s
t =290000 s
Flux density (μJy)
10⁵
10⁴
10³
10²
10¹
10⁰
10⁻¹
10⁻²
10⁻³
10⁻⁴
10²
10³
10⁴
10⁵
10⁶
Time since burst (s)

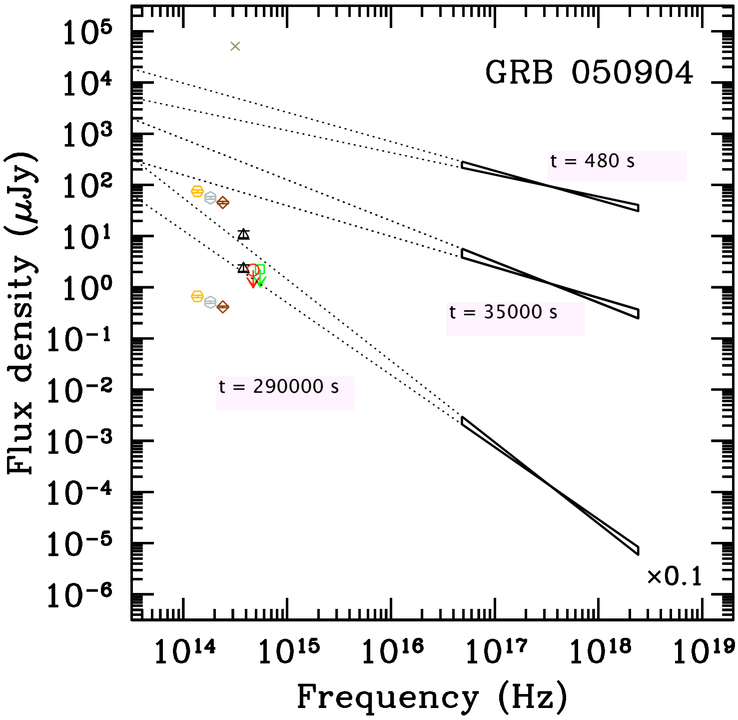
GRB 050904
t = 480 s
t = 35000 s
t = 290000 s
×0.1
Flux density (μJy)
10⁵
10⁴
10³
10²
10¹
10⁰
10⁻¹
10⁻²
10⁻³
10⁻⁴
10⁻⁵
10⁻⁶
10¹⁴
10¹⁵
10¹⁶
10¹⁷
10¹⁸
10¹⁹
Frequency (Hz)

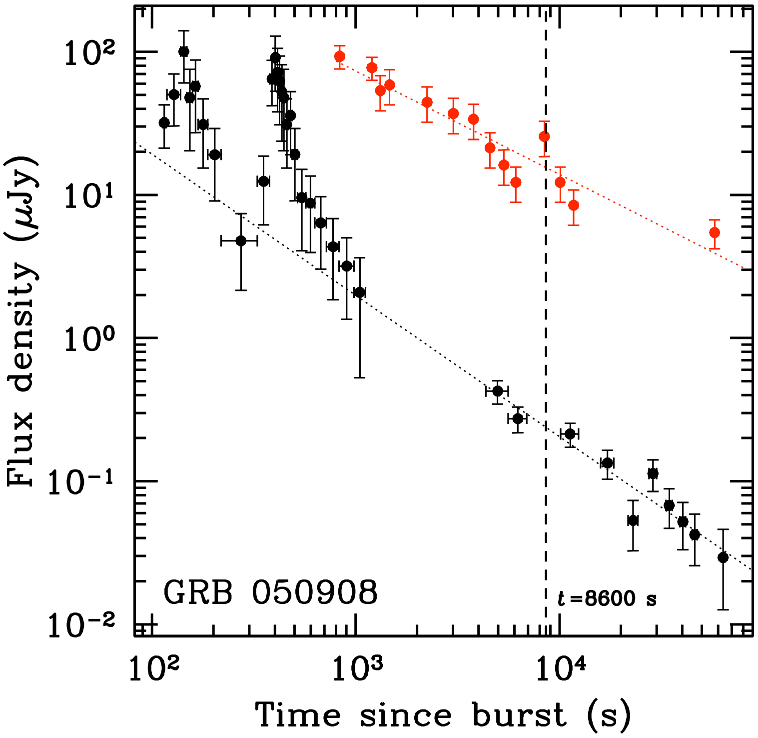
Flux density (μJy)
10²
10¹
10⁰
10⁻¹
10⁻²
10²
10³
10⁴
Time since burst (s)
GRB 050908
t = 8600 s

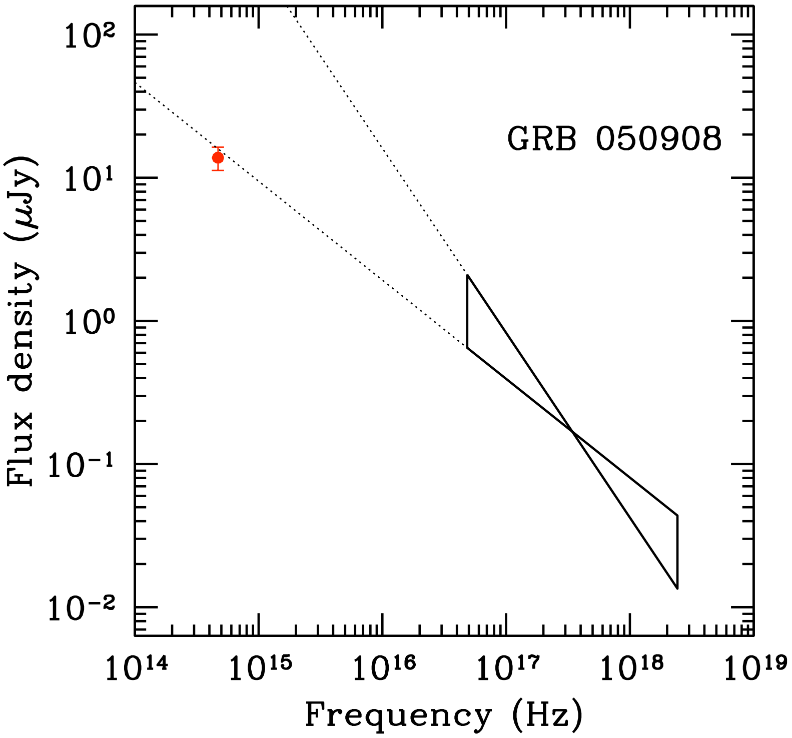
Flux density (μJy)
10²
10¹
10⁰
10⁻¹
10⁻²
10¹⁴
10¹⁵
10¹⁶
10¹⁷
10¹⁸
10¹⁹
Frequency (Hz)
GRB 050908

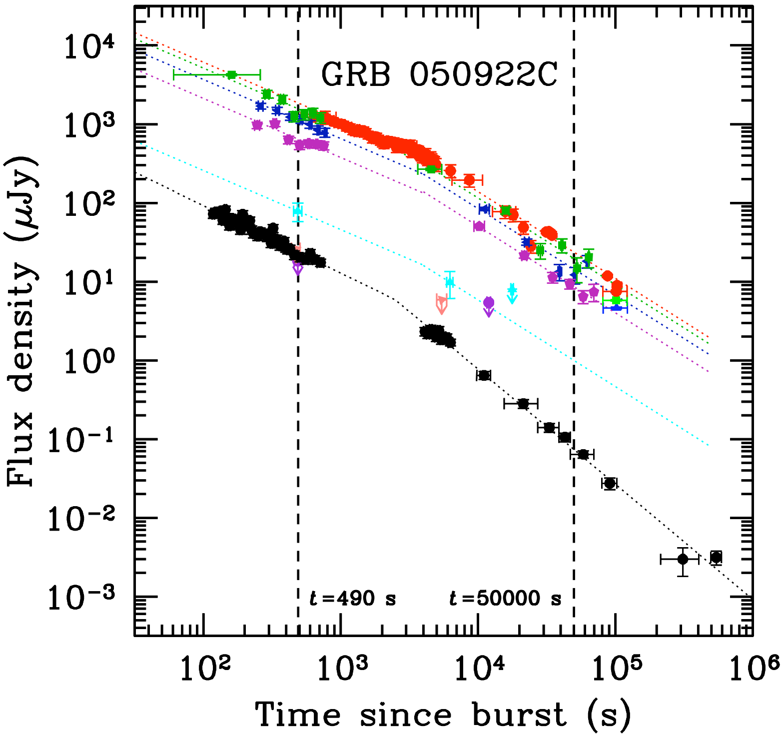
GRB 050922C
Flux density (μJy)
Time since burst (s)
t =490 s
t =50000 s
10⁴
10³
10²
10¹
10⁰
10⁻¹
10⁻²
10⁻³
10²
10³
10⁴
10⁵
10⁶

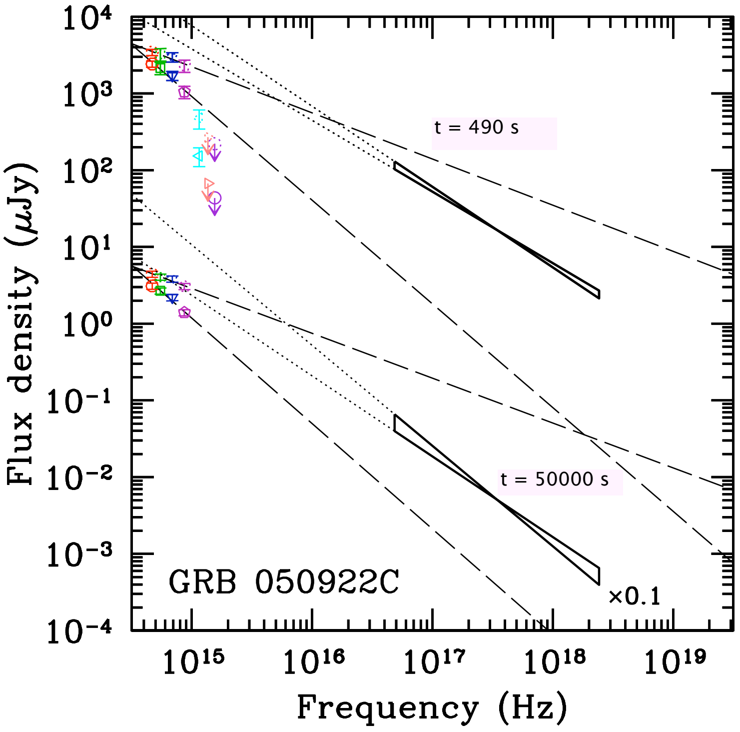
t = 490 s
t = 50000 s
×0.1
GRB 050922C
Flux density (μJy)
Frequency (Hz)
10⁴
10³
10²
10¹
10⁰
10⁻¹
10⁻²
10⁻³
10⁻⁴
10¹⁵
10¹⁶
10¹⁷
10¹⁸
10¹⁹

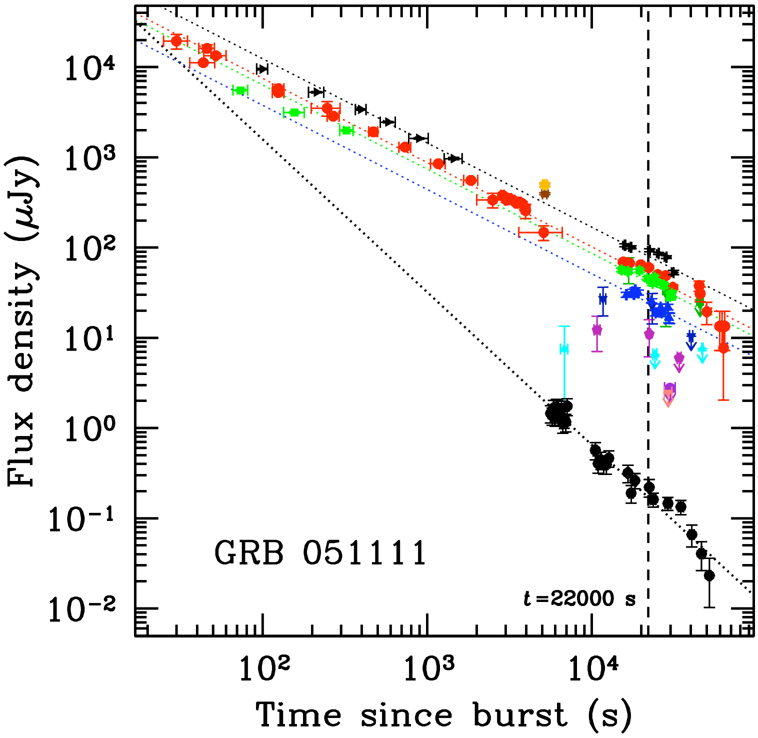
GRB 051111
t =22000 s
Flux density (μJy)
10⁴
10³
10²
10¹
10⁰
10⁻¹
10⁻²
10²
10³
10⁴
Time since burst (s)

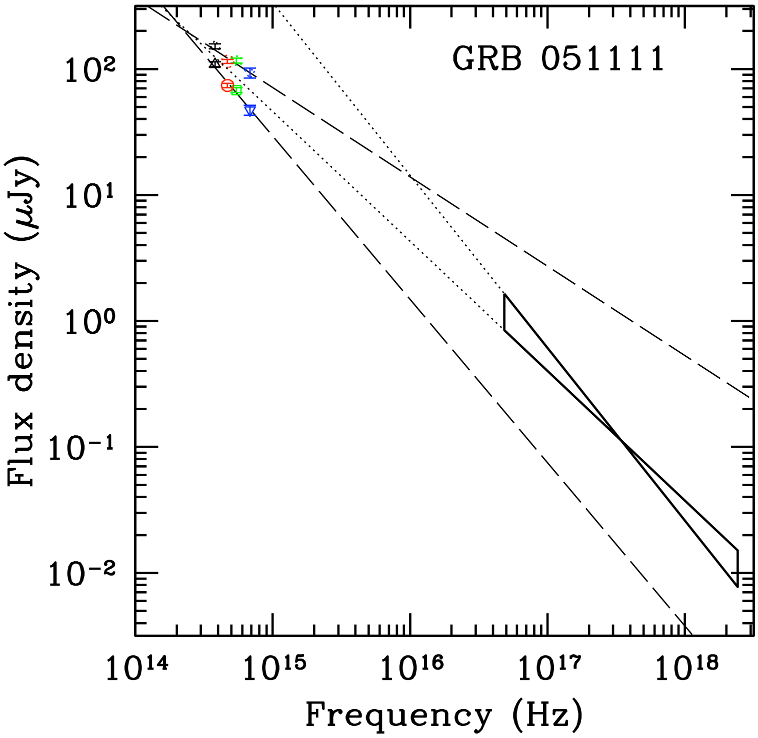
GRB 051111
Flux density (μJy)
10²
10¹
10⁰
10⁻¹
10⁻²
10¹⁴
10¹⁵
10¹⁶
10¹⁷
10¹⁸
Frequency (Hz)

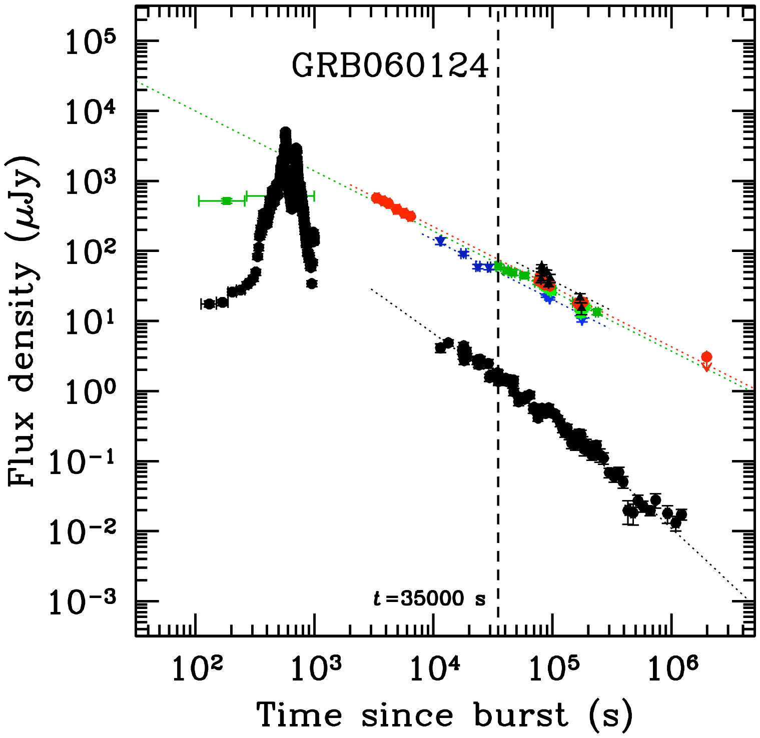
GRB060124
Flux density (μJy)
10⁵
10⁴
10³
10²
10¹
10⁰
10⁻¹
10⁻²
10⁻³
t = 35000 s
10²
10³
10⁴
10⁵
10⁶
Time since burst (s)

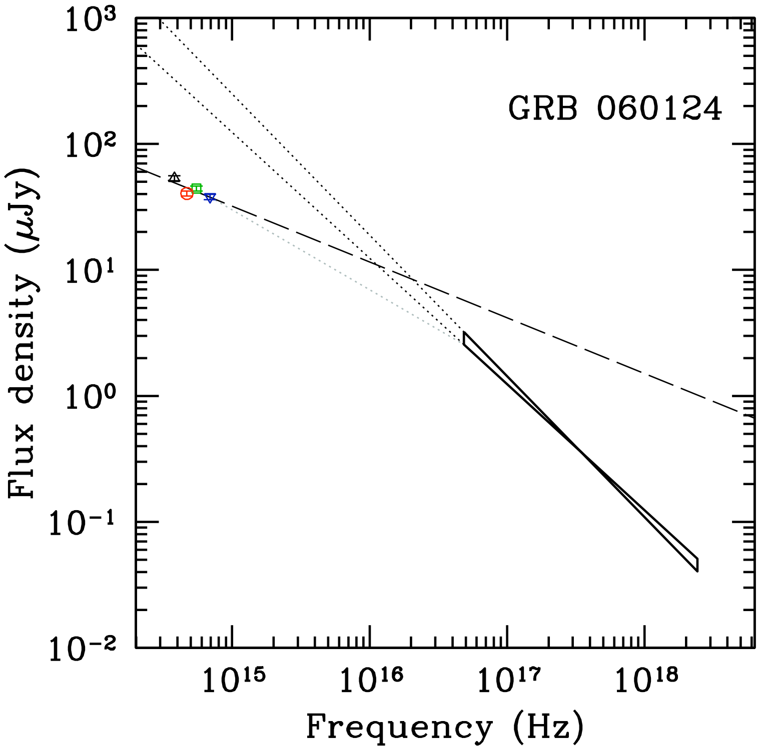
GRB 060124
Flux density (μJy)
10³
10²
10¹
10⁰
10⁻¹
10⁻²
10¹⁵
10¹⁶
10¹⁷
10¹⁸
Frequency (Hz)

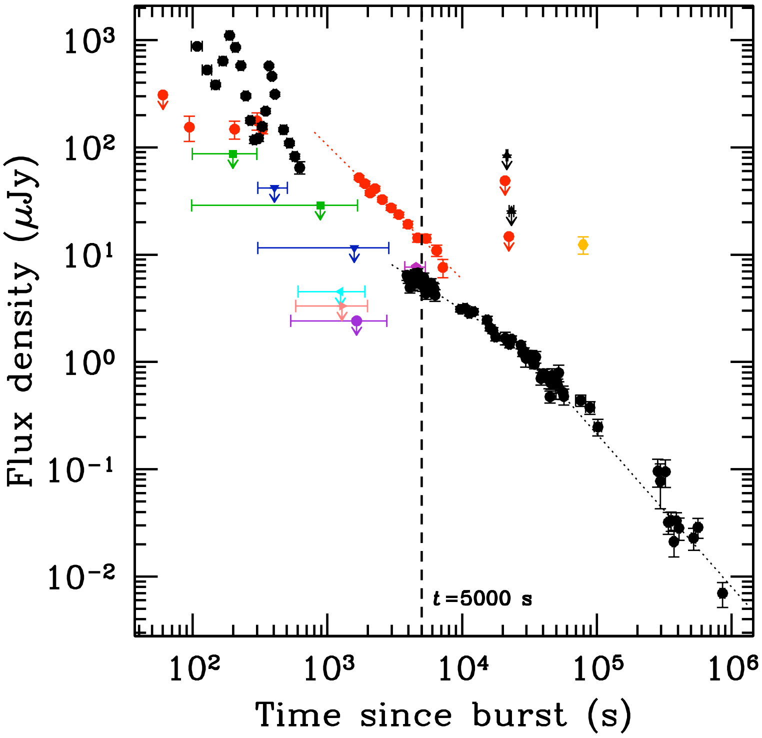

10^3
10^2
10^1
10^0
10^{-1}
10^{-2}
Flux density (μJy)
t =5000 s
10^2
10^3
10^4
10^5
10^6
Time since burst (s)

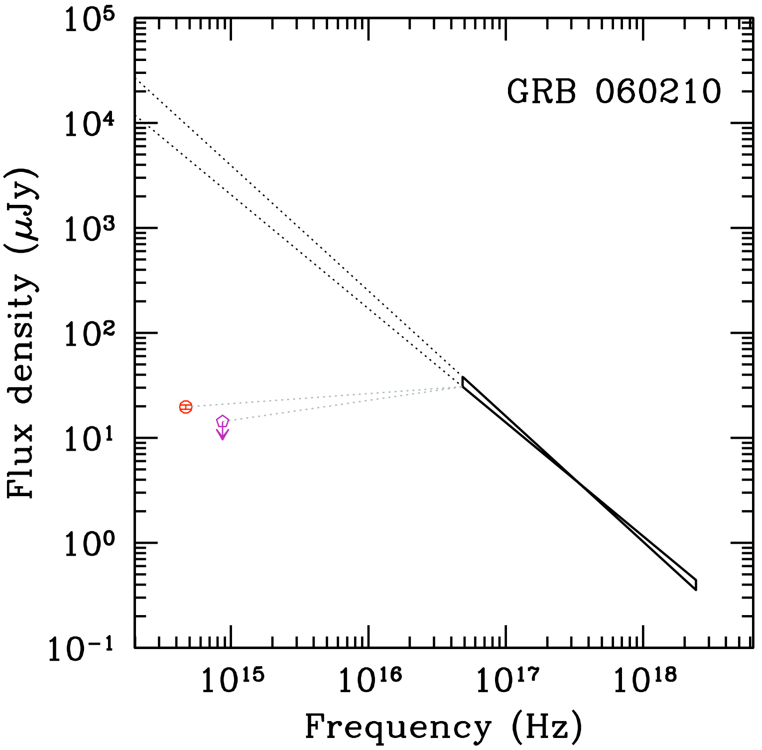

GRB 060210
10^5
10^4
10^3
10^2
10^1
10^0
10^{-1}
Flux density (μJy)
10^{15}
10^{16}
10^{17}
10^{18}
Frequency (Hz)

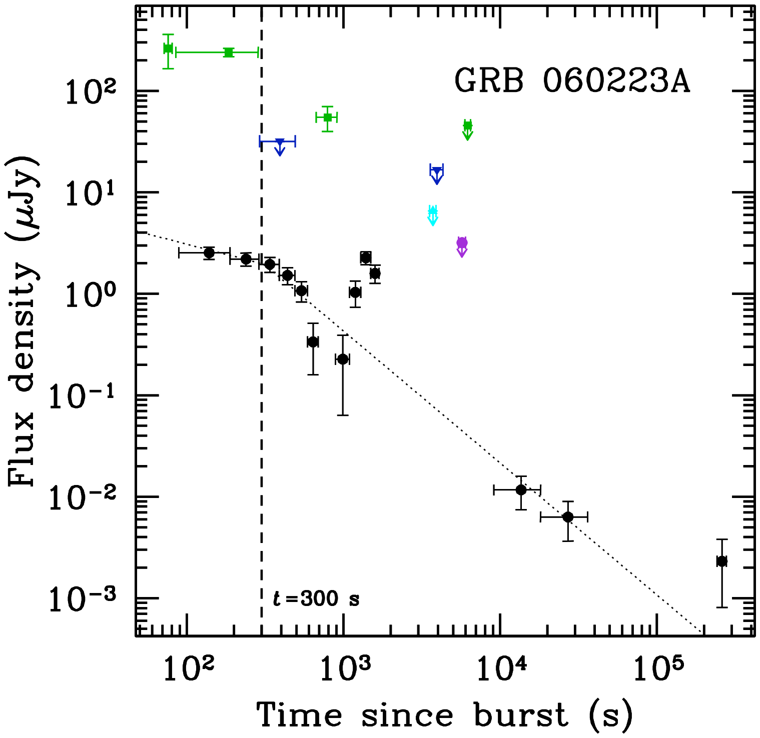
GRB 060223A
$t = 300$ s
Flux density (μJy)
10^{2}
10^{1}
10^{0}
10^{-1}
10^{-2}
10^{-3}
10^{2}
10^{3}
10^{4}
10^{5}
Time since burst (s)

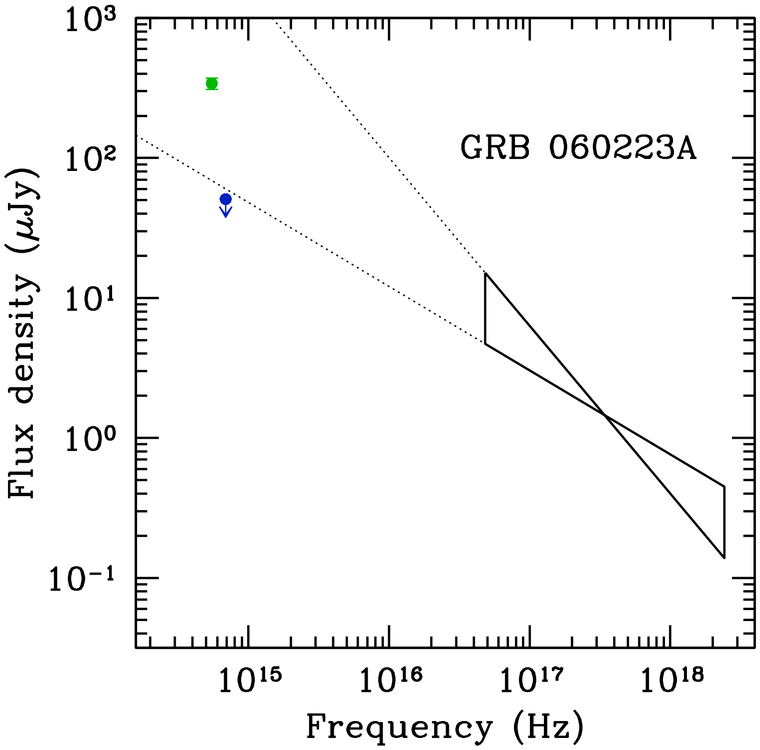
GRB 060223A
Flux density (μJy)
10^{3}
10^{2}
10^{1}
10^{0}
10^{-1}
10^{15}
10^{16}
10^{17}
10^{18}
Frequency (Hz)

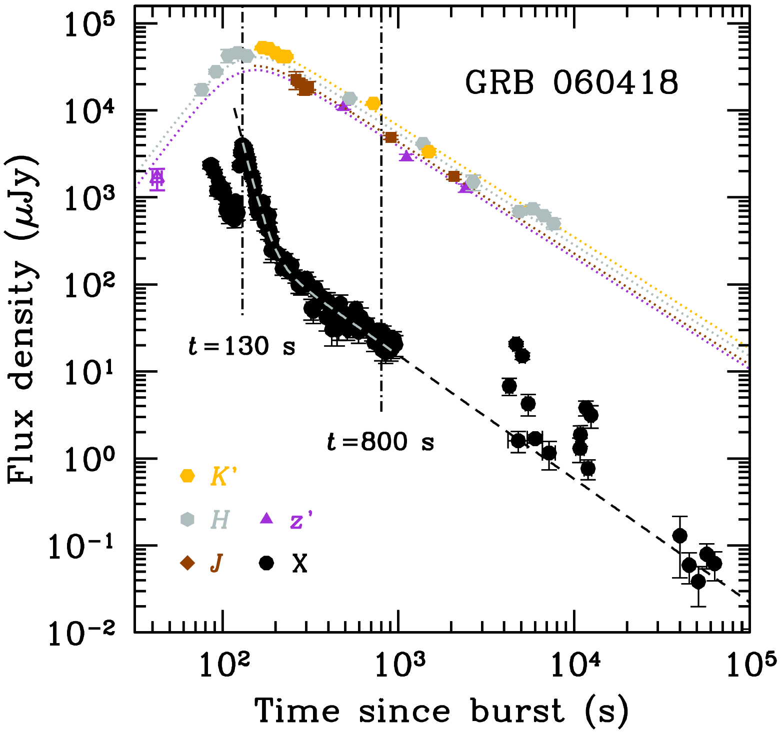
GRB 060418
Flux density (μJy)
Time since burst (s)
10^{-2}
10^{-1}
10^{0}
10^{1}
10^{2}
10^{3}
10^{4}
10^{5}
10^{2}
10^{3}
10^{4}
10^{5}
t = 130 s
t = 800 s
K'
H
z'
J
X

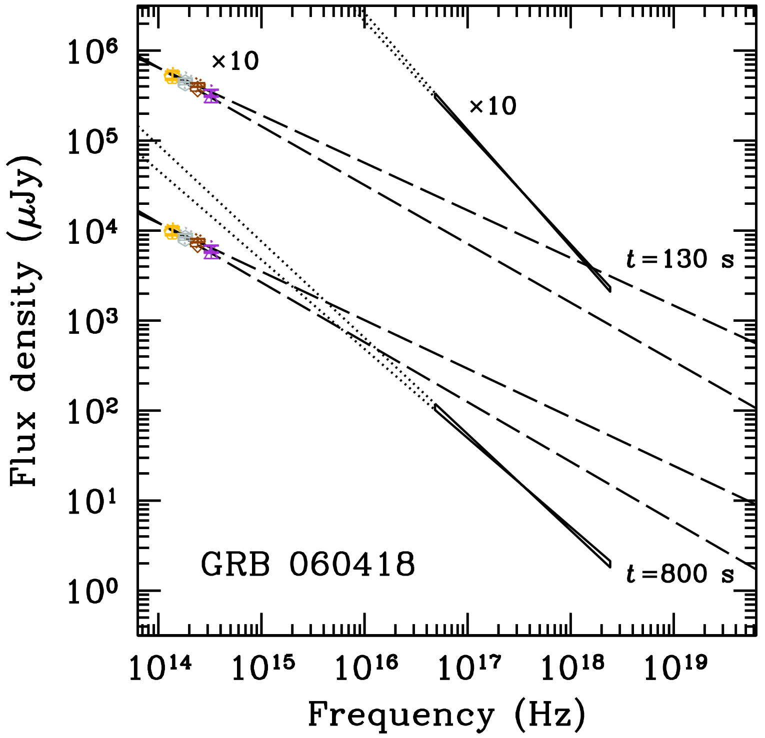
GRB 060418
Flux density (μJy)
Frequency (Hz)
10^{0}
10^{1}
10^{2}
10^{3}
10^{4}
10^{5}
10^{6}
10^{14}
10^{15}
10^{16}
10^{17}
10^{18}
10^{19}
×10
×10
t = 130 s
t = 800 s

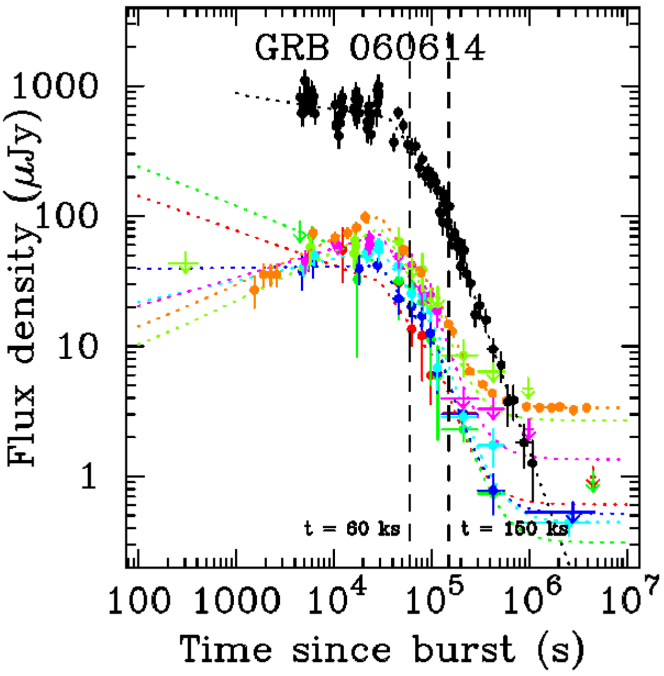
GRB 060614
1000
100
10
1
Flux density (μJy)
t = 60 ks
t = 150 ks
100
1000
10^4
10^5
10^6
10^7
Time since burst (s)

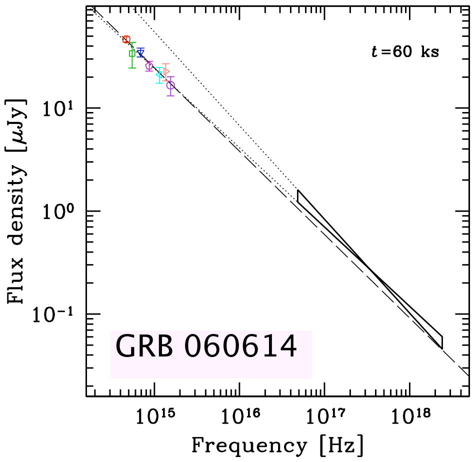
t=60 ks
10¹
10⁰
10⁻¹
Flux density [μJy]
GRB 060614
10¹⁵
10¹⁶
10¹⁷
10¹⁸
Frequency [Hz]

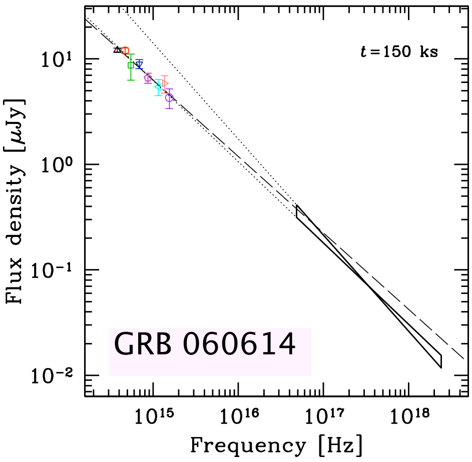
t=150 ks
10¹
10⁰
10⁻¹
10⁻²
Flux density [μJy]
GRB 060614
10¹⁵
10¹⁶
10¹⁷
10¹⁸
Frequency [Hz]

Bibliography

Achterberg, A., Gallant, Y. A., Kirk, J. G., & Guthmann, A. W. 2001, Monthly Notices of the RAS, 328, 393

Akerlof, C., Balsano, R., Barthelemy, S., et al. 1999, Nature, 398, 400

Amati, L. 2006, Monthly Notices of the RAS, 372, 233

Amati, L., Guidorzi, C., Frontera, F., et al. 2008, ArXiv e-prints, 0805.0377

Antonelli, L. A., Covino, S., Testa, V., et al. 2006, GRB Coordinates Network, 5546

Arabadjis, J. S. & Bregman, J. N. 1999, Astrophysical Journal, 510, 806

Ballester, P., Banse, K., Castro, S., et al. 2006, in Society of Photo-Optical Instrumentation Engineers (SPIE) Conference Series, Vol. 6270

Band, D., Matteson, J., Ford, L., et al. 1993, Astrophysical Journal, 413, 281

Baring, M. G. 2004, Nuclear Physics B Proceedings Supplements, 136, 198

Barth, A. J., Sari, R., Cohen, M. H., et al. 2003, Astrophysical Journal, Letters, 584, L47

Barthelmy, S. D. 2000, in Proc. SPIE, X-Ray and Gamma-Ray Instrumentation for Astronomy XI, ed. K. A. Flanagan & O. H. Siegmund, Vol. 4140, 50–63

Barthelmy, S. D., Chincarini, G., Burrows, D. N., et al. 2005, Nature, 438, 994

Baumgartner, W. H. & Mushotzky, R. F. 2006, Astrophysical Journal, 639, 929

Beardmore, A. P., Page, K. L., & Parsons, A. 2007, GRB Coordinates Network, 6610

Beardmore, A. P. & Parsons, A. 2007, GRB Coordinates Network, 6626

Belczynski, K., Bulik, T., & Rudak, B. 2002, Astrophysical Journal, 571, 394

Belczynski, K., Perna, R., Bulik, T., et al. 2006, Astrophysical Journal, 648, 1110

Berger, E. 2006, in American Institute of Physics Conference Series, Vol. 836, Gamma-Ray Bursts in the Swift Era, ed. S. S. Holt, N. Gehrels, & J. A. Nousek, 33–42

Berger, E. 2007, Astrophysical Journal, 670, 1254

Berger, E., Fox, D. B., Price, P. A., et al. 2007, Astrophysical Journal, 664, 1000

Berger, E., Kulkarni, S. R., Bloom, J. S., et al. 2002, Astrophysical Journal, 581, 981

Berger, E., Penprase, B. E., Cenko, S. B., et al. 2006, Astrophysical Journal, 642, 979

Berger, E., Price, P. A., Cenko, S. B., et al. 2005, Nature, 438, 988

Bersier, D., Stanek, K. Z., Winn, J. N., et al. 2003, Astrophysical Journal, Letters, 584, L43

Beuermann, K., Hessman, F. V., Reinsch, K., et al. 1999, Astronomy and Astrophysics, 352, L26

Bhattacharya, D. 2001, Bulletin of the Astronomical Society of India, 29, 107

Bianco, C. L. & Ruffini, R. 2005, Astrophysical Journal, Letters, 620, L23

Bjorkman, J. E. & Cassinelli, J. P. 1993, Astrophysical Journal, 409, 429

Blake, C. H., Bloom, J. S., Starr, D. L., et al. 2005, Nature, 435, 181

Blandford, R. D. & McKee, C. F. 1976, Physics of Fluids, 19, 1130

Bloom, J. S. 2007, GRB Coordinates Network, 6191

Bloom, J. S., Dupree, A., Chen, H.-W., & Prochaska, J. X. 2005, GRB Coordinates Network, 3672

Bloom, J. S., Frail, D. A., & Kulkarni, S. R. 2003, Astrophysical Journal, 594, 674

Bloom, J. S., Kulkarni, S. R., & Djorgovski, S. G. 2002, Astronomical Journal, 123, 1111

Bloom, J. S., Kulkarni, S. R., Djorgovski, S. G., et al. 1999, Nature, 401, 453

Bloom, J. S., Perley, D. A., Chen, H.-W., et al. 2007, Astrophysical Journal, 654, 878

Bloom, J. S., Perley, D. A., Li, W., et al. 2008, ArXiv e-prints, 0803.3215

Bloom, J. S., Prochaska, J. X., Pooley, D., et al. 2006, Astrophysical Journal, 638, 354

Blustin, A. J., Band, D., Barthelmy, S., et al. 2006, Astrophysical Journal, 637, 901

Boër, M., Atteia, J. L., Damerdji, Y., et al. 2006, Astrophysical Journal, Letters, 638, L71

Bohlin, R. C., Savage, B. D., & Drake, J. F. 1978, Astrophysical Journal, 224, 132

Bringer, M., Boër, M., Peignot, C., Fontan, G., & Merce, C. 1999, Astronomy and Astrophysics, Supplement, 138, 581

Burrows, D. N., Hill, J. E., Nousek, J. A., et al. 2000, in Proc. SPIE, X-Ray and Gamma-Ray Instrumentation for Astronomy XI, ed. K. A. Flanagan & O. H. Siegmund, Vol. 4140, 64–75

Burrows, D. N., Romano, P., Falcone, A., et al. 2005, Science, 309, 1833

Butler, N. R. & Kocevski, D. 2007a, Astrophysical Journal, 663, 407

Butler, N. R. & Kocevski, D. 2007b, Astrophysical Journal, 668, 400

Butler, N. R., Li, W., Perley, D., et al. 2006, Astrophysical Journal, 652, 1390

Calzetti, D., Kinney, A. L., & Storchi-Bergmann, T. 1994, Astrophysical Journal, 429, 582

Cameron, E. & Driver, S. P. 2007, Monthly Notices of the RAS, 377, 523

Cameron, P. B. & Frail, D. A. 2005, GRB Coordinates Network, 3676

Campana, S., Lazzati, D., Ripamonti, E., et al. 2007, Astrophysical Journal, Letters, 654, L17

Campana, S., Panagia, N., Lazzati, D., et al. 2008, Astrophysical Journal, Letters, 683, L9

Campana, S., Tagliaferri, G., Lazzati, D., et al. 2006, Astronomy and Astrophysics, 454, 113

Castro, S., Galama, T. J., Harrison, F. A., et al. 2003, Astrophysical Journal, 586, 128

Castro-Tirado, A. J., de Ugarte Postigo, A., Gorosabel, J., et al. 2005a, Astronomy and Astrophysics, 439, L15

Castro-Tirado, A. J. & Gorosabel, J. 1999, Astronomy and Astrophysics, Supplement, 138, 449

Castro-Tirado, A. J., Gorosabel, J., de Ugarte Postigo, A., et al. 2005b, GRB Coordinates Network, 3673

Castro-Tirado, A. J., Zapatero-Osorio, M. R., Caon, N., et al. 1999, Science, 283, 2069

Cen, R., Miralda-Escudé, J., Ostriker, J. P., & Rauch, M. 1994, Astrophysical Journal, Letters, 437, L9

Cenko, S. B. 2007, GRB Coordinates Network, 6196

Cenko, S. B., Kasliwal, M., Harrison, F. A., et al. 2006, Astrophysical Journal, 652, 490

Chen, H.-W., Perley, D. A., Pollack, L. K., et al. 2008, ArXiv e-prints, 0809.2608

Chen, H.-W., Prochaska, J. X., Ramirez-Ruiz, E., et al. 2007, Astrophysical Journal, 663, 420

Chester, M., Covino, S., Schady, P., Roming, P., & Gehrels, N. 2005, GRB Coordinates Network, 3670

Chevalier, R. A. & Li, Z.-Y. 2000, Astrophysical Journal, 536, 195

Chincarini, G., Moretti, A., Romano, P., et al. 2007, Astrophysical Journal, 671, 1903

Chincarini, G., Zerbi, F., Antonelli, A., et al. 2003, The Messenger, 113, 40

Christensen, L., Hjorth, J., & Gorosabel, J. 2004, Astronomy and Astrophysics, 425, 913

Cobb, B. E. & Bailyn, C. D. 2005, GRB Coordinates Network, 3694

Costa, E., Frontera, F., Heise, J., et al. 1997, Nature, 387, 783

Covino, S., Antonelli, L. A., Calzoletti, L., et al. 2007, GRB Coordinates Network, 6190

Covino, S., Antonelli, L. A., Molinari, E., et al. 2006a, GRB Coordinates Network, 4967

Covino, S., Antonelli, L. A., Romano, P., et al. 2005, GRB Coordinates Network, 3665

Covino, S., D'Avanzo, P., Klotz, A., et al. 2008, Monthly Notices of the RAS, 388, 347

Covino, S., di Stefano, E., Molinari, E., et al. 2006b, GRB Coordinates Network, 5234

Covino, S., Lazzati, D., Ghisellini, G., et al. 1999, Astronomy and Astrophysics, 348, L1

Covino, S., Malesani, D., Israel, G. L., et al. 2006c, Astronomy and Astrophysics, 447, L5

Covino, S., Stefanon, M., Sciuto, G., et al. 2004, in Proceedings of the SPIE, Volume 5492, pp. 1613-1622, ed. A. F. M. Moorwood & M. Iye

Crowther, P. A. 2007, Annual Review of Astronomy and Astrophysics, 45, 177

Cucchiara, A. & Fox, D. B. 2008, GRB Coordinates Network, 7456

Cummings, J., Barbier, L., Barthelmy, S., et al. 2006, GRB Coordinates Network, 4975

Cusumano, G., Mangano, V., Angelini, L., et al. 2006, Astrophysical Journal, 639, 316

Cusumano, G., Mangano, V., Chincarini, G., et al. 2007, Astronomy and Astrophysics, 462, 73

Dado, S., Dar, A., & De Rújula, A. 2007, Astrophysical Journal, 663, 400

Dai, X., Garnavich, P., Pogge, R., et al. 2007, GRB Coordinates Network, 6219

de Ugarte Postigo, A., Fatkhullin, T. A., Jóhannesson, G., et al. 2007, Astronomy and Astrophysics, 462, L57

D'Elia, V., Fiore, F., Meurs, E. J. A., et al. 2007, Astronomy and Astrophysics, 467, 629

D'Elia, V., Fiore, F., Perna, R., et al. 2008, ArXiv e-prints, 0804.2141

Della Valle, M., Chincarini, G., Panagia, N., et al. 2006a, Nature, 444, 1050

Della Valle, M., Malesani, D., Bloom, J. S., et al. 2006b, Astrophysical Journal, Letters, 642, L103

Dermer, C. D. 2004, Astrophysical Journal, 614, 284

Dermer, C. D. 2007, Astrophysical Journal, 664, 384

Dermer, C. D. & Mitman, K. E. 1999, Astrophysical Journal, Letters, 513, L5

Detmers, R. G., Langer, N., Podsiadlowski, P., & Izzard, R. G. 2008, Astronomy and Astrophysics, 484, 831

Djorgovski, S. G., Kulkarni, S. R., Bloom, J. S., et al. 1998, Astrophysical Journal, Letters, 508, L17

Dolcini, A., Farfanelli, F., Ciprini, S., et al. 2007, Astronomy and Astrophysics, 469, 503

Draine, B. T. & Salpeter, E. E. 1979, Astrophysical Journal, 231, 438

Dupree, A. K., Falco, E., Prochaska, J. X., Chen, H.-W., & Bloom, J. S. 2006, GRB Coordinates Network, 4969

Eichler, D. & Jontof-Hutter, D. 2005, Astrophysical Journal, 635, 1182

Eichler, D., Livio, M., Piran, T., & Schramm, D. N. 1989, Nature, 340, 126

Eldridge, J. J. 2007, Monthly Notices of the RAS, 377, L29

Eldridge, J. J., Genet, F., Daigne, F., & Mochkovitch, R. 2006, Monthly Notices of the RAS, 367, 186

Elíasdóttir, Á., Fynbo, J. P. U., Hjorth, J., et al. 2008, ArXiv e-prints, 0810.2897

Ellison, S. L., Churchill, C. W., Rix, S. A., & Pettini, M. 2004, Astrophysical Journal, 615, 118

Ellison, S. L., Vreeswijk, P., Ledoux, C., et al. 2006, Monthly Notices of the RAS, 372, L38

Evans, P. A., Barthelmy, S. D., Beardmore, A. P., et al. 2006, GRB Coordinates Network, 5544

Falcone, A. D., Barthelmy, S. D., Burrows, D. N., et al. 2006a, GRB Coordinates Network, 4966

Falcone, A. D., Burrows, D. N., & Kennea, J. 2006b, GRB Coordinates Network, 4973

Falcone, A. D., Burrows, D. N., Lazzati, D., et al. 2006c, Astrophysical Journal, 641, 1010

Fall, S. M. & Pei, Y. C. 1993, Astrophysical Journal, 402, 479

Fan, Y. Z., Wei, D. M., & Zhang, B. 2004, Monthly Notices of the RAS, 354, 1031

Fan, Y. Z., Zhang, B., & Wei, D. M. 2005, Astrophysical Journal, Letters, 628, L25

Fenimore, E. E., Madras, C. D., & Nayakshin, S. 1996, Astrophysical Journal, 473, 998

Fenimore, E. E., Ramirez-Ruiz, E., & Wu, B. 1999, Astrophysical Journal, Letters, 518, L73

Fiore, F., D'Elia, V., Lazzati, D., et al. 2005, Astrophysical Journal, 624, 853

Fishman, G. J. & Meegan, C. A. 1995, Annual Review of Astronomy and Astrophysics, 33, 415

Foley, R. J., Perley, D. A., Pooley, D., et al. 2006, Astrophysical Journal, 645, 450

Fontana, A. & Ballester, P. 1995, The Messenger, 80, 37

Ford, L. A., Band, D. L., Matteson, J. L., et al. 1995, Astrophysical Journal, 439, 307

Fox, D. B., Frail, D. A., Price, P. A., et al. 2005, Nature, 437, 845

Fox, D. W., Price, P. A., Soderberg, A. M., et al. 2003, Astrophysical Journal, Letters, 586, L5

Frail, D. A., Kulkarni, S. R., Costa, E., et al. 1997, Astrophysical Journal, Letters, 483, L91

Frail, D. A., Kulkarni, S. R., Sari, R., et al. 2001, Astrophysical Journal, Letters, 562, L55

Frail, D. A., Waxman, E., & Kulkarni, S. R. 2000, Astrophysical Journal, 537, 191

Frederiks, D. D., Palshin, V. D., Aptekar, R. L., et al. 2007, Astronomy Letters, 33, 19

Fruchter, A., Krolik, J. H., & Rhoads, J. E. 2001, Astrophysical Journal, 563, 597

Fruchter, A. S., Levan, A. J., Strolger, L., et al. 2006, Nature, 441, 463

Fryer, C. L. & Heger, A. 2005, Astrophysical Journal, 623, 302

Fryer, C. L., Rockefeller, G., & Young, P. A. 2006, Astrophysical Journal, 647, 1269

Fryer, C. L., Woosley, S. E., & Hartmann, D. H. 1999, Astrophysical Journal, 526, 152

Fuhrmann, L., Cucchiara, A., Marchili, N., et al. 2006, Astronomy and Astrophysics, 445, L1

Fynbo, J. P. U., Greiner, J., Kruehler, T., et al. 2008a, GRB Coordinates Network, 8225

Fynbo, J. P. U., Jakobsson, P., Möller, P., et al. 2003, Astronomy and Astrophysics, 406, L63

Fynbo, J. P. U., Prochaska, J. X., Sommer-Larsen, J., Dessauges-Zavadsky, M., & Møller, P. 2008b, Astrophysical Journal, 683, 321

Fynbo, J. P. U., Starling, R. L. C., Ledoux, C., et al. 2006a, Astronomy and Astrophysics, 451, L47

Fynbo, J. P. U., Watson, D., Thöne, C. C., et al. 2006b, Nature, 444, 1047

Fynbo, J. U., Jensen, B. L., Gorosabel, J., et al. 2001, Astronomy and Astrophysics, 369, 373

Gabasch, A., Bender, R., Seitz, S., et al. 2004, Astronomy and Astrophysics, 421, 41

Gal-Yam, A., Cenko, S. B., Berger, E., Krzeminski, W., & Lee, B. 2005, GRB Coordinates Network, 3681, 1

Gal-Yam, A., Fox, D. B., Price, P. A., et al. 2006, Nature, 444, 1053

Galama, T. J., Groot, P. J., van Paradijs, J., et al. 1998, Astrophysical Journal, Letters, 497, L13

Galama, T. J. & Wijers, R. A. M. J. 2001, Astrophysical Journal, Letters, 549, L209

Garnavich, P., Dai, X., Pogge, R., et al. 2007, GRB Coordinates Network, 6245

Gehrels, N., Chincarini, G., Giommi, P., et al. 2004, Astrophysical Journal, 611, 1005

Gehrels, N., Norris, J. P., Barthelmy, S. D., et al. 2006, Nature, 444, 1044

Gehrels, N., Sarazin, C. L., O'Brien, P. T., et al. 2005, Nature, 437, 851

Ghirlanda, G., Celotti, A., & Ghisellini, G. 2002, Astronomy and Astrophysics, 393, 409

Ghirlanda, G., Ghisellini, G., & Firmani, C. 2006, New Journal of Physics, 8, 123

Ghirlanda, G., Ghisellini, G., & Lazzati, D. 2004, Astrophysical Journal, 616, 331

Ghisellini, G. 2001, ArXiv Astrophysics e-prints, astro-ph/0111584

Ghisellini, G., Celotti, A., & Lazzati, D. 2000, Monthly Notices of the RAS, 313, L1

Golenetskii, S., Aptekar, R., Mazets, E., et al. 2005, GRB Coordinates Network, 4030

Golenetskii, S., Aptekar, R., Mazets, E., et al. 2006a, GRB Coordinates Network, 5710

Golenetskii, S., Aptekar, R., Mazets, E., et al. 2007a, GRB Coordinates Network, 6615

Golenetskii, S., Aptekar, R., Mazets, E., et al. 2007b, GRB Coordinates Network, 7155

Golenetskii, S., Aptekar, R., Mazets, E., et al. 2008, GRB Coordinates Network, 7482

Golenetskii, S., Aptekar, R., Mazets, E., et al. 2006b, GRB Coordinates Network, 4989

Gorosabel, J., Castro-Tirado, A. J., Guziy, S., et al. 2006, Astronomy and Astrophysics, 450, 87

Gorosabel, J., Pérez-Ramírez, D., Sollerman, J., et al. 2005, Astronomy and Astrophysics, 444, 711

Gorosabel, J., Rol, E., Covino, S., et al. 2004, Astronomy and Astrophysics, 422, 113

Gotz, D., Beckmann, V., Mereghetti, S., & Paizis, A. 2007, GRB Coordinates Network, 6607

Granot, J., Königl, A., & Piran, T. 2006, Monthly Notices of the RAS, 370, 1946

Greiner, J., Bornemann, W., Clemens, C., et al. 2008a, Publications of the ASP, 120, 405

Greiner, J., Klose, S., Reinsch, K., et al. 2003, Nature, 426, 157

Greiner, J., Kruehler, T., Fynbo, J. P. U., et al. 2008b, ArXiv e-prints, 0810.2314

Grindlay, J., Portegies Zwart, S., & McMillan, S. 2006, Nature Physics, 2, 116

Grupe, D., Burrows, D. N., Patel, S. K., et al. 2006, Astrophysical Journal, 653, 462

Guetta, D. & Piran, T. 2005, Astronomy and Astrophysics, 435, 421

Guetta, D. & Piran, T. 2006, Astronomy and Astrophysics, 453, 823

Guetta, D., Spada, M., & Waxman, E. 2001, Astrophysical Journal, 557, 399

Guidorzi, C., Mangano, V., Moretti, A., & Romano, P. 2007a, GRB Coordinates Network, 6870

Guidorzi, C., Monfardini, A., Gomboc, A., et al. 2005, Astrophysical Journal, Letters, 630, L121

Guidorzi, C., Romano, P., Vergani, S., & Moretti, A. 2007b, GRB Coordinates Network, 6192

Guidorzi, C., Vergani, S. D., Sazonov, S., et al. 2007c, Astronomy and Astrophysics, 474, 793

Haislip, J. B., Nysewander, M. C., Reichart, D. E., et al. 2006, Nature, 440, 181

Halpern, J. & Armstrong, E. 2007a, GRB Coordinates Network, 6203

Halpern, J. P. & Armstrong, E. 2007b, GRB Coordinates Network, 6195

Halpern, J. P. & Armstrong, E. 2007c, GRB Coordinates Network, 6199

Halpern, J. P. & Armstrong, E. 2007d, GRB Coordinates Network, 6208

Hammer, F., Flores, H., Schaerer, D., et al. 2006, Astronomy and Astrophysics, 454, 103

Hao, H., Stanek, K. Z., Dobrzycki, A., et al. 2007, Astrophysical Journal, Letters, 659, L99

Harrison, F. A., Yost, S. A., Sari, R., et al. 2001, Astrophysical Journal, 559, 123

Heger, A., Langer, N., & Woosley, S. E. 2000, Astrophysical Journal, 528, 368

Heise, J. 2003, in AIP Conf. Proc. 662: Gamma-Ray Burst and Afterglow Astronomy 2001: A Workshop Celebrating the First Year of the HETE Mission, ed. G. R. Ricker & R. K. Vanderspek, 229–236

Hirschi, R., Meynet, G., & Maeder, A. 2005, Astronomy and Astrophysics, 443, 581

Hjorth, J., Sollerman, J., Gorosabel, J., et al. 2005a, Astrophysical Journal, Letters, 630, L117

Hjorth, J., Watson, D., Fynbo, J. P. U., et al. 2005b, Nature, 437, 859

Holland, S. T. 2007, GRB Coordinates Network, 6194

Hopman, C., Guetta, D., Waxman, E., & Portegies Zwart, S. 2006, Astrophysical Journal, Letters, 643, L91

Hurkett, C. P., Osborne, J. P., Page, K. L., et al. 2006, Monthly Notices of the RAS, 368, 1101

Hurley, K., Boggs, S. E., Smith, D. M., et al. 2005, Nature, 434, 1098

Hurley, K., Dingus, B. L., Mukherjee, R., et al. 1994, Nature, 372, 652

Ioka, K., Kobayashi, S., & Zhang, B. 2005, Astrophysical Journal, 631, 429

Ioka, K., Toma, K., Yamazaki, R., & Nakamura, T. 2006, Astronomy and Astrophysics, 458, 7

Jakobsson, P., Fynbo, J. P. U., Ledoux, C., et al. 2006a, Astronomy and Astrophysics, 460, L13

Jakobsson, P., Fynbo, J. P. U., Paraficz, D., et al. 2005, GRB Coordinates Network, 4017

Jakobsson, P., Hjorth, J., Fynbo, J. P. U., et al. 2004, Astrophysical Journal, Letters, 617, L21

Jakobsson, P., Levan, A., Fynbo, J. P. U., et al. 2006b, Astronomy and Astrophysics, 447, 897

Jelinek, M., Kubanek, P., & Prouza, M. 2007, GRB Coordinates Network, 6197

Jensen, B. L., Fynbo, J. U., Gorosabel, J., et al. 2001, Astronomy and Astrophysics, 370, 909

Jin, Z. P. & Fan, Y. Z. 2007, Monthly Notices of the RAS, 378, 1043

Kalberla, P. M. W., Burton, W. B., Hartmann, D., et al. 2005, Astronomy and Astrophysics, 440, 775

Kann, D. A., Filgas, R., & Hoegner, C. 2007a, GRB Coordinates Network, 6206

Kann, D. A., Klose, S., & Zeh, A. 2006, Astrophysical Journal, 641, 993

Kann, D. A., Klose, S., Zhang, B., et al. 2007b, ArXiv e-prints, 0712.2186

Kann, D. A., Klose, S., Zhang, B., et al. 2008, ArXiv e-prints, 0804.1959

Karpov, S., Beskin, G., Bondar, S., et al. 2008, GRB Coordinates Network, 7452

Kelly, P. L., Kirshner, R. P., & Pahre, M. 2007, ArXiv e-prints, 0712.0430

Kennicutt, Jr., R. C. 1998, Annual Review of Astronomy and Astrophysics, 36, 189

King, A., Olsson, E., & Davies, M. B. 2007, Monthly Notices of the RAS, 374, L34

Kirk, J. G., Guthmann, A. W., Gallant, Y. A., & Achterberg, A. 2000, Astrophysical Journal, 542, 235

Klebesadel, R. W., Strong, I. B., & Olson, R. A. 1973, Astrophysical Journal, Letters, 182, L85

Klose, S., Greiner, J., Rau, A., et al. 2004, Astronomical Journal, 128, 1942

Klotz, A., Boër, M., Atteia, J. L., et al. 2005, Astronomy and Astrophysics, 439, L35

Kobayashi, S. & Zhang, B. 2003, Astrophysical Journal, 597, 455

Kobayashi, S. & Zhang, B. 2007, Astrophysical Journal, 655, 973

Kouveliotou, C., Meegan, C. A., Fishman, G. J., et al. 1993, Astrophysical Journal, Letters, 413, L101

Krimm, H. A., Boyd, P., Mangano, V., et al. 2007, GCNR, 26, 2

Krühler, T., Küpcü Yoldaş, A., Greiner, J., et al. 2008, ArXiv e-prints, 0805.2824

Kulkarni, S. R., Djorgovski, S. G., Odewahn, S. C., et al. 1999, Nature, 398, 389

Kumar, P. & Panaitescu, A. 2000, Astrophysical Journal, Letters, 541, L51

Kumar, P. & Panaitescu, A. 2003, Monthly Notices of the RAS, 346, 905

Kumar, P. & Panaitescu, A. 2008, ArXiv e-prints, 0805.0144

Kumar, P. & Piran, T. 2000, Astrophysical Journal, 532, 286

Lamb, D. Q., Donaghy, T. Q., & Graziani, C. 2004, New Astronomy Review, 48, 459

Lamb, D. Q. & Reichart, D. E. 2000, Astrophysical Journal, 536, 1

Landolt, A. U. 1992, Astronomical Journal, 104, 340

Lazzati, D. 2004, in AIP Conf. Proc. 727: Gamma-Ray Bursts: 30 Years of Discovery, ed. E. Fenimore & M. Galassi, 251–256

Lazzati, D. & Begelman, M. C. 2006, Astrophysical Journal, 641, 972

Lazzati, D., Covino, S., & Ghisellini, G. 2002, Monthly Notices of the RAS, 330, 583

Lazzati, D., Ramirez-Ruiz, E., & Ghisellini, G. 2001, Astronomy and Astrophysics, 379, L39

Le Floc'h, E., Charmandaris, V., Forrest, W. J., et al. 2006, Astrophysical Journal, 642, 636

Ledoux, C., Petitjean, P., Fynbo, J. P. U., Møller, P., & Srianand, R. 2006a, Astronomy and Astrophysics, 457, 71

Ledoux, C., Vreeswijk, P., Smette, A., Jaunsen, A., & Kaufer, A. 2006b, GRB Coordinates Network, 5237

Lee, W. H. & Ramirez-Ruiz, E. 2007, New Journal of Physics, 9, 17

Levan, A. J., Jakobsson, P., Hurkett, C., et al. 2007, Monthly Notices of the RAS, 378, 1439

Li, W., Filippenko, A. V., Chornock, R., & Jha, S. 2003, Astrophysical Journal, Letters, 586, L9

Liang, E. P. 1997, Astrophysical Journal, Letters, 491, L15

Lithwick, Y. & Sari, R. 2001, Astrophysical Journal, 555, 540

Lyutikov, M. 2006, Monthly Notices of the RAS, 367, 1594

MacFadyen, A. I. & Woosley, S. E. 1999, Astrophysical Journal, 524, 262

Maeder, A. & Meynet, G. 2000, Annual Review of Astronomy and Astrophysics, 38, 143

Maiolino, R., Marconi, A., & Oliva, E. 2001, Astronomy and Astrophysics, 365, 37

Maiorano, E., Masetti, N., Palazzi, E., et al. 2006, Astronomy and Astrophysics, 455, 423

Malesani, D., Covino, S., D'Avanzo, P., et al. 2007, Astronomy and Astrophysics, 473, 77

Malesani, D., Tagliaferri, G., Chincarini, G., et al. 2004, Astrophysical Journal, Letters, 609, L5

Mangano, V., Holland, S. T., Malesani, D., et al. 2007, Astronomy and Astrophysics, 470, 105

Masetti, N., Palazzi, E., Pian, E., et al. 2001, Astronomy and Astrophysics, 374, 382

Masetti, N., Palazzi, E., Pian, E., et al. 2003, Astronomy and Astrophysics, 404, 465

Mason, K. O., Blustin, A. J., Boyd, P., et al. 2006, Astrophysical Journal, 639, 311

Mazets, E. P., Aptekar, R. L., Cline, T. L., et al. 2008, Astrophysical Journal, 680, 545

McBreen, S., McBreen, B., Hanlon, L., & Quilligan, F. 2002, Astronomy and Astrophysics, 393, L29

McGlynn, S., Foley, S., McBreen, S., et al. 2008, Astronomy and Astrophysics, 486, 405

Medvedev, M. V. 2000, Astrophysical Journal, 540, 704

Meiring, J. D., Kulkarni, V. P., Khare, P., et al. 2006, Monthly Notices of the RAS, 370, 43

Melandri, A., Mundell, C. G., Kobayashi, S., et al. 2008, ArXiv e-prints, 0804.0811

Mereghetti, S., Paizis, A., Gotz, D., et al. 2007, GRB Coordinates Network, 6189

Mészáros, P. 2006, Reports of Progress in Physics, 69, 2259

Meszaros, P. & Rees, M. J. 1993, Astrophysical Journal, 405, 278

Meszaros, P. & Rees, M. J. 1997, Astrophysical Journal, 476, 232

Meszaros, P., Rees, M. J., & Wijers, R. A. M. J. 1998, Astrophysical Journal, 499, 301

Metzger, M. R., Djorgovski, S. G., Kulkarni, S. R., et al. 1997, Nature, 387, 878

Mihalas, D. & Auer, L. H. 1970, Astrophysical Journal, 161, 1129

Mirabal, N., Halpern, J. P., Chornock, R., et al. 2003, Astrophysical Journal, 595, 935

Mirabal, N., Halpern, J. P., Kulkarni, S. R., et al. 2002, Astrophysical Journal, 578, 818

Misra, K., Bhattacharya, D., Sahu, D. K., et al. 2007, Astronomy and Astrophysics, 464, 903

Molinari, E., Vergani, S. D., Malesani, D., et al. 2007, Astronomy and Astrophysics, 469, L13

Monfardini, A., Kobayashi, S., Guidorzi, C., et al. 2006, Astrophysical Journal, 648, 1125

Moretti, A., Baumgartner, W. H., Gehrels, N., et al. 2007, GRB Coordinates Network, 6859

Morton, D. C. 2003, Astrophysical Journal, Supplement, 149, 205

Mundell, C. G., Steele, I. A., Smith, R. J., et al. 2007, Science, 315, 1822

Nakar, E. 2007, Physics Reports, 442, 166

Nestor, D. B., Turnshek, D. A., & Rao, S. M. 2005, Astrophysical Journal, 628, 637

Nicastro, F., Fiore, F., Perola, G. C., & Elvis, M. 1999, Astrophysical Journal, 512, 184

Norris, J., Barbier, L., Burrows, D., et al. 2005, GRB Coordinates Network, 4013

Norris, J. P., Nemiroff, R. J., Bonnell, J. T., et al. 1996, Astrophysical Journal, 459, 393

Nousek, J. A., Kouveliotou, C., Grupe, D., et al. 2006, Astrophysical Journal, 642, 389

Nysewander, M., Ivarsen, K., Foster, A., et al. 2006a, GRB Coordinates Network, 4971

Nysewander, M., Reichart, D., Ivarsen, K., et al. 2006b, GRB Coordinates Network, 5545

Oates, S. R., Blustin, A. J., & Ziaeepour, H. Z. 2006, GRB Coordinates Network, 5243

O'Brien, P. T., Willingale, R., Osborne, J., et al. 2006, Astrophysical Journal, 647, 1213

Ohno, M., Uehara, T., Takahashi, T., et al. 2007, GRB Coordinates Network, 6638

Paczynski, B. 1998, Astrophysical Journal, Letters, 494, L45

Page, K., Goad, M., & Beardmore, A. 2006, GRB Coordinates Network, 5240

Palmer, D., Barbier, L., Barthelmy, S. D., et al. 2006, GRB Coordinates Network, 5551

Panaitescu, A. 2007, Monthly Notices of the RAS, 380, 374

Panaitescu, A. & Kumar, P. 2000, Astrophysical Journal, 543, 66

Panaitescu, A. & Kumar, P. 2001, Astrophysical Journal, Letters, 560, L49

Panaitescu, A. & Kumar, P. 2002, Astrophysical Journal, 571, 779

Panaitescu, A., Mészáros, P., Burrows, D., et al. 2006, Monthly Notices of the RAS, 369, 2059

Panaitescu, A. & Vestrand, W. T. 2008, ArXiv e-prints, 0803.1872

Pandey, S. B., Castro-Tirado, A. J., McBreen, S., et al. 2006, Astronomy and Astrophysics, 460, 415

Pastorello, A., Kawabata, K., Pian, E., et al. 2005, GRB Coordinates Network, 3892

Pedersen, K., Elíasdóttir, Á., Hjorth, J., et al. 2005, Astrophysical Journal, Letters, 634, L17

Pe'er, A., Mészáros, P., & Rees, M. J. 2006, Astrophysical Journal, 642, 995

Pe'er, A., Ryde, F., Wijers, R. A. M. J., Mészáros, P., & Rees, M. J. 2007, Astrophysical Journal, Letters, 664, L1

Pei, Y. C. 1992, Astrophysical Journal, 395, 130

Perez-Ramirez, D., de Ugarte Postigo, A., Gorosabel, J., et al. 2008, ArXiv e-prints, 0810.2107

Perley, D. A., Bloom, J. S., Levan, A. J., et al. 2008a, GRB Coordinates Network, 7749

Perley, D. A., Li, W., Chornock, R., et al. 2008b, ArXiv e-prints, 805

Perna, R. & Belczynski, K. 2002, Astrophysical Journal, 570, 252

Perna, R. & Lazzati, D. 2002, Astrophysical Journal, 580, 261

Perna, R., Lazzati, D., & Fiore, F. 2003, Astrophysical Journal, 585, 775

Péroux, C., Dessauges-Zavadsky, M., D'Odorico, S., Kim, T.-S., & McMahon, R. G. 2003a, Monthly Notices of the RAS, 345, 480

Péroux, C., Dessauges-Zavadsky, M., D'Odorico, S., Sun Kim, T., & McMahon, R. G. 2005, Monthly Notices of the RAS, 363, 479

Péroux, C., McMahon, R. G., Storrie-Lombardi, L. J., & Irwin, M. J. 2003b, Monthly Notices of the RAS, 346, 1103

Petitjean, P. 1999, Annales de Physique, 24, 1

Petitjean, P., Mueket, J. P., & Kates, R. E. 1995, Astronomy and Astrophysics, 295, L9

Petrovic, J., Langer, N., Yoon, S.-C., & Heger, A. 2005, Astronomy and Astrophysics, 435, 247

Pettini, M. 2004, in Cosmochemistry. The melting pot of the elements, ed. C. Esteban, R. García López, A. Herrero, & F. Sánchez, 257–298

Pettini, M., Ellison, S. L., Steidel, C. C., & Bowen, D. V. 1999, Astrophysical Journal, 510, 576

Pettini, M., Smith, L. J., Hunstead, R. W., & King, D. L. 1994, Astrophysical Journal, 426, 79

Pettini, M., Smith, L. J., King, D. L., & Hunstead, R. W. 1997, Astrophysical Journal, 486, 665

Pian, E., Mazzali, P. A., Masetti, N., et al. 2006, Nature, 442, 1011

Pian, E., Romano, P., Treves, A., et al. 2007, Astrophysical Journal, 664, 106

Piran, T. 1999a, Physics Reports, 314, 575

Piran, T. 1999b, in KITP Conference: Gamma Ray Bursts and their Afterglows

Piran, T. 2000, Physics Reports, 333, 529

Piran, T. & Shemi, A. 1993, Astrophysical Journal, Letters, 403, L67

Piranomonte, S., D'Avanzo, P., Covino, S., et al. 2008, ArXiv e-prints

Piranomonte, S., Magazzu, A., Mainella, G., et al. 2005, GRB Coordinates Network, 4032

Piranomonte, S., Vergani, S., D'Avanzo, P., & Tagliaferri, G. 2007, GRB Coordinates Network, 6612

Piro, L., Amati, L., Antonelli, L. A., et al. 1998, Astronomy and Astrophysics, 331, L41

Porciani, C., Viel, M., & Lilly, S. J. 2007, Astrophysical Journal, 659, 218

Prantzos, N. & Boissier, S. 2000, Monthly Notices of the RAS, 315, 82

Predehl, P. & Schmitt, J. H. M. M. 1995, Astronomy and Astrophysics, 293, 889

Prochaska, J. X. 1999, Astrophysical Journal, Letters, 511, L71

Prochaska, J. X., Bloom, J. S., Chen, H.-W., et al. 2004, Astrophysical Journal, 611, 200

Prochaska, J. X., Chen, H.-W., & Bloom, J. S. 2006, Astrophysical Journal, 648, 95

Prochaska, J. X., Dessauges-Zavadsky, M., Ramirez-Ruiz, E., & Chen, H.-W. 2008, Astrophysical Journal, 685, 344

Prochaska, J. X., Perley, D. A., Modjaz, M., et al. 2007, GRB Coordinates Network, 6864

Prochaska, J. X. & Wolfe, A. M. 2002, Astrophysical Journal, 566, 68

Prochter, G. E., Prochaska, J. X., & Burles, S. M. 2006a, Astrophysical Journal, 639, 766

Prochter, G. E., Prochaska, J. X., Chen, H.-W., et al. 2006b, Astrophysical Journal, Letters, 648, L93

Quilligan, F., McBreen, B., Hanlon, L., et al. 2002, Astronomy and Astrophysics, 385, 377

Quimby, R. M., Rykoff, E. S., Yost, S. A., et al. 2006, Astrophysical Journal, 640, 402

Racusin, J. L., Gehrels, N., Holland, S. T., et al. 2008a, GRB Coordinates Network, 7427

Racusin, J. L., Karpov, S. V., Sokolowski, M., et al. 2008b, ArXiv e-prints, 0805.1557

Rao, S. M., Turnshek, D. A., & Nestor, D. B. 2006, Astrophysical Journal, 636, 610

Rauch, M., Miralda-Escude, J., Sargent, W. L. W., et al. 1997, Astrophysical Journal, 489, 7

Rees, M. J. & Meszaros, P. 1994, Astrophysical Journal, Letters, 430, L93

Rees, M. J. & Meszaros, P. 1998, Astrophysical Journal, Letters, 496, L1

Rhoads, J. E. 1999, Astrophysical Journal, 525, 737

Ricker, G. R., Atteia, J.-L., Crew, G. B., et al. 2003, in American Institute of Physics Conference Series, Vol. 662, Gamma-Ray Burst and Afterglow Astronomy 2001: A Workshop Celebrating the First Year of the HETE Mission, ed. G. R. Ricker & R. K. Vanderspek, 3–16

Rol, E., Jakobsson, P., Tanvir, N., & Levan, A. 2006, GRB Coordinates Network, 5555

Rol, E., Osborne, J. P., Page, K. L., et al. 2007, Monthly Notices of the RAS, 374, 1078

Romano, P., Campana, S., Chincarini, G., et al. 2006, Astronomy and Astrophysics, 456, 917

Roming, P. W. A., Schady, P., Fox, D. B., Zhang, B., & Liang, E. 2005, Bulletin of the American Astronomical Society, 37, 1290

Roming, P. W. A., Schady, P., Fox, D. B., et al. 2006, Astrophysical Journal, 652, 1416

Ryde, F., Björnsson, C.-I., Kaneko, Y., et al. 2006, Astrophysical Journal, 652, 1400

Rykoff, E. S., Mangano, V., Yost, S. A., et al. 2006, Astrophysical Journal, Letters, 638, L5

Rykoff, E. S., Smith, D. A., Price, P. A., et al. 2004, Astrophysical Journal, 601, 1013

Rykoff, E. S., Yost, S. A., Krimm, H. A., et al. 2005a, Astrophysical Journal, Letters, 631, L121

Rykoff, E. S., Yost, S. A., Rujopakarn, W., et al. 2005b, GRB Coordinates Network, 4012

Sahu, K. C., Livio, M., Petro, L., et al. 1997, Nature, 387, 476

Sakamoto, T., Hullinger, D., Sato, G., et al. 2008, Astrophysical Journal, 679, 570

Sakamoto, T., Lamb, D. Q., Graziani, C., et al. 2004, Astrophysical Journal, 602, 875

Sakamoto, T., Lamb, D. Q., Kawai, N., et al. 2005, Astrophysical Journal, 629, 311

Salvaterra, R., Cerutti, A., Chincarini, G., et al. 2008, Monthly Notices of the RAS, 388, L6

Sari, R. 1997, Astrophysical Journal, Letters, 489, L37

Sari, R. 1998, Astrophysical Journal, Letters, 494, L49

Sari, R. & Esin, A. A. 2001, Astrophysical Journal, 548, 787

Sari, R. & Piran, T. 1997, Monthly Notices of the RAS, 287, 110

Sari, R. & Piran, T. 1999, Astrophysical Journal, 520, 641

Sari, R., Piran, T., & Halpern, J. P. 1999, Astrophysical Journal, Letters, 519, L17

Sari, R., Piran, T., & Narayan, R. 1998, Astrophysical Journal, Letters, 497, L17

Savage, B. D. & Sembach, K. R. 1996, Astrophysical Journal, 470, 893

Savaglio, S. 2006, New Journal of Physics, 8, 195

Savaglio, S., Glazebrook, K., & Le Borgne, D. 2008, ArXiv e-prints, 0803.2718

Sazonov, S. Y., Molkov, S. V., & Sunyaev, R. A. 2007, Astronomy Letters, 33, 656

Schady, P. & Falcone, A. D. 2006, GRB Coordinates Network, 4978

Schady, P., Mason, K. O., Page, M. J., et al. 2007, Monthly Notices of the RAS, 377, 273

Schady, P. & Parsons, A. 2007, GRB Coordinates Network, 6611

Schaefer, B. E., Gerardy, C. L., Höflich, P., et al. 2003, Astrophysical Journal, 588, 387

Schlegel, D. J., Finkbeiner, D. P., & Davis, M. 1998, Astrophysical Journal, 500, 525

Schmidt, M. 1999, Astrophysical Journal, Letters, 523, L117

Silva, A. I. & Viegas, S. M. 2001, Computer Physics Communications, 136, 319

Silva, A. I. & Viegas, S. M. 2002, Monthly Notices of the RAS, 329, 135

Soderberg, A. M., Nakar, E., Cenko, S. B., et al. 2007, Astrophysical Journal, 661, 982

Soderberg, A. M. & Ramirez-Ruiz, E. 2002, Monthly Notices of the RAS, 330, L24

Sollerman, J., Fynbo, J. P. U., Gorosabel, J., et al. 2007, Astronomy and Astrophysics, 466, 839

Sollerman, J., Östlin, G., Fynbo, J. P. U., et al. 2005, New Astronomy, 11, 103

Spruit, H. C. 2002, Astronomy and Astrophysics, 381, 923

Staff, J., Ouyed, R., & Bagchi, M. 2007, Astrophysical Journal, 667, 340

Stanek, K. Z., Dai, X., Prieto, J. L., et al. 2007, Astrophysical Journal, Letters, 654, L21

Stanek, K. Z., Garnavich, P. M., Jha, S., et al. 2001, Astrophysical Journal, 563, 592

Starling, R. L. C., van der Horst, A. J., Rol, E., et al. 2008, Astrophysical Journal, 672, 433

Starling, R. L. C., Vreeswijk, P. M., Ellison, S. L., et al. 2005a, Astronomy and Astrophysics, 442, L21

Starling, R. L. C., Wijers, R. A. M. J., Hughes, M. A., et al. 2005b, Monthly Notices of the RAS, 360, 305

Starling, R. L. C., Wijers, R. A. M. J., Wiersema, K., et al. 2007, Astrophysical Journal, 661, 787

Stratta, G., D'Avanzo, P., Piranomonte, S., et al. 2007, Astronomy and Astrophysics, 474, 827

Stratta, G., Fiore, F., Antonelli, L. A., Piro, L., & De Pasquale, M. 2004, Astrophysical Journal, 608, 846

Sudilovsky, V., Savaglio, S., Vreeswijk, P., et al. 2007, Astrophysical Journal, 669, 741

Tagliaferri, G., Antonelli, L. A., Chincarini, G., et al. 2005a, Astronomy and Astrophysics, 443, L1

Tagliaferri, G., Goad, M., Chincarini, G., et al. 2005b, Nature, 436, 985

Tagliaferri, G., Malesani, D., Vergani, S. D., et al. 2006, Nuovo Cimento B, proceedings of the conference "SWIFT and GRBs: Unveiling the Relativistic Universe", 121, 1163

Tanvir, N. R., Barnard, V. E., Blain, A. W., et al. 2004, Monthly Notices of the RAS, 352, 1073

Tanvir, N. R., Chapman, R., Levan, A. J., & Priddey, R. S. 2005, Nature, 438, 991

Taylor, G. B., Frail, D. A., Berger, E., & Kulkarni, S. R. 2004, Astrophysical Journal, Letters, 609, L1

Tejos, N., Lopez, S., Prochaska, J. X., Chen, H.-W., & Dessauges-Zavadsky, M. 2007, Astrophysical Journal, 671, 622

Thoene, C. C., Kann, D. A., Johannesson, G., et al. 2008, ArXiv e-prints, 0806.1182

Torii, K. 2005, GRB Coordinates Network, 3674

Tueller, J., Barbier, L., Barthelmy, S., et al. 2006, GRB Coordinates Network, 5242

Tytler, D. & Fan, X.-M. 1994, Astrophysical Journal, Letters, 424, L87

Unsöld, A., Struve, O., & Elvey, C. T. 1930, Zeitschrift fur Astrophysik, 1, 314

Usov, V. V. 1992, Nature, 357, 472

van Marle, A. J., Langer, N., Yoon, S.-C., & García-Segura, G. 2008, Astronomy and Astrophysics, 478, 769

van Paradijs, J., Groot, P. J., Galama, T., et al. 1997, Nature, 386, 686

Vergani, S. 2008, International Journal of Modern Physics D, Proceedings of the "High Energy Phenomena in Relativistic Outflows" workshop, September 24-28, 2007 Dublin, Ireland

Vergani, S. D. 2007, Astrophysics and Space Science, 311, 197

Vergani, S. D., Molinari, E., Zerbi, F. M., & Chincarini, G. 2004, Astronomy and Astrophysics, 415, 171

Vestrand, W. T., Wozniak, P. R., Wren, J. A., et al. 2005, Nature, 435, 178

Vestrand, W. T., Wren, J. A., Wozniak, P. R., et al. 2006, Nature, 442, 172

Vietri, M. & Stella, L. 1998, Astrophysical Journal, Letters, 507, L45

Villar-Sbaffi, A., St-Louis, N., Moffat, A. F. J., & Piirola, V. 2006, Astrophysical Journal, 640, 995

Villasenor, J. S., Lamb, D. Q., Ricker, G. R., et al. 2005, Nature, 437, 855

Vink, J. S. 2007, Astronomy and Astrophysics, 469, 707

Vladilo, G. 1998, Astrophysical Journal, 493, 583

Vladilo, G. 2002, Astronomy and Astrophysics, 391, 407

Vladilo, G., Centurión, M., Levshakov, S. A., et al. 2006, Astronomy and Astrophysics, 454, 151

Vreeswijk, P. & Jaunsen, A. 2006, GRB Coordinates Network, 4974

Vreeswijk, P. M., Ellison, S. L., Ledoux, C., et al. 2004, Astronomy and Astrophysics, 419, 927

Vreeswijk, P. M., Ledoux, C., Smette, A., et al. 2007, Astronomy and Astrophysics, 468, 83

Vreeswijk, P. M., Smette, A., Fruchter, A. S., et al. 2006, Astronomy and Astrophysics, 447, 145

Vreeswijk, P. M., Smette, A., Malesani, D., et al. 2008, GRB Coordinates Network, 7444

Wainwright, C., Berger, E., & Penprase, B. E. 2007, Astrophysical Journal, 657, 367

Watson, D., Fynbo, J. P. U., Ledoux, C., et al. 2006a, Astrophysical Journal, 652, 1011

Watson, D., Hjorth, J., Fynbo, J. P. U., et al. 2007, Astrophysical Journal, Letters, 660, L101

Watson, D., Hjorth, J., Jakobsson, P., et al. 2006b, Astronomy and Astrophysics, 454, L123

Watson, D., Reeves, J. N., Hjorth, J., et al. 2006c, Astrophysical Journal, Letters, 637, L69

Waxman, E. & Draine, B. T. 2000, Astrophysical Journal, 537, 796

Wei, D. M., Yan, T., & Fan, Y. Z. 2006, Astrophysical Journal, Letters, 636, L69

Weingartner, J. C. & Draine, B. T. 2000, in Bulletin of the American Astronomical Society, Vol. 32, Bulletin of the American Astronomical Society, 1466

Wiersema, K., Rol, E., Starling, R., et al. 2005, GRB Coordinates Network, 3699

Wijers, R. A. M. J. 2001, in Gamma-ray Bursts in the Afterglow Era, ed. E. Costa, F. Frontera, & J. Hjorth, 306

Wijers, R. A. M. J., Vreeswijk, P. M., Galama, T. J., et al. 1999, Astrophysical Journal, Letters, 523, L33

Williams, B. J., Borkowski, K. J., Reynolds, S. P., et al. 2006, Astrophysical Journal, Letters, 652, L33

Wilson, O. C. 1939, Astrophysical Journal, 90, 244

Wolfe, A. M., Turnshek, D. A., Smith, H. E., & Cohen, R. D. 1986, Astrophysical Journal, Supplement, 61, 249

Woosley, S. E. 1993, Astrophysical Journal, 405, 273

Woosley, S. E. & Bloom, J. S. 2006, Annual Review of Astronomy and Astrophysics, 44, 507

Woosley, S. E. & Heger, A. 2006, Astrophysical Journal, 637, 914

Wozniak, P. R., Vestrand, W. T., Panaitescu, A. D., et al. 2008, ArXiv e-prints, 0810.2481

Woźniak, P. R., Vestrand, W. T., Wren, J. A., et al. 2005, Astrophysical Journal, Letters, 627, L13

Woźniak, P. R., Vestrand, W. T., Wren, J. A., et al. 2006, Astrophysical Journal, Letters, 642, L99

Wren, J., Vestrand, W. T., Wozniak, P. R., White, R., & Pergande, J. 2007, GRB Coordinates Network, 6198

Yoon, S.-C. & Langer, N. 2005, Astronomy and Astrophysics, 443, 643

Yoon, S.-C. & Langer, N. 2006, in Astronomical Society of the Pacific Conference Series, Vol. 353, Stellar Evolution at Low Metallicity: Mass Loss, Explosions, Cosmology, ed. H. J. G. L. M. Lamers, N. Langer, T. Nugis, & K. Annuk, 63

Yoon, S.-C., Langer, N., Cantiello, M., Woosley, S. E., & Glatzmaier, G. A. 2008, in IAU Symposium, Vol. 250, 231–236

Zerbi, R. M., Chincarini, G., Ghisellini, G., et al. 2001, Astronomische Nachrichten, 322, 275

Zhang, B. 2006, Nature, 444, 1010

Zhang, B., Fan, Y. Z., Dyks, J., et al. 2006, Astrophysical Journal, 642, 354

Zhang, B. & Kobayashi, S. 2005, Astrophysical Journal, 628, 315

Zhang, B. & Mészáros, P. 2004, International Journal of Modern Physics A, 19, 2385

Ziaeepour, H. Z., Barthelmy, S. D., Gehrels, N., et al. 2006, GRB Coordinates Network, 5233